

Review of laser-driven ion sources and their applications

This content has been downloaded from IOPscience. Please scroll down to see the full text.

2012 Rep. Prog. Phys. 75 056401

(<http://iopscience.iop.org/0034-4885/75/5/056401>)

View the [table of contents for this issue](#), or go to the [journal homepage](#) for more

Download details:

IP Address: 149.220.164.158

This content was downloaded on 28/01/2015 at 15:13

Please note that [terms and conditions apply](#).

Review of laser-driven ion sources and their applications

Hiroyuki Daido^{1,2,4}, Mamiko Nishiuchi³ and Alexander S Pirozhkov^{3,4}

¹ Applied Laser Technology Institute, Tsuruga Head Office, Japan Atomic Energy Agency, Kizaki, Tsuruga-shi, Fukui-ken 914-8585, Japan

² Quantum Beam Science Directorate, 8-1-7 Umemidai, Kizugawa-shi, Kyoto-fu 619-0215, Japan

³ Advanced Beam Technology Division, Quantum Beam Science Directorate (at Kansai Photon Science Institute), Japan Atomic Energy Agency, 8-1-7 Umemidai, Kizugawa-shi, Kyoto-fu 619-0215, Japan

E-mail: pirozhkov.alexander@jaea.go.jp (A S Pirozhkov) and daido.hiroyuki@jaea.go.jp (H Daido)

Received 3 May 2011, in final form 22 November 2011

Published 17 April 2012

Online at stacks.iop.org/RoPP/75/056401

Abstract

For many years, laser-driven ion acceleration, mainly proton acceleration, has been proposed and a number of proof-of-principle experiments have been carried out with lasers whose pulse duration was in the nanosecond range. In the 1990s, ion acceleration in a relativistic plasma was demonstrated with ultra-short pulse lasers based on the chirped pulse amplification technique which can provide not only picosecond or femtosecond laser pulse duration, but simultaneously ultra-high peak power of terawatt to petawatt levels. Starting from the year 2000, several groups demonstrated low transverse emittance, tens of MeV proton beams with a conversion efficiency of up to several percent. The laser-accelerated particle beams have a duration of the order of a few picoseconds at the source, an ultra-high peak current and a broad energy spectrum, which make them suitable for many, including several unique, applications. This paper reviews, firstly, the historical background including the early laser-matter interaction studies on energetic ion acceleration relevant to inertial confinement fusion. Secondly, we describe several implemented and proposed mechanisms of proton and/or ion acceleration driven by ultra-short high-intensity lasers. We pay special attention to relatively simple models of several acceleration regimes. The models connect the laser, plasma and proton/ion beam parameters, predicting important features, such as energy spectral shape, optimum conditions and scalings under these conditions for maximum ion energy, conversion efficiency, etc. The models also suggest possible ways to manipulate the proton/ion beams by tailoring the target and irradiation conditions. Thirdly, we review experimental results on proton/ion acceleration, starting with the description of driving lasers. We list experimental results and show general trends of parameter dependences and compare them with the theoretical predictions and simulations. The fourth topic includes a review of scientific, industrial and medical applications of laser-driven proton or ion sources, some of which have already been established, while the others are yet to be demonstrated. In most applications, the laser-driven ion sources are complementary to the conventional accelerators, exhibiting significantly different properties. Finally, we summarize the paper.

(Some figures may appear in colour only in the online journal)

This article was invited by G Leuchs.

⁴ Authors to whom any correspondence should be addressed.

Contents

1. Introduction	2	<i>3.6. Laser-driven quasi-monoenergetic ion acceleration</i>	41
2. Mechanisms of laser-driven ion acceleration	5	<i>3.7. New target designs</i>	42
<i>2.1. Absorption of laser pulse in a plasma</i>	6	<i>3.8. Multi-pulse schemes</i>	43
<i>2.2. Acceleration by the electric charge-separation field at the target rear</i>	6	<i>3.9. Proton and heavier ion acceleration with lower density targets</i>	43
<i>2.3. Double-layer target in the Coulomb explosion regime</i>	13	<i>3.10. Section 3 summary</i>	44
<i>2.4. Coulomb explosion of a cluster</i>	15		
<i>2.5. Influence of the incidence angle</i>	16	4. Applications of laser-driven ion sources	45
<i>2.6. Radiation pressure dominant acceleration (the laser piston regime)</i>	16	<i>4.1. Laser-driven ion source properties</i>	45
<i>2.7. Hole boring and collisionless shock acceleration</i>	20	<i>4.2. Beam power and intensity of laser-driven ion sources</i>	46
<i>2.8. Ion acceleration with a dipole vortex in near-critical plasma</i>	21	<i>4.3. Applications which require high peak power, ultra-short proton/ion beams</i>	47
<i>2.9. Scalings in the optimum and non-optimum regimes</i>	24	<i>4.4. Applications which require repetitive, high average power proton/ion beams</i>	50
<i>2.10. Relations between the acceleration regimes</i>	24	<i>4.5. High-energy electron beam transport characterization</i>	54
<i>2.11. Achieving therapeutic ion energies: theoretical consideration</i>	27	<i>4.6. Space-related applications</i>	54
3. Experimental results of laser-driven ion acceleration	27	<i>4.7. Research activities towards laser-driven proton and ion medical accelerators</i>	55
<i>3.1. Present laser systems for ion acceleration</i>	27	<i>4.8. Demonstration of beam monochromatization and transport systems</i>	56
<i>3.2. On the contrast requirements</i>	28	<i>4.9. Section 4 summary</i>	58
<i>3.3. Proton and ion diagnostic instruments</i>	31		
<i>3.4. Proton acceleration from laser-irradiated thin foils</i>	36	5. Summary and future prospects	59
<i>3.5. Laser-driven heavy ion acceleration</i>	40	Acknowledgments	60
		References	60

1. Introduction

Laser-driven ion acceleration and its applications are now actively studied all over the world. By ions we here mean protons as well as greater mass ions; later in the text we will distinguish them, where necessary. The significant features of laser-driven ion beams compared with conventional ion accelerators are that the effective source size of ion emission is extremely small, typically it is $\sim 10 \mu\text{m}$. Another important feature is the ultra-short duration at the source of the ion bunch of the order of picoseconds. The acceleration gradients are of the order of $\text{MeV} \mu\text{m}^{-1}$, compared with $\sim \text{MeV m}^{-1}$ provided by radio frequency (RF) wave based accelerators. Although the laser-driven technique inherently has significant merits from the point of view of many unique applications, one still has numerous issues to overcome, such as increasing the particle energy, spectral and angular control of the beam, conversion efficiency from laser energy into the ion beam, possible activation issues, as well as stability of the acceleration parameters. Since the technology based on high-intensity short pulse lasers is really a new one, one can expect that it will bring completely new kinds of applications. Studies of physical processes involved in this technique also contribute to the extension of the field of laser interaction with matter and plasma, which is one of the fruitful research fields in the laser and plasma sciences.

In this paper, we firstly review the historic background of the present laser-driven ion sources, including plasma-based

accelerator concepts as well as laser–matter interaction physics, which makes energetic electrons and ions.

Since the first laser action was demonstrated by Maiman (1960) (Schawlow and Townes 1958, Basov *et al* 1961), laser sources generating ultra-high peak power and short wavelength electromagnetic waves have been developed with shorter and shorter pulse widths (Mourou *et al* 1998). In the 1970s, research on laser interaction with plasmas began, mainly motivated by laser-induced nuclear fusion (Nuckolls *et al* 1972). For this purpose, powerful CO₂ lasers (e.g. Apollonov *et al* 1980, Carlson *et al* 1981, Yamanaka *et al* 1981a) and glass lasers (e.g. Ahlstrom 1981, Yamanaka *et al* 1981b) were constructed. In particular, CO₂ lasers with a wavelength of $10 \mu\text{m}$ caused collective processes such as resonance absorption (Ginsburg 1961, Forslund *et al* 1977, Estabrook and Krueer 1978) as well as enhanced resonant absorption due to target surface rippling (Bach *et al* 1983), in which the absorbed laser energy went into hot electrons and then converted into energetic ions via charge-separation fields (Forslund and Brackbill 1982, Gitomer *et al* 1986). In the fusion context, the hot electrons, causing preheating of the compressed core plasma, appeared to be unsuitable as carriers of absorbed laser energy for efficient ablative target compression. In addition, energetic ions caused by the hot electrons brought a significant fraction of the absorbed laser energy away from the compressed region. Therefore, the CO₂ laser programmes declined, although many interesting scientific results were reported.

Enormous current density of the hot electrons produced with a high-power laser, which cannot be obtained with any other technique, produces megagauss class magnetic fields in a plasma (see Benjamin *et al* (1979), Yates *et al* (1982) and Stamper (1991) and references therein) and in laser-driven well-defined configurations such as straight bar (Hauer and Mason 1983), one turn coil (e.g. Daido *et al* 1986) and so on. In the 1980s, energetic (sub-MeV) proton acceleration in a corona plasma with a laser-driven strong magnetic field was proposed (Forslund and Brackbill 1982). This interpretation qualitatively explained the energetic (fast) proton and ion acceleration with the use of mainly CO₂ lasers (e.g. Priedhorsky *et al* 1981, Bach *et al* 1983, Villeneuve *et al* 1983, Tan *et al* 1984). Even at this stage, the irradiance of CO₂ lasers of $\sim 10^{16}$ W cm⁻² enters the relativistic regime, see (1.1) below. Some of the interesting phenomena might be explained by the relativistic effects (e.g. Carman *et al* 1981, Priedhorsky *et al* 1981, Bach *et al* 1983).

The first proposal of plasma-based ion acceleration was made in the 1950s (Veksler 1956). The concept was tested utilizing an induced electric field driven by an electron beam injected into a plasma (e.g. Mako and Tajima 1984). Model calculations of isothermal expansion of plasmas into vacuum, estimating the charge-separation fields which can potentially accelerate ions, were performed by Gurevich *et al* (1965) and Crow *et al* (1975). Then successive analyses were published by several authors (e.g. Denavit 1979, Kishimoto *et al* 1983). The main motivation of these plasma expansion studies was laser-plasma interaction and the energetic or fast ion energy loss for laser-induced fusion. The accelerated proton or ion energy was far below 1 MeV even though building-sized laser installations were employed. People had to wait for ultra-short pulse and ultra-high-intensity lasers and relevant experiments, which are described below.

In the 1990s, ultra-high peak power and ultra-short pulse (sub-ps to a few tens of fs) lasers were realized with the invention of the chirped pulse amplification (CPA) technique (Strickland and Mourou 1985) coupled with the invention of the Kerr lens mode-locking technique (Sarukura *et al* 1991, Spence *et al* 1991) as well as discovery of the titanium : sapphire (Ti : sapphire) laser medium (Moulton 1986). The peak power of CPA lasers is much higher than that of building-sized laser installations available in the 1980s, while the size is much smaller, typically tens of metres. At present, the achieved peak power is petawatt (PW, 10^{15} W) (Perry and Mourou 1994, Mourou *et al* 2006), which is one million times higher than a gigawatt electric power plant, although the lasers deliver this power in an ultra-short pulse only. Multi-PW and exawatt (EW, 10^{18} W) lasers are now under construction and planned to be built (Dunne 2006, Chambaret *et al* 2010). Details of the laser systems are reviewed in section 3.1. The availability of lasers with such capabilities stimulated active development of high-intensity physics, including laser-pumped x-ray lasers (Daido 2002), high-order harmonic generation followed by attosecond science (Corkum and Krausz 2007), electron acceleration (Esarey *et al* 2009), as well as ion acceleration (Borghesi *et al* 2006, this review).

When an ultra-high peak power laser pulse interacts with a target, a plasma is inevitably created due to heating and breakdown by a relatively long preceding light or, if it is suppressed, due to the optical field ionization (Keldysh 1964, review by Popov V S 2004) by the main pulse's foot. The plasma consists of charged particles, i.e. electrons and ions. First, we consider the motion of individual charged particles, i.e. their motion in vacuum.

The particles with the largest charge-to-mass ratio, namely the electrons, are accelerated by the laser first. The motion of electrons in this regime is governed by the dimensionless laser amplitude

$$a_0 = \frac{eE_0}{m_e c \omega} = \sqrt{\frac{I_0}{I_1}},$$

$$I_1 = 1.37 \times 10^{18} \text{ W cm}^{-2} (\mu\text{m}/\lambda)^2, \quad (1.1)$$

where e and m_e are the electron charge and mass, c is the velocity of light in vacuum, and I_0 , E_0 , λ and ω are the laser peak intensity (irradiance), electric field, wavelength and angular frequency, respectively. (In this review the laser wavelength and angular frequency are also denoted as λ_0 and ω_0 , respectively.) The value of I_1 is given here for linear polarization; for circular polarization, it is two times greater. For a typical laser wavelength of $\sim 1 \mu\text{m}$ and $I_0 \gg 10^{18} \text{ W cm}^{-2}$, the dimensionless amplitude is much larger than unity. In this case, a significant number of plasma electrons is accelerated up to the relativistic velocity during a few cycles of the laser electric field. Such a plasma is called a ‘relativistic plasma’ (Bulanov S V *et al* 1992, 1994, Mourou *et al* 2006), which has several unique features, for example, the relativistic plasma is essentially collisionless (Pegoraro *et al* 2005). Further, under the action of a high-irradiance laser, electron motion is governed by both magnetic and electric fields in the form of the Lorentz force. The electrons are accelerated towards the laser propagation direction; typical electron trajectories in vacuum under the action of plane electromagnetic waves are shown in figure 1. Note that in the case of ions the analogous dimensionless amplitude $a_i = eE_0/m_i c \omega$, where m_i is the ion mass, remains much less than unity for all experiments performed up to now and in nearly all theories and simulations discussed in this review; the irradiance value corresponding to $a_i = 1$ for protons is $I_i \approx 5 \times 10^{24} \text{ W cm}^{-2} (\mu\text{m}/\lambda)^2$.

In contrast to vacuum, in a plasma, and especially in a dense plasma, the particle motion is significantly affected by the collective fields, and the laser pulse itself is modified by non-linearities. While the electrons are pushed forward, the heavier ions respond slower, and relatively slowly varying (quasi-static) charge-separation fields are formed between the displaced electrons and the rest of the plasma. In addition, the electron current leads to quasi-static magnetic field generation. At a longer time scale protons, which have the highest charge-to-mass ratio among the ions, are accelerated by the slowly varying plasma fields, followed by heavier ions. We note that the protons, unless specially removed, are present on all solid targets as a part of hydrocarbon and water contamination. The relativistic effects essentially contribute

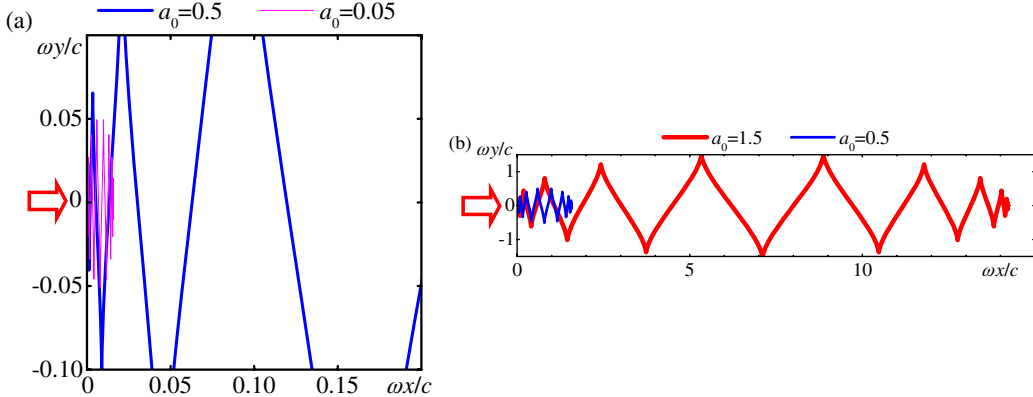


Figure 1. Trajectories of an electron in vacuum in the given optical fields of ultra-short linearly polarized plane electromagnetic waves representing laser pulses with different dimensionless amplitudes a_0 (1.1) for the pulse duration of $\tau_0 \approx 24/\omega$ (10 fs for $\lambda = 800$ nm); the laser is incident from the left as indicated by the arrows. The maximum electron displacement perpendicular to the pulse propagation is $a_0 c/\omega$, while the forward displacement (along the pulse propagation direction) is proportional to $a_0^2 \tau_0 c$. (a) The amplitudes are $a_0 = 0.05$ and 0.5 (part of the trajectory), (b) $a_0 = 0.5$ and 1.5, full trajectories. In each frame, the horizontal and vertical scales are equal; however, note the difference in the scales between the frames. At $a_0 = 0.05$, the intensity is much lower than the relativistic intensity, the perpendicular displacement is much larger than the forward displacement in one period. At $a_0 = 1.5$, the intensity is relativistic ($\approx 3 \times 10^{18} \text{ W cm}^{-2}$ at the laser wavelength of 1 μm), the forward displacement in one period exceeds the perpendicular one.

to the efficient acceleration of proton and ion beams. Details of the acceleration mechanisms are reviewed in section 2.

A particularly important property of plasmas is the laser light absorption. Historically, the resonance absorption (Ginsburg 1961, Forslund *et al* 1977, Estabrook and Krueer 1978) is one of the most important absorption mechanisms which is responsible for hot electron production by high-intensity nanosecond laser pulses. In the ultra-high-intensity ($I\lambda^2 > 10^{18} \text{ W cm}^{-2} \mu\text{m}^2$), ultra-short (pulse duration $\tau <$ picosecond) pulse regime, other absorption mechanisms become important, depending upon the plasma conditions and laser parameters (see later in section 2.1). Absorption in the ultra-high-intensity regime has been studied by many authors, both theoretically (Brunel 1987, Denavit 1992, Wilks *et al* 1992) and experimentally (Price *et al* 1995, Malka G and Miquel 1996, Beg *et al* 1997, Borghesi *et al* 1999, Ping *et al* 2008). The absorption is reviewed by Wilks and Krueer (1997) and Davies (2009).

Let us return back to the brief history in the 1990s. Hot electrons and energetic ions were paid much more attention after ultra-short and ultra-high peak power lasers appeared in the 1990s. Fews *et al* (1994) demonstrated plasma ion emission with energy of slightly more than 1 MeV from a picosecond laser pulse irradiated solid target in the fast ignition laser fusion research. Theoretical and computational studies were performed (e.g. Esirkepov *et al* 1999, Zhidkov *et al* 1999, Zhidkov and Sasaki 2000). Laser-driven ion acceleration attracted considerable attention when an intense proton beam with a maximum energy of 55 MeV was observed in 2000 (Snavely *et al* 2000, Hatchett *et al* 2000). In addition to such a proof-of-principle experiment using a single-shot based laser, various experiments were performed for the study of fundamental processes and their mechanisms (e.g. Krushelnick *et al* 2000b, Maksimchuk *et al* 2000, 2004, Murakami Y *et al* 2001, Mackinnon *et al* 2001, 2002, Nemoto *et al* 2001, Spencer *et al* 2001, 2003, Zepf *et al* 2001, Hegelich *et al* 2002, 2005, Roth *et al* 2002, 2005, Fritzler *et al* 2003, Fuchs

et al 2003, 2005, Matsukado *et al* 2003, McKenna *et al* 2003, 2004, 2005, Patel *et al* 2003, Borghesi *et al* 2004, Cowan *et al* 2004, Kaluza *et al* 2004, Ruhl *et al* 2004, Schreiber *et al* 2004, Oishi *et al* 2005, Ter-Avetisyan *et al* 2005) as well as on applications of the proton and ion beams (Borghesi *et al* 2006). Details of the experimental results are reviewed in section 3. Among the applications which have already been demonstrated are the plasma diagnostic techniques with the proton beam as a probe (Borghesi *et al* 2001; see also section 4 of this paper). Short proton beam duration, low emittance and large particle number allow measuring transient electric field distributions (Romagnani *et al* 2005). A nearly instantaneously generated proton bunch with a broad energy spectrum becomes chirped as it propagates from the target, i.e. exhibiting a regular temporal structure in which more energetic (faster) protons are situated at the front of the bunch followed by slower and slower protons. Such a property enables performing multi-frame (Borghesi *et al* 2001) or continuous time evolution measurements (Sokollik *et al* 2008, Ter-Avetisyan *et al* 2008a). There are many other promising applications of laser-driven proton/ion sources. Conventional RF wave based accelerators can benefit from a compact, low-emittance, ultra-short ion source which can be used as an injector for the post-acceleration stage (Krushelnick *et al* 2000a, Noda *et al* 2006, Antici *et al* 2008b). Proton and ion cancer therapy, which is now a popular treatment with conventional accelerators (Goitein *et al* 2002), can benefit from down-sizing the accelerator and decreasing its cost if a compact, high-quality laser-driven accelerator can be developed (Bulanov S V and Khoroshkov 2002a, Bulanov S V *et al* 2002b, 2004b, Fourkal *et al* 2003a, 2003b, Malka V *et al* 2004, Murakami M *et al* 2008, Bolton *et al* 2010). High energy density and short bunch duration of laser-driven ion beams allow heating of matter before it hydrodynamically expands (isochoric heating), producing warm dense matter (WDM) (Patel *et al* 2003, Dyer *et al* 2008). Protons and ions are promising alternatives (Roth *et al* 2001, Bychenkov *et al*

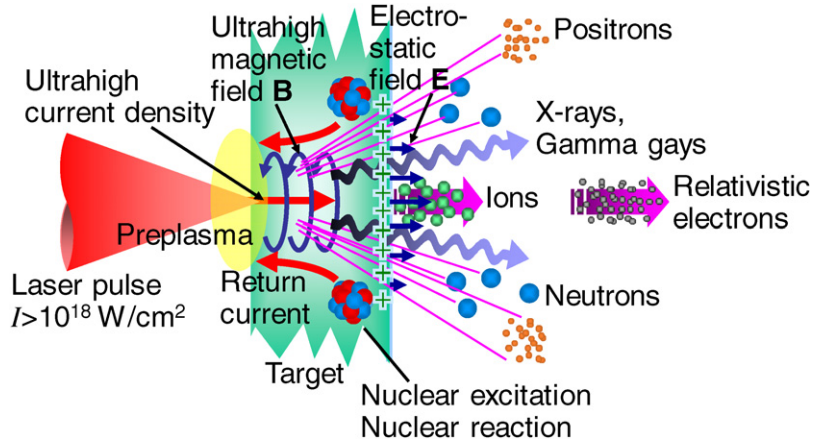


Figure 2. Sketch of the ultra-high intensity laser interacting with a plasma. Electrons are preferentially accelerated forward, towards the target rear side, followed by ion acceleration via the electric charge-separation field, which is one of the typical scenarios of ion acceleration. The relativistic plasma emits high-energy electrons, ions, incoherent x-rays as well as coherent high-order harmonics up to the x-ray spectral region. It also emits intense electromagnetic waves such as terahertz wave and can generate secondary particles and radiation such as neutrons, pions, hard x-ray and gamma radiation, neutrinos and so on. Note that the red arrows marked ‘Ultrahigh current density’ and ‘Return current’ point towards the electron motion, while the electric currents themselves are opposite to the arrow directions.

2001b) to electrons in fast ignition (Tabak *et al* 1994) in laser-driven fusion, because they exhibit simpler interaction with a high-density plasma and nearly ballistic propagation with the possibility of focusing or collimation (Sentoku *et al* 2000, Patel *et al* 2003). In addition, limited-bandwidth or quasi-monoenergetic proton/ion bunches have a localized energy deposition, Bragg peak (Bortfeld 1997) and propagate with a small elongation, which allows one to avoid (Honrubia *et al* 2009) the re-entrant cone (Kodama *et al* 2001). A laser-driven proton beam can be used for the production of radioactive materials for medical applications (Fritzler *et al* 2003, Ledingham *et al* 2004) and also for a thin layer activation (TLA) technique for tool wear testing (Ogura *et al* 2009). Compact laser-driven ion sources can also be used for laboratory-based radiobiological (Yogo *et al* 2009, 2011, Kraft *et al* 2010) and space research, material processing (Boody *et al* 1996) and so on. Details of the various applications are reviewed in section 4.

In the relativistic laser–plasma interaction, laser-irradiated targets emit high-energy electrons with broad spectra, incoherent x-rays, as well as coherent high-order harmonics (Bulanov S V *et al* 1994, Teubner and Gibbon 2009) as shown schematically in figure 2. They also emit intense electromagnetic waves such as terahertz (THz) waves (Hamster *et al* 1993, Sagisaka *et al* 2008, Wu *et al* 2008). Secondary particles and radiation such as neutrons (Norreys *et al* 1998, Ditmire *et al* 1999, Tanaka *et al* 2000), hard, up to multi-MeV photon energies, x-rays (Norreys *et al* 1999, Schwoerer *et al* 2001) and positrons (Cowan *et al* 1999) are also generated. There are proposals to generate pions (Bychenkov *et al* 2001a) and neutrinos (Bulanov S V *et al* 2005b, Terranova *et al* 2005) using laser-driven proton sources. Multiple quantum beams are inherently delivered simultaneously, in femtosecond or at most picosecond time scales, providing the possibility to employ new multiple beam pump-probe techniques, some of which will be briefly described in this review. Further details of these phenomena can be found in

Daido *et al* (2007). For completeness of the introduction and brief description of relativistic laser plasmas, we mention that in a low-density plasma ($\sim 10^{-5}$ – 10^{-4} of solid density), the longitudinal slowly oscillating field of a wake wave with phase velocity approaching c leads to electron acceleration (Tajima and Dawson 1979), which was experimentally realized up to GeV energies, including demonstration of mono-energetic electron bunches (e.g. Malka *et al* 2002, Modena *et al* 2002, Leemans *et al* 2006, Hafz *et al* 2008, Esarey *et al* 2009).

Various regimes of high-power laser–plasma interactions relevant to laser-driven ion/proton sources are depicted in figure 3 in the plane (intensity, pulse duration). One should bear in mind that these are two very important, but not the only parameters, and this figure presents some of the aspects but does not cover all the exciting possibilities which have been demonstrated and predicted, or have yet to be explored.

In the following, we describe the physical mechanisms of ion acceleration in section 2, experimental results on proton and ion accelerations in section 3 and application aspects in section 4.

2. Mechanisms of laser-driven ion acceleration

In this section, we describe several mechanisms of ion acceleration relevant to present experiments as well as promising new regimes, which are yet to be demonstrated experimentally. Our primary interest here is to find simple scaling laws which allow estimation of the achievable parameters of ion beams, in particular, the maximum ion energy, shape of the energy spectrum, etc. One should be careful, though, as the real laser-driven ion acceleration is a very complex process involving many physical phenomena at each interaction stage starting from ionization (see section 1), initial preplasma formation (see later in section 3.2), coupling (absorption) of the main pulse energy to the electrons (section 2.1), plasma evolution driven by the laser and

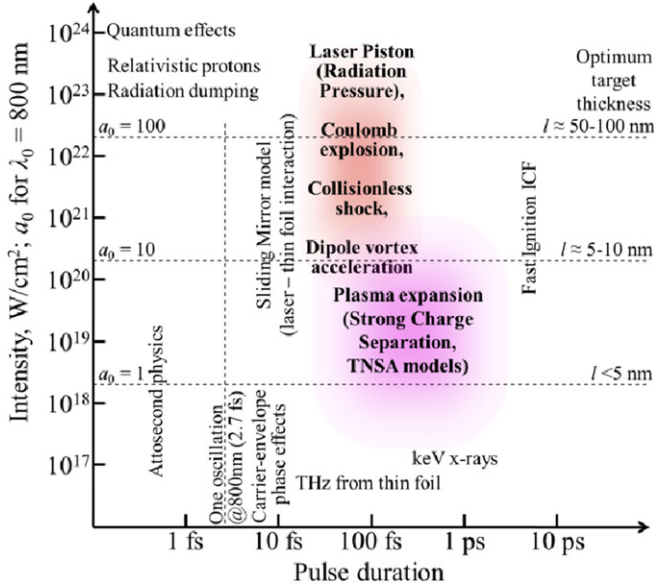


Figure 3. Some of the possible regimes and applications of high-intensity short-pulse laser–plasma interaction, many of which are described in this review, on the (intensity, pulse duration) plane. The regimes actually have no sharp borders, neither are they well separated; rather, they overlap with each other. The present PW (petawatt: 10^{15} W)-class lasers can achieve amplitudes (1.1) $a_0 \sim 100$, while future 10–100 PW lasers will achieve $a_0 \gg 100$. The target thickness l on the right corresponds to a characteristic optimum thickness for many high-contrast laser–thin-foil interaction regimes, including the sliding mirror model (Vshivkov *et al* 1998, Pirozhkov *et al* 2006a, 2006b) and several ion acceleration mechanisms, see sections 2.3 and 2.6 and equations (2.20) and (2.39) (here the electron density $n_e = 460n_{cr}$ is assumed, as e.g. in a fully ionized diamond-like carbon for $\lambda_0 = 800$ nm). ICF and TNSA stand for the inertial confinement fusion and target normal sheath acceleration, respectively.

collective plasma fields, and finally ion propagation during and after the acceleration process. Based on limited diagnostic capabilities, it may be difficult to determine a dominant acceleration mechanism (see also section 2.10). The parameters of plasma are typically not known precisely, either. For these reasons, models that calculate ion beam parameters starting from laser parameters often include phenomenological assumptions, which have some (limited) applicability ranges. Despite these difficulties, in most cases the experimentally observed features such as spectral shape, angular distribution, ion energies and conversion efficiencies can be described by the existing models.

2.1. Absorption of laser pulse in a plasma

Because the laser pulse interacts mostly with electrons (see section 1) and ions are affected by the collective plasma fields, we first briefly describe the mechanisms responsible for laser energy absorption to plasma electrons and waves, relevant to the conditions existing during laser-driven ion acceleration. We should mention that absorption itself is a very complex process which depends on the laser parameters such as irradiance, polarization and wavelength, preplasma state (see also section 3.2), incidence angle and so on. More details

about absorption can be found in reviews (Wilks and Kruer 1997, Mourou *et al* 2006, Davies 2009).

For originally solid targets which are used most frequently for ion acceleration, absorption is most efficient at the surface where the electron density n_e equals the critical density, $n_{cr} = m_e\omega_0^2/4\pi e^2 = \pi/r_e\lambda_0^2 \approx 1.1 \times 10^{21} \text{ cm}^{-3}(\mu\text{m}/\lambda_0)^2$, where $r_e = e^2/m_e c^2 \approx 2.8 \times 10^{-13} \text{ cm}$ is the classical electron radius. The absorption starts from lower intensity (preceding light) interaction ($I\lambda_0^2 \sim 10^{12}\text{--}10^{17} \text{ W } \mu\text{m}^2 \text{ cm}^{-2}$) and steep (sub- μm) plasma gradients. At this stage, it is dominated by the inverse bremsstrahlung and resonant absorption (Wilks and Kruer 1997). The main laser pulse can be absorbed due to several mechanisms. If the obliquely incident laser pulse is p-polarized and the plasma gradient length at the critical density, $L_{cr} = n_e/(dn_e/dx)|_{n_e \rightarrow n_{cr}}$, is relatively long (sub-wavelength or larger length), the resonant absorption can continue to play the role. For very sharp gradients and p-polarized pulses, vacuum heating or Brunel absorption (D'yachenko and Imshennik 1979, Brunel 1987) becomes important. For relativistic irradiances and relatively gentle plasma gradients, $J \times B$ heating (Kruer and Estabrook 1985), arising from the oscillating component of the ponderomotive force, is effective. In particular, it is assumed that the temperature of hot electrons resulting from this absorption mechanism is of the order of the ponderomotive potential; this gives the so-called ponderomotive hot electron temperature scaling widely used in the literature (see equation (2.6) later); the effectiveness of this absorption mechanism is reduced when a high-density plasma with a sharp gradient is present (Wilks and Kruer 1997).

Multi-dimensional effects, such as plasma surface bending or rippling, can significantly increase the absorption (Bach *et al* 1983); furthermore, absorption mechanisms which are originally absent, become important, e.g. resonant absorption in the case of normal incidence or s-polarization.

Finally, we mention here that the absorption can be very efficient in near-critical density or cluster jet targets (Ditmire *et al* 1996, 1999), which can also be used for ion acceleration (see later in sections 2.8 and 3.9).

2.2. Acceleration by the electric charge-separation field at the target rear

In many experiments, the characteristic quasi-thermal ion energy spectra are observed with a cut-off at some maximum energy $E_{i,max}$. Simple physical models (Mora 2003, 2005, Nishiuchi *et al* 2006, Lontano and Passoni 2006, Schreiber *et al* 2006a) based on plasma expansion into vacuum (Gurevich *et al* 1965, 1972, Crow *et al* 1975, Gurevich and Meshcherkin 1981, Dorozhkina and Semenov 1998, Kovalev and Bychenkov 2003) can describe the formation of these features. The laser pulse irradiating the target transfers its energy into the hot electrons, which penetrate through the target and form a strong electric charge-separation field at the target rear. This charge-separation field ionizes atoms, and the resulting ions start to expand into the vacuum behind the target, following the electrons (Pukhov 2001, Wilks *et al* 2001). The models assume that initially the ions are at rest and form a sharp boundary with

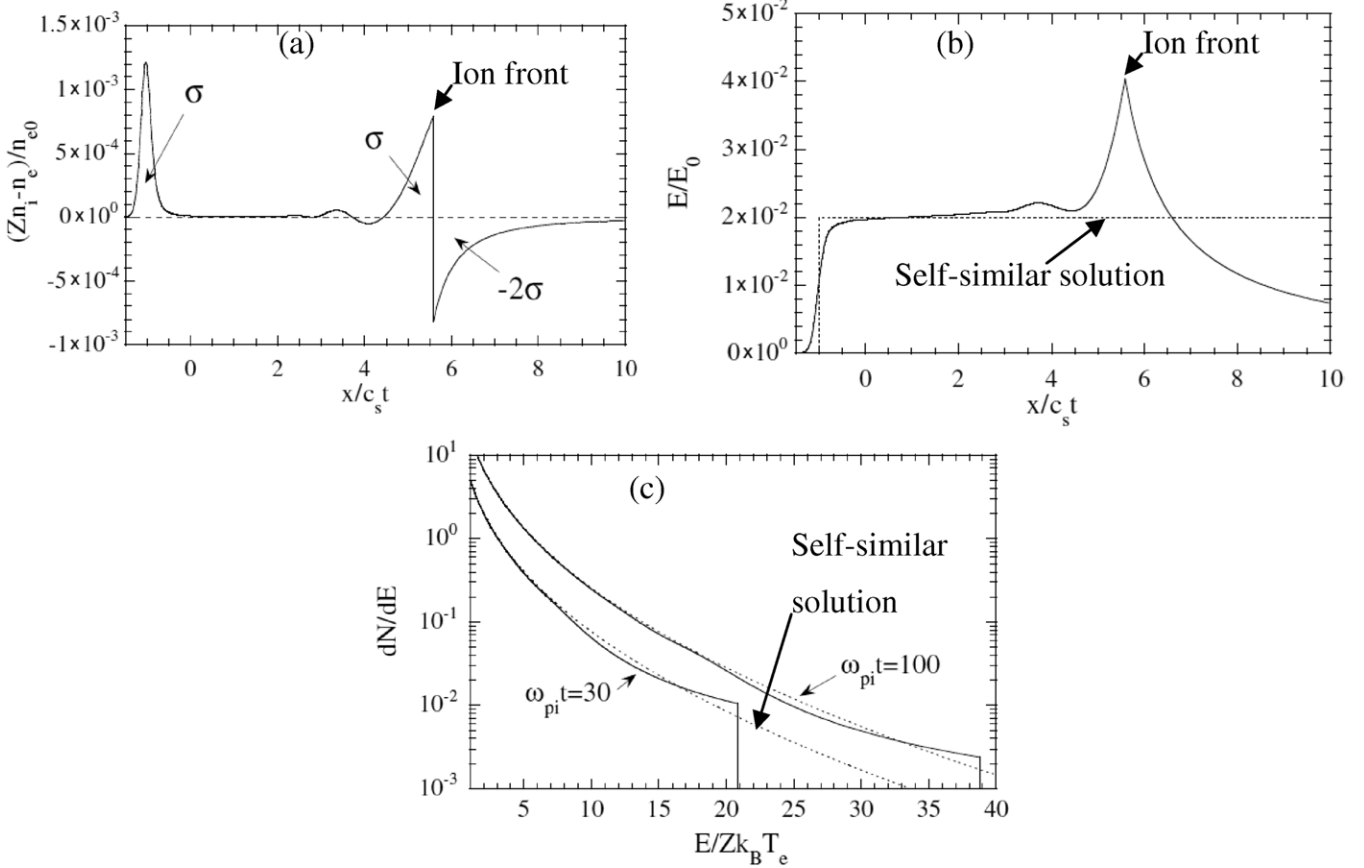


Figure 4. TNSA model. (a) Charge separation normalized to the initial plasma density n_{e0} , at $\omega_{pi}t = 50$. (b) Electric field E normalized to $E_0 = (4\pi n_{e0} T_e)^{1/2}$, at $\omega_{pi}t = 50$. The electric field peaks at the position of the ion front. The dotted line corresponds to the self-similar solution $E_{ss} = E_0/\omega_{pi}t$. (c) Energy spectrum per unit surface normalized to $n_{i0}\lambda_{D0}/Z_i T_e$, at $\omega_{pi}t = 30$ and $\omega_{pi}t = 100$. Energy is normalized to $Z_i T_e$. A sharp cut-off at some maximum ion energy is visible. The dotted lines show the self-similar solution without the cut-off. Reprinted with permission from Mora (2003).

the vacuum. The electrons, in contrast, redistribute to satisfy the Boltzmann distribution with electrostatic potential Φ :

$$n_e = n_{e0} \exp \frac{e\Phi}{T_e}. \quad (2.1)$$

The electrostatic potential satisfies the Poisson equation:

$$\frac{d^2\Phi}{dx^2} = 4\pi e(n_e - Z_i n_i). \quad (2.2)$$

In equations (2.1) and (2.2), n_e and T_e denote the hot electron density and temperature, n_i and eZ_i the ion density and charge and x is the spatial coordinate (the models are one-dimensional, 1D). The maximum ion energy $\mathcal{E}_{i,\max}$ in these models is proportional to the hot electron temperature T_e . The coefficient between T_e and $\mathcal{E}_{i,\max}$ depends on the details of the model, however.

2.2.1. Target normal sheath acceleration model. In the target normal sheath acceleration (TNSA) model (Hatchett *et al* 2000, Wilks *et al* 2001, Mackinnon *et al* 2002), the plasma is neutral except for a small area near the expansion front, the so-called plasma sheath. The width of this region is of the order of the

Debye length $\lambda_D = (T_e/4\pi n_e e^2)^{1/2}$. The initial electric field is

$$E_{\text{sheath},0} = \sqrt{\frac{2}{e_N}} \frac{T_e}{e \lambda_D} = \left(\frac{8\pi}{e_N} n_e T_e \right)^{1/2}. \quad (2.3)$$

Here $e_N \approx 2.71828$ is Euler's number.

Using the 1D expansion model, Mora (2003) found a good approximate solution to the problem. In particular, the ion energy at the expansion front at time t is

$$\mathcal{E}_i = 2Z_i T_e \left\{ \ln \left[\frac{\omega_{pi}t}{\sqrt{2e_N}} + \sqrt{\left(\frac{\omega_{pi}t}{\sqrt{2e_N}} \right)^2 + 1} \right] \right\}^2. \quad (2.4)$$

Here the ion plasma frequency is $\omega_{pi} = (4\pi Z_i n_{e0} e^2/m_i)^{1/2}$ and n_{e0} is the initial plasma density. The charge-separation, electric field and the resulting ion spectrum in the framework of the TNSA model are shown in figure 4.

2.2.2. Strong charge-separation field model. In the TNSA model, section 2.2.1, the plasma is assumed to be neutral except in the sheath region. However, in many cases this is not the case. A self-similar solution taking into account the charge separation during expansion of limited mass plasma

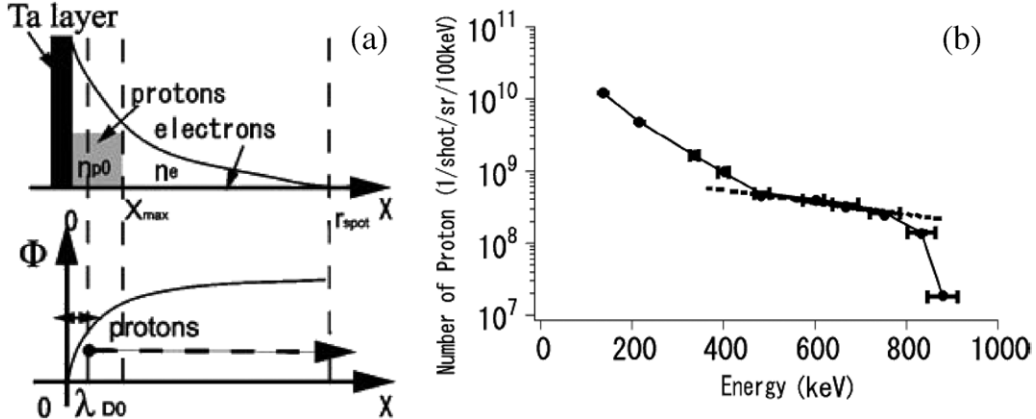


Figure 5. SCSF model. (a) Sketch of the 1D proton acceleration model. The upper frame shows the heavy ion (Ta, solid rectangle), proton (grey rectangle) and electron (solid line) density distributions. The lower frame shows the electric potential Φ . (b) The solid line with circles is the proton energy spectrum obtained in the experiment. The superimposed dotted line shows the spectrum predicted by the SCSF model. Reprinted with permission from Nishiuchi *et al* (2006).

is given by Murakami and Basko (2006) for several special cases in one- (1D), two- (2D) and three-dimensional (3D) geometries. Another model which solves equations (2.1) and (2.2) is the strong charge-separation field (SCSF) model (Passoni *et al* 2004, Passoni and Lontano 2004, Nishiuchi *et al* 2006) (figure 5). In this model it is assumed that the electrons form a negatively charged cloud at the target rear, while the heavy ions (e.g. metal) are still at rest. In the Poisson equation, the ion density n_i is zero behind the original target edge. The model describes the acceleration of a small number of light ions (e.g. protons) which are treated as test particles; this is in contrast to the TNSA model, which treats the accelerating ions as dominant species affecting the electron distribution. The energy gained by the light ion at position x_i along the target normal is

$$\mathcal{E}_i = 2Z_i T_e \ln \left[\frac{C_1 + x_i/\lambda_{D0}}{\sqrt{2}} \right]. \quad (2.5)$$

Here $C_1 \approx 2$ is a constant and $\lambda_{D0} = (T_e/4\pi n_{e0} e^2)^{1/2}$ is the initial Debye length.

2.2.3. Estimation of finite ion energies using planar 1D models. The ion energy tends to infinity at $t \rightarrow \infty$ (2.4) or $x \rightarrow \infty$ (2.5), which is the consequence of the planar 1D model and the tail of electron distribution function at infinite energy. In reality, the ion energy is always finite. In particular, for the TNSA and SCSF models the acceleration time t_{acc} or distance x_{acc} is limited. It is reasonable to assume that the 1D approximation breaks when the ion front extends to the distance of the order of the transverse size of the sheath (see equation (2.11) later) (Lontano and Passoni 2006, Nishiuchi *et al* 2006, Robson *et al* 2007).

The acceleration time t_{acc} , hot electron temperature T_e and density n_{e0} depend on the laser-target interaction conditions, in particular, on the irradiance (intensity), duration, contrast, preplasma state, etc. One of the approaches to derive the resulting spectra of proton beams from a wide range of laser pulse parameters was described by Fuchs *et al* (2006) (see the discussion on the applicable parameter region below, after

figure 7). The approach is based on the TNSA model and involves several assumptions. Some or all of these assumptions are used by many other authors, therefore it is essential to describe them and their applicability in this review. First, the model is isothermal, and the hot electron temperature is assumed to be equal to the ponderomotive potential (Wilks *et al* 1992, Malka and Miquel 1996), an assumption which is used by many authors:

$$T_e = \phi_{pond} = m_e c^2 \left[\sqrt{1 + a_0^2} - 1 \right]. \quad (2.6)$$

Second, it was found that a crude approximation

$$t_{acc} \approx 1.3 \tau_0, \quad (2.7)$$

where τ_0 is the laser pulse duration, provides good agreement with the broad range of experimental data and particle-in-cell (PIC) simulations (figure 6). A limit of the acceleration time is necessary because the isothermal approximation breaks after some time of the order of pulse duration.

Third, the plasma sheath radius r_s at the target rear surface is calculated assuming the ballistic propagation of the electrons from the front surface through the target of thickness l (Santos *et al* 2002, Fuchs *et al* 2003, Kaluza *et al* 2004) (figure 7):

$$r_s = r_0 + l \tan \theta. \quad (2.8)$$

Here r_0 is the focal spot radius. The half-divergence angle of the electron beam inside the target θ plays a role of a free (fitting) parameter; it is of the order of several to a few tens of degrees ($\theta = 8^\circ$ (Kaluza *et al* 2004), $\theta = 25^\circ$ (Fuchs *et al* 2003)).

Fourth, the conversion efficiency η of the laser energy W_L into hot electrons is calculated as (Feurer *et al* 1997, Key *et al* 1998)

$$\eta = 1.2 \times 10^{-15} \left(\frac{I_0}{W \text{ cm}^{-2}} \right)^{0.74}, \quad (2.9)$$

with maximum value $\eta = 0.5$ at $I_0 > I_0^* \approx 5.7 \times 10^{19} \text{ W cm}^{-2}$.

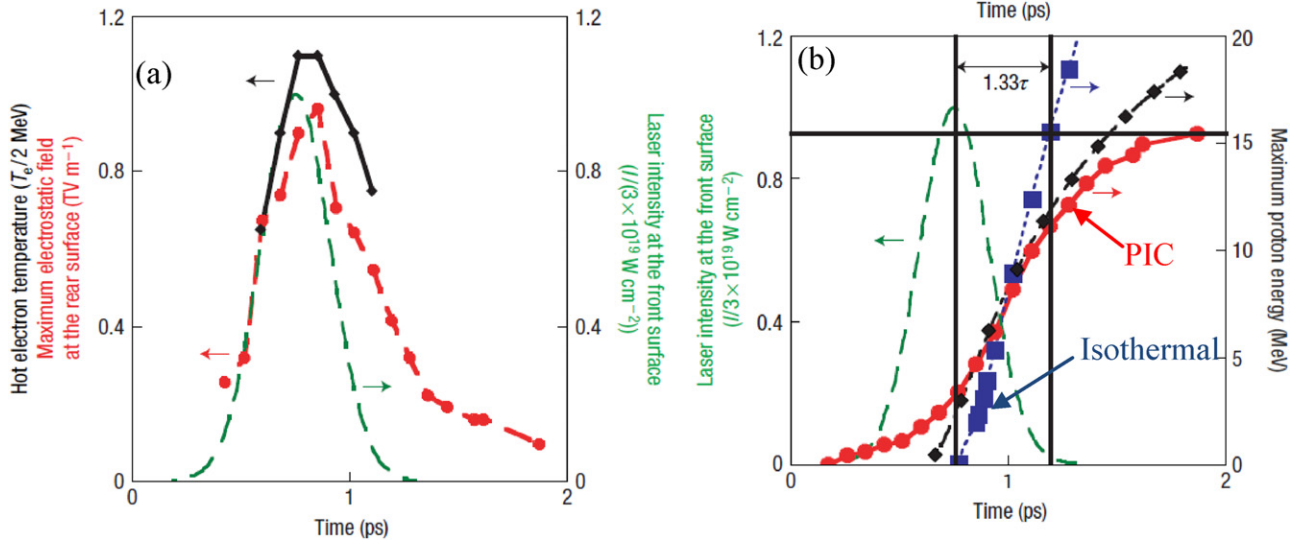


Figure 6. 2D PIC simulation and models of ion acceleration for the peak irradiance of $3 \times 10^{19} \text{ W cm}^{-2}$, pulse duration of 320 fs, focal spot radius of $3 \mu\text{m}$ and target thickness of $19 \mu\text{m}$; the pulse is shown in both frames by the green dashed line. (a) Evolution of the hot electron temperature (black solid line with diamonds) and maximum electrostatic field at the target rear side (red dashed line with circles). (b) Evolution of the maximum proton energy. The red solid line with circles is from the PIC simulation. The blue dotted line with squares corresponds to the isothermal model; the acceleration starts at the electrostatic field maximum, with the sheath density of $1.21 \times 10^{20} \text{ cm}^{-3}$ and hot electron temperature of 2.2 MeV, taken from the PIC simulation. The black dashed-dotted line with diamonds corresponds to a more precise two-phase model (Mora 2005) which includes adiabatic electron cooling due to the energy transfer to ions. Reprinted with permission from Fuchs *et al* (2006).

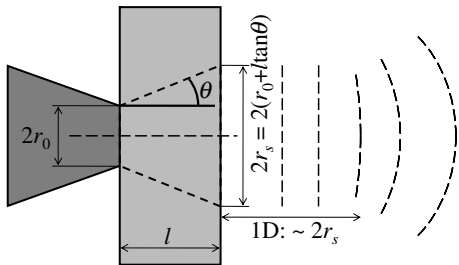


Figure 7. Estimation of the sheath size at the target rear; the hot electrons originating from the laser spot with the radius r_0 propagate ballistically through the target with thickness l , the half-angle of electron beam divergence is θ . These electrons form sheath with radius $r_s = r_0 + l \tan \theta$ (2.8). The 1D approximation is valid approximately up to a distance $2r_s$ from the target rear surface (2.11).

Fifth, the number N_e and density n_{e0} of hot electrons in the sheath are estimated as

$$N_e = \frac{\eta W_L}{T_e} \quad \text{and} \quad n_{e0} = \frac{N_e}{c\tau_0\pi r_s^2}, \quad (2.10)$$

i.e. assuming the cylindrical shape of the electron cloud with the length and radius equal to the laser pulse length $c\tau_0$ and sheath radius r_s (2.8), respectively.

In order to imitate the acceleration field decrease and acceleration stop at a distance, i.e. 3D effects, in the 1D model, it is necessary to limit the acceleration at the ion front position of the order of the sheath size (figure 7), which gives the acceleration length limit

$$x_{\text{acc}} = 2r_s = 2(r_0 + l \tan \theta). \quad (2.11)$$

A comparison of these models (isothermal (2.6)–(2.10), two phases and two phases with the acceleration limit (2.11)) with the experiment is shown in figure 8(a) (Robson *et al* 2007).

Although the isothermal (constant electron temperature) model with assumptions (2.6)–(2.11) is strongly simplified, it provides reasonable accuracy for a ‘normal’ contrast, 0.3-to-a few ps pulses focused up to the irradiances of mid- $10^{19} \text{ W cm}^{-2}$ onto reasonably thick (usually $>10 \mu\text{m}$) targets (Fuchs *et al* 2006); these conditions are typical for many experiments. Here ‘normal’ contrast means that the preceding light does not destroy a several- μm thick target, but the preplasma appears significantly before the main pulse; see section 3.2. However, one should be careful if the laser or target parameters are significantly different; here we list some of the many reasons which lead to the violation of model assumptions, in which case other models should be used. In particular, for short pulses (<100 fs, typical for Ti:sapphire lasers), the acceleration time is longer than that given by equation (2.7); e.g. a correction was suggested in Fuchs *et al* (2007a). Further, for a shorter scale preplasma, which corresponds to higher contrast shorter duration laser pulses, the hot electron temperatures at intensities $>10^{19} \text{ W cm}^{-2}$ are significantly lower than the ponderomotive temperature (2.6) (Carrié *et al* 2009, Haines *et al* 2009, Tanimoto *et al* 2009, Lefebvre *et al* 2010). In particular, Beg *et al* (1997) have obtained the following hot electron temperature scaling:

$$T_e \approx 0.47m_e c^2 a_0^{2/3} \approx 0.22 \text{ MeV} (I_{18} \lambda_{\mu\text{m}})^{1/3}, \quad (2.12)$$

where $I_{18} = I_0/10^{18} \text{ W/cm}^2$ and $\lambda_{\mu\text{m}} = \lambda_0/\mu\text{m}$. A similar or the same scaling has been observed in other experiments (Tanimoto *et al* 2009) and PIC simulations (Haines *et al* 2009, Lefebvre *et al* 2010); the maximum proton energy obtained in the model where the scaling (2.6) is replaced by (2.12) is shown in figure 8(b) by the black solid line. For nanometre-thick targets irradiated by high-contrast pulses, the electron temperatures can be higher; see section 3.4. Simultaneously,

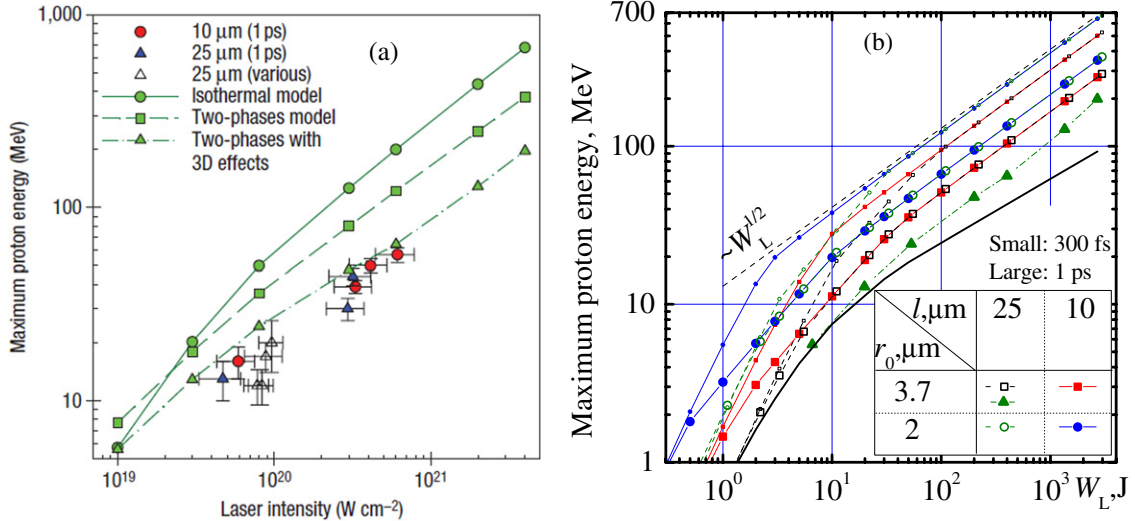


Figure 8. (a) Maximum proton energy versus laser intensity: comparison of models with experiment. The symbols with error bars are the experimental results obtained with 10 μm (red circles) and 25 μm (blue triangle) thick Al targets, fixed pulse duration of 1 ps and variable laser energy. The open triangles are the experimental results with 25 μm thick Al target and variable pulse duration and energy. The green symbols with lines are predictions of models. The green circles with the solid line correspond to the isothermal plasma expansion model (Mora 2003). The green squares with the dashed line correspond to the two-phase model with the linear electron temperature rise during irradiation and then adiabatic cooling due to energy transfer to the ions (Mora 2005). The green triangles with the dashed-dotted line correspond to the same model with 3D effects mimicked (the acceleration stops when the plasma longitudinal expansion becomes equal to twice the calculated initial lateral extension of the plasma sheath at the back of the target, figure 7 and equation (2.11)). Frame (a) is reprinted with permission from Robson *et al* (2007). (b) Maximum proton energy versus laser pulse energy W_L , calculations using the isothermal TNSA model (2.4) (Mora 2003) with the assumptions (2.6)–(2.10) (Fuchs *et al* 2006) and the acceleration distance limited by the sheath diameter (2.11): $x_{\text{acc}} = 2(r_0 + l \tan \theta)$, where $\theta = 25^\circ$ is the half-divergence angle of the electron beam inside the target, figure 7. Wavelength $\lambda_0 = 1.06 \mu\text{m}$, full-width at half-maximum (FWHM) pulse duration $\tau_0 = 300 \text{ fs}/1 \text{ ps}$ (small/large symbols, respectively); half-width at half-maximum (HWHM) spot radius $r_0 = 3.7 \mu\text{m}/2 \mu\text{m}$ (squares/circles, respectively), target thickness $l = 25 \mu\text{m}/10 \mu\text{m}$ (open/solid symbols, respectively). For comparison, triangles show the calculation by Robson *et al* (2007) using the two-phase model (Mora 2005) and limit for the acceleration distance. The black solid line without symbols corresponds to the calculation for $\tau_0 = 1 \text{ ps}$, $r_0 = 3.7 \mu\text{m}$, $l = 25 \mu\text{m}$ using the hot electron temperature (2.12) (Beg *et al* 1997, Haines *et al* 2009) and otherwise the same model, i.e. (2.7)–(2.11).

very thin targets absorb less energy due to the prompt density decrease (d’Humières *et al* 2010) and/or the relativistic foil transparency (Vshivkov *et al* 1998); Andreev *et al* (2008) have developed an adiabatic analytical model for the calculation of the maximum proton energy and spectrum taking into account the dependence of absorption on target thickness obtained from PIC simulations. On the other hand, for thick (millimetre order) targets deviations from ballistic propagation are observed (Yuan *et al* 2010). In general, the electron spectrum, propagation and angular distribution are much more complex than the assumed single-temperature population propagating ballistically within a constant-divergence cone (Santos *et al* 2007) (see also section 4.5). In addition, different absorption mechanisms result in different electron injection angles, e.g. resonance absorption produces an electron beam perpendicular to the target surface, while $J \times B$ heating produces an electron beam in the laser propagation direction; these two electron beams can co-exist in one experiment (Malka and Miquel 1996, Ping *et al* 2008, Ter-Avetisyan *et al* 2008c). The approximation (2.9) exhibits a break (discontinuity of derivative) at I_0^* , which in turn causes breaks in the dependences of ion energies on laser parameters, see below; such breaks are artificial and do not appear in real experiments. For longer pulses and higher intensities, further model elaboration is also required. In particular, for the pulse durations much longer than $2l/c$, the two-phase model with

the inclusion of linear temperature rise during the laser pulse irradiation and later adiabatic cooling (Mora 2005) gives better agreement with the experiment (figure 8(a), Robson *et al* 2007).

Let us calculate the maximum achievable energy of protons ($Z_i = 1$, ion mass equals proton mass, $m_i = m_p$) versus the laser energy using the TNSA model (2.4) with assumptions (2.6)–(2.11); the acceleration is limited by the time $1.3\tau_0$ (equation (2.6)) or by the moment when the ion front position x_i exceeds the transverse sheath size $2r_s$ (equation (2.11)), whichever is earlier. We assume a Gaussian laser pulse shape with the HWHM spot radius r_0 and FWHM duration τ_0 , in which the irradiance depends on time t and radius r as

$$I(t, r) = I_0 2^{-4t^2/\tau_0^2 - r^2/r_0^2}, \quad (2.13)$$

and the peak irradiance, I_0 , and peak power, P_0 , are

$$\begin{aligned} I_0 &= 2 \left(\frac{\ln 2}{\pi} \right)^{3/2} \frac{W_L}{r_0^2 \tau_0} \approx 0.65 \frac{W_L}{\pi r_0^2 \tau_0}, \\ P_0 &= 2 \left(\frac{\ln 2}{\pi} \right)^{1/2} \frac{W_L}{\tau_0} \approx 0.94 \frac{W_L}{\tau_0}. \end{aligned} \quad (2.14)$$

We do not specify the incidence angle here, because of its moderate or small effect on the ion acceleration in the TNSA regime found in the experiments with conventional ‘normal-contrast’ CPA lasers, likely because of hole boring in the

preformed plasma (Fuchs *et al* 2006); we note that in the case of a high-contrast laser pulse the ion energy in the target normal direction does depend on the laser incidence angle (Carroll *et al* 2010b, see also section 2.5). The maximum proton energy estimated in this way (equations (2.4), (2.6)–(2.11)) is plotted in figure 8(b) for several laser and plasma parameters. In general, to achieve the highest proton energy, the focal spot r_0 and target thickness l need to be as small as possible. Smaller focal spot means higher irradiance and therefore higher hot electron temperature, which, according to the model, gives higher proton energies; we note that in the case of an extremely small focal spot approaching the laser wavelength, the electron injection can be different, thus, the 1D theory considered here needs to be applied with caution. As for the target thickness, thinner target means smaller sheath radius (2.8) and therefore higher hot electron density (2.10) due to a reduced electron beam spread (Mackinnon *et al* 2002), which, according to (2.3), provides a larger accelerating field. However, we note that for large laser energies the influence of thickness becomes negligible; see section 2.2.6. In experiments, the minimum thickness is limited by the laser contrast; see sections 3.2 and 3.4. The choice of duration is not obvious (see below in section 2.2.6). For 1 ps pulses, the maximum proton energy in this model is overestimated by 40–60%, as can be seen from the comparison with the two-phase model (Mora 2005) with the acceleration limit (2.11) shown by the solid triangles (Robson *et al* 2007).

2.2.4. Analytical model based on a radially confined surface charge on the target rear side. Another analytical model which gives good agreement with a broad range of experiments solves the Poisson equation assuming exponential electron energy distribution (Schreiber *et al* 2006a). The potential at infinity remains finite because the transverse size of the charged region is determined by condition (2.11). The model has two fitting parameters, the half-angle of the hot electron cone θ (in (2.8)) and the conversion efficiency of the laser energy into the hot electrons; the value of θ change from 10° for ~ 1 J to 45° for ~ 100 J lasers. The conversion efficiency (2.9) and estimation of electron number (2.10) are used. The wavelength is not included, but approximately $1\text{ }\mu\text{m}$ is assumed as efficiency (2.9) is used. The maximum ion energy $\mathcal{E}_{i,\max}$ can be calculated from the equation

$$\frac{\tau_0 V_\infty}{r_s} = X \left(1 + \frac{1}{2} \frac{1}{1 - X^2} \right) + \frac{1}{4} \ln \frac{1 + X}{1 - X}. \quad (2.15)$$

Here $X = (\mathcal{E}_{i,\max}/\mathcal{E}_\infty)^{1/2}$, $V_\infty = (2\mathcal{E}_\infty/m_i)^{1/2}$, and $\mathcal{E}_\infty = Z_i T_e r_s / \lambda_D$ is the maximum energy which ions could gain in the case of infinite acceleration length. Within the model's framework, it can be shown that $\mathcal{E}_\infty = 2Z_i e (N_e T_e / c \tau_L)^{1/2} = 2Z_i m_e c^2 (2\eta P_0 / P_c)^{1/2}$. We note that the hot electron number N_e and temperature T_e are used in the model. However, they are included in the expressions for \mathcal{E}_∞ (and V_∞) not separately but as a product; therefore, due to the model assumption (2.10), the maximum ion energy does not explicitly depend on T_e . The relativistic power unit (\sim the ratio of electron energy at rest

$m_e c^2$ to the time it takes for light to travel across the classical electron radius $r_e = e^2/m_e c^2$)

$$P_c = 2m_e^2 c^5 / e^2 \approx 17 \text{ GW} \quad (2.16)$$

coincides with the critical power for relativistic self-focusing (Barnes *et al* 1987, Sun *et al* 1987). The dependence of the maximum proton energy versus laser energy is shown in section 2.11 (figure 23) by open diamonds; the focal spot radius is $r_0 = 1.5\text{ }\mu\text{m}$, target thickness $l = 10\text{ }\mu\text{m}$, electron divergence half-angle $\theta = 10^\circ$, pulse duration is optimum (see figure 10) but not smaller than $\tau_{0,\min} = 30$ fs.

2.2.5. Light-ion acceleration driven by a strong charge separation. An approximate analytical solution of the 1D problem of light-ion acceleration in the test-particle approximation with finite acceleration length is given by Lontano and Passoni (2006) (non-relativistic planar and spherical symmetry cases) and Passoni and Lontano (2008) (relativistic case), based on the assumption that the quasi-stationary electron cloud which accelerates light ions consists of only plasma-bound electrons; the electrons with kinetic energy larger than some maximum value quickly escape from the interaction region and do not contribute to the ion acceleration. A refined version of this solution has been used to model the influence of laser parameters on the ion energy by Passoni *et al* (2010a, 2010b). A comparison with other models can be found in Perego *et al* (2011).

Here we will use the ultrarelativistic case as more relevant to recent and future experiments. The maximum ion energy is

$$\mathcal{E}_{i,\max} = Z_i T_e \frac{e^{\varphi^*} (\varphi^* - 1) + 1}{e^{\varphi^*} - 1}, \quad (2.17)$$

where φ^* is the normalized maximum energy of bound electrons: $\varphi^* = \mathcal{E}_{e,\max} / T_e$.

There are two values which depend on the physics of the laser–target interaction, namely the hot electron temperature T_e and the maximum energy of bound electrons $\mathcal{E}_{e,\max}$. Generally speaking, these have to be measured or derived from the simulations. It turns out, however, that for a wide range of laser parameters the ponderomotive expression for the hot electron temperature (2.6) and a simple phenomenological fitting formula for φ^* give the maximum proton energy consistent with the experiments performed with a number of different laser systems with pulse duration ranging from 40 fs to 0.9 ps, energy W_L from 0.1 to 500 J and intensity from 3×10^{18} to $3 \times 10^{20} \text{ W cm}^{-2}$:

$$\varphi_{\text{fit}}^* = \frac{\mathcal{E}_{e,\max}}{T_e} = 4.8 + 0.8 \ln \left(\frac{W_L}{J} \right). \quad (2.18)$$

The fitting coefficients 4.8 and 0.8 in equation (2.18) were found by comparing the calculated maximum proton energy (2.17) with the experimental values obtained from the laser systems with the ‘normal’ contrast. An example of the dependence of the maximum proton energy versus laser energy for $\lambda_0 = 0.8\text{ }\mu\text{m}$ and $\tau_0 = 30$ fs calculated using model (2.17) and (2.18) is given later in section 2.11 (figure 23).

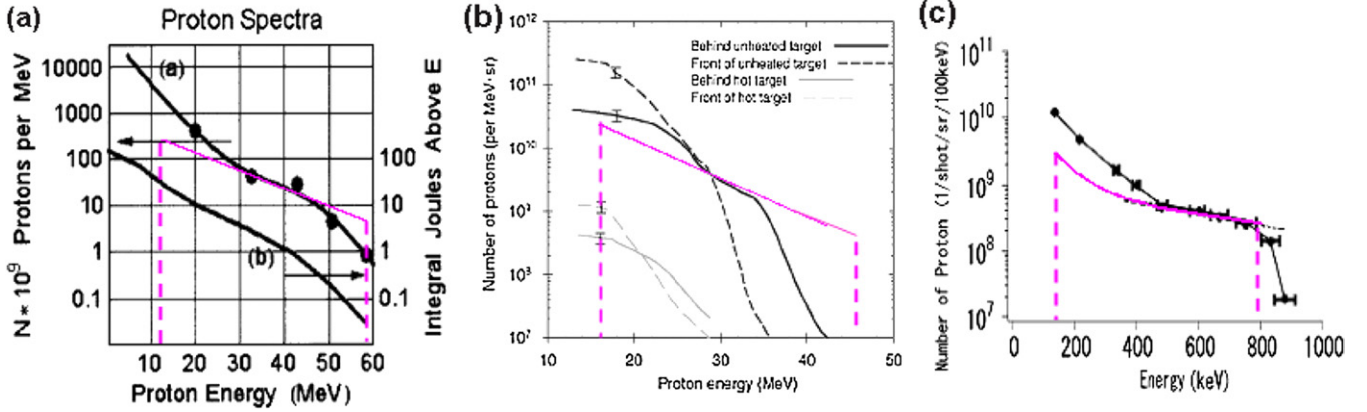


Figure 9. Comparison of the proton energy spectra from the analytical solution of the SCSF model (Passoni and Lontano 2008), pink lines, superimposed to the measured spectra, black lines with dots and/or error bars: (a) Snavely *et al* (2000), (b) McKenna *et al* (2004) and (c) Nishiuchi *et al* (2006). Reprinted with permission from Passoni and Lontano (2008).

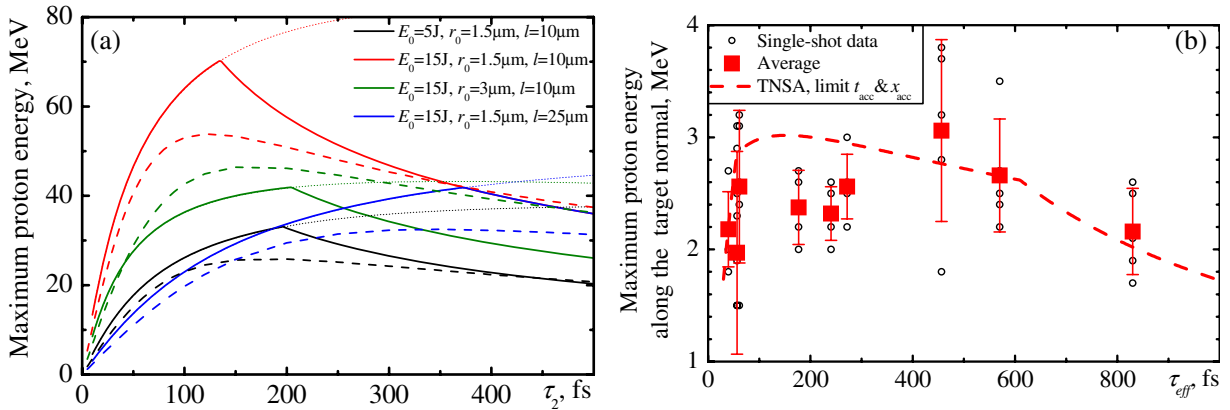


Figure 10. (a) Solid lines, calculated maximum proton energy versus the pulse duration within the framework of the TNSA model with the acceleration time limit (2.7) and the acceleration length limit (2.11) for several laser parameter sets; $\lambda_0 = 0.8 \mu\text{m}$, $\theta = 25^\circ$. The TNSA curves have breaks (discontinuities of derivatives) due to the transition between two acceleration limits: if the laser pulse is short, the acceleration time is limited by the pulse duration (2.7); if the pulse is long, the acceleration length is limited by the end of 1D approximation (2.11); these breaks are model artefacts as the actual transition between the acceleration limits happens gradually. Dotted lines, the same dependences continued without the acceleration length limit. Dashed lines, the dependences calculated for the same parameters using the analytical model (2.15) by Schreiber *et al* (2006a), $\theta = 25^\circ$. (b) Comparison of calculated maximum proton energy (TNSA + acceleration limits (2.7) and (2.11)) with the experimental data (Pirozhkov *et al* 2009b), pulse energy $W_L = 0.5 \text{ J}$ (held constant, i.e. the intensity decreases when the duration increases), $r_0 = 1.8 \mu\text{m}$, $\lambda_0 = 0.8 \mu\text{m}$, polyimide tape target with thickness $l = 7.5 \mu\text{m}$; the black open circles show the individual data points, the red solid squares show the average with error bars representing the standard deviations of shot-to-shot fluctuations. The model curve (the red dashed curve) exhibits two breaks. The first one at the duration of $\sim 60 \text{ fs}$ is due to the non-smooth dependence of the conversion efficiency into the hot electrons on the intensity (2.9). The second break at $\sim 600 \text{ fs}$ is due to the transition of the acceleration limit from (2.7) to (2.11).

The model can also reproduce well the high-energy part of the experimental proton spectra (figure 9). Low-energy part deviates from the measured spectra, because the number of low-energy protons is large and they are accelerated together with the heavier ions, thus the model assumptions are violated.

It is interesting to note that the target parameters and the pulse contrast are not included in equations (2.17) and (2.18), despite the fact that it is obvious that, for example, by choosing incorrect target thickness it is possible to decrease the maximum proton energy down to nearly zero. This is probably an indication of the fact that in each experiment used for benchmarking the theory the target and experimental conditions were somehow optimized, therefore equations (2.17) and (2.18) give the ion energy which *can* be achieved in a typical experiment with ‘normal’ pulse contrast choosing appropriate target and irradiation conditions. For ultra-high-

contrast lasers and sub- μm targets, equation (2.17) still can be used, but in this case the maximum energy of bound electrons differs from (2.18) and needs to be measured or taken from simulations. The pulse contrast is discussed in more detail in section 3.2.

2.2.6. Influence of the pulse duration. We noticed that to achieve higher proton energies, larger laser pulse energies and smaller focal spot sizes are required. Let us now discuss the choice of pulse duration. In a typical experiment, the duration can be varied by tuning, for example, the compressor or stretcher in the CPA laser system (see section 3.1) from some minimum value determined by the laser system capability, to essentially infinity. Figure 10(a) shows the calculated dependences of the maximum proton energy on

pulse duration using two models, namely TNSA with the acceleration time limit (2.7) and the acceleration length limit (2.11) (sections 2.2.1 and 2.2.3) and the model by Schreiber *et al* (2006a) (2.15) (section 2.2.4). Neglecting the longitudinal displacement of protons during the acceleration process, Fuchs *et al* (2006) found that the optimum pulse duration is $\tau_0 \sim 0.2\text{--}1\text{ ps}$. The acceleration length limit (2.11) leads to somewhat shorter optimum pulse durations, from a few hundred down to sub-100 fs, depending on the laser parameters and target thickness; for higher intensities and thinner targets, the optimum duration is shorter. The two models give similar values for the optimum pulse duration. They also show good agreement with experiment (Schreiber *et al* 2006a, Pirozhkov *et al* 2009b (figure 10(b))).

Finally, let us briefly discuss joining of TNSA curves with different thicknesses in figures 8(b) and 10(a), which looks surprising at first glance. For example, the maximum energy of protons for $l = 10\mu\text{m}$ and $l = 25\mu\text{m}$ is the same for pulses longer than $\sim 350\text{ fs}$ (figure 10(a)); note that this also holds for the analytical model (2.15), dashed lines in figure 10(a), although at somewhat longer durations of $>1\text{ ps}$; further, some experimental data also suggest that the proton energies are similar for different target thicknesses (e.g. figure 8(a)). A simple analysis shows that in both models, for long pulses the acceleration distance is limited by the condition (2.11), while the hot electron density at the target rear side is estimated using equation (2.10), i.e. $n_e \propto r_s^{-2}$, which gives the accelerating field (2.3) $E_{\text{acc}} \propto n_e^{1/2} \propto r_s^{-1}$. Thus, the ion energy estimate $E_i \sim E_{\text{acc}}x_{\text{acc}}$ is approximately independent of the sheath size r_s , i.e. on the target thickness l . Note that this holds for relatively long pulses, when indeed the condition (2.11) limits the acceleration; for shorter pulses, including the important region of durations close to the optimum, the acceleration is limited by the pulse duration, and higher ion energies are indeed achieved with thinner targets. One can make this analysis more rigorously, e.g. for the TNSA model the product $\omega_{\text{pit}}t$ in (2.4) at the end of acceleration for long pulses turns out to be approximately the same for thin and thick targets; one can check this by expanding the equations into series with the small parameter $1/a_0$ (i.e. this holds when $a_0 \gg 1$). Therefore, the final ion energy is also the same. We again note that this coincidence of ion energies holds only when the acceleration is limited by the sheath size in both cases; the latter indicates that the laser pulse duration is longer than optimum for thinner target. If the pulse duration is fixed and the pulse energy is changed, as e.g. in figure 8(b), for large pulse energies, the acceleration is very rapid and therefore limited by the sheath size (2.11), so that thick and thin targets give similar ion energies. On the other hand, for small pulse energies the acceleration is limited by the duration (2.7), therefore thinner targets give higher ion energies. We stress here that these conclusions are valid only approximately, within the models' frameworks, where the rear target side is sharp and ballistic electron transport is modelled by a simple diverging cone. The dependence on the target thickness becomes more complex if one considers further details, e.g. the electron beam filamentation, collisions, etc (section 4.5); Flacco *et al* (2010a) have found that the optimum pulse duration also depends

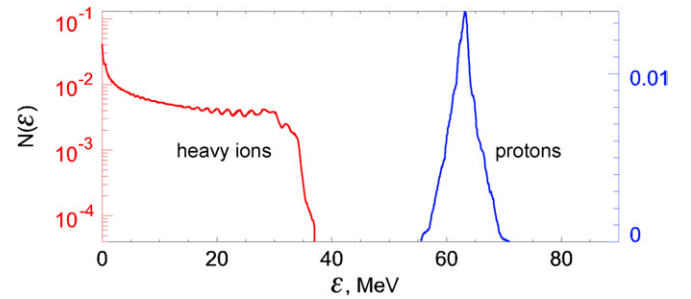


Figure 11. The proton (blue line) and heavy ion (red line) energy spectra at $t = 80 \times 2\pi/\omega_0$ from the 3D PIC simulations. The laser pulse is linearly polarized, $a_0 = 30$, $c\tau_0 = 15\lambda_0$, $r_0 = 12\lambda_0$, the incidence is normal. The mass-limited double-layer target consists of the first gold layer (a $10\lambda_0$ diameter disc with $l_1 = 0.5\lambda_0$, $m_i = 195.4m_p$, $Z_i = 2$, $n_{e1} = 9n_{\text{cr}}$) and the second proton layer (a $5\lambda_0$ diameter disc with $l_2 = 0.03\lambda_0$, $n_{e2} = 0.28n_{\text{cr}}$). Reprinted with permission from Esirkepov *et al* (2002).

on the target thickness due to the rear (not irradiated) target side expansion in the case of thinner targets and longer pulse durations; this effect is not included into the models considered here.

2.3. Double-layer target in the Coulomb explosion regime

The method of quasi-monoenergetic ion production using a double-layer target consisting of a front layer containing heavy ions and a thin rear layer of light ions (e.g. hydrogen) was proposed by Esirkepov *et al* (2002), figure 11. An example of such a target is a metal foil with a thin surface contamination containing hydrogen (water, hydrocarbon, etc). The laser pulse ionizes the front layer and expels the electrons from the foil, and the remaining ions create the quasi-static electric field. This electric field accelerates both heavy and light ions due to Coulomb explosion. For partially ionized heavy ions, the ratio $m_i Z_a / (m_a Z_i)$ can be sufficiently large. This leads to much higher efficiency of light-ion acceleration. Here m_i , m_a and eZ_i , eZ_a are the masses and electric charges of heavy and light ions, respectively ($m_i \gg m_a$). The number of expelled electrons should be sufficiently large to provide a strong Coulomb field. This requires a sufficiently thick front layer. However, it cannot be too thick, otherwise the laser pulse would not be able to create a strong field at the rear surface. Ideally, all target electrons should be expelled. The optimum target thickness was determined in a broad parameter range using multi-parametric 2D PIC simulations, figure 12 (Esirkepov *et al* 2006). It turns out that the most important target parameter is not the thickness itself, but rather the *areal electron density* $n_e l$. In dimensionless form, it is

$$\sigma = \frac{n_{el}}{n_{\text{cr}}\lambda}, \quad (2.19)$$

where n_e is the electron density, n_{cr} is the critical density, l is the target thickness and λ is the laser wavelength. The optimum dimensionless areal density derived from the simulations is

$$\sigma_{\text{opt}} = 0.4a + 3 \approx 0.4a. \quad (2.20)$$

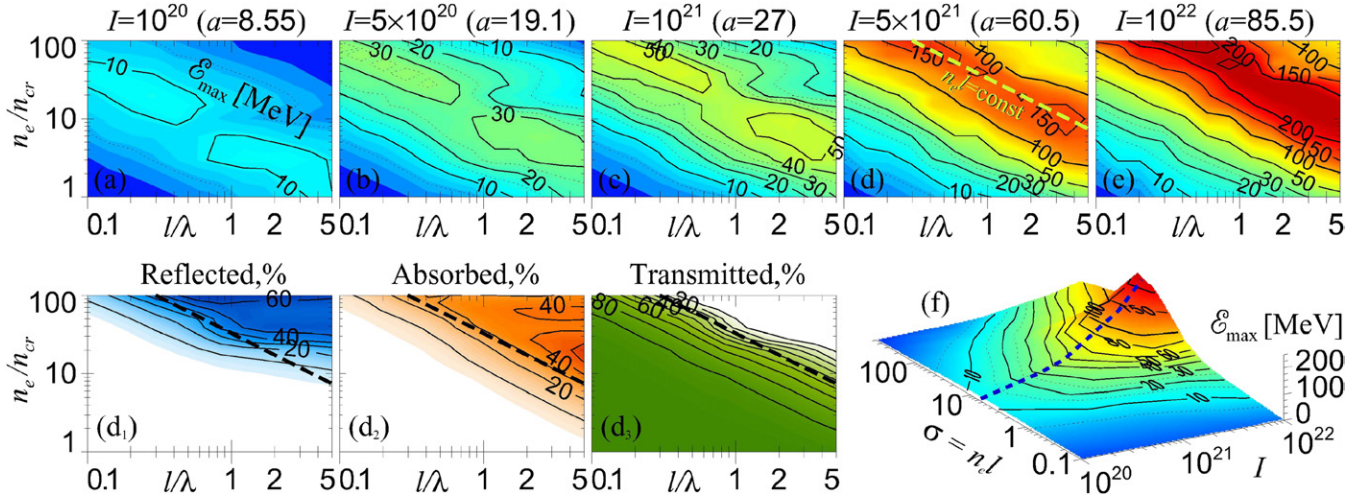


Figure 12. Results of multi-parametric 2D PIC simulations for the pulse duration $c\tau = 10\lambda$ and focal spot diameter $D = 10\lambda$. (a)–(e) Maximum proton energy (contours) versus target thickness l and density n_e (log–log scale) for several intensities. (d₁)–(d₃) Laser pulse reflection, absorption and transmission coefficients, respectively, related to frame (d). The dashed lines in (d), (d₁)–(d₃) correspond to the optimal product $n_e l$, which provides the maximum proton energy. (f) Maximum proton energy versus intensity ($\text{W}/\text{cm}^2(\mu\text{m}/\lambda)^2$) and dimensionless target electron areal density $\sigma = n_e l / (n_{cr}\lambda)$ (log–log scale). The dashed line corresponds to the optimum condition $\sigma_{opt} \propto \sqrt{I}$. Reprinted with permission from Esirkepov *et al* (2006).

Here a is the dimensionless laser amplitude (1.1). Note that in the parameter range under investigation $a \gg 1$. As seen from figures 12(a)–(e), for each intensity value there is a corresponding optimum line in the parameter plane (l, n_e) , described well by the optimum condition (2.20). It is worth noting that this condition is similar to the condition of relativistic transparency of a thin foil (Vshivkov *et al* 1998), which is of fundamental importance for the laser–thin-foil interactions (Bulanov S V 1975, Bratman and Samsonov 1995, Cherepenin and Kulagin 2004). In particular, the same kinds of optimum conditions (with different numerical coefficients) were established for the high-order harmonic and attosecond pulse generation during the laser–thin-foil interaction (Pirozhkov *et al* 2006a, 2006b). A similar condition holds for the optimum radiation pressure acceleration; see section 2.6. A simple physical explanation for the existence of the optimum areal density is as follows. If σ is too small, the laser pulse is almost fully transmitted through the target (figure 12(d₃)); on the other hand, if σ is too large, the laser pulse is not strong enough to expel substantial part of electrons; the pulse is efficiently reflected instead (figure 12(d₁)). In both cases non-linear processes such as harmonic generation and ion acceleration are inefficient.

The condition (2.20) can also be described from another point of view. The electric field created by the remaining ion layer (assuming all the electrons are expelled) is

$$E_i = 2\pi e Z_i n_i l = \pi \frac{m_e c \omega}{e} \sigma. \quad (2.21)$$

The optimum condition (2.20) then states that the driving laser electric field should be close to the maximum Coulomb electric field E_i . If the target is close to the solid density, the condition (2.20) implies a very thin front layer: for $n_e = 8 \times 10^{23} \text{ cm}^{-3}$ (fully ionized diamond-like carbon, DLC), $I = 1.4 \times 10^{20} \text{ W cm}^{-2}$ and $\lambda = 0.8 \mu\text{m}$ ($a = 8$), the optimum

thickness is $l = 11 \text{ nm}$. This requires a high-contrast laser pulse, such that the target is not destroyed by prepulses or a pedestal; see section 3.2.

The requirements for the rear (light atom) layer are different. It should be sufficiently thin in order to ensure equal initial conditions for all light ions, otherwise the spectrum of accelerated ions will be broadened. Furthermore, the number of light ions should be sufficiently small, such that the Coulomb repulsion between them during the acceleration process can be neglected. In this case, we can use the test-particle approximation.

The maximum energy of light ions can be estimated as follows (Esirkepov *et al* 2002, Bulanov S V *et al* 2004a, Esirkepov *et al* 2006). In the longitudinal direction (along the target normal), the region of large electric field (2.21) has size of the order of the laser focal spot radius $D/2$, where D is the laser spot diameter; most of the energy is gained by ions during this 1D acceleration stage (Bychenkov and Kovalev 2005a). Thus, the accelerated ion energy is $\mathcal{E}_a = e Z_a E_i D/2$. Using E_i from (2.21) and $\sigma = \sigma_{opt}$ from (2.20), we get the scaling

$$\frac{\mathcal{E}_a}{Z_a} \propto \sqrt{P}. \quad (2.22)$$

In the 2D PIC simulations (Esirkepov *et al* 2006) it was found that for protons $\mathcal{E}_p \approx 45 \text{ MeV} \sqrt{P/\text{PW}}$ (here PW represents petawatt) with the additional condition $c\tau_0 \geq D$, which was necessary to reduce the effect of the neutralizing current (for experiments on neutralizing currents, see Quinn *et al* (2009)). Note that in practice this condition is relatively easy to fulfil. The ion energy is proportional to the square root of the laser power. It does not depend separately on the intensity. The simple explanation is as follows. If a laser with the same power is focused more tightly, say, the spot size D decreases k times, the laser amplitude increases k times, and both the optimum σ_{opt} (i.e. the foil thickness) and the accelerating field

(2.21) increase k times. At the same time, the size of the region with the large longitudinal electric field $\sim D/2$ decreases k times, therefore the final ion energy remains nearly constant. We note that this holds if the optimum condition (2.20) is preserved, i.e. the laser amplitude is changed simultaneously with the target areal density. If one just decreases the spot without the corresponding increase in the target thickness or density corresponding to σ_{opt} , a part of the laser pulse would be simply transmitted but the acceleration field would not increase, thus the resulting ion energy would decrease. On the other hand, consider a typical situation, when originally the target thickness is much larger than the optimum; this is indeed typical because the optimum thickness of a solid target ($n_e = 500n_{\text{cr}}$) even for $a_0 = 100$ ($\sim 10^{22} \text{ W cm}^{-2}$) is $l \sim 0.08\lambda_0$. In this situation, the resulting ion energy would be relatively small, but decreasing the focal spot one increases the laser amplitude, such that the parameters approach the optimum condition (2.20), and as a result the ion energy increases.

An important assumption implied in the derivation of the maximum ion energy scaling above is the absence of neutralizing currents from both the cold surrounding regions and returning electrons. This might be difficult to implement in practice. A possible way is to use a target with transverse size of the order of or smaller than the laser focal spot diameter (mass-limited target, MLT) (Esirkepov *et al* 2002, Limpouch *et al* 2008). For example, consider a thin disc with diameter equal to the laser spot diameter D . If, as above, all electrons are removed by the laser pulse, which requires the condition $a_D = \pi\sigma$ (similar to equation (2.20), see also (2.39)), the potential of the charged disc is $\varphi = \pi Q_i/D$, where $Q_i = eZ_i n_i \pi D^2 l/4$ is the disc charge. Here $a_D = a/2^{1/2}$ is the amplitude at the edge of the disc. Noting that the power of a linearly polarized pulse with the FWHM diameter D is $P = 1.55 \times 10^{-5}(aD/\lambda)^2 \text{ PW}$ we get the energy of light ions which are accelerated from the surface of an MLT consisting of heavy ions in the optimum regime:

$$\frac{\mathcal{E}_a}{Z_a} \approx 230 \text{ MeV} \sqrt{P/\text{PW}}. \quad (2.23)$$

We can make estimates of the laser-driven accelerator in the Coulomb explosion regime for $\lambda_0 = 0.8 \mu\text{m}$, $\tau = 30 \text{ fs}$, $D = 2\lambda_0$, and a diamond-like carbon (DLC) target ($n_e = 460n_{\text{cr}}$) with a thin proton layer ($Z_a = 1$). In this case, the proton energy scales with the laser pulse energy, W_L , as $\mathcal{E}_p \approx 40 \text{ MeV} \sqrt{W_L/\text{J}}$ (section 2.11, figure 23, up-triangles) at the optimum target thickness of $l \approx 9 \text{ nm} \sqrt{W_L/\text{J}}$.

The thickness of the second layer should be thin enough to ensure the narrow energy spectrum of the accelerated light ions. If initially all ions are concentrated at the same point, all of them will have the same energy (neglecting their repulsion). For a sufficiently small width Δx of the original light ion distribution on the target in the planar geometry, the width of the resulting energy spectrum $\Delta\mathcal{E}_a$ can be estimated as energy gained by the ions at distance Δx in the electric field E_i in the vicinity of the target: $\Delta\mathcal{E}_a = eZ_a \Delta x E_i$. Thus, the relative spectral width is $\Delta\mathcal{E}_a/\mathcal{E}_a \approx \Delta x E_i / \varphi$. In the case of a charged disc, $E_i = 4Q_i/D^2$, $\varphi = \pi Q_i/D$, the relative width is

$$\Delta\mathcal{E}_a/\mathcal{E}_a \approx 4\Delta x / \pi D; \quad (2.24)$$

for a thin enough light ion layer, $\Delta x \ll D$, the resulting ion spectrum is quasi-monoenergetic. A more general expression for the ion spectral shape can be found in Esirkepov *et al* (2002).

The longitudinal, $\varepsilon_{||} = \Delta\mathcal{E}_a \Delta t$, and transverse, ε_{\perp} , emittances of the ion beam are determined by the dimensions of the rear layer Δx (thickness) and ρ (transverse radius) (Esirkepov *et al* 2002, Bulanov S V *et al* 2004b):

$$\varepsilon_{||} = \Delta\mathcal{E}_a \Delta t = \frac{2\Delta x^2}{\pi D} \sqrt{2m_a \mathcal{E}_a}, \quad (2.25)$$

$$\varepsilon_{\perp} = \pi\rho \sqrt{\frac{2l}{D}}. \quad (2.26)$$

Here Δt is the time spread of the ion beam. Note that ρ and l can be selected significantly smaller than the transverse size of the front layer D , which results in small transverse emittance values.

Equations (2.24)–(2.26) and the optimum condition (2.20) show that in order to generate a high-quality ion beam (high energy, low energy spread, small emittances) using the double-layer target, it is necessary to satisfy the above assumptions, i.e. use a target with small dimensions (MLT) with even smaller dimensions of the rear light-ion (proton) layer.

2.4. Coulomb explosion of a cluster

The Coulomb explosion of a cluster (Nishihara *et al* 2001, Bychenkov and Kovalev 2005b, Kovalev *et al* 2007a, 2007b) can be treated in a similar way (Esirkepov *et al* 2000). In this case, the condition that the electric field at the surface of a fully stripped cluster of radius R equals the laser field gives

$$R = 3a_0 n_{\text{cr}} \lambda_0 / (2\pi n_e), \quad (2.27)$$

which for the present and near-future lasers and solid-density cluster means $R \ll \lambda_0$. The ions which originate from the cluster surface are accelerated to the maximum energy

$$\mathcal{E}_{i,\text{max}} = 4\pi e^2 Z_i n_e R^2 / 3 = 3Z_i m_e c^2 a_0^2 n_{\text{cr}} / n_e. \quad (2.28)$$

For a laser pulse tightly focused to a spot diameter equal to $2\lambda_0$, the maximum ion energy is $\mathcal{E}_{i,\text{max}} \approx 25 \text{ MeV} \times Z_i(n_{\text{cr}}/n_e)(P_0/\text{TW})$; assuming $n_e = 460n_{\text{cr}}$ and $\tau = 30 \text{ fs}$, the ion energy is $E_i \approx 1.7 \text{ MeV} \cdot Z_i(W_L/\text{J})$, and the optimum cluster radius is $R \approx 19 \text{ nm} \cdot (W_L/\text{J})^{1/2}$.

In the Coulomb explosion of a cluster, the energy of an ion depends on its original position and density distribution, but in any case the largest energies are gained by the ions originally situated on the cluster surface; for example, in the case of uniform density distribution the energy of ions with the initial distance to the centre r_0 equals $4\pi Z_i e^2 n_e r_0^2 / 3$. This can be used for the production of shaped ion energy spectra (Bychenkov and Kovalev 2005b, Kovalev *et al* 2007a). In particular, mono-energetic spectra of light ions can be obtained if the light ions are situated on the cluster surface, similarly to the double-layer foil (disc) target; see section 2.3.

The ion energy scaling for the cluster has two peculiarities. First, the ion energy scales linearly with the laser power;

second, it is inversely proportional to the cluster density. It would be advantageous to decrease the cluster density and thus increase the ion energy. In this case, the optimum cluster radius (2.27) also increases. For low enough density, the cluster radius becomes larger than the laser wavelength, and the laser spot needs to be increased to irradiate the whole target. This leads to the dependence of the ion energy on laser power similar to the thin foil (disc) target (2.23), i.e. square root of power with the numerical coefficient ~ 200 MeV at 1 PW (here we assume that the laser spot is twice the cluster size: $r_0 = 2R$).

In sections 2.3 and 2.4 we have considered the simplest analytical models of the Coulomb explosion regime of ion acceleration. A more elaborate theory based on the kinetic description, which includes many additional effects, such as multi-stream flow regimes and formation of density singularities, has been published by Kovalev and Bychenkov (2005), and Kovalev *et al* (2007a, 2007b).

2.5. Influence of the incidence angle

In the description of the foil target, we ignored the effect of the incidence angle, which can be an additional degree of freedom for the optimization. 3D PIC simulations (Morita *et al* 2008) show that there is an optimum incidence angle at which the ion energies can be significantly greater than those at normal incidence. In particular, for the simulation parameters the proton energy increases from 20 MeV at normal incidence to 45 MeV at $\theta = 30^\circ$ incidence and p-polarization ($a_0 = 30$, $I_0 = 2 \times 10^{21} \text{ W cm}^{-2}$, duration 8λ FWHM, spot diameter 6λ FWHM, a mass-limited disc target with a heavy ion (gold) substrate of diameter 10λ , thickness 0.5λ and density $1.6 \times 10^{22} \text{ cm}^{-3}$, and a proton coating of diameter 5λ , thickness 0.03λ and density $5 \times 10^{20} \text{ cm}^{-3}$). This optimum is explained by the interplay between two counteracting effects, larger laser energy absorption at oblique incidence and larger efficiency of pushing the electrons out of the target at normal incidence.

Oblique incidence of laser pulse to a foil or disc causes another important effect, namely the deviation of the accelerated ion beam from the target normal. This effect can be understood by considering the acceleration in the boosted frame moving with velocity $V = c \sin \theta$ along the target surface; in this reference frame, the incidence is normal, but the target (including the electrons and ions) has the velocity $u' = -V$ in the reverse direction (Bourdier 1983), here the primes denote quantities in the boosted frame. After the acceleration along the foil normal up to the longitudinal momentum $p'_{i\parallel} = p_{i\parallel}$, the ions still have momentum along the foil (perpendicular to its normal) $p'_{i\perp} = -m_i c \tan \theta$; here we neglect the influence of the magnetic field, which can change $p'_{i\perp}$. Transformation back to the laboratory reference frame gives the angle between the ion beam and the target normal ϕ (Morita *et al* 2008):

$$\tan \phi = (\sqrt{1 + \kappa^2} - \kappa) \tan \theta, \quad \kappa = \frac{m_i c}{p_{i\parallel} \cos \theta}. \quad (2.29)$$

In the case of non-relativistic ions, i.e. $p_{i\parallel} \ll m_i c$, the deviation is proportional to v_i/c , or the square root of the kinetic energy E_i : $\phi \approx \sqrt{E_i/2m_i c^2} \sin \theta$. For example, it is $\approx 4^\circ$ for a

45 MeV proton beam and $\theta = 30^\circ$. In the relativistic case, the ion beam propagates approximately along the laser direction: $\phi \approx \theta$. We note that this effect is a consequence of the relativistic dynamic of the target and ion beam and it happens if the ions are accelerated predominantly perpendicular to the target irrespective of the acceleration mechanism. It should be considered in the experiments even for ion energies of a few tens of MeV/nucleon, especially if the detector acceptance angle is small. We also note that the ion beam direction can be shifted due to another effect, namely the target deformation caused by the amplified spontaneous emission; see section 3.2 (Lindau *et al* 2005, Lundh *et al* 2007, Zeil *et al* 2010).

2.6. Radiation pressure dominant acceleration (the laser piston regime)

If the laser irradiance is extremely high, the radiation pressure can cause another very efficient acceleration mechanism, the so-called radiation pressure dominant acceleration (RPDA) regime or laser piston regime, figure 13 (Esirkepov *et al* 2004).

When a high-irradiance laser pulse with sufficiently large focal spot interacts with a thin foil, it can push forward the electrons due to the radiation pressure; ideally, all electrons are involved. The ions respond slowly, and a large charge-separation field builds up and efficiently accelerates the main body of the irradiated target area, i.e. the ions. If this charge-separation field is strong enough to accelerate ions quickly to *relativistic* velocity, the distance between the electrons and ions remains relatively small, and instabilities do not have time to develop (Esirkepov *et al* 2004). Note that this scenario in the optimum condition borders with the Coulomb explosion mechanism described above. At the second stage, the ions and electrons moving together represent a relativistic mirror co-moving with the laser pulse, as in the 'light sail' paradigm. Even if at the early stage the foil is partly transparent to the laser due to relativistic effects, at a later time, when the foil velocity approaches c , it becomes highly reflective due to the laser frequency downshift in the co-moving frame. Further, due to the double Doppler effect, the frequency of the reflected light becomes $\omega_r \approx \omega_0/4\gamma^2$, where $\gamma \gg 1$ is the relativistic gamma-factor of the accelerated foil, and the reflected light energy significantly decreases; almost all of the laser pulse energy is transferred to the foil. At the *final acceleration phase*, the ions moving with nearly the same velocity as electrons take most of this energy due to their much larger mass. Note that this acceleration mechanism has much in common with Veksler's collective acceleration (Veksler 1956, 1957).

The radiation pressure, which is the relativistic invariant, is

$$P_{\text{rad}} = R' \frac{(E'_0)^2}{2\pi} = R' \frac{c - V}{c + V} \frac{E_0^2}{2\pi} = R' \frac{c - V}{c + V} \frac{2I_0}{c}. \quad (2.30)$$

Here E'_0 and R' are the laser field and foil reflectivity in the boosted reference frame moving with the foil. The acceleration is assumed to be not too large, therefore we use the transformation into the inertial frame; in the expression with irradiance I_0 circular polarization is assumed. R' coincides with reflectivity in terms of photon number, which is the relativistic invariant; we assume that the absorption is

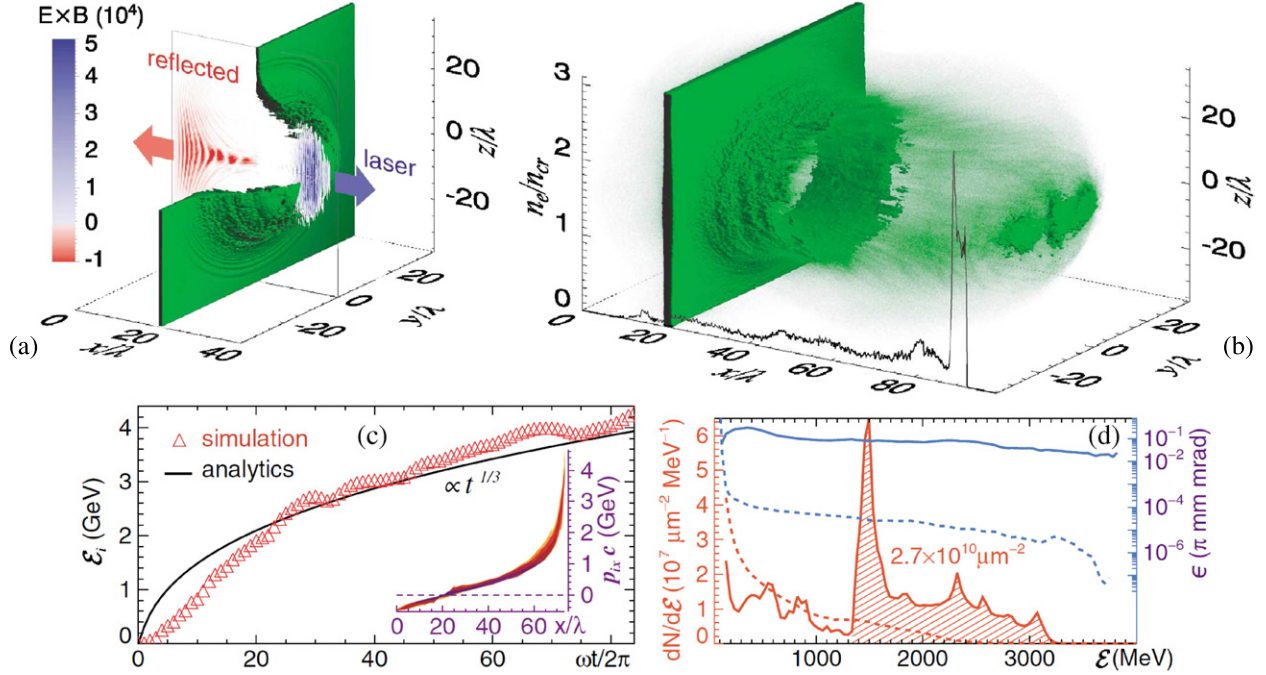


Figure 13. Ion acceleration in the radiation pressure dominant (laser piston) regime, 3D PIC simulations. The laser pulse is linearly polarized, $a_0 = 316$ ($I_0 = 1.37 \times 10^{23} \text{ W cm}^{-2} (\mu\text{m}/\lambda)^2$), $c\tau_{0\text{FWHM}} = 8\lambda$ with a sharp front starting from $a_0 = 100$, $r_{0\text{FWHM}} = 12.5\lambda$, the laser pulse energy is $E_0 = 10 \text{ kJ } (\lambda/\mu\text{m})$, the incidence is normal, the ions have $Z = 1$ and $m_i = m_p$ (i.e. protons). The target has thickness $l = \lambda$ and $n_e = 5.5 \times 10^{22} \text{ cm}^{-3} \times (\mu\text{m}/\lambda)^2 = 49n_{cr}$. (a) Ion density isosurface for $n_i = 8n_{cr}$ and the x component of the normalized Poynting vector $(e/m_e\omega c)^2 \mathbf{E} \times \mathbf{B}$ in the $(x; y = 0; z)$ plane, $t = 40 \times 2\pi/\omega$. (b) Isosurface for $n_i = 2n_{cr}$ and green gas for lower ion densities at a later time $t = 100 \times 2\pi/\omega$; the black curve shows the ion density along the laser axis. (c) Evolution of the maximum ion kinetic energy and the ion phase space projection (x, p_x) at $t = 80 \times 2\pi/\omega$. (d) The energy spectrum (red) and transverse emittance (blue) of ions (solid) and electrons (dashed) located in the region $50\lambda < x < 80\lambda, -\lambda < y, z < \lambda$ at $t = 80 \times 2\pi/\omega$. The hatched region contains 2.7×10^{10} particles per μm^2 area. The numerical values correspond to $\lambda = 1 \mu\text{m}$. Reprinted with permission from Esirkepov et al (2004).

negligible, i.e. $R' + T' = 1$, where T' is the transmission. The laser electric field at the foil position $x(t)$ is $E_0(t - x(t)/c)$. The foil velocity is $V = dx/dt = pc/(p^2 + m_i^2 c^2)^{1/2}$, where p is the individual ion momentum. These give the equation of motion (Esirkepov et al 2004, Bulanov S V et al 2004a)

$$\frac{dp}{dt} = R' \frac{E_0^2(t - x(t)/c)}{2\pi n_i l} \frac{\sqrt{p^2 + m_i^2 c^2} - p}{\sqrt{p^2 + m_i^2 c^2} + p}. \quad (2.31)$$

The reflectivity of a thin foil can be calculated within the sliding mirror approximation (Vshivkov et al 1998, Pirozhkov et al 2006a, 2006b, Macchi et al 2009a, 2010):

$$R' \approx \begin{cases} \frac{\pi^2 \sigma'^2}{1 + \pi^2 \sigma'^2}, & a < \sqrt{1 + \pi^2 \sigma'^2}, \\ \frac{\pi^2 \sigma'^2}{1 + a^2} \approx \frac{\pi^2 \sigma'^2}{a^2}, & a > \sqrt{1 + \pi^2 \sigma'^2}. \end{cases} \quad (2.32)$$

Here we assume circular polarization; $\sigma' = \sigma \lambda'/\lambda$ and λ' are the dimensionless areal electron density and laser wavelength in the boosted frame. When the foil velocity approaches c , σ' increases, and the reflectivity tends to 1; note that the dimensionless amplitude a is the relativistic invariant. If, at the beginning, the foil is transparent, i.e. $R \approx (\pi\sigma/a)^2$, the radiation pressure (2.30) does not depend on the laser amplitude, but it is rather determined by the foil parameters: $P_{\text{rad}} = 2m_e c^2 n_{cr} Ra^2 \approx 2\pi^2 m_e c^2 n_{cr} \sigma'^2$. This corresponds to

the case when the maximum charge separation is achieved; indeed, the maximum force which acts upon the ions is determined by the number of electrons, and the ‘excessive’ laser energy is transmitted through the foil.

For the simplest case of a constant-amplitude circularly polarized laser pulse ($E_0 = \text{const}$), constant reflectivity $R' = R$ and the initial conditions $p(t = 0) = 0$, solution to (2.31) is (Bulanov S V et al 2004a, 2005b)

$$\frac{2p^3 + 2(p^2 + m_i^2 c^2)^{3/2}}{3m_i^2 c^2} + p - \frac{2}{3}m_i c = \frac{RE_0^2}{2\pi n_i l} t. \quad (2.33)$$

The explicit solution can be found in Bulanov S V et al (2009). At $t \rightarrow \infty$, the foil achieves relativistic velocity, $R \approx 1$, and the solution has an asymptote (Esirkepov et al 2004, Bulanov S V et al 2004a, 2005b)

$$p \approx \frac{\mathcal{E}_i}{c} \approx m_i c \left(\frac{3E_0^2 t}{8\pi n_i l m_i c} \right)^{1/3} = m_i c \left(\mu s \frac{ct}{\lambda} \right)^{1/3}, \quad t \rightarrow \infty, \quad \mu = \frac{m_e Z}{m_i}, \quad s = \frac{a^2}{\sigma}, \quad (2.34)$$

$$x_{\text{acc}} \approx ct.$$

Here x_{acc} is the acceleration distance. For protons, $\mu_p = m_e/m_p \approx 1/1836$; for almost all fully ionized heavier ions, $\mu \approx \mu_p/2 \approx 1/3672$. The dimensionless parameter s characterizes the ratio between the pulse intensity and foil areal electron density.

Let us now consider the non-relativistic case ($p \ll m_i c$), which is valid for $t \ll 2\pi n_i l m_i c / R E_0^2$. The acceleration time approximately coincides with the pulse duration: $t_{\text{acc}} \approx \tau$. The ion momentum (2.33), energy and acceleration length can be approximated as

$$\begin{aligned} p &\approx \frac{R E_0^2}{2\pi n_i l} \tau \approx 2m_i c (\mu R s) N, & p \ll m_i c, \\ \mathcal{E}_i &\approx \frac{R^2 E_0^4}{8\pi^2 n_i^2 l^2 m_i} \tau^2 \approx 2m_i c^2 (\mu R s)^2 N^2, & \mathcal{E}_i \ll m_i c^2, \\ x_{\text{acc}} &\approx \frac{R E_0^2 \tau^2}{4\pi n_i l m_i} \approx \lambda (\mu R s) N^2, \end{aligned} \quad (2.35)$$

where $N = c\tau/\lambda$ is the number of cycles in the pulse, and the dimensionless parameters μ and s are defined in (2.34).

The maximum ion energy which can be obtained using a finite-duration laser pulse with energy W_L can be calculated from (2.31) without the assumption of constant pulse amplitude; here we assume $R' = 1$. Introducing the phase $\psi = \omega_0(t - x(t)/c)$ and the normalized part of the laser energy interacted with the target at phase ψ :

$$w(\psi) = \int_{-\infty}^{\psi} \frac{E_0^2(s/\omega_0)}{4\pi \omega_0 n_i l m_i c} ds,$$

the ion momentum and energy are expressed as (Bulanov S V *et al* 2005b)

$$\begin{aligned} p &= m_i c \frac{w(w+1)}{w+1/2}, \\ \mathcal{E}_i &= \sqrt{m_i^2 c^4 + p^2 c^2} - m_i c^2 = m_i c^2 \frac{w^2}{w+1/2}. \end{aligned} \quad (2.36)$$

The laser energy assuming a flat-top spatial profile with area S is

$$W_L = Sc \int_{-\infty}^{\infty} \frac{E_0^2(t)}{4\pi} dt,$$

which means that the maximum value of w (after the interaction with all laser pulses) is $w_{\text{max}} = W_L/n_i l S m_i c^2 = W_L/N_i m_i c^2$, where $N_i = n_i l S$ is the number of ions within the laser spot. Thus, at the end of the pulse the ion kinetic energy and conversion efficiency are (Esirkepov *et al* 2004, Bulanov S V *et al* 2005b)

$$\begin{aligned} \mathcal{E}_{i,\text{max}} &= \frac{2W_L}{2W_L + N_i m_i c^2} \frac{W_L}{N_i} = 2m_i c^2 \frac{(\mu s N)^2}{1 + 2\mu s N}, \\ \eta &= \frac{N_i \mathcal{E}_{i,\text{max}}}{W_L} = \frac{2W_L}{2W_L + N_i m_i c^2}. \end{aligned} \quad (2.37)$$

If the laser energy is much larger than the total rest energy of ions ($W_L \gg N_i m_i c^2$), almost all laser energy goes into the ion kinetic energy: $\mathcal{E}_{i,\text{max}} \approx W_L/N_i > m_i c^2$, $\eta \approx 1$, which means that this acceleration mechanism approaches an ideal one. It is worth noting that if the foil achieves relativistic velocity, the acceleration time becomes much longer than the pulse duration τ . Using the approximate solution (2.34) for a constant-field

pulse and the final ion energy $\mathcal{E}_{i,\text{max}} \approx W_L/N_i$, we find that the acceleration time and length are (Esirkepov *et al* 2004, Bulanov S V *et al* 2005b)

$$\begin{aligned} t_{\text{acc}} &\approx \frac{2}{3} \left(\frac{W_L}{N_i m_i c^2} \right)^2 \tau \gg \tau, \\ x_{\text{acc}} &\approx ct_{\text{acc}} \gg c\tau. \end{aligned} \quad (2.38)$$

As we can see, the RPDA, at least within the ‘light sail’ approximation, has many advantages compared with other acceleration mechanisms. In order to implement this idealized scenario, however, several conditions should be met. First, in order to repel all electrons, which corresponds to the maximum achievable acceleration (see (2.32)), the laser electric field should be of the order of the maximum charge-separation field, or in terms of the dimensionless amplitude (Macchi *et al* 2009a)

$$a \approx \pi\sigma = \pi \frac{n_e l}{n_{\text{cr}} \lambda_0} \quad (2.39)$$

(compare with the conditions (2.20), $\sigma_{\text{opt}} \approx 0.4a$ for $a \gg 1$). In other words, the condition should be near the onset of the relativistic transparency of a thin foil (Vshivkov *et al* 1998). Note that in the case of $a \gg \pi\sigma$, most of the laser pulse is transmitted before the foil reaches the relativistic velocity; on the other hand, if $a \ll \pi\sigma$, the acceleration is small as the foil is ‘too heavy’. Second, the ions must be quickly accelerated up to relativistic velocity to suppress the development of instabilities (see below). Using approximation (2.35) and condition (2.39), we can find that the ion momentum becomes comparable to $m_i c$ within one laser period when $a = m_i/2\pi Z m_e$. For protons, this means $a \approx 300$ ($I_0 \approx 1.2 \times 10^{23}$ W/cm²(μm/λ₀)²), which can be achieved with the laser systems such as ELI (Chambaret *et al* 2010) and HiPER (Dunne 2006). 1D and 2D PIC simulations suggest that the intensity requirement can be substantially relaxed by using circular polarization, which induces much less electron heating (Liseikina and Macchi 2007, Klimo *et al* 2008, Liseikina *et al* 2008, Robinson *et al* 2008, Rykovanov *et al* 2008, Yan *et al* 2008, Chen M *et al* 2009, Macchi *et al* 2009b) and target structuring (Chen M *et al* 2009). Third, the focal spot size must be relatively large to keep the quasi-1D dynamics; for this reason, a super-Gaussian or flat-top pulse is advantageous compared with a Gaussian one (Klimo *et al* 2008, Liseikina *et al* 2008, Robinson *et al* 2008, Bulanov S S *et al* 2008b). Fourth, for large ion energies the Rayleigh length should be at least of the order of the acceleration length; other possibilities include several laser pulses focused consequently further and further, or focusing by an axicon-type lens (McLeod 1954, Bunkin *et al* 1983). Another elegant way is to employ a cocoon formed by the plasma to confine the laser pulse, which can in this case propagate without divergence much longer than the Rayleigh length (Esirkepov *et al* 2004, Bulanov S V *et al* 2005b). Fifth, the pulse duration should be sufficiently short, such that the instabilities do not destroy the foil, but sufficiently long, such that the very efficient *final acceleration phase* is achieved.

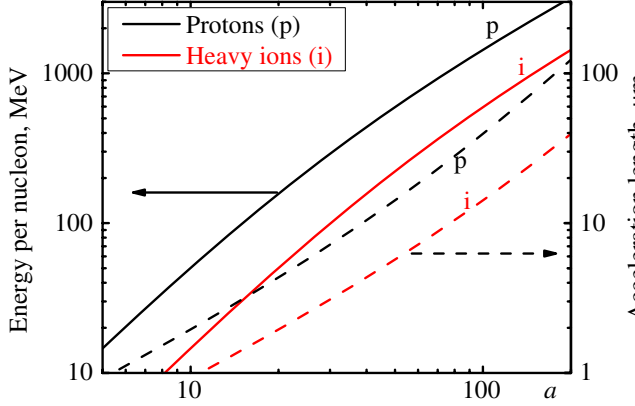


Figure 14. Kinetic energy of protons and fully ionized heavy ions (solid lines) and corresponding acceleration lengths (dashed lines) versus dimensionless laser amplitude in the idealized 1D ‘light sail’ scenario of the RPDA (or laser piston) (2.40); wavelength $\lambda = 800$ nm, pulse duration $\tau = 30$ fs (number of cycles $N = 11$).

The ion energy and efficiency (2.37) in the optimum case (2.39) are

$$\begin{aligned}\mathcal{E}_{i,\max}^* &\approx 2m_i c^2 \frac{(\pi \mu a N)^2}{1 + 2\pi \mu a N}, \\ \eta^* &\approx \frac{2\pi \mu a N}{1 + 2\pi \mu a N}.\end{aligned}\quad (2.40)$$

Here, again, $\mu = m_e Z_i / m_i$ and $N = c\tau/\lambda$ ((2.34), (2.35)). The final acceleration stage is achieved when $2\pi \mu a N > 1$, which corresponds to $aN > 300$ and $aN > 600$ for protons and fully ionized heavy ions, respectively. The dependence of ion energy and acceleration length on the laser amplitude a in the optimum case and number of cycles in the pulse $N = 11$ are shown in figure 14 for protons and fully ionized heavy ions. The dependence of proton energy on the laser pulse energy is shown later in figure 23 by stars ($\lambda_0 = 0.8 \mu\text{m}$, $\tau = 30$ fs, flat-top shape in space and time); the different connecting lines correspond to the spot radius fixed at $1.5 \mu\text{m}$ (dashed line) and determined by the condition that the Rayleigh length equals the acceleration length (solid line). From (2.40) it follows that at a fixed pulse energy longer pulses with smaller a (and correspondingly thinner targets with smaller ion number, see (2.39)) provide larger ion energies: $\mathcal{E}_{i,\max} \propto \tau$ for $2\pi \mu a N \ll 1$ and $\mathcal{E}_{i,\max} \propto \tau^{1/2}$ in the opposite limit. However, for longer pulses the instabilities (see below) destroy the foil, and the simple ‘light sail’ scenario is no longer valid.

The results of 3D PIC simulation of the RPDA regime are shown in figure 13 (Esirkepov *et al* 2004). The parameters of the laser pulse satisfy the conditions formulated above: the amplitude is $a = 316$, the laser pulse starts with a sharp edge (jump from 0 to $a = 100$) and then continues as a Gaussian pulse with FWHM length of $c\tau_0 = 8\lambda_0$. The laser has a relatively wide focal spot ($25\lambda_0$ FWHM). Note that the target parameter σ (2.19) is 49, which means that the condition (2.39) is nearly satisfied ($\pi\sigma = 154$, at the beginning $a = 100$ and then increases up to a maximum of 316). The ions are accelerated up to an energy of a few GeV, with a pronounced peak at 1.5 GeV and a tail up to above 3 GeV. The dependence of the maximum ion energy versus time obtained in simulations

follows the analytical approximation (2.34). The estimate of the ion energy using the idealized equation (2.40) gives 2.3 GeV. Extensive 2D PIC simulations show that the idealized ‘light sail’ model gives a good approximation for the maximum ion energy; however, it overestimates the efficiency (Macchi *et al* 2009a).

The foil accelerated by the radiation pressure is the subject of Rayleigh–Taylor-like instability (Pegoraro and Bulanov S V 2007, 2009). The perturbation growth with wave vector k perpendicular to the laser propagation direction (axis y) is given by

$$\begin{aligned}\delta y_{\text{rel}} &\propto \exp \left[\left(\frac{t}{\tau_{\text{rel}}} \right)^{1/3} - iky \right], \\ \delta y_{\text{non-rel}} &\propto \exp \left[\frac{t}{\tau_{\text{non-rel}}} - iky \right]\end{aligned}\quad (2.41)$$

in the relativistic and non-relativistic limits, respectively. The 3D equations can be found in Bulanov S V *et al* (2009). The wavenumber of the fastest growing mode is $k_{\max} \approx k_0 = 2\pi/\lambda_0$ (Pegoraro and Bulanov S V 2009); the modes with larger k (shorter scale lengths) are smoothed by the driver pulse. For a constant-amplitude laser pulse, the instability growth times are

$$\begin{aligned}\tau_{\text{rel}} &= \frac{1}{3c\lambda_0} \sqrt{\frac{\pi R_0}{2k^3}} = \frac{a_0}{3c} \sqrt{\frac{Z_i}{2k^3 l} \frac{m_e n_{\text{cr}}}{m_i n_e}}, \\ \tau_{\text{non-rel}} &= \frac{\lambda_0}{c} \sqrt{\frac{1}{2\pi k R_0}} = \frac{1}{ca_0} \sqrt{\frac{l}{2k Z_i} \frac{m_i n_e}{m_e n_{\text{cr}}}},\end{aligned}\quad (2.42)$$

respectively. Here R_0 is the normalized radiation pressure

$$R_0 = \frac{E_0^2}{m_i n_i l \omega_0^2}. \quad (2.43)$$

It is notable that the instability growth rates in these two cases depend differently on the radiation pressure, and, as a consequence, on the amplitude a_0 , the ion mass m_i and charge Z_i , and the target density n_e : in the relativistic case, the growth time increases at larger amplitudes a_0 and smaller densities n_e and ratios m_i/Z_i , while in the non-relativistic case, the dependence is reversed. Further, in the relativistic case the instability grows slowly due to the power 1/3 in the exponent (2.41). For the parameters of the simulation (figure 13) and $\lambda_0 = 0.8 \mu\text{m}$, $k = 2\pi/\mu\text{m}$, the non-relativistic instability growth time at the beginning of the pulse (with $a_0 = 100$) is $\tau_{\text{non-rel}} = 2.5$ fs and the exponent after one laser period is $2\pi/\omega_0 \tau_{\text{non-rel}} = 1$; the relativistic instability growth time is $\tau_{\text{rel}} = 0.06$ fs and the exponent after time $t = 80 \times 2\pi/\omega_0$ (shown in figure 13(d)) is $(t/\tau_{\text{rel}})^{1/3} = 15$. We can see that the target is not significantly perturbed at the early acceleration stage, and it is indeed accelerated as a whole at the beginning. However, at the time shown, instabilities have sufficient time to grow; an indication of this is the proton spectrum (figure 13(d)), which is not perfectly mono-energetic, as it could be without the instabilities. Interestingly, the instability at the relativistic acceleration stage is not necessarily to be avoided. The instability effectively reduces the target areal density with time, which leads to larger maximum energy

which grows as t (Pegoraro and Bulanov 2007), albeit the number of ions with this energy is much smaller. This is similar to the regime of gradual areal density decreasing described in the following paragraph. In the non-linear stage, instability leads to the formation of plasma clumps (cusps) accelerated separately (Bulanov S V *et al* 2009). The small transverse size of the clumps increases the luminosity of the RPDA laser accelerator, which is inversely proportional to the ion beam cross-section. The clump formation can also be employed to obtain quasi-monoenergetic ion spectrum even in the case of non-uniform transverse intensity distribution. Higher on-axis intensity leads to target bending, which in turn enhances instability in the periphery, where the target becomes dispersed and therefore transparent. Thus, only a central clump is efficiently accelerated, giving rise to a quasi-monoenergetic ion spectrum (Yan *et al* 2009).

As the foil becomes relativistic, the optimum condition (2.39) cannot be always satisfied if the areal foil density is constant, because in the boosted frame co-moving with the foil the laser amplitude a_0 (1.1) remains the same (it is relativistically invariant), but the dimensionless areal density σ' increases due to the laser frequency downshift (note that the areal density n_{el} is the relativistic invariant, which follows from the particle number invariance, but the dimensionless areal density σ (2.19) depends on the wavelength). The optimum condition in this case is velocity-dependent:

$$a \approx \pi \sigma' = \pi \frac{n_{el}}{n_{cr} \lambda_0} \sqrt{\frac{c + V}{c - V}}. \quad (2.44)$$

However, if we allow the amplitude to *increase* or the areal density n_{el} to *decrease* with time, this optimum condition can be satisfied even in the ultra-relativistic case. It turns out that a gradually decreasing areal density can indeed provide larger ion energies and larger efficiencies (Bulanov S V *et al* 2009, 2010a, 2010b). The decrease in the areal density can be, for example, due to transverse foil expansion caused by the ponderomotive force of a focused laser pulse, or due to the instabilities described above. In particular, combining a laser pulse having a tailored dependence on time with a foil target in which the areal density n_{el} gradually decreases, it is possible to achieve faster ion momentum growth than in the case of non-expanding foil $p_{nl=\text{const}} \propto t^{1/3}$ (2.34). Moreover, the phase of a laser pulse interacting with foil at the moment t tends to a finite value at $t \rightarrow \infty$, which means that a finite-duration laser pulse can accelerate the target up to unlimited ion energies. The transverse foil expansion also leads to slower rates of instability development. Interestingly, even for a non-relativistic case the transverse expansion of the foil is advantageous from the efficiency point of view, namely despite the decrease in the particle number, the efficiency is larger than in the non-expanding foil case (2.37).

We again mention here the similarity in the optimum conditions for the RPDA (2.39) and the Coulomb explosion regime (2.20). The important consequence is that these two acceleration regimes are not perfectly separated: the Coulomb explosion gradually changes into the radiation pressure regime when the laser amplitude increases (Esirkepov *et al* 2006). Bulanov S S *et al* (2008a, 2008b) described a composite

acceleration regime, directed Coulomb explosion (DCE), in which both processes, the radiation pressure and Coulomb explosion, contribute to the ion energy.

The relativistic ions obtained in the radiation pressure acceleration can be further accelerated in the wakefield, similar to the case of electron acceleration (Tajima and Dawson 1979). 2D PIC simulations show that an exawatt (27 kJ, 30 fs) pulse can produce a high-quality quasi-monoenergetic 76 GeV proton beam in such a staged configuration (Zhang *et al* 2010). Note that the requirement of relativistic ion velocity at the first, radiation pressure, stage is essential as it allows trapping of the protons into the acceleration phase of the wakefield.

2.7. Hole boring and collisionless shock acceleration

If an overdense target is relatively thick, it cannot be treated as a thin foil, as in the ‘light sail’ RPDA acceleration regime; see section 2.6. However, the plasma is still pushed forward by the radiation pressure (2.30), the so-called hole boring process (Wilks *et al* 1992). This gives rise to another kind of radiation pressure acceleration mechanism, hole boring acceleration or collisionless shock acceleration (Denavit 1992, Zhidkov *et al* 2002, Silva *et al* 2004, Macchi *et al* 2005, Zhang *et al* 2007a, 2007b). Ion acceleration attributed to collisionless shocks has been reported by Henig *et al* (2009a) (protons up to 8 MeV using 0.6 J, 45 fs, 20 TW, 10^{20} W cm $^{-2}$ laser irradiating overdense micro-sphere targets) and Wei *et al* (2004) (helium up to 13 MeV using 180 J, 0.5–0.7 ps, 0.25 PW laser irradiating an underdense gas jet target).

In a simple 1D quasi-stationary model of hole boring acceleration (Schlegel *et al* 2009), the laser pulse piles up the electrons, forming a thin electron spike in front of the pulse; an electron-free area appears behind the spike, figure 15. It is assumed that the laser pulse is totally reflected from the electron spike. The ions left behind are pulled by the arising charge-separation field, thus forming the second ion spike. In the boosted frame moving with the hole boring velocity, the unperturbed plasma ions impinging on these moving spikes are accelerated (‘reflected’) by the electric field existing between the spikes; at the turning point, the ion velocity changes sign, and at zero velocity the ion density tends to infinity, see the sharp rear edge in figure 15. Analogously, the electron spike also has a sharp rear edge. Thus, an electrostatic shock propagating into a plasma is formed (hence there is another name for this acceleration mechanism, collisionless shock acceleration). In contrast to the electrostatic collisionless shocks in low-density plasmas, in the case of high-density, low-temperature—i.e. small thermal velocity and large ($\gg 1$) Mach number—plasmas, the unperturbed plasma electrons and ions can be nearly totally reflected by the laser ponderomotive pressure and the longitudinal charge separation electric field between the two spikes. For this reason, a circularly polarized laser pulse normally incident to the target is advantageous for this mechanism, as in this case the plasma is heated less effectively (Macchi *et al* 2005, Zhang *et al* 2007a, 2007b).

Unlike the ‘light sail’ case, hole boring has a quasi-stationary velocity, because the radiation pressure is balanced by the momentum change of the continuously reflecting

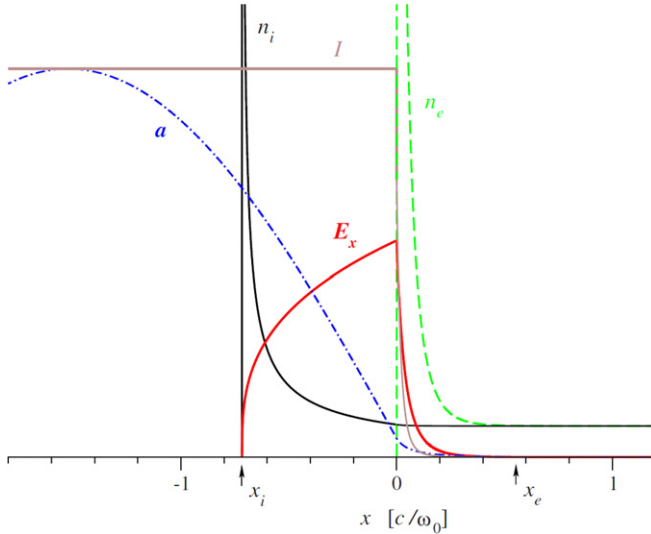


Figure 15. Quasi-stationary 1D model of hole boring acceleration. The curves, scaled to arbitrary units, correspond to the amplitude (a) and intensity ($I \propto E^2 + B^2$) of the standing wave formed by the incident and reflected waves, electron and ion densities (n_e, n_i) and charge-separation field (E_x) for the laser amplitude $a_0 = 50$ and deuterium plasma with $n_{0e} = 2n_{0i} = 40n_{cr}$. The axis x is along the laser propagation direction, 0 and x_i correspond to the positions of the sharp rear side edges of the electron and ion spikes, respectively, and x_e corresponds to the beginning of the electron spike, beyond which the plasma is unperturbed. Reprinted with permission from Schlegel *et al* (2009).

particles of the unperturbed plasma, mostly ions due to their larger mass. Assuming the reflectivity is $R' = 1$, the shock velocity (also called the hole boring velocity) is $V_s = c\Xi^{1/2}/(1 + \Xi^{1/2})$, where $\Xi = I_0/m_i n_i c^3$ is the dimensionless pistonning parameter; this expression is the extension of the classical result to the relativistic case (Robinson *et al* 2009c). In the boosted frame moving with the shock, the ions are reflected by the shock, with maximum ion velocity $V'_i = V_s$, which corresponds to the laboratory frame velocity $V_i = 2V_s/(1 + V_s^2/c^2)$; here we use the relativistic velocity transformation law (Landau and Lifshitz 2003). The maximum kinetic ion energy (in the laboratory frame) is

$$E_i = m_i c^2 \frac{2\Xi}{1 + 2\sqrt{\Xi}} = m_e c^2 \frac{2a_0^2 n_{cr} Z_i}{n_e + 2a_0 \sqrt{\frac{m_e}{m_i} n_{cr} n_e Z_i}}. \quad (2.45)$$

Here we assume circular polarization. In the non-relativistic and ultra-relativistic limits, (2.45) gives $E_i \approx 2m_e c^2 a_0^2 Z_i n_{cr} / n_e$ and $E_i \approx c^2 a_0 (m_e m_i Z_i n_{cr} / n_e)^{1/2}$, respectively. The ion energies are higher for smaller densities. However, the model is applicable for $n_e > (1 + a_0^2)^{1/2} n_{cr} \approx a_0 n_{cr}$ (Schlegel *et al* 2009) as it assumes total laser pulse reflection rather than relativistic transparency of a thick plasma. The calculated proton energy for tightly focused Gaussian laser pulses ($\lambda_0 = 0.8 \mu\text{m}$, $r_0 = 1.5 \mu\text{m}$, $\tau_0 = 30 \text{ fs}$) and $n_e = a_0 n_{cr}$ is shown in figure 23 by left-pointing triangles. Assuming negligible electron heating, the conversion efficiency of laser energy into the ions is $\eta = 2\sqrt{\Xi}/(1 + 2\sqrt{\Xi})$. For further model details and comparison with 1D PIC simulations, see Schlegel *et al* (2009) and Robinson *et al* (2009c).

The 1D model of hole boring described above predicts a mono-energetic ion spectrum. This is indeed confirmed in the 1D PIC simulations for relatively small amplitudes, e.g. $a_0 \sim 10\text{--}20$; however, even for constant-intensity pulses, as a_0 increases, the finite acceleration time, which is in contrast to the instantaneous ion reflection assumed in the model, causes periodical oscillations of the hole boring velocity and periodical overtaking of the electron spike by the ion spike, which in turn results in broad ion spectra (Schlegel *et al* 2009, Robinson *et al* 2009c).

When the ions accelerated by the shock reach the target rear surface, they can get an additional energy due to the charge-separation field at the target rear side (Zhidkov *et al* 2002, Silva *et al* 2004, d'Humières *et al* 2005), as described in section 2.1, provided that the velocity of front-accelerated ions is larger than the velocity of those from the rear surface. In the non-relativistic case this means the target thickness is $l < 4\lambda_D M^2/Z_i$, where $\lambda_D = (T_e/4\pi e^2 n_e)^{1/2}$ is the Debye length of the hot electron component and M is the Mach number.

Another scenario is the transition from the collisionless shock to the 'light sail' model of the radiation pressure acceleration; in this case, the acceleration is stable when at the transition point the velocity achieved by the shock acceleration is close to relativistic (Qiao *et al* 2009), which corresponds to $I_0 \sim m_i n_i c^3$. For protons, $\lambda_0 \sim 1 \mu\text{m}$ and $n_e \sim 100 n_{cr}$ this requires intensity $\sim 10^{23} \text{ W cm}^{-2}$, similar to the condition of ion acceleration to the relativistic velocity in one laser cycle within the laser piston ('light sail') radiation pressure model (see the discussion after equation (2.39)).

2.8. Ion acceleration with a dipole vortex in near-critical plasma

The acceleration mechanisms considered in the previous subsections are based on a high-contrast laser pulse interaction with a solid-density sharp-gradient target. Here we describe another model, which is based on a laser pulse interaction with an underdense or near-critical plasma, figure 16 (Kuznetsov *et al* 2001, Matsukado *et al* 2003, Bulanov S V *et al* 2005a, Bulanov S V and Esirkepov 2007, Yogo *et al* 2008, Bulanov S S *et al* 2010, Nakamura T *et al* 2010). In contrast to the previous models, this model includes the magnetic field and is intrinsically multi-dimensional.

When the laser pulse enters the near-critical plasma, it can form a channel due to relativistic self-focusing (for relativistic self-focusing, see Mourou *et al* (2006) and references therein). Note that if multiple filaments are formed in this process, the acceleration efficiency decreases, therefore measures should be taken in order to ensure the formation of a single self-focusing channel, such as the matching of the numerical aperture of the focusing optics, or, in other words, the focal spot size, to the plasma waveguide (channel) (Mourou *et al* 2002, Bulanov S S *et al* 2010) and/or preparation of the gentle plasma profile at the front side of the plasma (Bulanov S V *et al* 2005a). In the sufficiently thick near-critical plasma almost all the laser pulse energy is absorbed. The laser pulse accelerates fast electrons inside the channel. The current of accelerated

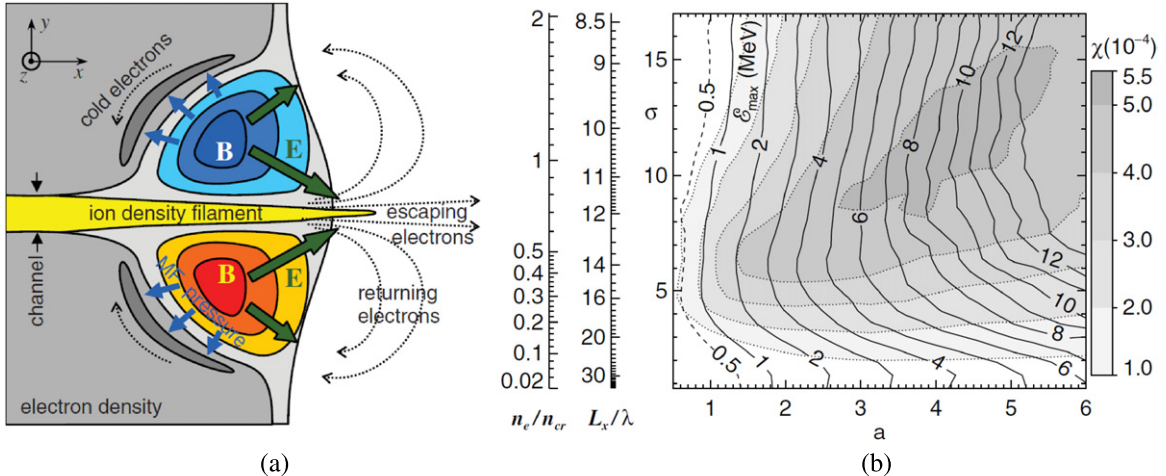


Figure 16. (a) Sketch of the mechanism of ion acceleration with a dipole vortex in an underdense or near-critical plasma. A laser pulse incident from the left self-focuses and accelerates electrons along the axis. These fast electrons together with the return current form the toroidal magnetic field. The magnetic field pressure expels the cold electron fluid, forming the long-living charge-separation field, which in turn accelerates and collimates the ions from the ion density filament. Reprinted with permission from Bulanov S V and Esirkepov (2007). (b) Results of multi-parametric PIC simulations: curves, the maximum proton energy; grey scale, the conversion efficiency. Each point on the map corresponds to the parameter pair (a, σ) , $\sigma = \int n_e(x) dx / n_{cr} \lambda_0$. The laser pulse is Gaussian in space and time, $c\tau_{FWHM} = 20\lambda_0$, spot size is $15\lambda_0$ (FWHM), pulse energy $\approx 0.2a^2$ J. The plasma density and thickness are connected through the relation $n_e l^3 = \text{const}$ following from the conservation of particle number in the region evaporated by amplified spontaneous emission. Reprinted with permission from Matsukado *et al* (2003).

electrons together with the return current lead to the formation of the toroidal quasi-static magnetic field with a typical magnitude $|B| \sim m_e c \omega_0 / e \approx 100$ MG and larger. After the laser pulse and fast electrons pass, this field is sustained by the vortical motion of electrons, which corresponds to the existence of the dipole vortices (Bulanov S V *et al* 2005a, Nakamura T and Mima 2008a); the motion of these electrons is not necessarily relativistic. If the plasma density gradient is steep (the scale length is shorter than the self-focusing channel width), the vortices move perpendicularly to the plasma density gradient. In particular, this leads to a quick expansion of the magnetized region at the channel exit on the rear side of the target. In contrast, if the plasma density gradient is gentle, the vortices move along the channel axis in the forward direction at the target rear side and in the backward direction at the target front side. In the latter case, the lifetime of the magnetic field is determined by the ion response, which is relatively slow, typically sub-ps. During the existence of the magnetic field, the cold electron fluid is expelled from the magnetized region by the magnetic field pressure, which leads to the formation of positively charged regions and an electrostatic sheath with electric field $E \sim \nabla B^2 / 8\pi e n_e$. This long-living charge separation accelerates ions in the ion density filament, which is formed near the axis (Kuznetsov *et al* 2001, Bulanov S V *et al* 2005a, Bulanov S V and Esirkepov 2007, Bulanov S S *et al* 2010). The ion filament has been studied with simulations by Popov K I *et al* (2010). Although the magnetic field itself causes a weak defocusing of the ion beam, the electrostatic field leads to ion beam collimation. In the most favourable condition, when the magnetized region moves along the axis to the low-density region, the electron density decreases and the electric current, which supports the magnetic field, quickly removes the electrons from the near-axis region. This leads to the Coulomb explosion of the remaining ions. In addition,

near the axis the magnetic field changes its direction. During the evolution, the magnetic field redistributes such that the strongest magnetic field can concentrate around the axis. This can lead to reconnection and magnetic field annihilation. The quick change in the magnetic field induces an electric field, which can also accelerate ions (Bulanov S V *et al* 2005a).

The acceleration in the near-critical plasma sensitively depends on the plasma density profile. The profile which provides multi-MeV proton acceleration with a few TW laser was found through PIC simulations by Bulanov S V *et al* (2005a). This profile consists of a few tens of μm near-critical plasma slab surrounded by a low-density, long-scale length plasma corona. Experimentally, such a profile can be implemented using a foil exploding due to the amplified spontaneous emission (ASE) (Matsukado *et al* 2003) or a controlled separate prepulse. Optimization of exploding foils (London and Rosen 1986) requires extensive hydrodynamic simulations followed by multi-dimensional PIC simulations (Matsukado *et al* 2003, Andreev *et al* 2009, d'Humières *et al* 2010). Another option is to design a special gas jet, which has the advantage of being replenishable and repetitive (Fiedorowicz *et al* 2000, Fukuda *et al* 2009).

Ion acceleration in the underdense or near-critical plasma was observed in several experiments; see section 3.9. In particular, Willingale *et al* (2006) observed acceleration of He^{2+} ions up to 40 MeV using 340 J, 1 ps laser pulses ($5.5 \times 10^{20} \text{ W cm}^{-2}$, $a_0 = 21$) focused into the supersonic He jet with an electron density of $\sim (2-4) \times 10^{19} \text{ cm}^{-3}$. Terawatt-class femtosecond lasers produced protons with an energy of several MeV during interaction with near-critical density plasma from thin foils evaporated by ASE (Matsukado *et al* 2003, Yogo *et al* 2008). A 4 TW, 150 mJ laser accelerated ions up to 10–20 MeV/nucleon in the cluster jet (Fukuda *et al* 2009).

Scalability of this ion acceleration mechanism has been studied with PIC simulations and analytical calculations by Bulanov S S *et al* (2010) and Nakamura T *et al* (2010). In order to achieve optimum acceleration, it is necessary to meet several conditions. First, the laser spot size should match the size of the self-focusing channel in order to avoid filamentation. Second, the laser pulse energy should be depleted near the rear side of the target, in which case on the one hand the dipole vortex is created at the exit side of the channel, and on the other hand the laser energy is not wasted to transmission. The amplitude of the laser pulse after self-focusing, a_{SF} , and the self-focusing channel radius, r_{SF} , are determined by the laser power P_0 and plasma density n_e (Bulanov S S *et al* 2010):

$$\begin{aligned} a_{SF} &= \left(8\pi \frac{P_0}{P_c} \frac{n_e}{n_{cr}}\right)^{1/3}, \\ r_{SF} &= \frac{c}{\omega_{pe}} \sqrt{a_{SF}} = \frac{\lambda_0}{2\pi} \sqrt{a_{SF} \frac{n_{cr}}{n_e}} \\ &= \frac{\lambda_0}{2^{1/2}\pi^{5/6}} \left(\frac{n_{cr}}{n_e}\right)^{1/3} \left(\frac{P_0}{P_c}\right)^{1/6}. \end{aligned} \quad (2.46)$$

Here $P_c \approx 17$ GW is the relativistic self-focusing critical power, equation (2.16). For a plasma slab, to avoid filamentation the initial laser focal spot size should be close to the self-focusing channel radius r_{SF} . If the focal spot is fixed, the density should be optimized to satisfy this requirement.

The optimum plasma length l can be estimated from the assumption that all laser energy is transferred to the electrons in the channel. If each electron has an average energy of $\sim a_{SF} m_e c^2$, the optimum thickness is (Bulanov S S *et al* 2010)

$$l = a_{SF} K c \tau_0 \frac{n_{cr}}{n_e} = 2\pi^{1/3} K c \tau_0 \left(\frac{n_{cr}}{n_e}\right)^{2/3} \left(\frac{P_0}{P_c}\right)^{1/3}, \quad (2.47)$$

where $K = 1/13.5$ in the 3D geometry. Note that the first equality in condition (2.47) is similar to the optimum condition for the thin foil (2.20), (2.39), where the laser wavelength is substituted by the laser pulse length $c\tau_0$; however, the self-focused amplitude itself depends on the plasma density. For constant laser pulse parameters, the optimum plasma density and thickness satisfy the condition $n_e^{2/3} l = \text{const}$, which agrees well with the optimum dependence found with the help of multi-parametric 2D PIC simulations, figure 17 (Bulanov S S *et al* 2010).

The maximum proton energy can be estimated as

$$\mathcal{E}_{p,\max} = a_{SF} \gamma_e^2 m_e c^2, \quad (2.48)$$

where γ_e is the Lorentz factor of fast electrons, which can be found from the PIC simulations. Thus, a 1 PW, 19 J laser pulse focused down to a $1.5\lambda_0$ spot (FWHM) onto an optimum target ($n_e = 3n_{cr}$, $l = 50\lambda_0$) accelerates protons up to 1.3 GeV, with $\sim 4 \times 10^8$ protons with energies above 1 GeV (the estimated conversion efficiency is $\sim 0.4\%$), figure 18.

The scalings for the self-focusing, optimum conditions, and the proton energy agree with the 2D PIC simulations over a wide range of parameters, when the laser pulse is shorter than the target thickness ($c\tau_0 < l$) and the density satisfies the condition $1.6n_{cr} < n_i < 10n_{cr}$. Outside

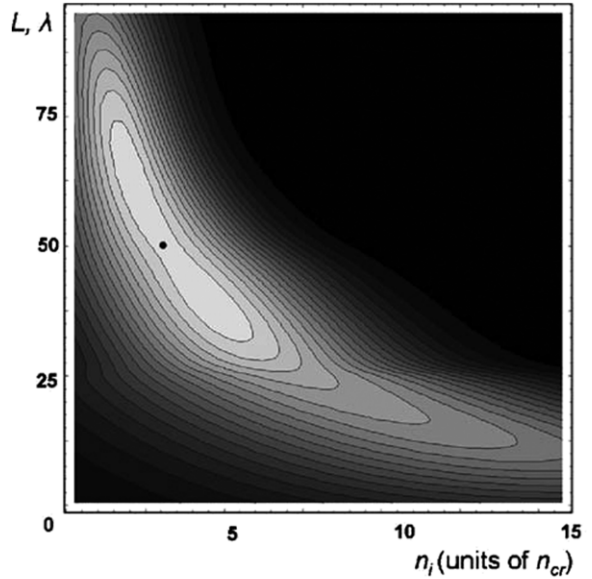


Figure 17. Multi-parametric 2D PIC simulations of the ion acceleration in near-critical density targets (Bulanov S S *et al* 2010). Dependence of the maximum proton energy on the plasma density n_i and thickness L for constant laser parameters $P_0 = 1$ PW, $W_L = 19$ J and spot size $1.5\lambda_0$ (FWHM). The black dot corresponds to the maximum proton energy of 1.3 GeV (figure 18). Reprinted with permission from Bulanov S S *et al* (2010).

the region determined by these inequalities, other processes and acceleration mechanisms not accounted for in the model become important.

The maximum proton energies obtained in several papers using the PIC simulations over a wide range of laser pulse energies are shown in figure 19(a). One conclusion which follows from the figure is that tighter focusing and the shortest pulse duration provide higher proton energies. It is also interesting to compare the simulations with the uniform plasma slab (Bulanov S S *et al* 2010, green squares) and with the profiled target, including two lower density regions at the front and rear sides and the corresponding density ramps (Nakamura T *et al* 2010, blue diamonds). The laser pulse shapes and parameters are similar in these two simulation series, although the plasma optimization is performed in different ways. The profiled targets are advantageous at lower laser energies, while the simple targets show better performance at higher laser energies. This may indicate that at laser powers typically available at the moment the preplasma and rear-side low-density regions are essential for efficient ion acceleration, while for the future laser systems a step-like density profile is sufficient, as the extremely high irradiance laser can propagate through the relatively dense target and expel enough electrons to support the magnetic fields at the rear side.

The solid line in figure 19(a) shows an analytical scaling (Nakamura T *et al* 2010)

$$\mathcal{E}_{p,\max} = \frac{1}{2} \gamma_a m_e c^2 \frac{n_1}{n_2}, \quad (2.49)$$

where $\gamma_a \approx a_{SF}/2^{1/2}$ and n_1 ($\sim n_{cr}$) and n_2 ($\ll n_1$) are the densities of the plasma and the rear-side low-density region, respectively. The optimum relation for the simulation

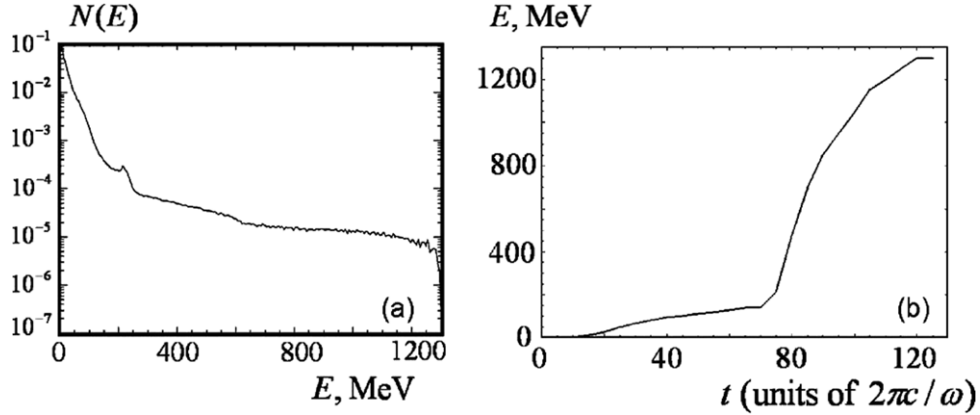


Figure 18. Parameters of the proton beam accelerated by a 1 PW, 19 J laser pulse focused to the spot $1.5\lambda_0$ (FWHM) onto the optimum target ($n_e = 3n_{cr}$, $l = 50\lambda_0$). (a) Energy spectrum. (b) Dependence of the maximum proton energy on time, demonstrating the onset of rapid acceleration at $t \approx 702 \times (2\pi/\omega_0)$, corresponding to the formation of quasi-static fields at the rear side of the target. Reprinted with permission from Bulanov S S *et al* (2010).

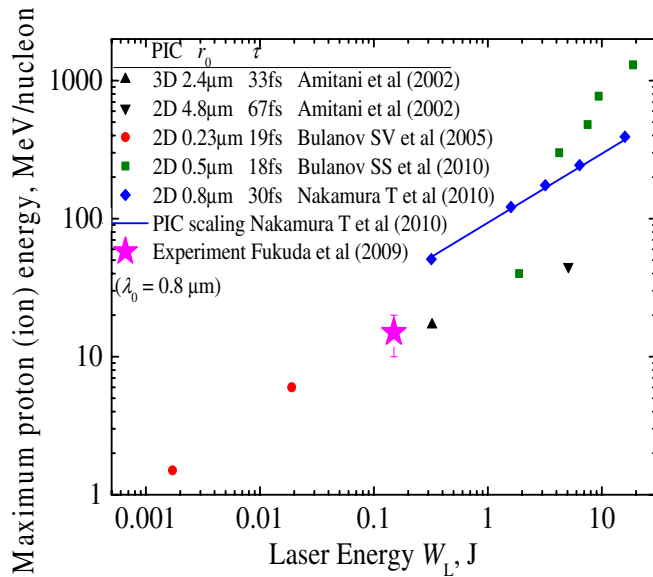


Figure 19. Acceleration with a dipole vortex in near-critical plasma: maximum proton (ion) energy versus laser energy obtained with PIC simulations, the numbers are calculated for $\lambda_0 = 0.8 \mu\text{m}$. Both uniform plasma slabs (Amitani *et al* 2002, Bulanov S V *et al* 2005a, Bulanov S S *et al* 2010) and profiled targets (Bulanov S V *et al* 2005a, Nakamura T *et al* 2010) were studied in the simulations. The star shows the experimental results by Fukuda *et al* (2009).

parameters is $n_1 \approx 8n_2$. In this case, (2.49) gives $\mathcal{E}_{p,\max} = 2\sqrt{2}a_{SF}m_e^2 \approx 1.4a_{SF}$ MeV. The scaling found from the PIC simulation is $\mathcal{E}_{p,\max} \approx 17$ MeV (P_0/TW) $^{1/2}$; this scaling for $\tau = 30$ fs is shown in figure 23 by down-pointing triangles.

2.9. Scalings in the optimum and non-optimum regimes

Important information which is expected from a theory, simulation or experiment is a scaling of the ion energy, conversion efficiency, etc, with the laser parameters, e.g. irradiance, power or pulse energy. However, care should be taken as these scalings depend on the conditions, in particular, on matching between the laser and target parameters. Ideally, for each point on the scaling curve all remaining parameters should be optimized, e.g. for the scaling of maximum ion

energy versus laser pulse energy, the pulse duration, spot size, target thickness and density, etc, should all be optimized or pushed to their limits to provide maximum ion energy. Certainly, this idealized case can hardly be implemented in simulations or experiments. For this reason, the scalings are obtained with some of the parameters fixed. This often gives a scaling which looks ‘better’, i.e. with a steeper inclination, than the scaling in the optimum case. An example is shown in figure 20 (2D PIC simulations, Bulanov S S *et al* 2008a). Panel (a) shows the dependence of the proton energy on target thickness l for several values of the laser power P , from which the optimum thickness can be determined. In panel (b) the proton energy is plotted versus the laser power. The squares correspond to the optimum target thickness; here the proton energy follows the square-root ($\propto P^{1/2}$) scaling (2.23). The triangles correspond to the fixed thickness $l_f = 0.1\lambda_0$, which provides smaller proton energy except at one point $P_f \approx 1$ PW where l_f coincides with the optimum. At $P > P_f$, the scaling is slower than the optimum one; however, at $P < P_f$ the scaling is faster (steeper): it is approximately linear ($\propto P$), although the achievable proton energies are clearly smaller. Thus, a ‘better’ (steeper) scaling often indicates lack of optimization at smaller laser pulse energies/powers/irradiances and limited data at higher values of the corresponding laser pulse parameters.

2.10. Relations between the acceleration regimes

The laser–plasma interaction is in general a very complex process, which depends on many parameters. Some of the regimes relevant to the laser–foil interaction are shown in the (laser irradiance I_0 (amplitude a_0), target thickness l (areal density σ)) plane in figure 21; note that the borders between the regimes are not sharp and drawn along some arbitrary lines. The models described above and shown in figure 21 are highly simplified; that is why they are useful but also why their applicability is limited. In a real experiment or simulations no model can explain all the features; however, a model can explain some of the significant features. In most cases, two (or more) models should be used to explain different properties, e.g. different parts of the ion spectra or different ion species;

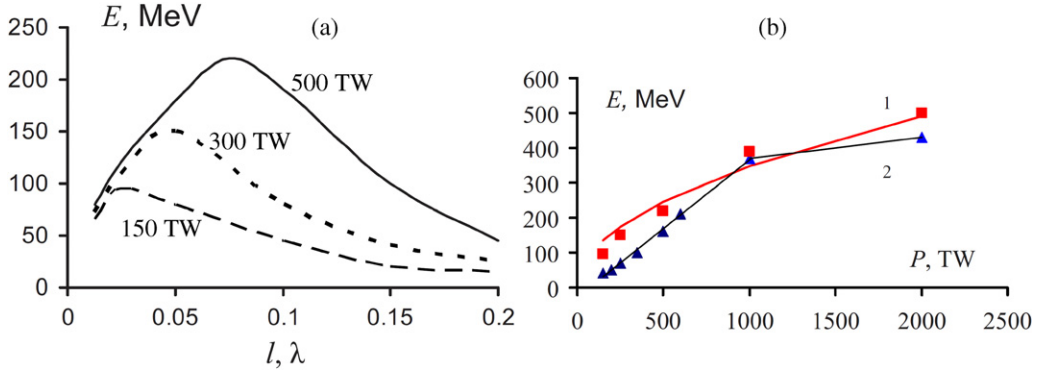


Figure 20. Maximum proton energy versus target thickness (a) and laser power (b), 2D PIC simulations (Bulanov S S *et al* 2008a). The laser pulse is Gaussian with a duration of 30 fs and spot size of $1\lambda_0$ (FWHM). The double-layer target consists of fully ionized Al with an electron density of $400n_{\text{cr}}$ and variable thickness l , and fixed-thickness hydrogen layer ($10n_{\text{cr}}, 0.05\lambda$). In (b) the squares and triangles correspond to the optimum target thickness and fixed thickness $l = 0.1\lambda_0$, respectively. Reprinted with permission from Bulanov S S *et al* (2008a).

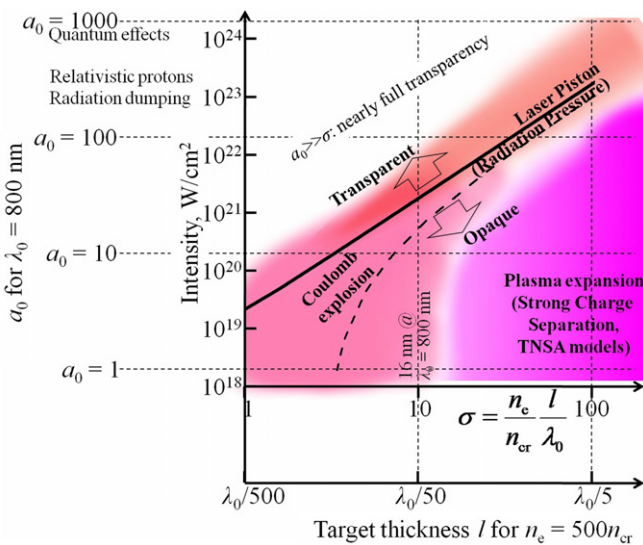


Figure 21. Several regimes of laser-driven ion acceleration employing thin foil targets on the (intensity (amplitude a_0), target thickness (dimensionless areal density σ)) plane. The borders of the regimes are not sharp; rather, there are gradual transitions between them. The solid line represents the condition of the relativistic transparency of a thin foil (2.45), which, for $a \gg 1$, coincides with the condition that the laser field equals the maximum electric field of the charged plane with the areal charge density $n_e l = \sigma n_{\text{cr}} \lambda_0$ (2.21). The dashed line represents the optimum condition for the proton acceleration found in the PIC simulation (2.20) (Esirkepov *et al* 2006).

for example, protons observed at the rear side of a foil target can be due to the acceleration at the front and rear sides, with the high-energy part of the spectrum dominated by protons from the rear side (Fuchs *et al* 2007a).

Typically, several acceleration regimes can take place at different acceleration stages (Esirkepov *et al* 1999); examples include the DCE regime (end of section 2.6) or collisionless shock acceleration followed by acceleration in the charge-separation field (section 2.7). A composite acceleration regime consisting of the TNSA, ‘enhanced TNSA’ and breakout afterburner (BOA) stages was identified by Yin *et al* (2006, 2007), figure 22. After the first TNSA stage (figure 22(a)), the enhanced TNSA follows (figure 22(b)), which is characterized

by efficient heating of electrons due to the penetration of the laser pulse into the sufficiently expanded target. Finally, in the BOA stage (figure 22(c)), the laser pulse penetrates through the target (cf the optimum (transparency) condition in sections 2.3 and 2.6). Ideally, transparency occurs near the peak pulse intensity (Henig *et al* 2009c). The penetrating part of the laser pulse continuously pushes the electrons, which transfer their momentum to the ions through the Buneman-type instability (Albright *et al* 2007). The latter regime is a kind of radiation-pressure dominant one. The BOA is capable of producing ion spectra with quasi-monoenergetic features; further, in the presence of different ion species, the ions with larger ratio Z_i/m_i (typically protons) detach from the target during the TNSA stage, and heavier ions are accelerated predominantly in the BOA stage. To give an example, carbon ions with a quasi-monoenergetic spike at 240 MeV (20 MeV/nucleon) were obtained in the 2D PIC simulations (Yin *et al* 2007) using a $\lambda_0 = 1 \mu\text{m}$, 20 J, constant-intensity (flat-top) pulse with the linear rise during 52 fs, focused into a $4 \mu\text{m}$ diameter spot ($10^{21} \text{ W cm}^{-2}$, $a_0 = 27$); the target was a 30 nm thick carbon slab with $n_e = 660n_{\text{cr}}$ ($\sigma = 20$, not far from the relativistic transparency condition (2.20), (2.39)).

Summarizing, several acceleration mechanisms can act simultaneously or in stages and similar ion energies with similar scalings can be achieved in different regimes, as can also be seen from figure 23, where the proton energy scalings from several models are presented. Therefore, care should be taken when assigning a dominant acceleration regime in a simulation and especially in an experiment. Additional measurements or dependences are necessary, e.g. electron spectra, laser absorption, reflection, transmission, etc. The analytical models described in this section may help one to identify the acceleration regime, provided that only one regime is dominant. For example, for a pure Coulomb explosion regime the maximum ion energy gained in the electrostatic field is proportional to the ion charge, therefore fully ionized carbon ions would be accelerated with up to six times larger energy than protons. For a pure RPDA (‘light sail’ mode), where the whole target is accelerated to the same velocity, the ion energy is proportional to the ion mass, therefore carbon ions would have 12 times the proton energy. For a combination of acceleration mechanisms, these relations may not hold.

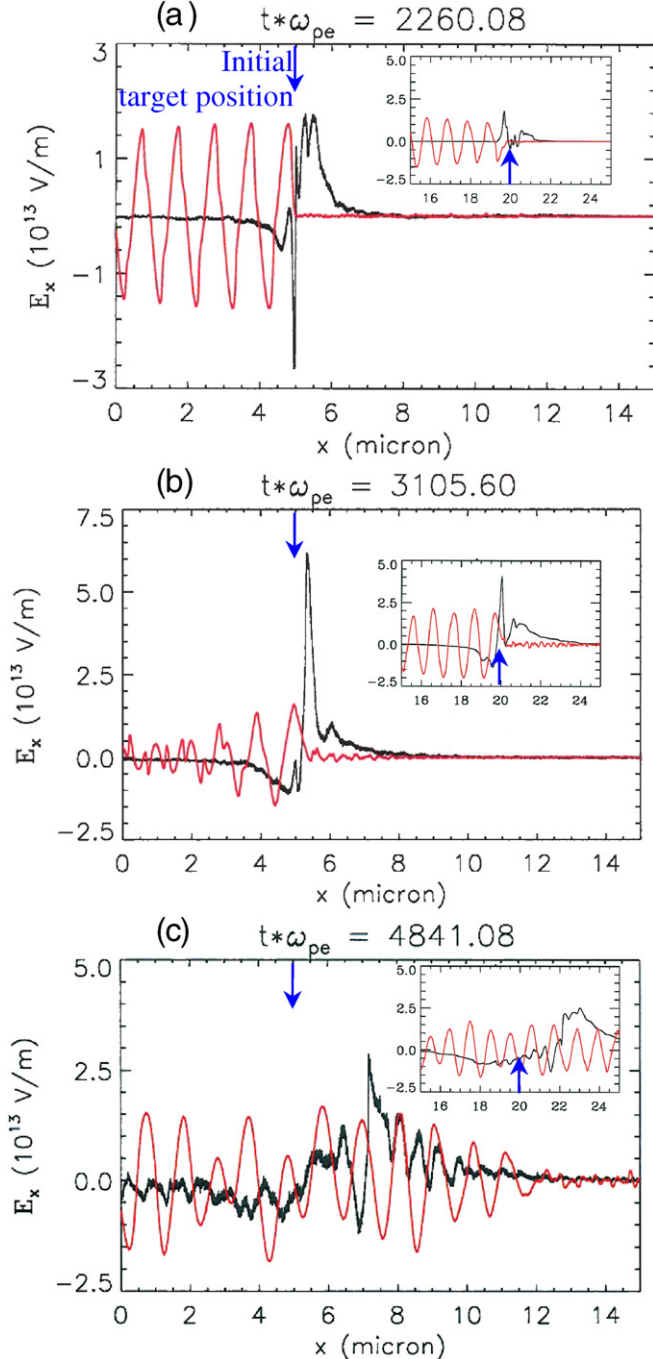


Figure 22. BOA acceleration of carbon ions, results of PIC simulations (2D in the main frames, 1D in the insets). The black and red lines show the longitudinal and transverse (in arb. units) electric fields, respectively; in 2D, the electric fields along the laser beam centre are shown. The ultra-thin target has a thickness of 30 nm and density of $660n_{cr}$, the laser intensity is $I_0 = 10^{21} \text{ W cm}^{-2}$. From top to bottom, the frames correspond to the different acceleration stages: TNSA, enhanced TNSA and BOA, respectively. Reprinted with permission from Yin *et al* (2007).

Apart from achievable ion energies, another important aspect of laser-driven ion acceleration is the spectral shape. For many of the applications, a limited bandwidth or quasi-monoenergetic spectrum is necessary or beneficial. Such spectra are expected in the Coulomb explosion of

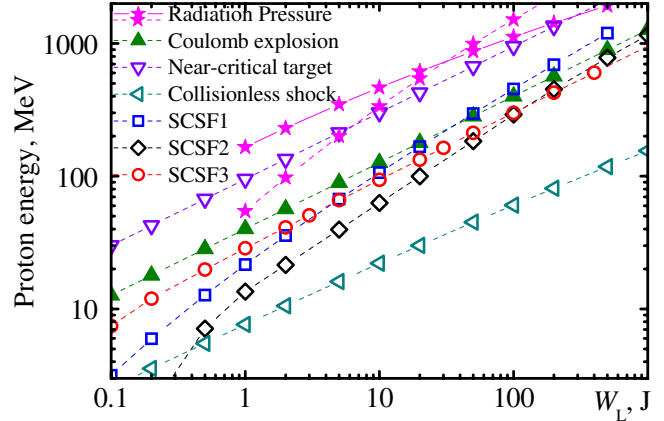


Figure 23. Proton energy versus laser pulse energy for several acceleration mechanisms, calculations using idealized models; the parameters are wavelength $\lambda_0 = 0.8 \mu\text{m}$, Gaussian pulse with duration $\tau_0 = 30 \text{ fs}$ (FWHM) and spot radius $r_0 = 1.5 \mu\text{m}$ (HFHM). The open symbols indicate the maximum proton energy of broad energy spectra, while the solid symbols indicate the energy of a quasi-monoenergetic peak predicted by models. The pink solid stars are for the ‘light sail’ model of RPDA (2.40) (Esirkepov *et al* 2004) with the optimum target areal density (2.39) (Macchi *et al* 2009a) and flat-top spot and pulse shapes, instabilities are not taken into account; the stars connected with the dashed (i) and solid (ii) lines correspond to the spot radius r_F (i) fixed at $1.5 \mu\text{m}$ and (ii) adjusted to provide Rayleigh length $2\pi r_F^2/\lambda_0$ equal to the acceleration length. For $W_L > 30 \text{ J}$ (i) predicts higher proton energies but requires some method to keep the laser pulse focused, e.g. the cocoon (see text in section 2.6); for $W_L < 30 \text{ J}$, (ii) predicts higher proton energies because the acceleration length is short and $r_F < 1.5 \mu\text{m}$. The green solid up-triangles are for the Coulomb explosion of the thin disc in the optimum regime (2.20), (2.23) (Esirkepov *et al* 2006). The violet down-triangles are for the acceleration with a dipole vortex in the near-critical plasma (section 2.8): $E_{p,\max} \approx 17 \text{ MeV} (P_0/TW)^{1/2}$ (Nakamura T *et al* 2010). The left-triangles are for collisionless shock acceleration (hole boring) (2.45) (Robinson *et al* 2009c, Schlegel *et al* 2009) and minimum density at which the target is not transparent, $n_e = a_0 n_{cr}$. The blue squares are for the SCSF model (2.17), (2.18) (Passoni and Lontano 2008). The black diamonds are for the SCSF model (2.15) (Schreiber *et al* 2006a), target thickness $l = 10 \mu\text{m}$, electron divergence half-angle $\theta = 10^\circ$, the pulse duration is optimum (see figure 10(a)) but not smaller than $\tau_{0,\min} = 30 \text{ fs}$ (the optimum duration becomes shorter than 30 fs for pulse energies larger than $\sim 100 \text{ J}$). The red circles are for the SCSF model (2.5) (Nishiuchi *et al* 2006) with the electron temperature (2.6), the Debye length calculated using density from (2.8)–(2.10) and the acceleration length (2.11).

a double-layer target or in the RPDA before instability development. Quasi-monoenergetic or peaked spectra are also predicted by theories and simulations of ion acceleration in multi-species plasmas (Tikhonchuk *et al* 2005, Brantov *et al* 2006, Robinson *et al* 2009a, Andriyash *et al* 2010).

The simple models presented here can provide guidance for the parameter choice in experiments and simulations. Understanding the underlying physics is also useful for conscious decisions on laser pulse tailoring (e.g. choice of wavelength, duration, polarization, temporal and spatial profiles, multiple pulses, etc) and possibly selecting more sophisticated targets than those considered here (e.g. mass-limited spoke targets (Strangio *et al* 2007), flat-top cone targets (Flippo *et al* 2008), holed targets (Pae *et al* 2009),

laser-machined cone targets (Matsuoka *et al* 2010), etc); some of the new target designs are discussed in section 3.7.

2.11. Achieving therapeutic ion energies: theoretical consideration

Concluding section 2, we would like to mention cancer treatment with laser-driven ion sources as one of the potential applications with significant social impact; see section 4.7. In order to use an ion source for cancer therapy, it must satisfy several requirements (Khoroshkov and Minakova 1998, Bulanov S V and Khoroshkov 2002a). The energy of protons required to treat deep tumours is ~ 250 MeV. It is ~ 400 MeV/nucleon for heavier ions, e.g. carbon (Brahme *et al* 2001). For shallow tumours, the required ion energy is correspondingly lower. For precise tumour irradiation, the relative energy spread should be $\sim 1\%$; another possibility is simultaneous irradiation of a certain range of depths with a highly controllable (tailored) particle spectrum. The required number of particles is $\sim (1-5) \times 10^{10} \text{ s}^{-1}$. There are strict requirements on stability, controllability, emittance, duty cycle, etc. All these factors make the application of laser-driven ion beams to cancer therapy challenging. Here we discuss acceleration mechanisms which could potentially be used for a laser-based medical ion accelerator.

Protons have the largest charge-to-mass ratio, and therefore they are the easiest ions to accelerate. Figure 23 shows the proton energies versus the laser pulse energy, calculated using models with known simplified scalings described in section 2. Theoretically, a sub-10 J laser can achieve ~ 200 MeV protons employing the acceleration with dipole vortex in a near-critical or underdense plasma. Somewhat larger laser energies ($\sim 20-40$ J) are required if the Coulomb explosion, TNSA or SCSF mechanisms are employed. Finally, the laser piston regime (radiation pressure in the ‘light sail’ mode) can provide up to 0.3–0.5 GeV protons employing a 10 J laser, provided that the instability does not inhibit the acceleration. Among these models, the laser piston holds promise as having the highest conversion efficiency (tens of %) and quasi-monoenergetic spectrum (again, if instability does not develop). Coulomb explosion of a double-layer target also gives a quasi-monoenergetic spectrum. In contrast, the TNSA, SCSF and dipole vortex mechanisms provide very broad spectra; the values shown in figure 23 are the maximum cut-off proton energies, which means that only a minority of all accelerated protons have such an energy. Acceleration in the near-critical or underdense plasma can provide relatively large proton energy with moderate energy of laser pulse; further, in the case of a gas jet target, repetitive operation is straightforward; finally, the contrast requirement (section 3.2) is relaxed compared with other mechanisms in which thin solid targets are employed.

From figure 23 we conclude that even if laser technology is pushed to the limits (the shortest pulse duration and a spot size of the order of the wavelength), a sub-PW class laser is required to achieve therapeutic proton energies, especially if a quasi-monoenergetic spectrum and high conversion efficiency are also required. This conclusion is supported by the 2D

PIC simulations (figure 20). Certainly, for shallow tumours treatable with $\sim 60-80$ MeV protons, the requirements for the laser driver are significantly relaxed.

3. Experimental results of laser-driven ion acceleration

In this section, we describe the experimental aspects of laser-driven proton and heavier ion acceleration. First of all, we briefly review the present ultra-high peak power laser systems. For the driver lasers, not only a high peak power and stability, but also well controllable temporal and spatial profiles are required. Secondly, we briefly describe how to measure various parameters of laser-driven ion beams including ion detection with magneto-electric analysers, the online time-of-flight (TOF) technique, filtered nuclear track detectors, nuclear activation techniques and so on. Then thirdly, we summarize the present achievements of proton and heavier ion acceleration experiments such as maximum proton energy versus laser pulse intensity and energy, proton and ion spectral shapes versus laser shooting conditions and so on, with various kinds of laser irradiated targets. The readers can compare these with the theoretical models and simulations described in section 2. Finally, we formulate problems yet to be resolved and tasks for future experiments.

3.1. Present laser systems for ion acceleration

Modern high-power laser systems are based on the chirped pulse amplification (CPA) concept (Strickland and Mourou 1985) coupled with a stable ultra-short laser oscillator (Sarukura *et al* 1991, Spence *et al* 1991). A simplified schematic layout of a typical CPA system is shown in figure 24. Present Nd : glass and Ti : sapphire laser systems can deliver laser pulses having a duration of typically 0.3–1 ps and 30–100 fs, respectively, with an ultra-high peak power up to 1 PW (Perry *et al* (1999); for a review, see Mourou *et al* (2006)).

Apart from the pulse energy and duration, which together determine the power, an important characteristic is the minimum achievable focal spot, which together with the power determines the irradiance (intensity). Higher intensity is required to achieve larger ion energies in most acceleration regimes (see section 2). The achievable focal spot size is limited by the aberrations and diffraction. For an ideal beam, the diffraction-limited focal spot size is of the order of λF , where $F = f/D$ is the *f*-number, *f* is the effective focal length of focusing optics (usually off-axis parabolas (OAPs) are used), and *D* is the beam diameter; there is also a numerical coefficient omitted here, which depends on the beam shape. For the smallest focal spots, the *f*-number should be decreased; however, it is limited by practical issues such as geometry and debris deposition on the OAP. Nakatsutsumi *et al* (2010) demonstrated a technique of intensity enhancement using a small (several mm size) elliptical plasma mirror which refocuses laser light focused by a usual OAP; in their implementation, an *f*/0.4 elliptical plasma mirror allowed a $0.9 \mu\text{m}$ focal spot (FWHM) with ~ 8 fold estimated increase in the intensity to be achieved; simultaneously, the contrast was

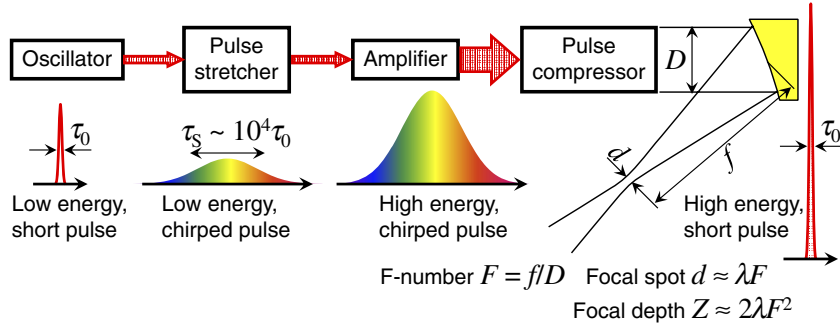


Figure 24. Schematic diagram of a CPA system. A short, small-energy pulse after the oscillator with duration τ_0 is stretched to a much longer duration τ_s , amplified to large energy, and recompressed. The compressed pulse is focused with an off-axis parabolic mirror. Here D , f , F and λ are the laser beam diameter, effective focal length of the off-axis parabolic mirror, f -number of the focusing optics and the central wavelength of the laser pulse, respectively.

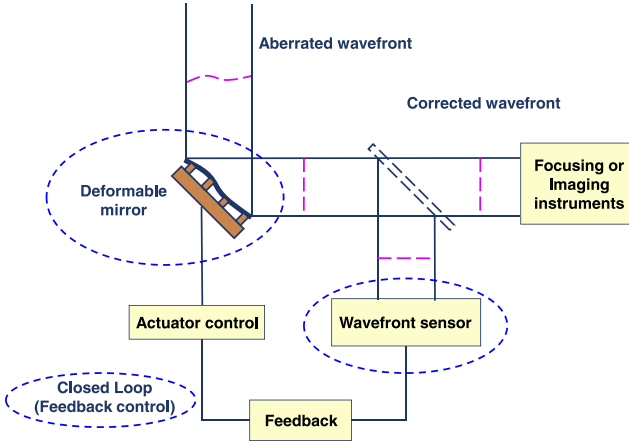


Figure 25. Schematic diagram of the deformable mirror system including feedback control for correcting wavefront distortions. The detector providing feedback may be a wavefront sensor or focal spot imaging system. (Courtesy of Dr Tae Moon Jeong.)

improved (about plasma mirrors and contrast, see section 3.2). The presence of geometrical aberrations is another obstacle to overcome. Aberrations not only reduce the intensity, but can also lead to irregular-shaped ion beams (Fuchs *et al* 2003). Practically, it becomes increasingly more difficult to preserve the wavefront quality when the laser beam diameter increases. Laser systems with beam diameter larger than several centimetres greatly benefit from an active wavefront quality control using one or two deformable mirrors, figure 25 (Druon *et al* 1998, Yoon *et al* 1998, Perry *et al* 1999, Baumhacker *et al* 2002, Bahk *et al* 2004, 2005 Danson *et al* 2004), which can typically provide nearly diffraction-limited focal spot sizes. The Strehl ratio which is defined as the ratio of the observed peak intensity to the theoretical maximum (Strehl 1895) approaches 1. Next-generation lasers for ion acceleration in the radiation pressure dominant regime must implement active wavefront control to achieve super-Gaussian or flat-top-like focal spot shapes (Chen M *et al* 2008, Bulanov S S *et al* 2008b).

3.2. On the contrast requirements

The preceding light, if not properly controlled, can alter or destroy the target well before the main pulse arrives (Kaluza

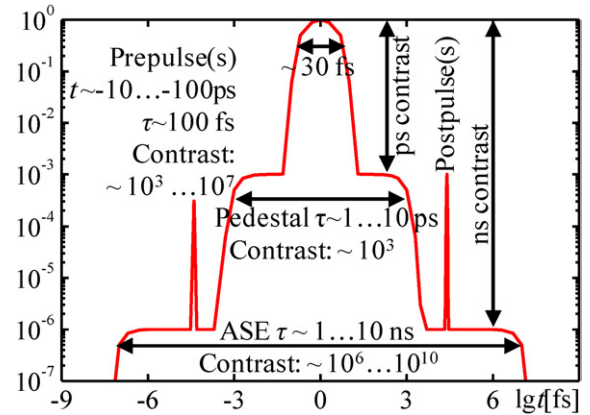


Figure 26. Typical temporal structure of an intense ultra-short laser pulse with several kinds of preceding light: leakage from the regenerative amplifier (if it is used), ASE, picosecond pedestal and prepulses. The main pulse duration (30 fs) corresponds to a typical minimum duration of Ti : sapphire lasers; other laser types have different main pulse durations.

et al 2004, McKenna *et al* 2006). Several kinds of preceding light should be taken into account, as shown schematically in figure 26. A leakage pulse from a regenerative amplifier, if it is employed in the laser system, is situated ~ 10 ns before the main pulse and has a typical contrast of $\sim 10^5$ and duration similar to or somewhat longer than the main pulse due to the different material dispersion. The ASE has a typical contrast of $\sim 10^6$ – 10^{10} and duration of a few ns. There is also a few to several tens of ps pedestal with a typical contrast of 10^3 – 10^5 ; this pedestal is caused by the misalignment and imperfections of the compressor gratings or by some other high-order dispersion sources. Finally, there are possible prepulses at a few tens of or a hundred ps before the main pulse with a broad range of contrasts and duration similar to or somewhat longer than the main pulse one. Didenko *et al* (2008) demonstrated that these prepulses are transformed from postpulses at similar absolute delay values by the non-linearity of the chirped pulse amplifiers; the prepulse intensity is $\sim B^2 I_{\text{post}}$, where B is the b -integral and I_{post} is the postpulse intensity. Thus, the pulse must be clean in terms of both prepulses and postpulses before injection into the amplifier chain.

In this review, we sometimes refer to experimental conditions as ‘low’, ‘normal’ or ‘high’ contrast. ‘Low’ contrast

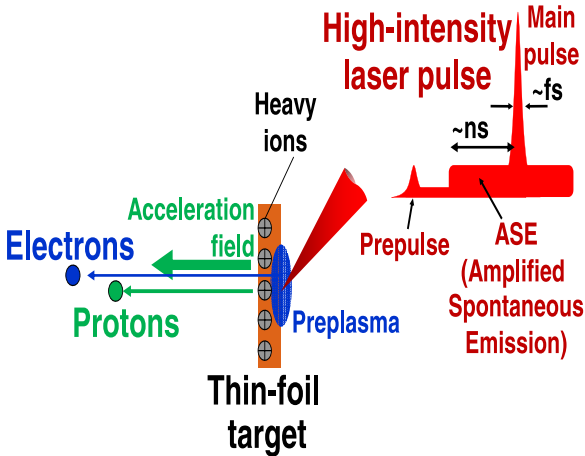


Figure 27. Schematic view of a laser-irradiated thin foil. An ASE pulse prior to an ultra-high-intensity laser pulse drives a shock wave into the foil; when it traverses through, the foil brakes out.

means the target is significantly affected, e.g. evaporated or destroyed, by the preceding light (typically, by the ASE or prepulse several ns before the main pulse). ‘Normal’ contrast means that the preceding light does not completely destroy a several- μm thick target, but a relatively large scale preplasma appears on the front target side significantly before the main pulse. ‘High’ contrast means the preplasma does not appear, or appears just before the main pulse and its effect is negligible.

The preceding light can (and usually does) cause damage to the solid target before the intense main laser pulse arrives, figure 27. For most of the acceleration regimes, this reduces the plasma fields which accelerate ions (see section 2). Hydrodynamic calculation of a thin foil before the main pulse irradiation shows that the shock wave from a typical ASE irradiation propagating through the target and target heating by x-rays destroy the target rear surface (Mackinnon *et al* 2001, Kaluza *et al* 2004, Lundh *et al* 2007, Sagisaka *et al* 2009). The electron density scale length l_{ss} at the rear side of the target becomes larger than the Debye length, and the charge-separation field decreases as l_{ss}^{-1} (Hatchett *et al* 2000, Mackinnon *et al* 2001, Grismayer and Mora 2006, Fuchs *et al* 2007b). There also exists some range of parameters, when the rear side is bent by the shock wave, but still keeps a short scale length (Lindau *et al* 2005, Lundh *et al* 2007, Zeil *et al* 2010). In this case, the proton beam is deflected from the normal direction of the target rear surface, which makes the measured proton energy smaller if one observes protons in a small acceptance angle along the target normal. This deflection can be used for active steering of the proton beam using an auxiliary nanosecond pulse (Lundh *et al* 2008). Interestingly, for relatively thick targets a few tens of μm scale preplasma contributes positively to the ion acceleration because of stronger main pulse absorption and self-focusing, while the sufficient target thickness prevents rear surface deterioration (Bychenkov *et al* 2001a, Sentoku *et al* 2002, McKenna *et al* 2008).

The ASE and prepulses can be strongly suppressed by fast, a few hundred ps rise-time, Pockels cell optical switches; however, this can only be done in a time window longer than the stretched pulse duration (τ_s in figure 24), typically

~ 1 ns. To increase the contrast within this time, one can employ plasma mirrors, which act on the compressed pulse as picosecond gated temporal switches and thus reflect only the ultra-short high-intensity pulse, figure 28 (Gold *et al* 1991, Kapteyn *et al* 1991, Backus *et al* 1993, Gold 1994, Ziener *et al* 2003; Doumy *et al* 2004; Lévy *et al* 2007, Hörlein *et al* 2008). A single (double) plasma mirror system provides a contrast ratio improvement of the order of 10^2 (10^4). Another possibility for improving the contrast is to use harmonics of a driving laser. The second harmonic is most frequently used as it is more efficient. For sub-ps lasers, second harmonic generation is relatively straightforward; for femtosecond lasers special consideration is necessary in order to preserve the pulse duration and simultaneously achieve high conversion efficiency (Mironov *et al* 2012). The second harmonic of high-power lasers has been used for contrast improvement in experiments on high-order harmonic generation from solid targets (Teubner *et al* 2004) and ultraintense laser–solid interactions, including ion acceleration (Buffeouchou *et al* 2010). For suppression of nanosecond preceding light (ASE), it is possible to use the optical parametric chirped pulse amplification (OPCPA) technique (Dubietis *et al* 1992, Ross *et al* 1997, Kiriyama *et al* 2007). Significant contrast improvement has been achieved using a non-linear temporal filter inserted at the intermediate, recompressed pulse stage, of a double CPA or OPCPA laser system (Kalashnikov *et al* 2005); several such techniques have been demonstrated, among which are the use of saturable absorbers (Kiriyama *et al* 2010, Fourmaux *et al* 2011), non-linear elliptical polarization rotation (Tapié and Mourou 1992; Homoelle *et al* 2002) and cross-polarized wave generation (XPW) (Jullien *et al* 2005). In the two latter techniques, the achieved contrast is limited by the extinction ratio of polarizers. A 10^{11} contrast at 50 TW is demonstrated by Chvykov *et al* (2006). A saturable absorber can also be employed in a stretched pulse position, in which case it removes prepulses situated at several to tens of nanoseconds before the main pulse (Fourmaux *et al* 2011). An alternative to the double CPA or OPCPA techniques is the implementation of a hybrid laser comprising solid-state front-end with an excimer amplifier of second or third harmonic (Clady *et al* 2006, Zvorykin *et al* 2010). The achieved sub-nanosecond contrast ratio is $>10^{10}$. A comparison of proton acceleration results employing several contrast improvement techniques (XPW, saturable absorber and saturable absorber combined with double plasma mirror) can be found in Flacco *et al* (2010b).

For efficient acceleration by the TNSA mechanism, a sharp plasma boundary at the target rear side is required (section 2.1), otherwise the accelerating sheath field (2.3) is reduced from $\sim T_e/e\lambda_D$ to T_e/el_{ss} , namely the Debye length λ_D is replaced by the plasma scale length l_{ss} , when $l_{ss} > \lambda_D$ (Hatchett *et al* 2000, Mackinnon *et al* 2001, Grismayer and Mora 2006, Fuchs *et al* 2007b). Therefore, the laser contrast should be sufficiently high such that the target rear side remains unperturbed before the arrival of hot electrons. Obviously, the required contrast is higher for thinner targets, which provides conditions for higher ion energies (section 2.1). If the target is mainly perturbed by the ASE, which is typical of many experiments, it is possible to estimate the necessary ASE

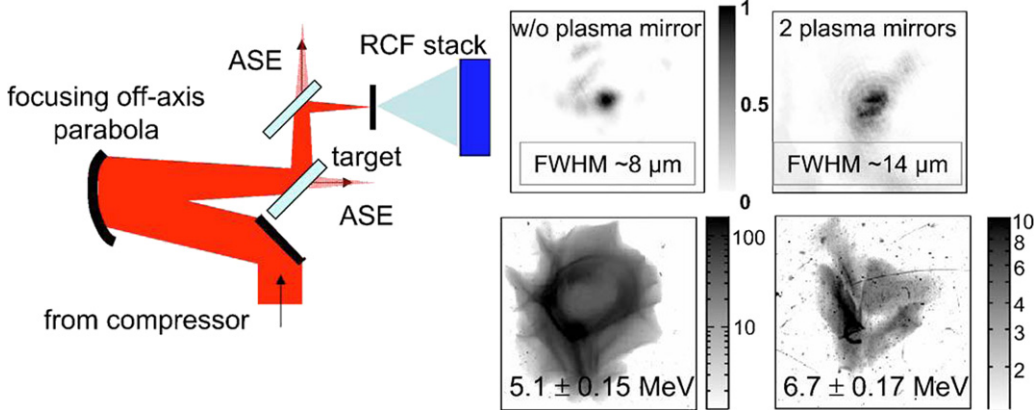


Figure 28. Schematic diagram of a double plasma mirror setup. Plasma mirrors represented by two tilted parallel rectangles transmit the low-intensity preceding light (ASE, prepulses, pedestal) but reflect the ultra-high-intensity main laser pulse due to rapid plasma formation. The two top frames on the right show the focal spot images without and with plasma mirrors. The two bottom frames on the right show two of the RCF layers from a stack detecting the proton beam accelerated from a 30 nm thick SiN target using plasma mirrors, the grey scale shows the dose in units of Gy. No proton beam was detected from such thin targets without plasma mirrors. Reprinted with permission from Antici *et al* (2007).

contrast for a given target thickness and material and ASE duration. The ASE with intensity I_{ASE} produces pressure P which is nearly insensitive to the target material:

$$P = 4 \times 10^{12} \text{ Pa} \left(\frac{I_{\text{ASE}}}{10^{15} \text{ W/cm}^2} \frac{\mu\text{m}}{\lambda_0} \right)^{2/3} \quad (3.1)$$

(Lindl 1995); here Pa represents pascal (pressure unit). The shock and particle velocities v_s and v_p are (Lundh *et al* 2007)

$$\begin{aligned} v_s &= \frac{c_s}{2} (\sqrt{1+x} + 1), \\ v_p &= \frac{c_s}{2\alpha} (\sqrt{1+x} - 1). \end{aligned} \quad (3.2)$$

Here $x = 4\alpha P/\rho_0 c_s^2$, $\alpha \sim 1-1.6$ is the empirical material constant (Marsh 1980, Lundh *et al* 2007), c_s is the sound velocity and ρ_0 is the original material density. Solving equations (3.1) and (3.2), we find the required ASE contrast for the main pulse intensity I_0 :

$$C_{\text{ASE}} = 8000 \frac{I_0}{\text{W/cm}^2} \frac{\mu\text{m}}{\lambda_0} \tau_{\text{ASE}}^3 \left(\frac{\alpha \text{ Pa}}{\rho_0 l (l - c_s \tau_{\text{ASE}})} \right)^{3/2}. \quad (3.3)$$

First, it is obvious that the ASE duration should be shorter than l/c_s , because the shock velocity is always greater than c_s (3.2). Second, we see a rather strong dependence of the required contrast on the ASE duration, especially when it approaches l/c_s . To give an example, for $I_0 = 10^{20} \text{ W cm}^{-2}$, $\lambda_0 = 0.8 \mu\text{m}$, $\tau_{\text{ASE}} = 0.5 \text{ ns}$, $l = 6 \mu\text{m}$ aluminum target ($\alpha = 1.40$, $\rho_0 = 2.7 \text{ g cm}^{-3}$, $c_s = 5.24 \mu\text{m ns}^{-1}$, $l/c_s \approx 1.15 \text{ ns}$), the required contrast is $C_{\text{ASE}} = 5 \times 10^5$. For $\tau_{\text{ASE}} = 0.8 \text{ ns}$, it increases up to 5×10^6 . For $\tau_{\text{ASE}} = 1 \text{ ns}$, which is close to l/c_s , the required contrast is 4×10^7 , almost two orders of magnitude higher than in the case of 0.5 ns ASE.

For the implementation of the Coulomb explosion and radiation pressure (laser piston, ‘light sail’) regimes of ion acceleration, the front target surface should not be perturbed before the interaction with the main pulse, which imposes an even higher constraint on the pulse contrast. The front surface starts to deteriorate when the preceding light fluence

approaches the laser-induced damage threshold F_{LIDT} . Thus, an estimate for the required contrast for the preceding light with the duration τ_{pre} is

$$C = \frac{I_0 \tau_{\text{pre}}}{F_{\text{LIDT}}}. \quad (3.4)$$

The laser-induced damage threshold depends on many parameters, including the target surface material and quality and the duration τ_{pre} . The damage threshold can be estimated *in situ* using the laser pulse reflectivity from the target: when the target is damaged, the reflectivity decreases (Pirozhkov *et al* 2009a, 2009b), see figure 30 in this section. For a nanosecond ASE, the typical value is about ten to a few tens of J cm^{-2} (figure 30(b)). For $I_0 = 10^{20} \text{ W cm}^{-2}$ and $\tau_{\text{ASE}} = 1 \text{ ns}$, we obtain the required contrast $C_{\text{ASE}} = 10^{10}$. The necessary contrast of picosecond pedestal and sub-ps foot pulse can be estimated in a similar way, using the damage threshold at the appropriate pulse duration. For a typical picosecond damage threshold of $\sim 1 \text{ J cm}^{-2}$ and a pedestal duration of 1 ps for the same peak intensity of $10^{20} \text{ W cm}^{-2}$ we obtain $C_{\text{ps}} = 10^8$, which is in practice an even more stringent requirement than for the ASE contrast.

Knowledge of the laser contrast is necessary for both the development of contrast improvement techniques and understanding experimental results. However, accurate determination of the contrast is still a challenge, taking into account the set of requirements including (1) high dynamic range (higher than 10^{10}), (2) long temporal measurement interval (ideally longer than the stretched pulse duration such as a few ns and the time separation between the main pulse and all prepulses), (3) high temporal resolution and small sampling interval (ideally smaller than the main pulse duration) and (4) applicability to full-power, on-target diagnostic. The conventional technique of power contrast measurement is a high-dynamic range third-order cross-correlation (Luan *et al* 1993, Divall and Ross 2004, Hong *et al* 2005), which requires many thousands of shots and is usually performed with a high-repetition, smaller power laser operation mode. It should be

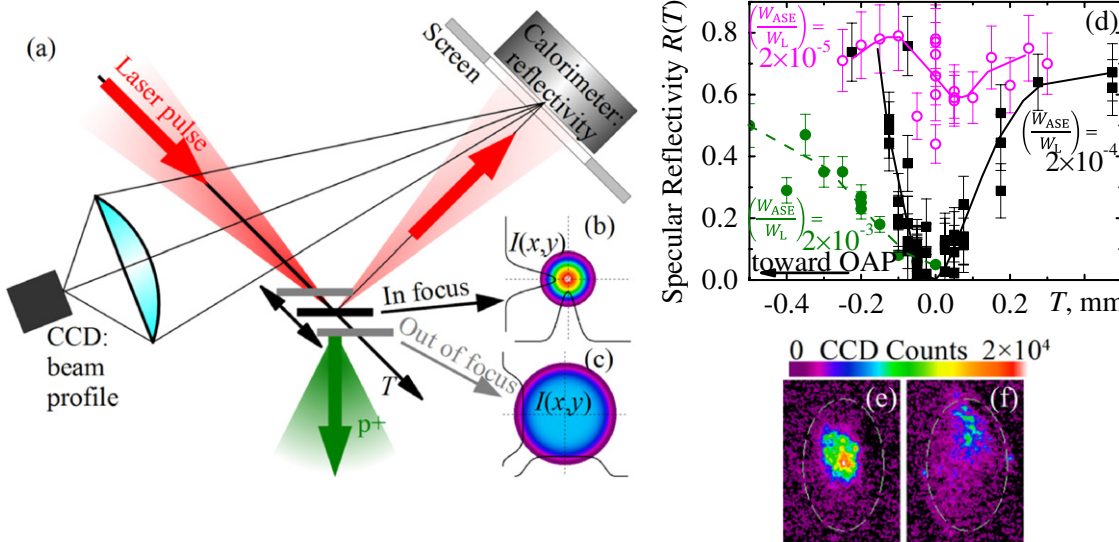


Figure 29. Schematic layout of the on-target contrast diagnostic based on the target reflectivity measurement (Pirozhkov *et al* 2009a). Full-power laser pulses irradiate targets in the real shooting conditions. The spot size is varied by moving the target along the laser beam; the idealized intensity distributions in and out of focus are shown in (b) and (c), respectively. A calibrated in-vacuum calorimeter is used to measure the target specular reflectivity dependence on the target position T , (d) (single shot data are shown, the experimental parameters are given in the table of figure 30). The lens images the surface of the calorimeter and surrounding screen onto the CCD to measure the reflected beam profile; two examples from the experiment shown by the open diamonds in figure 30 are given in (e) and (f): (e) corresponds to the target position T with relatively small preplasma ($T = -1.41$ mm, i.e. target far from focus), while (f) corresponds to the target position closer to the focus ($T = -0.71$ mm), where the preplasma leads to the reflected beam break-up. The dashed ellipses represent the 96 mm diameter calorimeter edge; the images are squeezed due to the oblique observation angle.

noted that cross-correlators tend to produce artificial prepulses which are difficult to distinguish from the real ones because their delays and contrasts are similar (Didenko *et al* 2008). In addition, the focal spot of the ASE and prepulses may differ from that of the main pulse, therefore the power and on-target-intensity contrasts are in principle not the same.

Several contrast diagnostic techniques overcoming some of the disadvantages of conventional scanning cross-correlators have been demonstrated. One research direction is the development of single-shot techniques (Collier *et al* 2001, Dorner *et al* 2008, Zhang *et al* 2008, Shah *et al* 2009). Another direction is measuring the actual effect of a full-power laser pulse, with all its prepulses, on the target, under the real shot conditions. If the preplasma is relatively large, interferometry can be used to measure the plasma density distribution (Gizzi *et al* 1994, Da Silva *et al* 1995, Borghesi *et al* 1996, Sagisaka *et al* 2006). The effect of the ASE can be monitored using XUV imaging and time-resolved emission measurement of the plasma (Ragozin *et al* 2006). For the ion acceleration employing ultra-thin (nanometre-thick) foils, even small ($\text{sub-}\mu\text{m}$) preplasma is sometimes not acceptable, as the laser pulse interaction is sensitive to the sub-wavelength preplasma scales. It is possible to use this sensitivity for a contrast diagnostic employing properties of the reflected main laser pulse itself, without the additional probe pulses. This diagnostic works at full laser power and under actual shooting conditions, and requires relatively small number of shots. The idea was tested experimentally in three laboratories (Pirozhkov *et al* 2009a). The experimental setup for measuring the reflectivity and reflected beam profile is shown in figure 29. When the contrast is sufficiently high, namely the preplasma is not created, the target specular reflectivity is high ($\sim 50\text{--}70\%$) even at the best

focus position (figure 30). Under lower contrast conditions, the specular reflectivity is high at a distance from the focus, similar to the plasma mirror regime, but near the preplasma formation threshold it starts to decrease and becomes close to zero near the focus. The reflectivity becomes small because the preplasma formation causes the reflected beam break-up (figures 29(d) and (e)) and enhanced absorption (Gibbon and Bell 1992, Borghesi *et al* 1999, Ping *et al* 2008). The ratio of the spot area at the position where the reflectivity is still high to the minimum focal spot area gives an estimate for a necessary contrast improvement factor. Experimentally, the high target reflectivity has been demonstrated up to the intensities $\sim 10^{21} \text{ W cm}^{-2}$ (Streeter *et al* 2011); at such intensities, a significant portion of the reflected energy can be in the form of harmonics of laser radiation (Hörlein *et al* 2008, Streeter *et al* 2011). The PIC simulations show high reflectivity for the intensities of mid- $10^{22} \text{ W cm}^{-2}$ (Esirkepov *et al* 2006) and larger (Esirkepov *et al* 2004); thus, this contrast diagnostic is applicable for the prospective regimes of laser-ion acceleration (sections 2.3 and 2.6) and other types of present and future experiments, e.g. harmonic generation at plasma surfaces (Teubner and Gibbon 2009).

3.3. Proton and ion diagnostic instruments

One of the simplest yet most powerful ion detectors is based on the specific way in which ions interact with matter, namely the presence of the Bragg peak: for a specific ion energy, most of the energy is deposited at a certain depth (figure 31). Typically, a filtered stack of nuclear track detectors such as CR-39 (Silk and Barnes 1959, Ilic and Durrani 2003) or radiochromic films (RCFs) (McLaughlin *et al* 1991, Vatnitsky

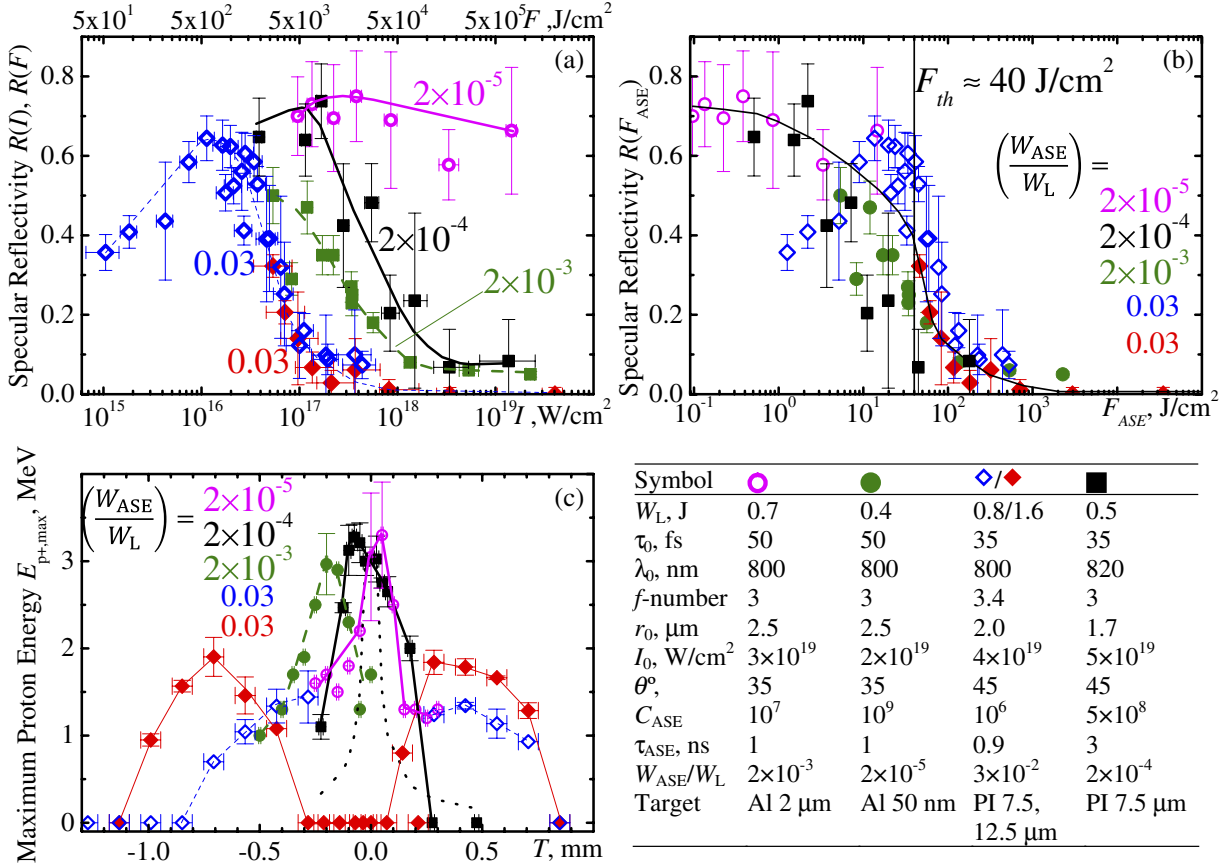


Figure 30. On-target contrast diagnostic based on the specular target reflectivity measurement (figure 29) (Pirozhkov *et al* 2009a). The data are obtained with three different laser systems and different contrast conditions (see the table; PI denotes polyimide targets). (a) and (b) show the dependences of the specular reflectivity R on the average intensity I and fluence F of the main pulse (a) and fluence of the ASE F_{ASE} (b). (c) shows the maximum proton energy in the target normal direction $E_{p+,\text{max}}$ versus target position T . All data are averaged over several shots. The lines are drawn to guide the eye. The dotted line in (c) corresponds to the maximum proton energy estimate according to a simple ‘intensity root’ rule; this much narrower curve is not consistent with the experimental data.

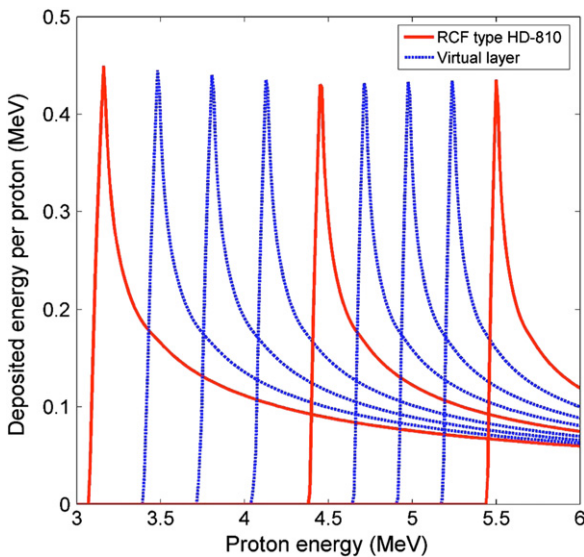


Figure 31. An example of a stack detector of proton beams. The red solid lines show the energy deposited into three HD-810 RCFs versus the proton energy. The blue dashed curves correspond to virtually inserted layers used for the proton distribution reconstruction. Reprinted with permission from Nürnberg *et al* (2009).

1997, Niroomand-Rad *et al* 1998) is used as an inexpensive 2D detector without magnetic or electric fields. In this case, layers at different depths are used to derive the ion beam footprints with rough energy bins determined by the corresponding ion stopping ranges. The energy deposited outside the Bragg peak should also be taken into account; a procedure to reconstruct the proton energy spectrum using an RCF stack can be found in Nürnberg *et al* (2009). If the proton energy is larger than several MeV, the activation technique is also applicable for the stacked detectors (Hatchett *et al* 2000, Santala *et al* 2001, McKenna *et al* 2006); the activation technique can provide a very high dynamic range due to a high saturation level (Clarke *et al* 2008). Typical energy deposition curves and an example of data recorded on the RCF stack are shown in figures 31 and 32, respectively (Nürnberg *et al* 2009). Typically, the proton beam has a smooth envelope with divergence which decreases when the proton energy increases, figure 33. However, in some cases the reverse dependence of divergence on proton energy has been reported (Ter-Avetisyan *et al* 2009). Further, especially in the case of thin targets, the proton beam can exhibit an irregular (Antici *et al* 2009) or a hollow (i.e. a ring or doughnut shape) structure (e.g. Murakami Y *et al* 2001, Antici *et al* 2007, Safronov *et al* 2008), e.g. figure 28. Care, however, needs to be taken as saturated or over-etched CR-39 detectors can produce

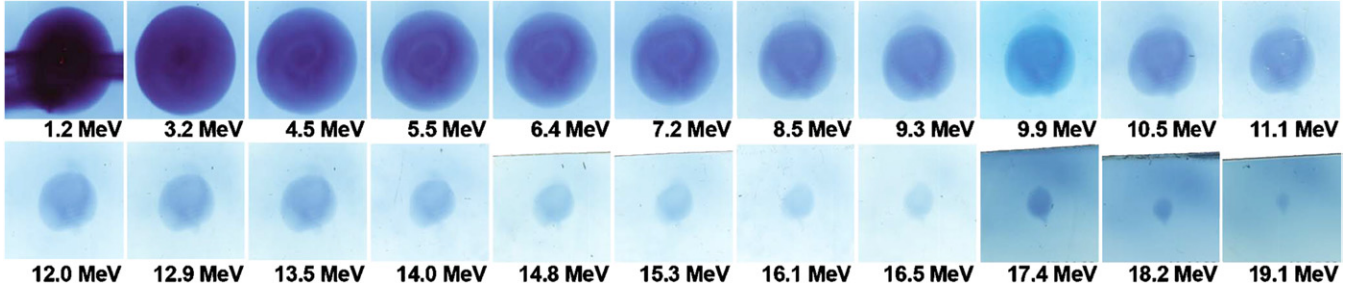


Figure 32. Data from an RCF stack (19 HD-810 and three MD-55 films are shown; an additional six MD-55 layers contained no image). The number below each frame corresponds to the proton Bragg peak energy. Reprinted with permission from Nürnberg *et al* (2009).

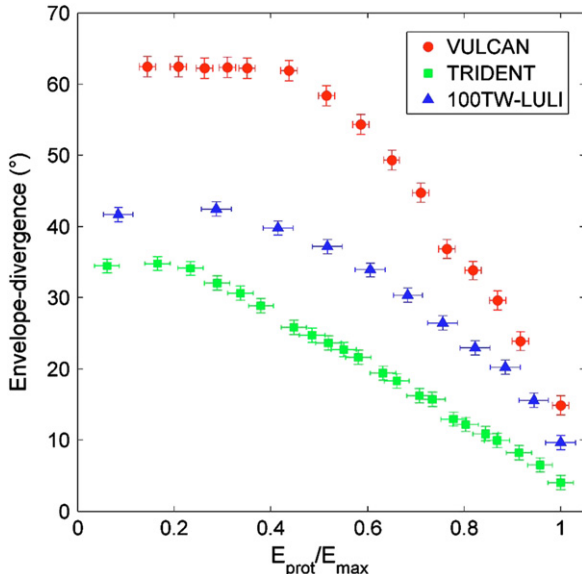


Figure 33. Full divergence angle of the proton beams versus the proton energy normalized by the maximum proton energy E_{max} for the corresponding shots (circles: 29.7 MeV, squares: 19 MeV, triangles: 16.2 MeV); the data are obtained with three different lasers. Reprinted with permission from Nürnberg *et al* (2009).

artificial rings; a careful analysis of real and artificial rings in proton beams is given by Gaillard *et al* (2007). It has also been shown that the shape of the laser focal spot and target material affect the shape of the resulting proton beam (Fuchs *et al* 2003). In applications which rely on the smooth spatial distribution of the ion beam, such effects can be avoided by appropriate tuning of the laser and choice of the target.

Nuclear activation diagnostic can be selectively sensitive to some of the ion species. Offermann *et al* (2010, 2011) have used a lithium fluoride activation detector for the diagnostic of carbon ions and distinguishing them from protons. The reactions employed were $^7\text{Li}(^{12}\text{C}, ^6\text{He})^{13}\text{N}$ and $^{19}\text{F}(^{12}\text{C}, ^{13}\text{C})^{18}\text{F}$; the resulting ^{13}N and ^{18}F isotopes decay via positron emission, which can be identified by measuring the corresponding decay times; the spatial profile of the carbon beam can be revealed by an auto-radiograph of the LiF detector plate.

2D electronic detectors which provide short (a few seconds) readout times were demonstrated, which is especially important for repetitive laser systems. These detectors are

based on a fast scintillator coupled to a CCD (Robinson *et al* 2009b, Carroll *et al* 2010a), or micro-channel plate (MCP) coupled to a phosphor screen and CCD (Mróz *et al* 2000, Ter-Avetisyan *et al* 2005, Harres *et al* 2008, Prasad *et al* 2010). The CCD should typically have a low noise and large gain, i.e. a suitable choice may be a cooled electron-multiplied CCD. Further, although the time gating is not absolutely necessary, it helps one to discriminate signals produced by protons, ions, electrons and x-rays (to all of which the scintillators and MCPs are sensitive), due to the different flight times, typically in the nanosecond time scales for the protons and ions. The signal caused by electrons in these detectors can also be suppressed by magnets. The scintillators with different emission colours can be stacked to obtain several channels with different ion energies (Green *et al* 2009).

The conventional technique to precisely identify the ion species as well as their energy spectra is a Thomson parabola ion energy analyser (Thomson 1911, Olsen *et al* 1973, Mróz *et al* 2000, Harres *et al* 2008, Carroll *et al* 2010a, Jung *et al* 2011) which is shown schematically in figure 34(a). Such an analyser works with nuclear track detectors (e.g. CR-39), imaging plates (IP) (Amemiya and Miyahara 1988, Mori *et al* 2006, Mančić *et al* 2008), RCFs or MCPs as the recoding detector. A brief but comprehensive comparison of the CR-39, IP and scintillator as a detector for the Thomson parabola is given by Carroll *et al* (2010a). An example of the proton and heavier ion traces recorded by the Thomson parabola ion analyser is shown in figure 34(b); the constant energy per charge and constant velocity lines are shown to clarify the output of the analyser. The input pinhole or pinhole array can be situated sufficiently close to the ion source, in which case the Thomson parabola analyser works with spatial magnification. Such a setup can be used to reveal fine features of the ion source, such as energy-dependent divergence and source position (Schreiber *et al* 2006b, Nakamura T *et al* 2008b, Ter-Avetisyan *et al* 2009). This information is especially important when a small-emittance ion beam is necessary for the applications, e.g. proton radiography, section 4.3. A modified Thomson parabola design with wedged electrodes (Carroll *et al* 2010a) allows high-resolution energy and charge-to-mass ratio measurements while keeping a compact setup; gold ions with charge state up to 42+ have been identified and resolved using the CR-39 detector. A high-resolution, high-dispersion Thomson parabola for >100 MeV/nucleon ion energies is described by Jung *et al* (2011).

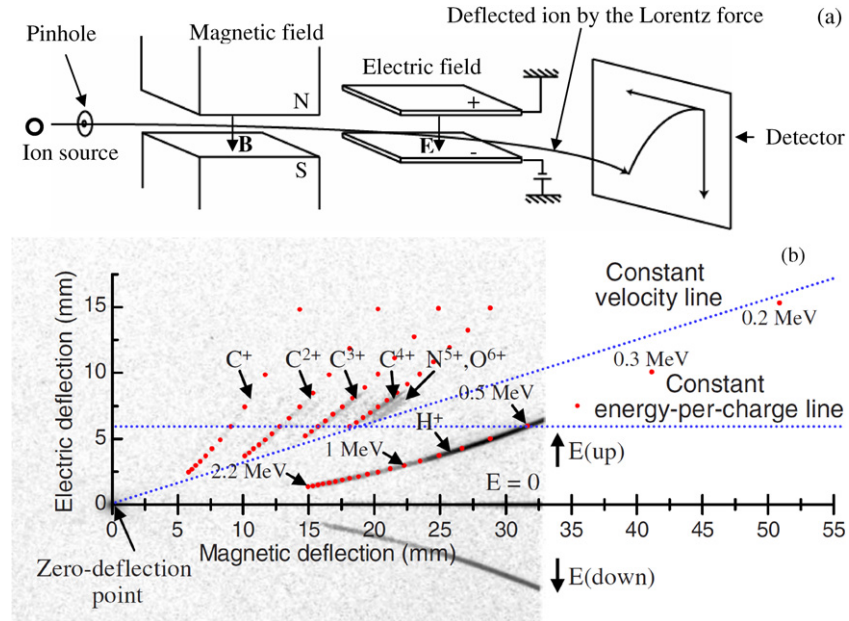


Figure 34. (a) Schematic view of the Thomson parabola ion analyser. (b) Proton and heavier ion traces recorded on the IP detector. The protons and ions were accelerated by an intense laser pulse from a Ti : sapphire laser irradiating a $5\text{ }\mu\text{m}$ copper tape target. The upper, lower and central traces were obtained with the electric field upward, downward and absent, respectively. The red circles on each trace represent energy points with 0.1 MeV intervals. The dotted lines represent the constant energy per charge and constant velocity lines corresponding to the maximum energy and velocity of carbon ions. (b) is reprinted with permission from Choi *et al* (2009a).

A TOF ion spectrometer, figure 35 (Nakamura S *et al* 2006, Yogo *et al* 2007), due to its simple and fast readout, can be used as a real-time diagnostic with high repetition rate lasers. A proton detector which combines the TOF spectrometer with Thomson parabola ion analyser has been demonstrated (Choi *et al* 2009a, 2009b). An imaging TOF proton spectrograph based on a fast plastic scintillator, slit and optical streak camera has been used by Safronov *et al* (2008); the spectrograph produces energy-resolved 1D images of the proton beam.

Proton beams can be used as probes in various experiments, providing space- and time-resolved information about density and field distributions. Several detectors can be used, e.g. a stack of CR-39 or RCF films; applications of the proton radiography with these detectors are described in section 4. Here we describe another technique, proton streak deflectometry, which can display the plasma field distributions, such as those in the ion acceleration processes (Sokollik *et al* 2008), figure 36. The working principle is as follows; first, the laser-driven proton beam with wide spectral bandwidth is generated at the rear side of the target. The beam is divided into beamlets by a mesh and spreads out temporally because of the velocity dispersion. A properly configured pinhole array made in the slit is placed between the proton source and the magnetic analyser. The resulting proton beam is analysed with a velocity dispersive device, e.g. a magnetic spectrometer, and recorded on a 2D detector such as an MCP; the time gating helps one to select protons with the desirable energy interval. The influence of transient fields on the protons can be traced back in time because protons with a specific energy arrive at the object to probe it at a definite time. The advantage of this method is the possibility of continuous recording of transient fields on a picosecond time scale. This technique was used for

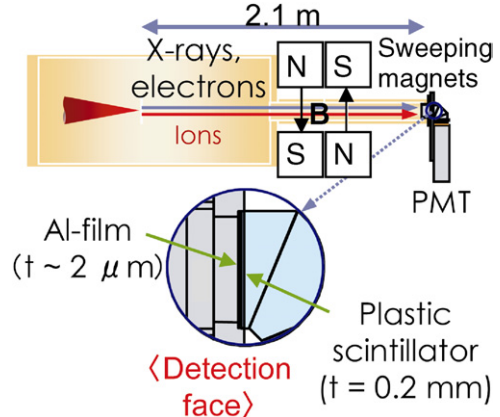


Figure 35. Schematic view of the TOF ion spectral analyser. Here, PMT stands for photo-multiplier tube. The sweeping magnets with magnetic field $|B| \sim 0.03\text{ T}$ and length of $\sim 50\text{ mm}$ repel the electrons (Nakamura S *et al* 2006); the protons are insignificantly shifted by this magnetic field. The circle in the lower part shows details of the plastic scintillator whose thickness is 0.2 mm , which is thin enough such that the hard x-rays mostly pass through producing a low signal. An aluminum thin film whose thickness is $2\text{ }\mu\text{m}$ in front of the plastic scintillator is placed to cut the visible and infrared light. The detailed setup of the TOF proton spectrometer can be found in Yogo *et al* (2007).

the investigation of the electric fields occurring at the rear side of a laser irradiated thin metallic foil, figure 36; in particular, these fields are responsible for ion acceleration. Figure 37 shows the results of the experiment and computer simulation. 3D proton ray tracing with an electric field model described by Romagnani *et al* (2005) and Mora (2003) allows estimating the field parameters. In particular, from the simulation shown in figure 37(b) the extracted electric field consists of two

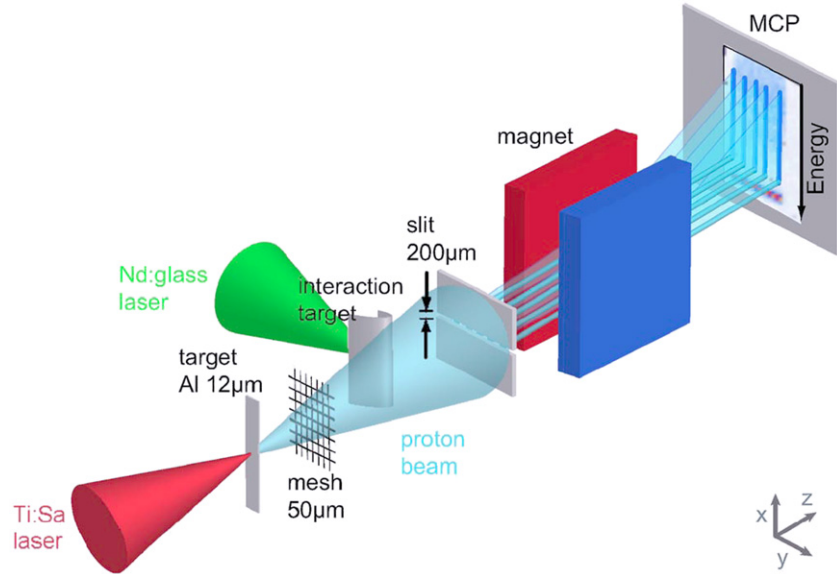


Figure 36. Experimental setup for the proton streak method. The proton beam from a Ti : sapphire laser-irradiated foil is deflected by fields from the rear side of another, interaction target, irradiated by an Nd : glass laser. The induced fields near the interaction target are analysed employing the known velocity dispersion of the magnet; the proton TOF is used to unveil the time dependence, figure 37. Reprinted with permission from Sokollik *et al* (2008).

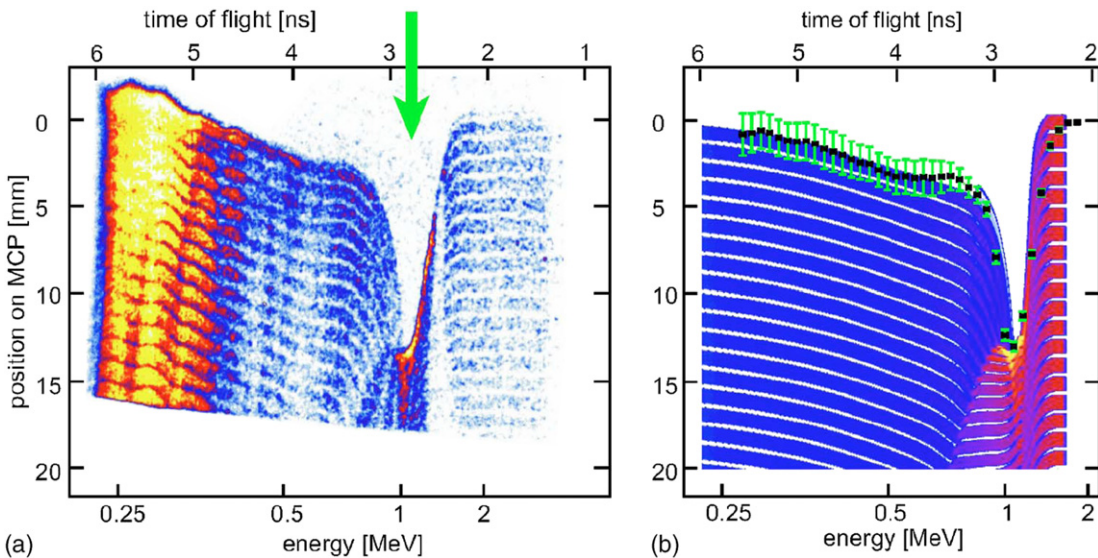


Figure 37. (a) A proton streak image taken with a 2.3 J ($4 \times 10^{17} \text{ W cm}^{-2}$) laser pulse on the interaction target indicated in figure 36. The arrow represents the time of the Nd : glass laser shooting. (b) Simulated proton streak signal including an extracted deflection curve from the experimental data; the simulation employs a model electric field consisting of two components associated with the accelerated ion front and the background charge. Reprinted with permission from Sokollik *et al* (2008).

components associated with the accelerated ion front (peak field $3 \times 10^8 \text{ V m}^{-1}$, scale length $100 \mu\text{m}$, decay time 3 ps, propagation velocity 10^6 m s^{-1}) and the background target charge (maximum charge density 10^{-4} C m^{-2} , linear growth time 10 ps, decay time 600 ps).

There are other proton and ion detectors, not used or used only rarely for laser-driven ion beams, e.g. semiconductor detectors, multi-wire proportional chambers (MWPCs), etc. Applicability of such detectors in laser experiments needs to be tested as noise generated by the electromagnetic pulse, electrons or x-rays can affect their operation.

The ion detectors are usually sensitive to neutral atoms of comparable velocity, which may appear, for example, in

the charge exchange process during ion travel through gas and plasma; these atoms become immediately ionized as they start to interact with the detector medium. Such neutral atoms or lower-charge-state ions, which appear before or during their way through magnetic and/or electric fields in such devices as Thomson parabolas or magnetic ion spectrographs, come to the detector undeflected or relatively little deflected, which may cause higher-than-real energy identification. Note that the stack detectors (e.g. layers of CR-39 and RCF films) and TOF-type detectors are not affected by this issue. The ion detectors can also be sensitive to neutrons, as neutrons can cause recoil ions or induce nuclear reactions producing ions (e.g. Frenje *et al* 2002). When a significant number of protons and ions with

Table 1. Detectors commonly used for laser-driven ion diagnostics and measurements. Sensitivity: L: light, UV: ultraviolet, x: x-rays, e-: electrons; the notation ‘•’ represents ‘sensitive’.

	Spatial resolution	Time resolution	Treatment/ display time	Single-particle sensitivity	Dynamic range (DR)	Sensitivity			Features/refs
						L	UV, x	e-	
Solid-state nuclear track detectors, e.g. CR-39 (allyl diglycol carbonate), etc	~ a few to a few tens of μm (pit size, depends on the ion kind and energy and etching time)	No	A few hours (etching, scanning, pit counting)	Yes	$\sim 10^2$ – 10^6 (background $\sim 10^2$ – 10^4 cm^{-2} , saturation $\sim 10^6$ – 10^8 cm^{-2})	—	—	—	(1) Sensitive to ions only ^a , single particles
Radiochromic film (RCF)	~3–10 μm (film, scanner)	No	Several minutes (scanning)	No	$\sim 10^2$ – 10^3 (e.g. 10 – 10^4 Gy)	—	•	•	(2) Self-developing
Imaging plate	Sub-100 μm (scanner)	No	Several minutes (scanning)	No	$\sim 10^5$	—	•	•	(3) Reusable, high DR
Activation	Sub-mm (contact radiography)	No	Tens of minutes–a few hours (decay time)	No	Very high ($> 10^5$)	—	—	—	(4) Very high DR
Micro-channel plate (MCP)+phosphor screen + CCD	~several 10s of μm (imaging system)	~a few 100 ps (MCP gate time)	~a few seconds (CCD readout)	Yes	$\sim 10^3$	—	•	•	(5) Online, single particles
Scintillator + gated I-CCD or EM-CCD	~several 100 μm (multiple scattering, imaging system)	~a few 100 ps (scintillation time)	~a few seconds (CCD readout)	No	$\sim 10^3$	•	•	•	(6) Online, stackable in depth

^a Solid-state nuclear track detectors can also detect neutrons via production of secondary charged particles, although the detection efficiency is small, typically of the order of 10^{-4} (e.g. Frenje *et al* 2002).

(1) Ilic and Durrani (2003), Séguin *et al* (2003), Gaillard *et al* (2007).

(2) Vatnitsky (1997), Niroomand-Rad *et al* (1998), Hey *et al* 2008, Nürnberg *et al* (2009).

(3) Amemiya and Miyahara (1988), Mori *et al* (2006), Mančić *et al* (2008), Choi *et al* (2009b).

(4) Hatchett *et al* (2000), Clarke *et al* (2008).

(5) Mróz *et al* (2000), Ter-Avetisyan *et al* (2005), Harres *et al* (2008), Prasad *et al* (2010).

(6) Carroll *et al* (2010a).

energy larger than several MeV per nucleon are accelerated, a detector response to secondary neutrons originating from p–n reactions may cause a misleading interpretation of the results.

Table 1 lists detectors most commonly used in laser ion acceleration experiments; the parameters shown in the table are those which are or can be achieved; however, some of the parameters cannot be achieved simultaneously. The achievable parameters also depend on many factors, e.g. ion species, energy/noise/background level, etc.

The measurement of the properties of electrons which are generated simultaneously with ions is also very important for understanding of proton and ion acceleration driven by intense lasers. Ideally, one should measure the electron spectrum and spatial distribution in the interaction region using, e.g., Thomson scattering (Glover *et al* 1994, Glenzer *et al* 1999, Tomassini *et al* 2003), bremsstrahlung radiation (Chen C D *et al* 2008, MacPhee *et al* 2008), optical transition radiation (Mancossi *et al* 2006, Santos *et al* 2007, Bellei *et al* 2010), Čerenkov radiation (Ter-Avetisyan *et al* 2008c) or optical probe reflectometry (Antici *et al* 2008a). Some information can also be extracted analysing the spectra of electrons left at the target; the electron spectra can be obtained in this case with a magnetic electron energy analyser coupled with a scintillator or IP (Tanaka *et al* 2005, Li *et al* 2006, Chen H *et al* 2008a, 2008b).

The change of the escaping electron spectra due to the target charging is discussed by Fill (2005). Both target charging and proton acceleration effects on the escaping electron spectra are discussed by Link *et al* (2011).

3.4. Proton acceleration from laser-irradiated thin foils

Many laser-driven proton acceleration experiments have been performed all over the world (Borghesi *et al* 2006, 2009). A flat thin metallic or insulator foil is one of the most popular targets, although more elaborate target designs are becoming more and more important (see sections 3.6 and 3.7). In this section, based on the theoretical framework described in section 2, we summarize the experimental results. Among numerous experiments, we choose those in which one can directly see or easily estimate important conditions such as laser and target parameters, table 2. The readers can see a set of graphs which represents the correlation between the proton/ion beam and laser parameters. Although each data point has been taken with a different laser facility, the readers can see a general view of the experimental data in the world. We also describe the physical interpretation of these results.

The maximum proton and ion energy versus laser pulse energy (W_L) and intensity (I_0) are shown in figures 38(a) and

Table 2. Experimental data used in figures 38 and 40.

No.	Reference	Pulse energy W_L (J)	Pulse duration τ (fs)	Irradiance I_0 (W cm^{-2}) ^a	Contrast	Target and thickness (μm)	Incidence angle ($^\circ$)	Proton/ion energy $\mathcal{E}_{\text{p(i)}}$, (MeV/nucleon)
1	Snavely <i>et al</i> (2000)	423	500	3×10^{20}	1×10^4	CH 100	0	58
2	Krushelnick <i>et al</i> (2000b)	50	1000	5×10^{19}		Al 125	45	30
3	Nemoto <i>et al</i> (2001)	4	400	6×10^{18}	5×10^5	Mylar 6	45	10
4	Mackinnon <i>et al</i> (2002)	10	100	1×10^{20}	1×10^{10}	Al 3	22	24
5	Patel <i>et al</i> (2003)	10	100	5×10^{18}		Al 20	0	12
6	Spencer <i>et al</i> (2003)	0.2	60	7×10^{18}	1×10^6	Mylar 23	0	1.5
7	Spencer <i>et al</i> (2003)	0.2	60	7×10^{18}	1×10^6	Al 12	0	0.9
8	McKenna <i>et al</i> (2004)	233	700	2×10^{20}	1×10^7	Fe 100	45	40
9	Kaluza <i>et al</i> (2004)	0.85	150	1.3×10^{19}	2×10^7	Al 20	30	4
10	Oishi <i>et al</i> (2005)	0.12	55	6×10^{18}	1×10^5	Cu 5	45	1.3
11	Fuchs <i>et al</i> (2006)	10	320	6×10^{19}	1×10^7	Al 20	0 and 40	20
12	Neely <i>et al</i> (2006)	0.3	33	1×10^{19}	1×10^{10}	Al 0.1	30	4
13	Willingale <i>et al</i> (2006)	340	1000	6×10^{20}	1×10^5	He jet 2000		10
14	Ceccotti <i>et al</i> (2007)	0.65	65	5×10^{18}	1×10^{10}	Mylar 0.1	45	5.25
15	Robson <i>et al</i> (2007)	310	1000	6×10^{20}	1×10^7	Al 10	45	55
16	Robson <i>et al</i> (2007)	160	1000	3.2×10^{20}	1×10^7	Al 10	45	38
17	Robson <i>et al</i> (2007)	30	1000	6×10^{19}	1×10^7	Al 10	45	16
18	Antici <i>et al</i> (2007)	1	320	1×10^{18}	1×10^{11}	Si_3N_4 0.03	0	7.3
19	Yogo <i>et al</i> (2007)	0.71	55	8×10^{18}	1×10^6	Cu 5	45	1.4
20	Yogo <i>et al</i> (2008)	0.8	45	1.5×10^{19}	2.5×10^5	Polyimide 7.5	45	3.8
21	Nishiuchi <i>et al</i> (2008)	1.7	34	3×10^{19}	2.5×10^7	Polyimide 7.5	45	4
22	Flippo <i>et al</i> (2008)	20	600	1.1×10^{19}	1×10^6	Flat-top cone Al 10	0	30
23	Safronov <i>et al</i> (2008)	6.5	900	1×10^{19}		Al 2	0	8
24	Henig <i>et al</i> (2009b)	0.7	45	5×10^{19}	1×10^{11}	DLC 0.0054	0	13
25	Fukuda <i>et al</i> (2009)	0.15	40	7×10^{17}	1×10^6	CO_2+He cluster jet 2000		10
26	Zeil <i>et al</i> (2010)	3	30	1×10^{21}	2×10^8	Ti 2 μm	45	17
27	Gaillard <i>et al</i> (2011)	82	670	1.5×10^{20}	1×10^9	Flat-top cone Cu 12.5	0	67.5

^a Different authors do or do not include the incidence angle in the irradiance definition.

(b). The corresponding data are listed in table 2. Clearly, the maximum proton/ion energy tends to increase with the laser pulse energy/intensity. To guide the eye, power-law trend lines $\propto W_L^{1/2}$, $\propto I_0^{1/2}$ and $\propto I_0$ are drawn in the figures; we see that these trend lines do not contradict the scalings presented in section 2. In the majority of experiments performed up to now, the acceleration regime is close to the TNSA or strong charge separation field (SCSF) ones. In both regimes, the proton energy is proportional to the hot electron temperature, which in turn in the relativistic intensity regime is often proportional to the square root of intensity (2.6). Other acceleration regimes exhibit similar scalings versus the intensity or pulse energy (section 2, figure 23). One should not exclude other experimental parameters, though: for example, if the target is moved out of focus, the focal spot increases; this leads to longer quasi-1D acceleration, which partly compensates for the lower intensity. This gives a weaker dependence of proton energy on the target position than expected from the simple ‘intensity root’ rule (Green *et al* (2010), see also figure 30(c)). Another example is the incidence angle and laser polarization. Although in some cases their effect may be insignificant (e.g. Fuchs *et al* (2006), section 2.1), in other regimes the ion and/or proton beam properties can be affected, e.g., by the laser polarization at oblique incidence (p-, s-, circular) (Fukumi *et al* 2005), by the polarization at normal incidence (linear, circular) (Henig *et al* (2009b) and Steinke *et al* (2010), see the end of this section) and by the incidence angle under high-contrast conditions (Carroll *et al* (2010b), see also section 2.5).

We note that the trend lines shown in figure 38 are *not* the scalings as used in section 2, because in different experiments the optimization parameters were different and none of the parameters were the same through all the data; further, these trend lines depend on the particular selection of results among the published papers. However, assuming that in each particular experiment cited here the conditions were well optimized, we can use these trends as examples of ‘practically achievable’ proton/ion energies, though keeping in mind the above reservations. One can see several data points (data numbers 24–27) situated significantly above the general trends. These data are obtained with ultra-high-contrast lasers, nanometre-scale foils or by use of novel target techniques (see sections 3.7 and 3.9).

Another very important parameter is the conversion efficiency defined as the ratio of the total ion beam energy and the laser pulse energy; usually only ions above some selected particle energy \mathcal{E}_1^* , or in some particle energy interval, are included. For such applications as ion-driven fast ignition or isotope production the conversion efficiency is actually among the most important parameters. The particle energy ranges, for which the efficiencies are reported, vary from paper to paper; this needs to be taken into account when comparing results from different papers. For example, in the data obtained with large pulse energy, low contrast ratio ($<10^5$) lasers, the efficiencies are $>2\%$ into 13–42 MeV protons (McKenna *et al* 2004), 5% into 4–55 MeV protons (Robson *et al* 2007) or even $>10\%$ into 10–58 MeV protons

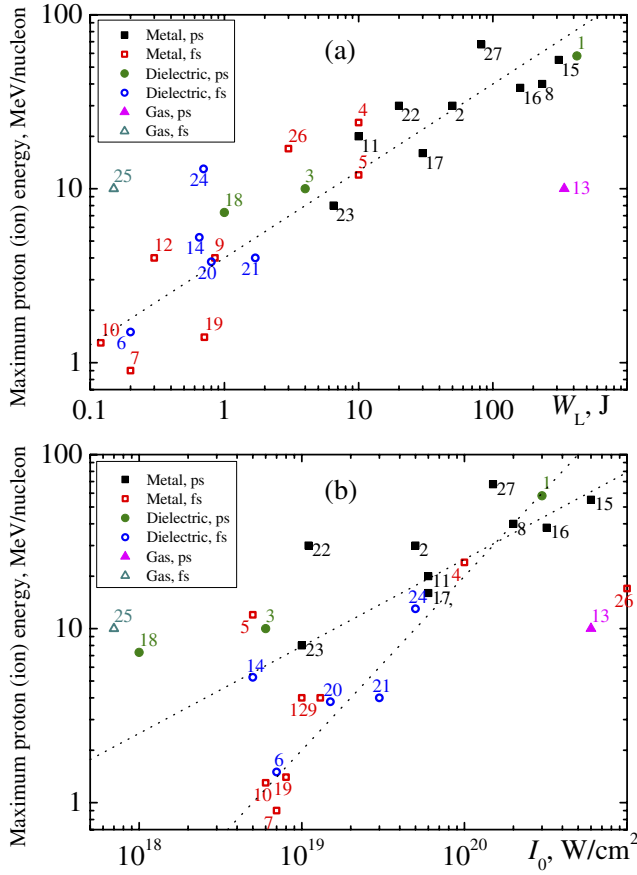


Figure 38. Experimental results; the numbers correspond to references listed in table 2. Maximum energy of protons (ions) versus the laser pulse energy (*a*) and intensity (*b*). The squares, circles and triangles denote metal, dielectric and gas targets, respectively. The solid and open symbols correspond to sub-picosecond, relatively large energy lasers, and a few tens of femtosecond, smaller energy lasers, respectively. The dotted trend lines are $4 \text{ MeV} \times (W_L/\text{J})^{0.5}$ in (*a*), $2.5 \text{ MeV} \times (I_0/10^{18} \text{ W cm}^{-2})^{0.5}$ and $0.2 \text{ MeV} \times (I_0/10^{18} \text{ W cm}^{-2})^{0.5}$ in (*b*).

(Snavely *et al* 2000) (for the definition of low, normal and high contrasts, see section 3.2). On the other hand, the data obtained with high contrast, small energy (<a few J), short pulse (<100 fs) lasers show conversion efficiencies >1% (Neely *et al* (2006), 1% into 0.9–4 MeV protons; Henig *et al* (2009b), 2.5% into 20–40 MeV carbon ions). ‘Normal’ and ‘low’ contrast, small-energy lasers provide an efficiency of 0.05–3% (Nishiuchi *et al* (2008), 3% into 0.8–4 MeV protons; Yogo *et al* (2007), 0.05% into 0.6–1.4 MeV protons). Although the achievable conversion efficiency in experiments with small-energy femtosecond lasers is similar to those of large-energy, sub-picosecond or picosecond lasers, the value of minimum ion energy \mathcal{E}_i^* above which the conversion efficiency is given is notably different. When the laser energy decreases, the conversion efficiency also decreases and becomes zero when the maximum achievable ion energy reduces down to the chosen minimum value \mathcal{E}_i^* . For example, figure 39 shows the experimental results obtained with a 1 ps pulse duration, several hundred joule laser (Robson *et al* 2007); the efficiency into protons above 4 MeV is a linear function of the laser energy. Even stronger dependence is reported by Fuchs *et al*

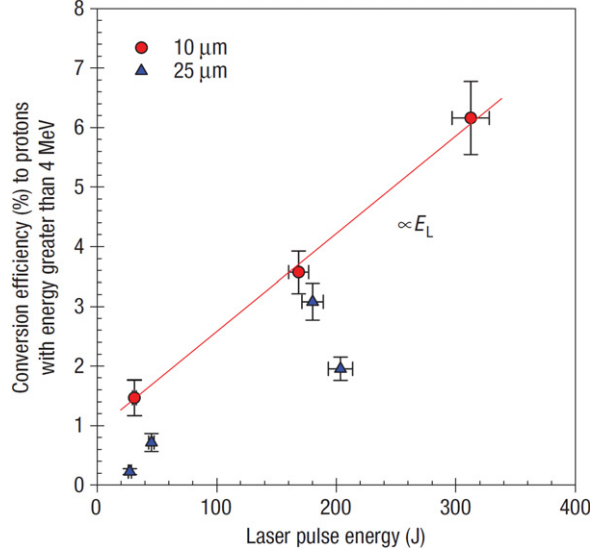


Figure 39. Conversion efficiency (into protons above 4 MeV) versus laser pulse energy; the pulse duration is fixed at 1 ps. Al targets with thicknesses of 10 and 25 μm are used. The conversion efficiency depends linearly on the laser pulse energy, with higher efficiency for thinner targets. Reprinted with permission from Robson *et al* (2007).

(2006). The analysis also reveals that the efficiency strongly depends upon other laser parameters and shooting conditions, especially the contrast ratio (Neely *et al* 2006) and target thickness (Fuchs *et al* 2006, Neely *et al* 2006, Robson *et al* 2007, Safronov *et al* 2008, 2010); higher contrast pulses and thinner targets tend to provide greater conversion efficiencies. The conversion efficiency into relatively low-energy ions can be increased by positioning the target out of focus, in which case the effect of larger spot area prevails over the effect of smaller intensity (Green *et al* 2010).

Theoretically, the performance of a thin foil target is well understood in several regimes (section 2), such as TNSA (Wilks *et al* 2001), the SCSF regime (Nishiuchi *et al* 2006, Passoni and Lontano 2008), the Coulomb explosion regime (Esirkepov *et al* 2002, 2006) and radiation pressure acceleration (Esirkepov *et al* 2004). In all these regimes, the target thickness should be very small. Therefore, in many experiments the dependence of ion acceleration on the target thickness has been investigated. It was found that a decrease in the target thickness gave rise to an increase in the proton energy, up to some, specific for each experiment, optimum thickness. After this, the proton energy decreased. Depending on the laser contrast, the optimum thickness can be in the micrometre or nanometre range. Targets with thicknesses from a few tens down to a few μm have been studied, e.g., by Mackinnon *et al* (2002), Kaluza *et al* (2004), Nayuki *et al* (2006) and Fuchs *et al* (2006). Several experimental works have been performed using targets with thickness from a few μm down to tens of or several nm employing ultra-high contrast laser pulses (Neely *et al* 2006, Antici *et al* 2007, Ceccotti *et al* 2007, Safronov *et al* 2008, 2010, Henig *et al* 2009b, Steinke *et al* 2010). The increase in the proton energy when the target thickness decreases from tens of to several μm is attributed to the geometrical factor in, e.g., the TNSA model, because the sheath radius (2.8) (figure 7) is smaller and the hot electron

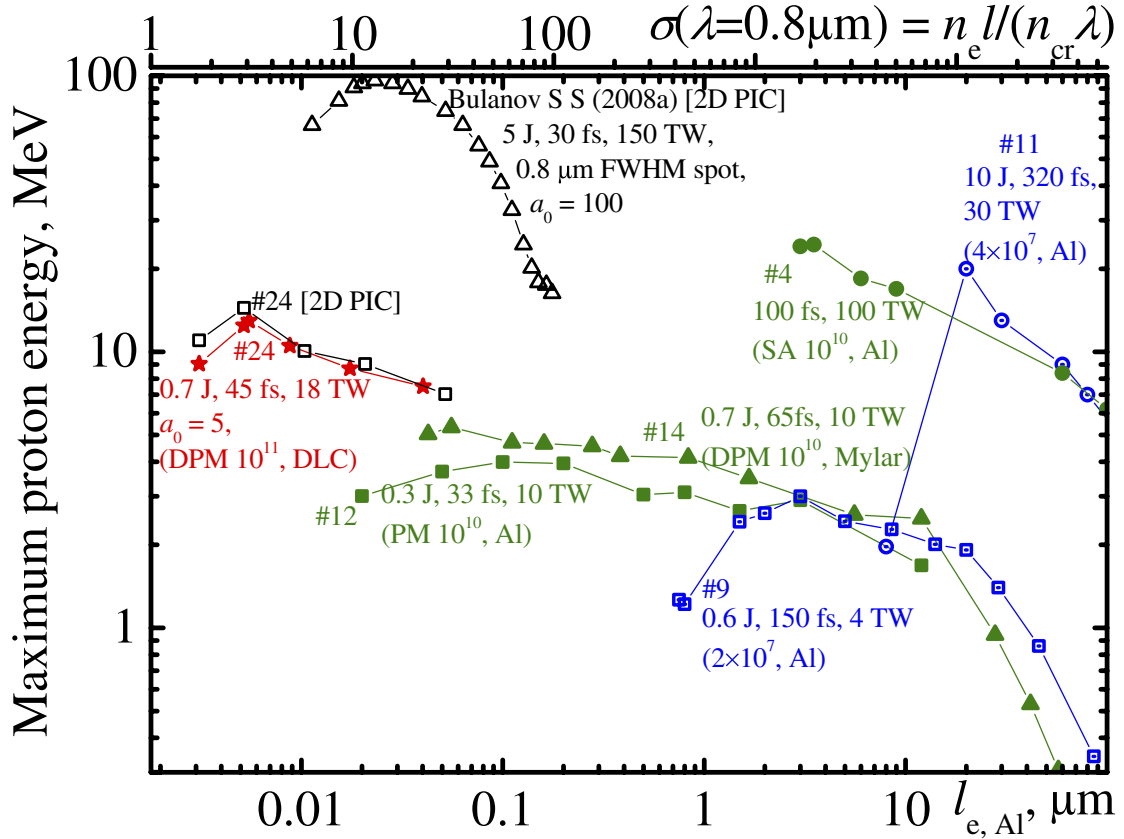


Figure 40. Maximum proton energy as a function of the normalized target thickness, which is the target areal electron density divided by the electron density of fully ionized aluminum: $l_{e,Al} = n_e l / n_{e,Al}$; the top axis shows the dimensionless areal electron density (2.19) for $\lambda = 0.8 \mu\text{m}$. Blue open circles and squares with central dots correspond to the standard CPA laser systems, the optimum thickness is determined by the onset of target rear surface destruction due to the ASE. Green solid squares, triangles and circles correspond to the laser systems with a contrast of $\sim 10^{10}$ achieved with a plasma mirror (PM), double plasma mirror (DPM) and amplification of high-energy seed pulse cleaned with a saturable absorber (SA), respectively; the optimum target thickness of several tens or a hundred nm is probably determined by the pre pulses or pedestal at ps or sub-ps time scales. The solid stars correspond to the contrast of $\sim 10^{11}$ achieved with the DPM, the optimum thickness of the diamond like carbon (DLC) target $\sim 5 \text{ nm}$ is described by the relation (2.20), which is the optimum for a clean laser pulse interacting with an ultra-thin foil in the ultra-relativistic regime $a_0 \gg 1$, where a_0 is the dimensionless laser amplitude (1.1); the black open squares are from 2D PIC simulations. Black open triangles are the results of 2D PIC simulations using an intense ($a_0 = 100$), prepulse-free laser pulse (Bulanov S S *et al* 2008a). The numbers followed by the '#' sign denote reference numbers, table 2.

density at the target rear side is higher (Kaluza *et al* 2004, Fuchs *et al* 2006). For a few- to sub- μm thick targets, this geometrical factor cannot account for the observed proton energy increase (Neely *et al* 2006). Hot electron recirculation (Mackinnon *et al* 2002, Sentoku *et al* 2003) can explain the continued ion energy increase as the thickness decreases. For sub- μm thick targets, we also note higher hot electron temperatures, which can be attributed to stronger laser absorption in a partly expanded, near-critical density target (Antici *et al* 2007, 2009). The target is expanded during the ps pedestal and fs pulse foot irradiation. For the same reason, targets thinner than the optimum give smaller proton energies because they are decomposed substantially. If the contrast is sufficiently high ($> 10^{10}$), the optimum thickness decreases to a few nm (Henig *et al* 2009b, Steinke *et al* 2010), in which case it is determined by the condition of best matching of a relativistic-intensity laser pulse to a thin foil (see equations (2.20) and (2.39) and right part of figure 3), which coincides with the condition of relativistic transparency of a thin foil (Vshivkov *et al* 1998).

An overview of the experimentally obtained dependences of the maximum proton energy on foil thickness is shown in figure 40. In order to show experiments with different target materials on the same graph, we normalize the target areal electron density $n_e l$ to the electron density of fully ionized Al; this is valid normalization for the ultra-thin foils, where the areal electron density is most important, section 2. Note that for relatively thick (micrometre-scale) targets, the thickness itself is more important, section 2. For comparison, the results of the 2D PIC simulations using a very intense ($a_0 = 100$), prepulse-free laser pulse are also shown (Bulanov S S *et al* 2008a). For conventional CPA laser systems (blue open squares and circles with central dots) with a typical contrast of $\sim 10^7$, the optimum target thickness is several to a few tens of μm determined by the onset of rear target side damage due to the ASE. For laser systems with contrast $\sim 10^{10}$ (solid circles, squares and triangles) the optimum target thickness is several tens to a hundred nm determined probably by the target perturbation on the ps or sub-ps time scales. For laser systems with a sufficiently clean pulse (stars) the optimum thickness

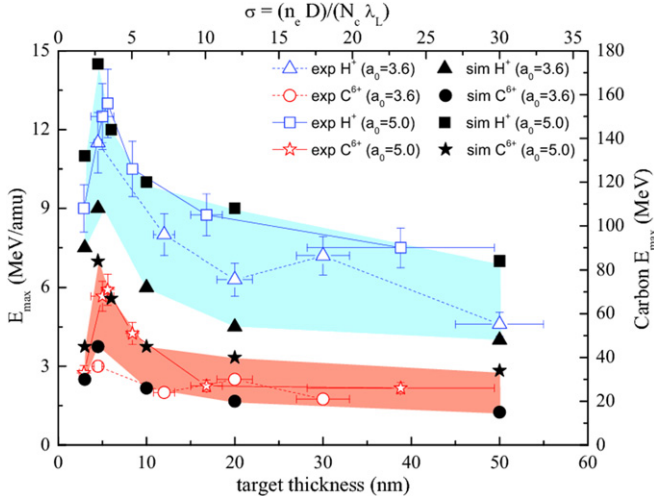


Figure 41. Experimental demonstration of laser-driven acceleration with the ultra-high-contrast linearly polarized laser and nanometre-thick DLC targets. Dependence of the maximum proton and carbon ion energies on the target thickness, comparison of the experimental data (open symbols with error bars) and 2D PIC simulations (solid symbols). The triangles and squares are for protons, $a_0 = 3.6$ and 5.0 , respectively; the amplitude is different due to changes in the focusing conditions. The circles and stars are for C^{6+} ions and the same laser amplitudes. The top axis shows the dimensionless areal density (2.19). Reprinted with permission from Steinke *et al* (2010).

of several nanometres is close to the relativistic matching condition (2.20) and (2.39)). Interestingly, for the clean laser pulses used in the simulations the achieved proton energies are much smaller for target thicknesses larger than ~ 100 nm. This indicates that a preplasma, which increases absorption, plays a significant (positive) role in ion acceleration from μm -thick targets (Bychenkov *et al* (2001a), Sentoku *et al* (2002), McKenna *et al* (2008), see also sections 2 and 3.2). We also note that in order to reproduce the experimental results, the simulations often have to include the hydrodynamical part to take into account the finite contrast effect, followed by multi-dimensional PIC simulations (Matsukado *et al* 2003, Andreev *et al* 2009, d'Humières *et al* 2010).

Henig *et al* (2009b) and Steinke *et al* (2010) demonstrated ion acceleration with ultimately thin diamond-like carbon (DLC) targets with thickness down to a few nm which were irradiated by a 0.7 J, 45 fs titanium sapphire laser, figures 41 and 42. DLC foils combine the advantages of high mechanical strength and high laser-induced damage threshold, which make them less contrast-demanding. The ultra-high contrast of 10^{11} was achieved using a double plasma mirror. The laser pulses were tightly focused to a $3.6 \mu\text{m}$ spot which provided an intensity of up to $5 \times 10^{19} \text{ W cm}^{-2}$ and dimensionless amplitude of $a_0 = 5$ for linear and 3.5 for circular polarizations. The experimentally obtained optimum target thickness was 5.3 nm (figure 41), which corresponds to $\sigma_{\text{opt}} \approx 3.3$. This agrees reasonably well with the relativistic optimum condition for clean laser pulses obtained with PIC simulations (2.20): $\sigma_{\text{opt,PIC}} \approx 0.4a_0 + 3 = 5$ (Esirkepov *et al* 2006). At the optimum target thickness, for linear polarization the maximum proton energy was 13 MeV. At the same time,

maximum carbon ion energy was ≈ 5.5 times larger, 71 MeV (figure 42(a)). Under other focusing conditions with smaller amplitude $a_0 = 3.6$, the maximum proton energy was nearly the same (~ 12 MeV), which may be explained by longer quasi-1D acceleration due to effectively larger focus (compare with the scaling (2.22) and the discussion below it).

Another interesting result of this experiment is the polarization dependence. Although the proton and ion energies were a bit smaller in the case of circular polarization (10 MeV and 45 MeV, respectively, figure 42(b)), the measured escaping electron temperatures were significantly lower. This confirms weaker electron heating by circularly polarized pulses obtained in the PIC simulations, section 2.6. Further, reproducible quasi-monoenergetic features appeared in the carbon ion energy spectra, figure 42(b), which were absent in the case of linear polarization. This peak (20–40 MeV) contained a significant portion of the laser pulse energy (2.5%).

3.5. Laser-driven heavy ion acceleration

Apart from protons, heavier ions also represent interest for various applications, see section 4. As a pioneering work, Clark *et al* (2000) observed heavy ions from the front target surface without prior target heating; 50 J laser pulses accelerated Pb^{46+} ions up to an energy of 430 ± 40 MeV (~ 2 MeV/nucleon), Al^{13+} ions up to 150 ± 10 MeV (~ 5.6 MeV/nucleon), and C^{6+} ions up to 90 ± 10 MeV (7.5 MeV/nucleon).

In the majority of experiments, the protons take most of the energy from the accelerating field; however, if the contamination layer containing protons is removed by resistive or laser heating, heavier ions are accelerated (Hegelich *et al* 2002, 2005, 2006, Roth *et al* 2002, Flippo *et al* 2007, McKenna *et al* 2003, 2004, 2007b). In these experiments, 20–30 J laser pulses produced ions with typical energies of a few to 5 MeV/nucleon; the total ion energy was up to 200 MeV (Pd^{22+}). Laser pulses with several hundred joule energy produced ions with energies >10 MeV/nucleon and total energies of several hundred MeV (e.g. McKenna *et al* (2004): Fe ions with energies up to 700 MeV).

Carbon ion acceleration has been demonstrated using ultra-high contrast laser systems employing double plasma mirrors and nanometre-thick targets without prior heating. In these cases, carbon ions and protons were accelerated simultaneously. Carbon ions with energies up to 185 MeV (15 MeV/nucleon) have been obtained using 40–50 J, 700 fs laser pulses focused at normal incidence to an intensity close to $10^{20} \text{ W cm}^{-2}$ on 30 nm thick DLC targets (Henig *et al* 2009c). Moderate-energy short-pulse (5 J, 50 fs), ultra-high-contrast laser pulses focused at normal incidence to intensities of $(6\text{--}7) \times 10^{20} \text{ W cm}^{-2}$ accelerated carbon ions up to 90 MeV (7.5 MeV/nucleon) (Carroll *et al* 2010b); in the oblique incidence case (35°) the carbon ion energies were smaller (60 MeV, or 5 MeV/nucleon). A relatively small energy laser (0.7 J, 45 fs, $5 \times 10^{19} \text{ W cm}^{-2}$, contrast 10^{11}) focused on 5.3 nm DLC targets accelerated carbon ions up to 70 MeV, figure 42 (Henig *et al* 2009b) (see also the end of section 3.4).

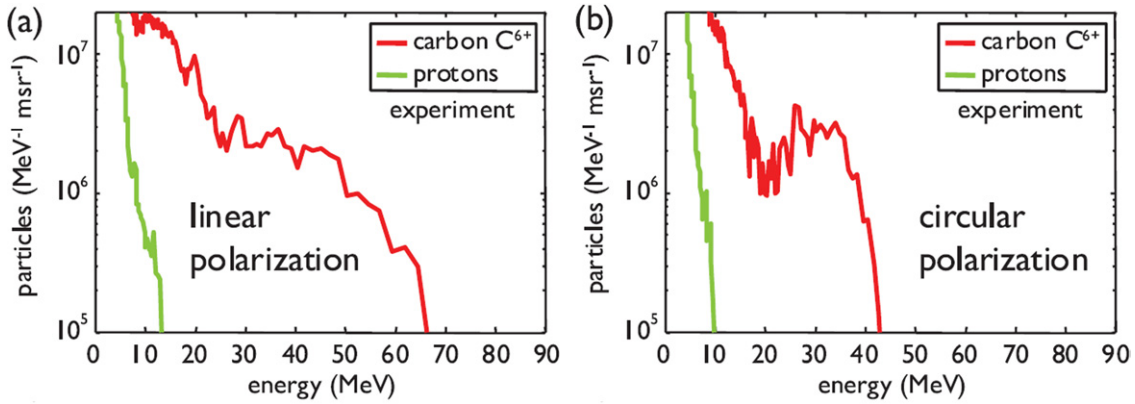


Figure 42. Experimentally observed proton and carbon ion energy spectra from 5.3 nm thick DLC targets for the linear (*a*) and circular (*b*) polarizations. Reprinted with permission from Henig *et al* (2009b).

Carbon ion acceleration and focusing have been demonstrated by Offermann *et al* (2011) using 10 μm -thick diamond hemispherical targets heated by a continuous 8 W laser. Two laser systems with substantially different parameters have been employed. With 80 J, 600 fs, $2 \times 10^{20} \text{ W cm}^{-2}$ laser pulses, the maximum C^{6+} ion energy was 160 MeV (13.3 MeV/nucleon), which is somewhat lower than, but comparable to the case of nanometre-thick targets and similar laser parameters (Henig *et al* 2009c, 185 MeV). On the other hand, with 1 kJ, 10 ps, $5 \times 10^{18} \text{ W cm}^{-2}$ laser pulses, the maximum C^{6+} ion energy was significantly lower, 30 MeV (2.5 MeV/nucleon).

3.6. Laser-driven quasi-monoenergetic ion acceleration

A significant feature of the present laser-driven ion sources is a wide energy spectrum, diverging beam originating from a few to several μm diameter effective source, section 4.1 and figure 45. Both characteristics are sometimes advantageous, but also sometimes disadvantageous, depending upon the specific application or purpose, see section 4. Several kinds of monochromatization techniques have been reported, including multi-species plasma and structured or heated targets, as described in this section. The external devices for monochromatization and collimation or focusing are described in section 4.

Thermal-like ion spectra which are typically observed in laser-driven ion acceleration experiments are consequences of different acceleration conditions experienced by ions situated originally at different distances from the focus and different depths from the target surface. Therefore, the spectrum can be made monoenergetic if the accelerated ions originally occupy a limited volume, i.e. the conditions are approximately the same; for ion acceleration from the rear side of a foil target this can be implemented employing a double-layer target with a thin, transversely small rear layer of ions (protons) to be accelerated (Esirkepov *et al* 2002, section 2.3). The experimental implementation (Schwoerer *et al* 2006, Pfotenhauer *et al* 2008) is based on 5 μm Ti foil with 10–20 μm , 0.2–0.5 μm thick poly(methyl methacrylate) (PMMA) microdots produced from a PMMA layer either by microstructuring with femtosecond laser ablation or by lithography. The proton contamination

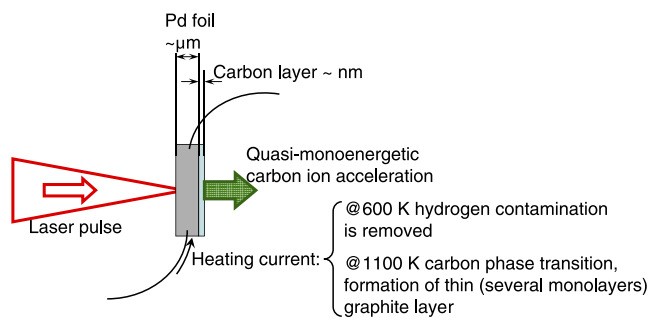


Figure 43. A schematic diagram of the laser-irradiated heated target scheme for quasi-monoenergetic carbon ion acceleration. At the temperature of 600 K, hydrogen contamination is removed, and at 1100 K the carbon ions form an ultra-thin layer on the Pd surface. In the experiment (Hegelich *et al* 2006), C^{5+} ions are accelerated forming a peak around 3 MeV/nucleon with a spectral width of 0.5 MeV/nucleon.

which inevitably appears under typical vacuum conditions within a few seconds is removed by several shots of nanosecond ablation laser just before irradiation with the main 10 TW pulse (0.8 J, 80 fs, ASE contrast 10^8) tightly focused to an intensity of up to $5 \times 10^{19} \text{ W cm}^{-2}$. The resulting proton spectra exhibit quasi-monoenergetic peaks with an energy of up to 2.5 MeV and relative bandwidth as small as 8%. Importantly, when the number of ablation pulses removing the proton contamination is large enough (four or ten, depending on the ablation laser fluence), the reproducibility of quasi-monoenergetic peak appearance approaches 100%. In addition to the small size of the proton-containing microdot, proton acceleration in multi-species plasma also contributes to the formation of the spectral peak, which is accelerated near the sheath formed by the heavy ion front (e.g. Tikhonchuk *et al* 2005, Brantov *et al* 2006, Robinson *et al* 2009a, Andriyash *et al* 2010); this also explains why the peak energy is smaller than the cut-off energy achievable with a standard foil target.

Hegelich *et al* (2006) have reported the observation of mono-energetic carbon ions using a 20 TW, 0.8 ps laser. In their experiment, a 20 μm thick palladium foil was heated up to 1100 K, figure 43. At this temperature, there is no more proton contamination, and due to a specific surface chemistry, the carbon atoms remain on the surface as a very thin

(monolayer-scale) layer, which leads to quasi-monoenergetic carbon spectra with an ion energy of ~ 3 MeV/nucleon, width of ~ 0.5 MeV/nucleon and spectral density of $\sim 2 \times 10^6$ MeV $^{-1}$ msr $^{-1}$.

Ter-Avetisyan *et al* (2006) demonstrated quasi-monoenergetic deuteron acceleration employing cooled heavy-water ice droplet targets irradiated by a titanium sapphire laser which delivered 40 fs pulses with a contrast of 10^8 focused up to an intensity of 10^{19} W cm $^{-2}$. Energetic deuterons having nearly mono-energetic spectrum with bandwidth of 0.3 MeV and peak at 2 MeV have been observed in the experiment. The explanation included two factors; (i) a quasi-stationary potential jump created due to the spatial separation of the deuterons and the oxygen ions (i.e. the multi-species plasma effect) and (ii) a short acceleration time of ~ 40 fs due to the spherical target geometry. The appearance probability of the mono-energetic peak is $\sim 10\%$, which is accounted for by the laser beam pointing and contrast stability.

Palmer *et al* (2011) demonstrated quasi-monoenergetic, low background proton acceleration using a CO₂ laser ($\lambda = 10 \mu\text{m}$) irradiating a hydrogen gas jet (see section 3.9).

3.7. New target designs

In most of the laser-driven ion acceleration experiments described above, thin flat foils with much larger scales compared with the size of the laser focus have been used. Here we consider some of the more sophisticated target designs which provide or can potentially provide advantages over the standard targets.

The proton source sizes have been measured in several experiments using targets with rear side grooves, knife edge or mesh radiograph techniques. It turns out that the real source sizes (note that these are different from the virtual source, see section 4.1) are much larger than the focal spot, typically a few tens or even hundreds of μm (Borghesi *et al* 2004, Cowan *et al* 2004, Ruhl *et al* 2004, Schreiber *et al* 2004, Roth *et al* 2006, Nürnberg *et al* 2009). This is also confirmed by the rear-side hot electron distribution measurement using optical probe reflectometry (Antici *et al* 2008a). The lateral electron transport (along the target surface) can even lead to charging of the target edges, where additional ion sources a few mm apart from the focal spot appear (McKenna *et al* 2007a). However, the laterally moving electrons stop or reflect at the target edges. This electron confinement effect leads to a larger hot electron density and therefore enhanced ion acceleration in the TNSA and SCSF regimes if the transverse size of the target is small enough. As discussed in section 2.3, small transverse target size is also required for the Coulomb explosion regime as in this case the neutralizing current of cold electrons (Quinn *et al* 2009) is minimized. Further, small transverse size of the target or light-ion or proton layer (dot) helps one to obtain quasi-monoenergetic spectrum (sections 2.3 and 3.6). Thus, the concept of mass-limited target (MLT) (or reduced mass target (RMT), or controlled amount of matter (CAM)) can potentially provide benefits under a wide range of experimental conditions. Ideally, the target should be completely isolated, e.g. by levitating or injecting into the interaction region (e.g.

a droplet target, Ter-Avetisyan *et al* (2006)). As this approach is not always available or may be technically difficult, it can be useful to isolate the targets causally, i.e. to a large extent, employing thin support wires or spokes (Strangio *et al* 2007). The behaviour of hot electrons and proton acceleration in the case of MLTs were studied by Buffeouchoux *et al* (2010); the laser contrast, improved using second harmonic generation, was high enough, and the preplasma did not overfill the targets. Compared with large-area foil targets ($\sim 10^5 \mu\text{m}^2$ and larger), the MLT targets (a few $\times 10^3 \mu\text{m}^2$) provided larger hot electron densities and temperatures and more uniform hot electron distribution, which led to increased proton energies from ~ 6 to ~ 14 MeV and conversion efficiencies from $\sim 0.1\text{--}0.2\%$ to 4% (proton energies > 1.5 MeV) and, in addition, to a smaller proton beam divergence.

A highly directional proton beam with plateau-shaped spectrum extending to energies up to 8 MeV from spherical targets of $15 \mu\text{m}$ diameter is observed in the laser propagation direction using 20 TW, 10^{20} W cm $^{-2}$ Ti : sapphire laser pulses (Henig *et al* 2009a). The result is explained by the acceleration in a converging shock driven by the laser irradiation to the small spherical target.

With the use of flat-top cone targets, Flippo *et al* (2008) demonstrated a maximum proton energy of at least 30 MeV (limited by the detector stack thickness; simulations indicate the possibility of 40–45 MeV protons) at an intensity of 10^{19} W cm $^{-2}$ with 20 J, 600 fs laser pulses. This proton energy is significantly higher than those produced with a standard flat $10 \mu\text{m}$ Au foil (19 MeV under similar conditions). The proton acceleration enhancement is attributed to the guiding and microfocusing of the laser pulse, larger absorption on the cone walls and preformed underdense plasma filling the inner volume, and better conditions of hot electron transport to the flat-top surface. Experiments with higher intensity (80 J, 600 fs, 1.5×10^{20} W cm $^{-2}$, 10^6 contrast) showed that a high contrast is mandatory to avoid laser pulse absorption in the preplasma far from the cone top, which reduces the proton energy and number significantly (Gaillard *et al* 2010). Further experiments with higher contrast (10^9 contrast, 82 J, 670 fs, 1.5×10^{20} W cm $^{-2}$) (Gaillard *et al* 2011) resulted in a maximum proton energy of up to 67.5 ± 2.0 MeV, with a conversion efficiency into > 4 MeV protons of 1.75%. The proton energy obtained with the flat-top cone targets is somewhat higher than that obtained in the same experiments with the RMT ($230 \mu\text{m}$ optimum diameter, 59 ± 2 MeV). The experiments have also demonstrated that the highest proton energies are obtained when the laser hits the cone target with some offset from the centre, which is confirmed with 2D Cu K α x-ray imaging. Based on PIC simulations, this is attributed to efficient electron acceleration along the cone wall at grazing incidence, where locally the laser is p-polarized.

A potentially useful and practical approach for shooting of conical structures in flat foils has been demonstrated by Matsuoka *et al* (2010). The cones have been machined by smaller energy laser pulses just before full-energy irradiation; thus, the manufacturing cost has been considerably reduced and alignment simplified.

3.8. Multi-pulse schemes

Another path for the optimization and control of laser-driven ion acceleration, which up to now has received relatively little attention in experiments, is the employment of multi-pulse irradiation schemes.

Markey *et al* (2010) used beam splitting and recombination before the final amplifiers in the CPA laser chain to make a double pulse with all-optically-controllable energy ratio and delay. The individual pulse durations were 0.7 ps and the delay varied from 0 (single pulse) to 2.5 ps. Two parameter sets were explored, namely with the first to second pulse energy ratio of 0.1 : 1 (0.4 : 1), total energy of 130 J (60 J) and main pulse irradiance of $2.4 \times 10^{19} \text{ W cm}^{-2}$ ($0.8 \times 10^{19} \text{ W cm}^{-2}$). The targets were relatively thick 100 μm gold foils used to avoid electron recirculation and a possible contribution of front side acceleration. In the configuration with the 10% prepulse at 1.5 ps before the main pulse, the conversion efficiency into protons above 4 MeV was 3.3 times greater and the maximum proton energy was 1.3 times higher than in the case of zero delay (single pulse), i.e. 0.56% versus 0.17% and 20 MeV versus 15 MeV, respectively. A similar enhancement was observed for the 40% prepulse, when the delay was 0.75 ps. In addition to these, the low-energy parts of the proton spectra in the target normal direction were suppressed at the optimal delays, which can be an important advantage for applications requiring quasi-monoenergetic ion spectra.

Pfotenhauer *et al* (2010) demonstrated a cascaded (two-stage) proton acceleration which allows spectrally controlling the proton beam. Two pulses from the same Ti : sapphire laser (0.5 J and 0.3 J, 80 fs, $1.7 \times 10^{19} \text{ W cm}^{-2}$ and $0.7 \times 10^{19} \text{ W cm}^{-2}$) with controllable delay irradiated two 2 μm -thick titanium foil targets aligned as successive source and amplifier with a separation of 5.86 mm. The central part of the proton beam accelerated from the first target stretched by the TOF dispersion was subsequently modified by the transient fields of the second target. Thus, a part of the spectrum, controllable with the optical delay between two laser pulses, was strongly suppressed; part of the protons from a particular spectral region were additionally accelerated, while the others were decelerated (cf phase rotation, section 4.8.1, and microlens, section 4.8.2). When the delay was tuned such that protons near the cut-off spectral region were affected, a distinct and well-separated proton peak was observed at an energy of 1.65 MeV with the FWHM bandwidth of 150 keV. This peak energy was higher by 200 keV than the high-energy cut-off from the single target alone (1.45 MeV under these conditions).

Further development of multi-pulse and/or multi-stage techniques described in this section may allow ion or proton acceleration with relatively small energy bandwidth and narrow beam divergence up to higher energies without increasing the total laser energy.

3.9. Proton and heavier ion acceleration with lower density targets

Other techniques to accelerate energetic ions employ targets with densities lower than the solid ones, which can be

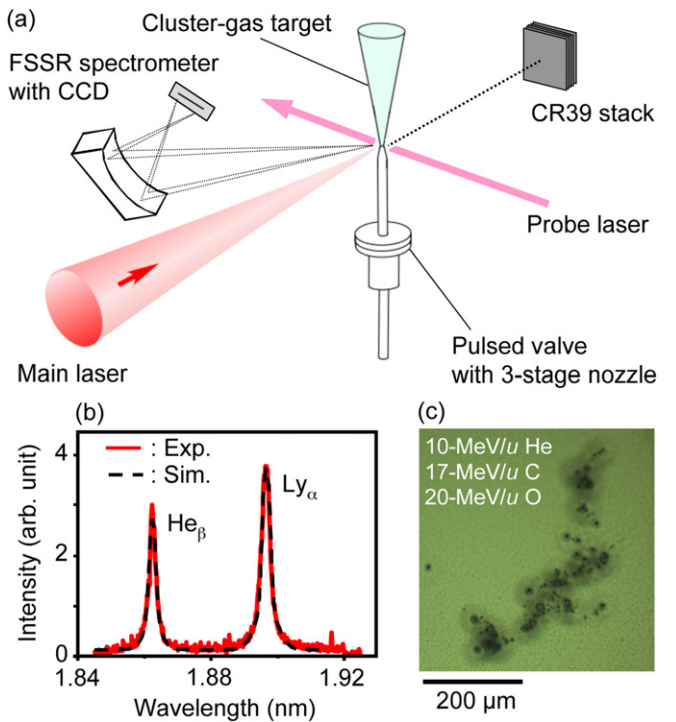


Figure 44. Ion acceleration using a cluster jet target.
 (a) Experimental setup schematic; a Ti : sapphire laser (150 mJ, 40 fs) irradiates a pulsed cluster gas jet target backed with a mixture of He and CO₂; the ions are recorded with a CR-39 stack in the forward direction; the FSSR x-ray spectrometer is used to measure the plasma density using spectral line shapes, which gives $n_e \sim 10^{20} \text{ cm}^{-3}$. (b) (c) Image of the 11th layer of CR-39 after etching; the numbers indicate energies of helium, carbon and oxygen ions, which all may be accelerated in the experiment. These pits are visible at the same positions on several CR-39 layers, indicating the ion beam penetrating through the detector stack and stopping at the depth corresponding to the Bragg peak. Reprinted with permission from Fukuda *et al* (2009).

implemented in several ways. The most straightforward is to use a pulsed high-pressure gas jet. Gas jet targets have several advantageous properties, such as adjustable density, contamination-free composition, possibility of debris-free operation and being less contrast-demanding. Krushelnick *et al* (1999) have demonstrated a few MeV ions (1.0 MeV deuterons, 3.6 MeV He and >6 MeV Ne ions) in the radial direction from the gas target in which the Coulomb explosion of the laser-produced channel takes place. Willingale *et al* (2006, 2007, 2008) reported acceleration of He ions up to an energy of 40_{-8}^{+3} MeV in the axial (forward) direction irradiated by 340 J, 1 ps laser pulses. Fukuda *et al* (2009) reported acceleration of ions having energy of 10–20 MeV/nucleon using 150 mJ, 40 fs laser pulses focused to a cluster jet target (mixture of 10% CO₂ and 90% He); the ions were recorded on the TOF and CR-39 stack detectors, figure 44. These ion energies are higher than can be typically achieved with such laser pulses using foil targets. Based on the 2D PIC simulations, the acceleration is attributed to the near-critical/underdense plasma model (Kuznetsov *et al* 2001, Matsukado *et al* 2003, Bulanov S V *et al* 2005a, Bulanov S S *et al* 2010, Nakamura T *et al* 2010), where the nearly fully absorbed laser pulse accelerates electrons, which generate ultra-high magnetic field

which in turn sustains charge-separation field (for more details, see section 2.8). The presence of clusters is important, as confirmed in shots with He gas only. In particular, after the prepulse absorption, a relatively dense plasma with peak electron density of $\sim 10^{20} \text{ cm}^{-3}$ is formed, which is supported by x-ray spectroscopy (Faenov *et al* 1994). A small laser energy and self-replenishable gas jet target make this method attractive for applications where repetitive ion acceleration is required.

For the laser wavelength of $\lambda_0 \sim 1 \mu\text{m}$, a gas jet cannot typically provide densities several times larger than the critical density, which is required for efficient ion acceleration (section 2.8). However, because n_{cr} scales as λ_0^{-2} , this can be easily achieved for longer laser wavelengths. Palmer *et al* (2011) demonstrated proton acceleration up to 1.1 MeV using an intense CO₂ laser ($\lambda_0 = 10 \mu\text{m}$, $\sim 3 \text{ J}$, 0.5 TW, train of several pulses 6 ps each, $\sim 6 \times 10^{15} \text{ W cm}^{-2}$, $a_0 \sim 0.5$) and hydrogen gas jet target with variable density up to 10^{20} cm^{-3} ($\sim 10n_{\text{cr}}$). The resulting proton beam has advantageous properties, i.e. quasi-monoenergetic spectrum with a relative width of 4% and the absence of other ion species. The acceleration is attributed to the radiation pressure driven shock (section 2.7) with the irradiance enhanced by relativistic self-focusing.

Similar effects as those for gas and cluster targets are expected if one uses an aerogel or fibre target. For example, Okihara *et al* (2006) reported relatively high-energy carbon ions having energy of 5 MeV and protons of 2 MeV employing fibrous PTFE targets driven by 120 mJ, 50 fs laser pulses. We also note that the density of an originally solid target can become close to the critical density or even underdense due to the prepulse or ASE irradiation, see sections 3.2 and 3.4 (a few μm -thick targets, e.g. Matsukado *et al* (2003)) or ps pedestal or femtosecond pulse foot (nanometre-thick targets, e.g. Antici *et al* (2007), (2009)).

3.10. Section 3 summary

In this section, we briefly show a typical design of present ultra-high peak power laser systems used for ion acceleration, describe detectors and techniques for measurement of various parameters of the laser-driven ion beams, and summarize the experimental achievements.

At the present stage, the performance of a standard few- μm -thick foil target irradiated with ‘normal’ contrast laser pulses (section 3.2) has been studied extensively and understood relatively well. The general trend is to use thinner targets and higher contrast pulses. Additionally, many ideas and techniques have been tested in proof-of-principle experiments, e.g. use of various advanced targets, circular polarization, contrast improvement techniques, multi-pulse and multi-stage acceleration, etc. However, much experimental work needs to be done. As directions for future research, we can identify the following.

- (1) Achieving the final stage of the radiation pressure dominant regime, when the foil moves as a whole and a significant (tens of %) portion of laser energy is transferred

to the ions. This is probably the most important long-term goal for the laser-driven ion acceleration research field; it includes tailoring of the laser pulse and target (section 2.6), avoiding or exploiting instabilities, finding optimum conditions, etc.

- (2) Optimization of various targets described in sections 3.6 and 3.7; these targets typically comprise several components and have several geometrical parameters, therefore finding an optimum for given laser parameters is not an easy task and should include analytical models, extensive realistic simulations starting from preceding light absorption and preplasma formation (e.g. Nagatomo *et al* 2010) and experiments. Without such optimization the high potential of these targets cannot be fully exploited.
- (3) Combination of several techniques, which have already been demonstrated, in one experiment. To give an example, highly desirable is a combination of a clean (ultra-high-contrast) laser pulse, focusing to a sub- μm spot, nanometre-thick double-layer target in an optimum regime (equations (2.20) and (2.39)), and the mass-limited target (MLT) concept.
- (4) Experimental optimization of ion acceleration with a dipole vortex in near-critical density plasmas (sections 2.8 and 3.9), including preparation of the optimum density profile. Demonstration of scalability of the scheme to larger laser powers. Search for conditions which lead to quasi-monoenergetic ion spectra.
- (5) Active tailoring of the driving laser pulses (acceleration using multiple pulses and one or several targets, optimization of temporal shape on different time scales, spatial profile, polarization, etc). Much theoretical and experimental work is necessary to fully exploit possibilities of the available lasers.
- (6) Achieving (quasi-)monoenergetic ion beams in the Coulomb explosion and radiation pressure dominant regimes.
- (7) Measurement of ion beam properties in the multi-100 MeV/nucleon energy range is a potential issue, in particular due to smaller deflection by detector’s fields and an expected strong background caused by simultaneously generated electrons, x-rays, neutrons, electromagnetic pulse, etc. Taking these into account, the energy range of detectors presently used with laser-driven sources should be extended (Jung *et al* 2011), or detectors used with conventional accelerators should be appropriately modified. Another issue may be the angular deviation of high-energy ions, section 2.5. Finally, the detectors should ideally provide ‘online’ capability.
- (8) It is necessary to obtain a thorough understanding of laser-target interaction during acceleration employing as many diagnostics as possible, including not only ion beam diagnostics, but also full characterization of the laser pulse before and *after* the interaction (i.e. reflected, transmitted or scattered radiation parameters (e.g. Pirozhkov *et al* 2009a, Palaniyappan *et al* 2010), possible non-linear effects such as harmonics generation (e.g. Teubner *et al* 2004, Hörlein *et al* 2008, Choi *et al* 2011, Streeter *et al* 2011), measurements of electron properties (e.g. Li *et al*

2006, Manclossi *et al* 2006, Santos *et al* 2007, Kiefer *et al* 2009, Bellei *et al* 2010), time-resolved optical imaging (Symes *et al* 2010), characterization of plasma densities and fields using interferometry (e.g. Borghesi *et al* 1996, Sagisaka *et al* 2006, Kar *et al* 2008a) or proton imaging/deflectometry (Borghesi *et al* 2001, Mackinnon *et al* 2004), x-ray diagnostics (e.g. Gaillard *et al* 2011) and so on.

4. Applications of laser-driven ion sources

The generation of multi-MeV ion beams driven by intense ultra-short laser pulses has been intensively studied, as described in section 3. At the same time, several applications have been proposed and tested such as proton imaging and deflectometry (Borghesi *et al* 2001, Mackinnon *et al* 2004), injectors for the conventional accelerators (Krushelnick *et al* 2000a, Noda *et al* 2006, Antici *et al* 2008b), laser-driven stand-alone accelerators (Esirkepov *et al* 2004), material engineering (Boody *et al* 1996, Torrisi *et al* 2003, Rosinski *et al* 2005), production of short-lived isotopes (Fritzler *et al* 2003, Ledingham *et al* 2003) for medical diagnostics with the positron emission tomography (PET) technique (Ollinger and Fessler 1997), ion fast ignition in laser-induced nuclear fusion (Roth *et al* 2001, Bychenkov *et al* 2001b) and ion sources for particle therapy (Bulanov S V and Khoroshkov 2002a, Bulanov S V *et al* 2002b, 2004b, Fourkal *et al* 2002, 2003a, 2003b, Malka V *et al* 2004, Murakami M *et al* 2008). Importantly, one needs to take into account the original and unique properties of the presently available laser-driven sources, such as divergence, wide spectral bandwidth, short pulse duration at the source, small source size, laminarity (small emittance) and so on. On the other hand, such properties can be modified, e.g. a focused and quasi-monochromatic beam can be obtained if one uses magnetic or RF devices (Schollmeier *et al* 2008, Ter-Avetisyan *et al* 2008b, Nishiuchi *et al* 2009, 2010, Ikegami *et al* 2009, Roth *et al* 2009, Harres *et al* 2010). Even without such devices, the laser-driven proton beam can be monochromatized (Esirkepov *et al* 2002, Hegelich *et al* 2006, Schwoerer *et al* 2006, Ter-Avetisyan *et al* 2006) and converged (Patel *et al* 2003, Toncian *et al* 2006, 2011, Kar *et al* 2008b) if one uses a properly configured target irradiated by a well-controlled ultra-intense laser pulse(s). In this section, we review the application aspects of laser-driven proton and ion sources. Firstly, we show the beam intensity characterization and applications which utilize the ultra-high peak intensity and ultra-short pulse duration of the proton beam, such as radiography, isochoric heating and so on. Secondly, we show the high average power beam applications such as ion implantation and radioactive isotope production. We show issues existing in the development of compact laser-driven proton and ion sources for future industrial accelerators and medical applications, in particular, several techniques for beam focusing and monochromatization.

4.1. Laser-driven ion source properties

In this section, we describe the properties of laser-driven ion sources directly related to the applications; for this reason,

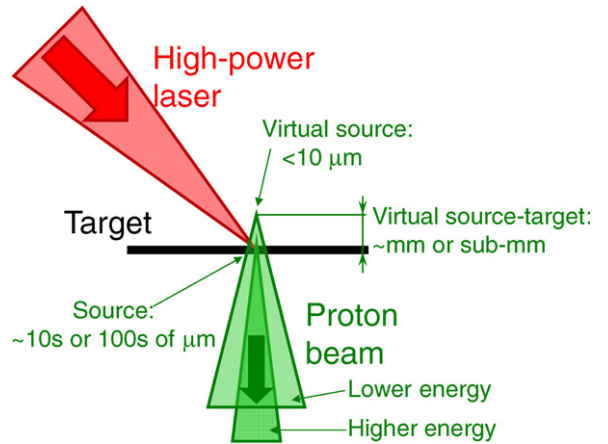


Figure 45. Schematic diagram of laminar proton beam acceleration by an intense laser pulse. The beam appears to be originating from a small (diameter $<10\text{ }\mu\text{m}$) virtual source located in front of the laser-irradiated target surface. A higher energy component represented by the darker colour is concentrated in a narrower divergence angle.

emphasis is made on the presently available, mostly proton, sources.

Based on the experimental characterization of proton beams from laser irradiated thin foil targets (Borghesi *et al* 2004, Cowan *et al* 2004, Ruhl *et al* 2004, Schreiber *et al* 2004, Roth *et al* 2005, 2006, Nishiuchi *et al* 2007, 2008, Nürnberg *et al* 2009), the beams are produced at the rear target surface with a source diameter many times larger than that of the laser irradiation area, up to a few tens or even hundreds of μm . The beam is diverging, and it appears that it comes from a spot with a typical diameter of less than $10\text{ }\mu\text{m}$, a so-called virtual source, located behind the real, large diameter source (i.e. in front of the target), figure 45. The higher energy component is situated closer to the beam axis (Snavely *et al* 2000). Roth *et al* (2005) and Nürnberg *et al* (2009) have shown the comparison of experimental results obtained at several relatively high-energy laser installations (figure 33). Similar properties of the proton beam can be found with smaller energy and lower intensity lasers (Nishiuchi *et al* 2007, 2008). The particle energy gradually decreases as the radial distance from the beam axis increases; in other words, the proton beam divergence decreases at higher particle energies (figures 32 and 33) (Roth *et al* 2005, Nürnberg *et al* 2009), as is shown schematically in figure 45. In contrast, using a smaller femtosecond laser ($\sim 1\text{ J}$, a few tens of fs), Ter-Avetisyan *et al* (2009) have experimentally shown the opposite proton beam characteristics, namely the high-energy component has a smaller source size but larger divergence angle. We also note that Schreiber *et al* (2006b) demonstrated that during the acceleration, a beam pointing for lower energy protons, such as those with energy less than a half of the high-energy cut-off, changes as a function of time, with a typical deviation of ~ 3 mrad. On the other hand, the pointing deviation of the high-energy component has not been detected. Such a precise characterization is beneficial not only for the understanding of the mechanism, but also for precise determination of the proton energy range, for which the proton beam is suitable for high-quality radiography, injection into post-accelerator, etc.

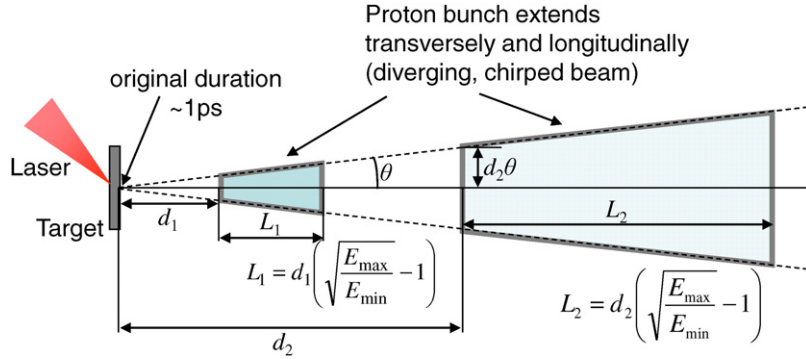


Figure 46. Propagation of an ion bunch with energy spread from \mathcal{E}_{\min} to \mathcal{E}_{\max} and half-divergence angle θ ; in the equations, energies far below the relativistic ones are assumed. Here d_1 and d_2 are the distances between the target and the protons with minimum energy \mathcal{E}_{\min} at different moments of time, $L_i = d_i [(\mathcal{E}_{\max}/\mathcal{E}_{\min})^{1/2} - 1]$ are the corresponding lengths of the proton bunch, and the durations of the bunch at distances d_i are $\tau_i = d_i (m_p/2)^{1/2} [(\mathcal{E}_{\min})^{-1/2} - (\mathcal{E}_{\max})^{-1/2}]$. The beam intensity drops rapidly due to spread in both the longitudinal and transverse directions as shown quantitatively in the figure.

The most significant feature of the laser-driven ion beam is ultra-high peak power in a short time period. Another feature is that the acceleration length is extremely short, leading to a potentially very compact source. Further, in contrast to the conventional (RF-based) ion sources, due to the charge neutralization by co-moving electrons (Cowan *et al* 2004), the space charge effect does not limit the current density. Therefore, a low voltage and high current density ion source can be implemented. For example, a picosecond proton beam which contains $>10^{10}$ protons was demonstrated (Cowan *et al* 2005). Such a beam has never been achieved by any accelerator except the laser-driven source.

On the other hand, the stability of the laser-driven ion sources remains an issue. For practical applications, fluctuations in the ion energy spectrum, position of the virtual source, its size, angular beam profile and other properties of the source and possibly beam transport system should be characterized precisely shot by shot and reduced to the required level.

4.2. Beam power and intensity of laser-driven ion sources

Before describing specific applications, we estimate the proton beam current, power and intensity and their dependence on the distance from the target, which may be key issues for many applications. For example, if the laser pulse energy is 1 J and the conversion efficiency into the proton beam is 1%, the total number of protons is around 10^{10} – 10^{11} /shot, depending on the proton energy spectrum. If the proton beam duration at the source is ~ 1 ps and the source size is $100 \mu\text{m}$, the peak current and current density are 1–10 kA and 10–100 MA cm $^{-2}$, and the beam power and intensities are 10 GW and $\sim 10^{14}$ W cm $^{-2}$, respectively. In another example related to ion-induced fast ignition (see below), the ignitor ion/proton beam with 10 kJ energy and 1 ps duration has the original power of 10 PW. In both examples, the values reduce rapidly when such beams with broad spectra diverge in space and spread in time, figure 46.

The beam power and intensity can be estimated based on the experimental results reviewed in section 3 and analytical approximations of the spectral shape and beam properties. For

many applications, we can assume instantaneous emission of the beam, because the spread due to the time of flight is much longer than the original duration. Further, we can assume that the space charge effects are negligible. This assumption is supported by experiments, which can be explained by the neutralizing effect of co-moving electrons (Cowan *et al* 2004). Under these assumptions, the beam with the energy distribution $dN(\mathcal{E})/d\mathcal{E}$ at distance d has the following dependences of power P and current i on time t :

$$\begin{aligned} P(d, t) &= \mathcal{E}(d, t) \frac{dN(d, t)}{dt} \\ &= \mathcal{E}(d, t) \left. \frac{dN(\mathcal{E})}{d\mathcal{E}} \right|_{\mathcal{E}=\mathcal{E}(d,t)} \frac{d\mathcal{E}(d, t)}{dt} \\ &= \frac{2\sqrt{2}}{d} \sqrt{\frac{\mathcal{E}(d, t)^5}{m_i}} \left. \frac{dN(\mathcal{E})}{d\mathcal{E}} \right|_{\mathcal{E}=\mathcal{E}(d,t)}, \\ i(d, t) &= eZ \frac{dN(d, t)}{dt} = \frac{eZ}{\mathcal{E}(d, t)} P(d, t) \\ &= \frac{2\sqrt{2}eZ}{d} \sqrt{\frac{\mathcal{E}(d, t)^3}{m_i}} \left. \frac{dN(\mathcal{E})}{d\mathcal{E}} \right|_{\mathcal{E}=\mathcal{E}(d,t)}. \end{aligned} \quad (4.1)$$

Here $\mathcal{E}(d, t) = m_i v^2/2 = m_i (d/t)^2/2$ is the energy of a particle with mass m_i corresponding to the distance d and time t ; we assume here $v \ll c$.

For example, the beam power formulae relevant to fast ignition by the ion beam can be found in Honrubia *et al* (2009). They assume a parallel beam obtained with a specially configured target, i.e. the beam intensity is proportional to power. The quasi-monoenergetic (QM) ion beam with a Gaussian energy distribution

$$\frac{dN^{\text{QM}}(\mathcal{E})}{d\mathcal{E}} = \frac{N_0}{\Delta} \sqrt{\frac{4 \ln 2}{\pi}} \exp \left(-(4 \ln 2) \frac{(\mathcal{E} - \mathcal{E}_0)^2}{\Delta^2} \right), \quad (4.2)$$

has a beam power on target

$$\begin{aligned} P^{\text{QM}}(d, t) &= \frac{N_0 d^4 m_i^2}{t^5 \Delta} \sqrt{\frac{\ln 2}{\pi}} \\ &\times \exp \left[-(4 \ln 2) \left(\frac{d^2 m_i}{2 t^2 \Delta} - \frac{\mathcal{E}_0}{\Delta} \right)^2 \right], \end{aligned} \quad (4.3)$$

where $N_0 \approx W/\mathcal{E}_0$ is the total number of ions, W the beam energy, \mathcal{E}_0 the mean kinetic ion energy and Δ the energy spread (FWHM). For $\Delta \ll \mathcal{E}_0$, the maximum power at distance d is achieved at the time $t \approx d/V_0$, where $V_0 = (2\mathcal{E}_0/m_i)^{1/2}$ is the velocity corresponding to the energy \mathcal{E}_0 :

$$\begin{aligned} P_{\max}^{\text{QM}}(d) &\approx \frac{\mathcal{E}_0 N_0}{d} \left(4 \sqrt{\frac{\ln 4}{\pi}} \sqrt{\frac{\mathcal{E}_0^3}{\Delta^2 m_i}} + \frac{25}{8\sqrt{\pi \ln 4}} \sqrt{\frac{\Delta^2}{\mathcal{E}_0 m_i}} \right) \\ &\approx 4 \sqrt{\frac{\ln 4}{\pi}} \frac{W}{d \Delta} \sqrt{\frac{\mathcal{E}_0^3}{m_i}}. \end{aligned} \quad (4.4)$$

Note that the second part in the brackets is much smaller than the first one for $\Delta \ll \mathcal{E}_0$, thus it can be neglected.

On the other hand, an ion beam with a Maxwellian energy distribution

$$\frac{dN^{\text{Maxwell}}(\mathcal{E})}{d\mathcal{E}} = \frac{2N_0}{T^{3/2}} \sqrt{\frac{\mathcal{E}}{\pi}} \exp\left(-\frac{\mathcal{E}}{T}\right), \quad (4.5)$$

has a power on target

$$P^{\text{Maxwell}}(\tau, t) = \frac{8W}{3\sqrt{\pi}\tau} \left(\frac{\tau}{t}\right)^6 \exp\left(-\frac{\tau^2}{t^2}\right), \quad (4.6)$$

where $\tau = d/(2T/m_i)^{1/2}$ is the pulse time scale and T is the temperature (MeV). The beam energy is $W = 3TN_0/2$, the maximum power at distance d is achieved at time $t = \tau/3^{1/2}$:

$$P_{\max}^{\text{Maxwell}}(d) = \frac{108}{e_N^3} \sqrt{\frac{2}{\pi}} \frac{N_0}{d} \sqrt{\frac{T^3}{m_i}} = \frac{72}{e_N^3} \sqrt{\frac{2}{\pi}} \frac{W}{d} \sqrt{\frac{T}{m_i}}, \quad (4.7)$$

where $e_N = 2.71828\dots$ is Euler's number.

In both cases, the maximum beam power is inversely proportional to the distance d . For example, a Maxwellian proton beam with beam energy $W = 10$ kJ and temperature $T = 4$ MeV has a maximum power of ≈ 1.6 PW and duration of ≈ 8 ps at a distance $d = 0.5$ mm; this should be compared with the power at the source of ~ 10 PW for the original duration of 1 ps. On the other hand, a quasi-monoenergetic beam can provide high power at much longer distances due to the reduced spread in time, e.g. a carbon ion beam with the same total energy of 10 kJ and $\mathcal{E}_0 \approx 400$ MeV, $\Delta = 40$ MeV has similar power (1.1 PW) and duration (8 ps) at a 27 times longer distance $d = 13.5$ mm.

If we now consider a diverging beam from a point-like source, which is the ordinary case of laser-driven beams, as shown schematically in figure 46, the formulae for intensity and current density should incorporate the beam divergence effect. Generally speaking, the divergence angle depends on the particle energy in a broad-bandwidth beam. In the simplest case of a quasi-monoenergetic beam, the divergence is approximately constant, in which case the maximum beam intensity I and current density j are

$$\begin{aligned} I_{\max}^{\text{QM}}(d) &= \frac{P_{\max}^{\text{QM}}(d)}{2\pi d^2(1 - \cos \theta)} \approx \frac{P_{\max}^{\text{QM}}(d)}{\pi d^2 \theta^2} \propto \frac{1}{d^3}, \\ j_{\max}^{\text{QM}}(d) &= \frac{i_{\max}^{\text{QM}}(d)}{2\pi d^2(1 - \cos \theta)} \approx \frac{i_{\max}^{\text{QM}}(d)}{\pi d^2 \theta^2} \propto \frac{1}{d^3}. \end{aligned} \quad (4.8)$$

Here θ is the half-divergence angle; the approximations are valid for $\theta \ll 1$.

4.3. Applications which require high peak power, ultra-short proton/ion beams

There are two kinds of ion beam applications, which differ in their primary requirement. The first one requires an ultra-high-intensity, short ion beam. The second requires a high average intensity beam. We should be careful as these two properties cannot always be clearly separated. First, we describe the applications which mainly utilize the former characteristics.

4.3.1. Probing plasma density and fields with proton beams.

Probing of fast dynamical phenomena with laser-generated proton beam is a unique and powerful technique. The proton beam is sensitive to the electric and magnetic fields due to deflections caused by them, as well as to the density due to stopping and scattering. For high-resolution probing, a highly laminar, small emittance beam is required. Two techniques of proton beam emittance characterization have been tested using the proton imaging techniques. One way is to use a target with grooves or structures at the rear side, which are imprinted into the proton beam and therefore revealed on a foot-print detector, e.g. CR-39 or RCF stack (Cowan *et al* 2004). In the experiments with $10\text{--}50\ \mu\text{m}$ thick grooved targets a transverse emittance of less than $0.004\ \text{mm mrad}$ for 10 MeV protons has been measured; a refined analysis with smaller proton energy bin has shown that the emittance was actually smaller by a factor of two (Kemp *et al* 2007). Such emittance values are much smaller than can be achieved in conventional accelerators. Transfer of the patterns from the target rear side to the proton foot-print profiles is affected by the transverse beam properties (model by Brambrink *et al* (2006a)); in particular, in the case of a far from ideal (large transverse emittance) beam with trajectory crossings, the pattern would be smeared out. The heated (section 3.5) grooved targets can also be used to determine the emittance of the accelerated heavier ion beams; Brambrink *et al* (2006b) measured the normalized transverse emittance of a 16.5 MeV (2.75 MeV/nucleon) oxygen beam to be $0.09\ \text{mm mrad}$ and compared the emittance and divergence properties of heavier ion beams with those of protons. Another method of transverse emittance measurement is to use a shadow image of a mesh which is placed between the source and the detector (Borghesi *et al* 2004). In this experiment the proton beam is transmitted through and scattered by the mesh; a particle transport code calculates the trajectories of the proton beam. Then the recorded mesh images are transformed into the virtual source size and virtual source position, from which one can estimate the transverse emittance value: $\varepsilon \approx \beta \rho_0 \Delta \theta$, where ρ_0 is the radial extent of the proton-emitting region on the rear surface of the target, $\beta = v/c$, v and c are the proton and light velocity, respectively, and $\Delta \theta \approx \alpha/2x$ is the degree of laminarity of the source; here α and x are the virtual source size and distance between the virtual source and target, respectively. In the experiment (Borghesi *et al* 2004) $\rho_0 = 80\ \mu\text{m}$, $\alpha = 8\ \mu\text{m}$, $x = 400\ \mu\text{m}$, $\Delta \theta \approx 10\ \text{mrad}$, giving $\varepsilon \approx 0.1\pi\ \text{mm mrad}$ for 15 MeV protons. If the thickness of the mesh is large enough for the proton beam to penetrate through, one can use a technique similar to that used in geometrical ray optics (Baez 1952) for the determination of the virtual source

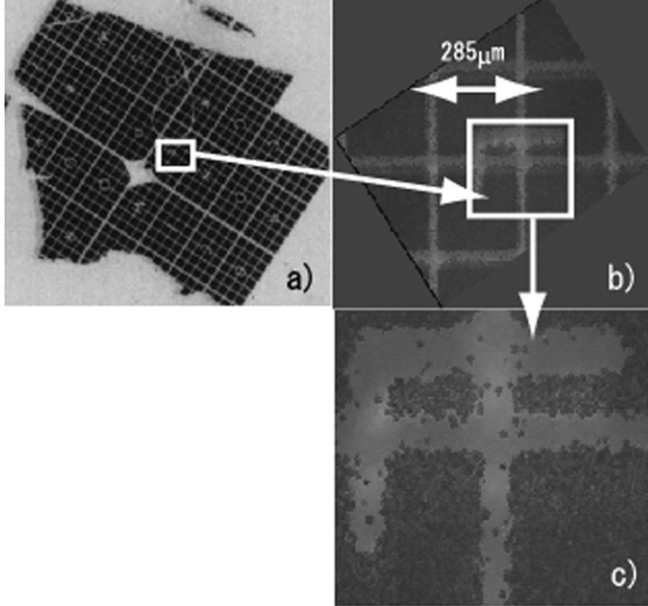


Figure 47. Single-shot proton projection images (Nishiuchi *et al* 2007). (a) A Cu mesh backlighted with protons with energies $>470\text{ keV}$. The darker regions correspond to the proton tracks in the etched CR-39 detector. (b) Magnified image of rotated letter ‘L’. The scale corresponds to the CR-39 detector plane, which in turn corresponds to $63\text{ }\mu\text{m}$ on the object (mesh) plane. (c) Close look of the proton shadowgraph around letter ‘L’. Individual proton tracks with pit radius $\sim 5\text{ }\mu\text{m}$ are visible.

size (Nishiuchi *et al* 2007). The corresponding experimental result of proton projection images are shown in figure 47. The clear mesh image can be seen with several μm resolution.

Mackinnon *et al* (2003a) have shown high-contrast Moiré fringes arising when the proton beam passes through a couple of gratings and confirmed that the beam originates from a point source close to the original target surface. Simulations show that the Moiré fringes can be used as a high precision diagnostic of proton beam deflection from electric and magnetic fields in plasmas (Mackinnon *et al* 2003b).

The source characteristics such as short duration, high degree of laminarity and small source size allow observing fast dynamic phenomena with high resolution. The laser plasma proton beams were used as probes for measuring distributions of electric and magnetic fields in laser-produced plasmas employing solid and gas targets (Borghesi *et al* 2001, 2002a, 2002b, 2003, 2005, Mackinnon *et al* 2004, 2006, Romagnani *et al* 2005, 2008, Kar *et al* 2007, Cecchetti *et al* 2009). In particular, Romagnani *et al* (2008) demonstrated collisionless shock waves and ion-acoustic solitons excited in ionized low-density background plasmas during intense laser–solid target interactions.

Figure 48 shows the experimental setup of proton radiography employing a 7–10 MeV proton beam produced by a CPA₂ laser (Romagnani *et al* 2005). Figure 49 shows typical experimental data obtained with proton imaging (frames (b)–(g)) and deflectometry (frame (h)); each frame corresponds to a different probing time. In this case, the protons produced by the CPA₂ laser probe a proton acceleration region around another thin foil irradiated by an intense and short CPA₁ laser

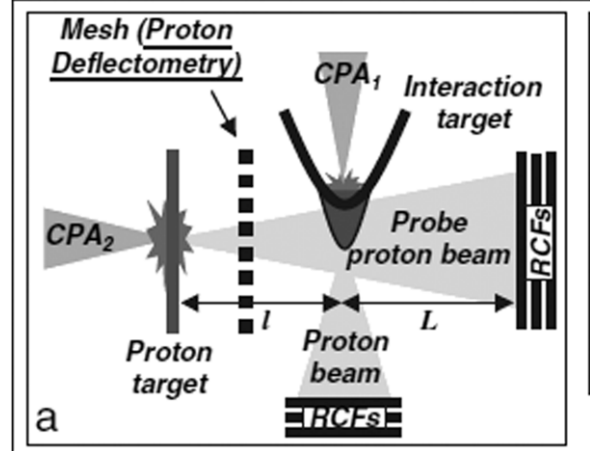


Figure 48. Schematic view of proton radiography of a laser-produced plasma. The CPA₂ laser pulse irradiates the proton target which emits a probe proton beam. This intense proton beam probes a plasma which needs to be characterized, in this case it is the proton acceleration region produced by the CPA₁ pulse. The RCF stack is used for the multi-frame recording of the time evolution of electric field distribution, employing the dependence of Bragg peak (penetration) depth on the proton velocity (energy). Reprinted with permission from Romagnani *et al* (2005).

pulse. The electric field due to the initial electron sheath and the predicted peak of the accelerating field at the expanding ion front are visible.

Cecchetti *et al* (2009) measured $\sim 45\text{ T}$ azimuthal magnetic fields generated during irradiation of solid targets with 1 ns, $5 \times 10^{14}\text{ W cm}^{-2}$ laser pulses using proton deflectometry from two directions, perpendicular and parallel to the target, in each shot. Comparison of the obtained results with magnetohydrodynamic simulations confirmed that the main source of the magnetic field was the $\vec{\nabla}T_e \times \vec{\nabla}n_e$ mechanism.

Nilson *et al* (2006) performed experimental characterization of magnetic reconnection and plasma diagnostics in two-beam laser–solid interactions using several probing techniques including optical probing (shadowgraphy, interferometry) and proton deflectometry. These allowed interpretation of the experimental results and identifying megagauss magnetic fields and their dynamics (for a review, see Stamper (1991)).

Ravasio *et al* (2010) used proton beam for radiography of shocks produced by a nanosecond laser in a low-density carbon foam target. The steep plasma density profiles can be resolved with the help of Monte Carlo simulations. This technique can be useful for the investigation of warm dense matter (WDM) properties.

The application of laser-driven proton radiography to a compressed core plasma in inertial confinement fusion (Borghesi *et al* 2001, Mackinnon *et al* 2006) has a very high potential. In this case, the image on the detector can be formed by multiple scattering in the dense plasma, i.e. the probed value is the density (Mackinnon *et al* 2006), or simultaneously by scattering and the presence of electric and magnetic fields (Li *et al* (2008), Rygg *et al* (2008), see below). For an ignition-scale experiment, protons with

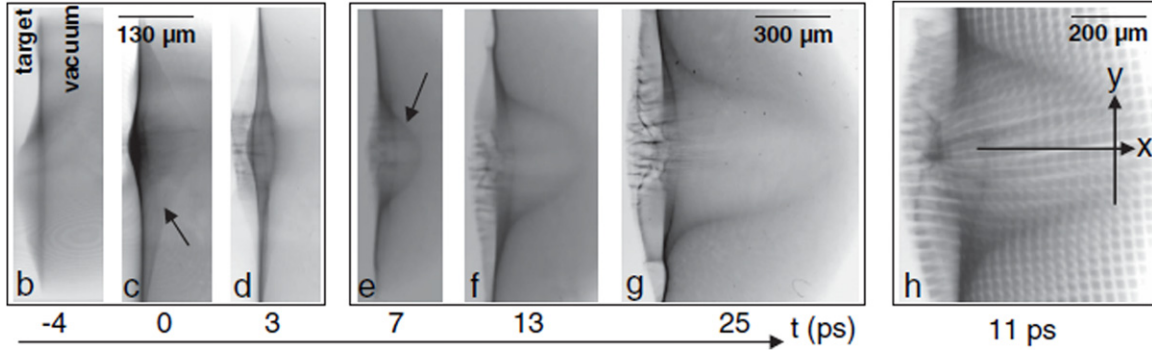


Figure 49. Results of plasma probing employing a proton beam, figure 48; darker regions correspond to higher proton densities. (b)–(g) represent typical proton imaging data (without a mesh) at probing times ~ -4 ps, 0 ps, 3 ps, 7 ps, 13 ps and 25 ps, respectively; (h) is the proton deflectometry data (with a mesh, see figure 48). Note that the magnification $M = 30$ in (b)–(d) and $M = 15$ in (e)–(h). The scales refer to the interaction target plane (scales on the detector are M times larger). The darker region indicated by the arrow in (c) shows that the probing protons are deflected away from the interaction target rear surface; this deflection is absent at ~ 3 ps (d). From (c), the estimate for the peak field is $\sim (4\text{--}5) \times 10^{11} \text{ V m}^{-1}$, in agreement with the computer simulation. At ~ 7 ps (frame (e)), an expanding ion front, delimited by a bell-shaped thin region of proton accumulation, is observed (indicated by the arrow in (e)). Reprinted with permission from Romagnani *et al* (2005).

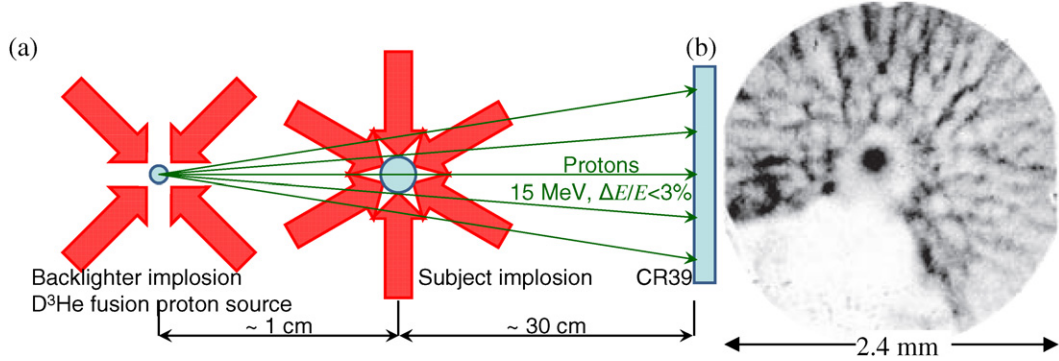


Figure 50. (a) Schematic of the experimental setup of mono-energetic proton radiography; a 15 MeV mono-energetic isotropic proton source is generated via D^3He fusion reaction in the imploded backscatterer target. The protons passing through the subject implosion are detected with a CR-39 nuclear track detector; two kinds of images, namely proton density and mean proton energy map, are used to identify density and fields distributions (Rygg *et al* 2008, Li *et al* 2008). (b) A proton image of a $430 \mu\text{m}$ radius spherical plastic target with attached gold cone during implosion, which is 1.56 ns after the onset of the implosion laser. Darker regions correspond to the higher proton fluence. (b) is reprinted with permission from Rygg *et al* (2008).

>50 MeV energy are required to diagnose the asymmetry of an imploded core plasma (Mackinnon *et al* 2006). Unlike experiments described previously in this review, a feature of fusion plasma is relatively long (~ 0.1 ns) time scales. This requires protection of the proton-generating target from debris originated at the long-living fusion plasma; e.g. in a proof-of-principle experiment (Mackinnon *et al* 2006) a $6 \mu\text{m}$ Al foil has been employed; such a foil does not deteriorate the resulting proton image. Further, due to the long time scale in a typical experimental configuration, protons with different velocities still probe nearly the same plasma due to an insufficient TOF difference, which means the time scale of the phenomenon is slower than the accessible time range in this case. Thus, a broad proton spectrum, which is typical of present-day experiments, cannot provide the advantage of multiple frame imaging, contrary to the diagnostics of ps and fs laser-produced plasmas. Instead, such a spectrum leads to a contribution of protons with different energies to the image in each detector layer; such images can be treated with realistic proton transport simulations. A different approach was demonstrated by Rygg *et al* (2008) and Li *et al* (2008); in these experiments, the

probe proton beam was obtained from a highly monochromatic ($\Delta E/E < 3\%$), spherically isotropic 15 MeV proton source generated by the deuterium and helium 3 fusion reaction driven by laser implosion of the backscatterer target, figure 50(a). Two kinds of compressed core plasma images were demonstrated, namely proton density and proton mean energy maps in which the energy is obtained via analysis of pit size and contrast (Séguin *et al* 2003). Figure 50(b) shows an image of a $430 \mu\text{m}$ radius spherical plastic target with an attached gold cone during implosion. The technique reveals the complex structure of magnetic and electric fields in both spherical and cone-in-shell (Kodama *et al* 2001) targets. In particular, the radial electric field which changes from 10^9 V m^{-1} inward to 10^8 V m^{-1} outward, has been identified.

4.3.2. Ion-driven fast ignition. Ultra-high-intensity proton (Roth *et al* 2001) and ion (Bychenkov *et al* 2001b) beams can be used as sources for fast ignition in laser-induced fusion (Tabak *et al* 1994). In this scheme, nanosecond laser beams compress a target to make a core plasma. A picosecond proton

or ion ignitor beam irradiates the core to efficiently burn the fuel. This requires a high-intensity proton/ion beam, which can potentially be provided by a laser-driven source. The proton and ion beam ignition scenarios were simulated by Temporal *et al* (2002), Temporal (2006) and Honrubia *et al* (2009). Honrubia *et al* (2009) calculated that the required proton and carbon ion beam energies are ~ 13 kJ in the case of Maxwellian distributions with temperatures of 4 MeV for proton and 100 MeV for carbon ions. This energy reduces down to 9.5 kJ for a quasi-monoenergetic carbon ion beam in the energy range 25–40 MeV/nucleon and relative bandwidth of 10%, i.e. with a relatively broad spectrum. If a laser to ion conversion efficiency of 10% is assumed, the required laser energy is ~ 100 kJ, which is similar to that found in electron-driven fast ignition. Honrubia *et al* (2009) also pointed out that heavier ions can be produced farther from the compressed core, as they propagate nearly ballistically; longer distance makes easier to design the fast ignition configuration. Limited-bandwidth (e.g. Maxwellian spectrum within the 7–19 MeV range, Temporal *et al* (2002)) or quasi-monoenergetic ion beams (e.g. Gaussian spectra with $\sim 10\%$ relative bandwidth, Temporal (2006), Honrubia *et al* (2009)) are more favourable for fast ignition as they have smaller time spread and in addition more localized heating area near the Bragg peak. The issues to be considered for the development are firstly the ion energy of the order of 25–40 MeV/nucleon; such energies have been achieved by PW class, large-energy lasers (Hatchett *et al* 2000). Secondly, the laser to ion energy conversion efficiency should be as high as possible, such as 10%, otherwise we cannot find significant reduction of the required laser energy compared with the traditional laser-induced fusion. However, the efficiency of the quasi-monoenergetic source is notably lower at the moment; an optimization of the conversion efficiency into a limited bandwidth or energy range is required. Naumova *et al* (2009) proposed another, simplified geometry; in this case, the hole boring ion acceleration (section 2.7) of the laser-irradiated pellet itself may lead to the ignition.

4.3.3. Isochoric plasma heating. The collimation or focusing of ions, first demonstrated with PIC simulations (Sentoku *et al* 2000, Wilks *et al* 2001), is a quite important subject which is applicable to many fields of science. For example, Patel *et al* (2003) proposed and Dyer *et al* (2008) experimentally demonstrated the fast isochoric heating of dense plasmas for the equation-of-state measurement. In this experiment, the sample thickness should be less than the distance of the Bragg peak from the surface. Thus uniform heating of a dense plasma with thickness of a few μm can be achieved, which is advantageous compared with optical laser heating, in which case local heating with a penetration depth of < 100 nm occurs, and one needs a few tens of nm ultra-thin foils for realizing uniform isochoric heating.

Mančić *et al* (2010) and Pelka *et al* (2010) demonstrated the application of proton-induced isochoric heating of materials for studying ultrafast phase transitions in WDM states. In both cases, a second ultra-short laser pulse produced x-rays, which were used for x-ray absorption near-edge spectroscopy (XANES) (Mančić *et al* 2010) or 90° scattering

measurement (Pelka *et al* 2010). These experimental results can be used to test the equation of state (EOS) and theories describing properties of matter in such hard-to-reach states. The results have importance, for example, for planetary science and astrophysics, where extreme conditions of matter are studied.

Summarizing section 4.3, we note that the applications described here utilize the single shot based interaction between an ultra-high intensity, short proton beam and matter. These subjects are really original and unique. Such ultra-high-intensity proton and ion sources bring us distinguished scientific tools at present as well as potential industrial applications with significant advantages in the future, in particular, in fusion research (Roth *et al* 2001, 2005, Borghesi *et al* 2001, Temporal *et al* 2002, Temporal 2006, Mackinnon *et al* 2006, Honrubia *et al* 2009, Naumova *et al* 2009), ultra-fast probing of objects and plasmas with sensitivity to electric and magnetic fields and density, including their fast dynamics (Borghesi *et al* 2002a, 2002b, 2003, 2005, Roth *et al* 2002, Mackinnon *et al* 2003b, 2004, Romagnani *et al* 2005, 2008, Nilson *et al* 2006, Kar *et al* 2007, Nishiuchi *et al* 2007, Cecchetti *et al* 2009, Ravasio *et al* 2010), material science including extreme conditions and WDM (Patel *et al* 2003, Dyer *et al* 2008, Mančić *et al* 2010, Pelka *et al* 2010, McKenna *et al* 2011), solid-state physics, planetary and stellar astrophysics (Mančić *et al* 2010, Pelka *et al* 2010), etc.

4.4. Applications which require repetitive, high average power proton/ion beams

At present, the repetition rate of an ultra-high-intensity laser is usually 10 Hz or less. Diode-pumped solid-state laser technology can potentially increase the repetition rate. If one needs an average current comparable to the present RF-wave based accelerators, a repetition rate of a few kHz is necessary. For example, 10^{10} protons/pulse at 1 kHz repetition rate give us an average current of $\sim 1 \mu\text{A}$ which is comparable to the synchrotron; the latter, however delivers a highly monochromatic beam.

An important aspect of a repetitive source is its stability. Pirozhkov *et al* (2009b, 2010) demonstrated contrast dependence of stability of the laser-driven proton source operated at 1 Hz employing a tape target system, figure 51. A laser pulse with higher contrast ratio achieved with a double CPA laser system with a saturable absorber after the first CPA (Kiriyama *et al* 2009) provides not only higher maximum energy, but also more stable operation of the proton source. Although the stability at the moment is not enough for many applications, especially the industrial and medical ones, the presently available stability is sufficient for performing several proof-of-principle experiments, such as the demonstration of DNA double-strand breaks in human cancer cells employing laser-driven proton beam (Yogo *et al* 2009) and proton beam focusing, monochromatization and transport (Nishiuchi *et al* 2009, 2010), see section 4.8.

4.4.1. Laser-driven ion implantation.

In the moderate proton energy range of around or even less than 1 MeV, we

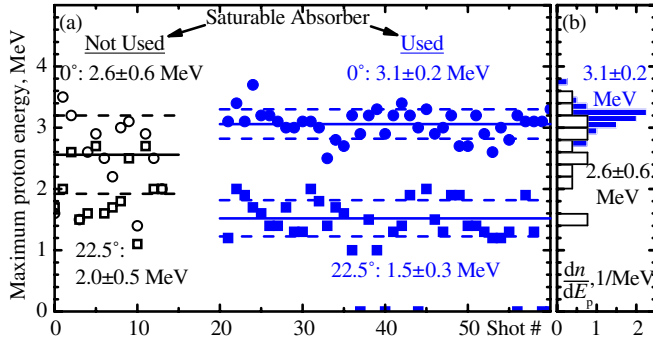


Figure 51. Repetitive proton acceleration using a $7.5\text{ }\mu\text{m}$ thick polyimide tape target (Pirozhkov *et al* 2009b, 2010). Consecutive shots are shown: 13 shots without and 40 shots with the saturable absorber. The laser pulse energies and durations are $0.9\text{ J}/28\text{ fs}$ and $0.7\text{ J}/35\text{ fs}$, respectively. (a) Maximum proton energy versus shot number; solid symbols, with the saturable absorber (higher contrast); open symbols, without saturable absorber (lower contrast); circles, along the target normal direction (0°); squares, at 22.5° off the normal (this measures the tail of the large-divergence low-energy proton beam component). Horizontal solid and dashed lines represent the average and average \pm standard deviation values, respectively. (b) The corresponding histograms of maximum proton energy distributions for the target normal direction. In both frames, the numbers after the ‘ \pm ’ signs are the standard deviations.

find a number of potential applications of the repetitive ion source, including, e.g., laser-driven ion implantation (Boody *et al* 1996). Torrisi *et al* (2003), Lorusso *et al* (2005) and Rosinski *et al* (2005) performed feasibility studies of ion implantation using a large-scale ASTERIX iodine laser facility. They pointed out that the laser-driven source has several advantages, namely (i) it delivers higher charge state leading to a greater depth of implantation, (ii) it provides almost any kind of ion species and (iii) it is easy to bias the ion source to positive high voltage, which is important for moving substrates. The most important issue is that the proton or ion source should satisfy the requirement of ion yield within a specific time. Depending on the implantation purpose, the required ion fluence ranges from 10^{13} to $10^{17}\text{ ions cm}^{-2}$ (Torrisi *et al* 2003). If we assume the laser energy of 0.1 J , 1 kHz repetition rate, the conversion efficiency of laser energy into protons of 10% and a desired average energy of 0.5 MeV , the proton yield per second is $\sim 10^{14}$. In this case, 10^3 s (17 min) of laser operation is necessary for achieving the ion fluence of 10^{17} cm^{-2} if one can focus all ions into an area of 1 cm^2 . Another, but connected requirement, is the available average ion current. The maximum current from a conventional machine is $\sim 0.1\text{ mA}$ (Boody *et al* 1996). On the other hand, the laser-based machine in the above example provides an average current of 0.02 mA . If the process needs high peak intensity and/or simultaneous illumination with x-rays or some other radiation kinds, the laser-driven source has a significant and unique advantage. Implantation is one of the interesting candidates for industrial applications, but the presently available ion yield should be increased.

4.4.2. Micro- and nanostructure ionography.

In a stopping radiography mode, the best contrast and spatial resolution of

images can be achieved if the stopping range of the probing particles slightly exceeds the sample thickness (Faenov *et al* 2009a, 2009b). For relatively thick (mm and sub-mm) objects, multi-MeV proton energies are required (e.g. Roth *et al* (2002), $\sim\text{mm}$ scale object radiography in a single shot). For micro- and nanostructure imaging, protons or ions with an energy of $<1\text{ MeV/nucleon}$ are required. In addition, the beam quality should be sufficiently high and the particle number large. In the relatively low particle energy region, the laser-driven sources have a significant advantage, because they can produce ultra-short and intense beams free from space charge limitations, owing to automatic charge neutralization. Faenov *et al* (2009a, 2009b) demonstrated ion radiography with sub- μm spatial resolution and depth sensitivity better than 100 nm employing a laser-irradiated cluster gas target as an ion source. The experimental setup and sample images are shown in figures 52 and 53, respectively. Faenov *et al* (2009a, 2009b) pointed out that the isotropic and homogeneous ion distribution is most important for the imaging. From this point of view, a CO_2 cluster jet target provides good results. Between the two detectors used in the experiment, namely in the forward and transverse directions, the transverse detector CR-39(2) (figure 52) gives better homogeneity, leading to better quality radiographs. The distances between the ion source and CR-39s are between 14 and 16 cm. Compared with a solid target, the cluster target delivers relatively easily the specific heavy ion species without energetic protons. On the other hand, a useful particle number obtained during a single laser shot whose energy and pulse width are 100 mJ and 40 fs , respectively, is 10^8 in $4\pi\text{ sr}$, which is relatively small compared with that from a laser-driven thin foil target. In this application the source repetition rate should be as high as possible, and from this point of view a self-replenishable gas jet target has an advantage.

4.4.3. Nuclear reactions and high-energy physics by laser-driven proton beams.

If the maximum energy of the proton beam is larger than several MeV, one can use it for driving nuclear reactions (Ledingham *et al* 2004, Clarke *et al* 2006a, 2006b) and their applications to the production of useful isotopes, for example, short lived radioisotopes for PET (Ollinger and Fessler 1997). The most important issue is the yield (per unit time) of protons with energy larger than the threshold of a specific nuclear reaction. For example, one of the commonly used radiopharmaceuticals, the ^{18}F fluoro-deoxy-glucose ($^{18}\text{FFDG}$), contains ^{18}F , which is the positron emission isotope whose lifetime is about 110 min. A reaction which can be used for this isotope production is $^{18}\text{O}(\text{p},\text{n})^{18}\text{F}$; the reaction threshold is $\sim 2.4\text{ MeV}$ and the cross-section peak is 500 mb at 5 MeV. Another useful isotope is ^{11}C with the lifetime of about 20 min and possible reaction of $^{11}\text{B}(\text{p},\text{n})^{11}\text{C}$ with the threshold of about 2.8 MeV and peak cross-section of 430 mb at 6 MeV. The values of reaction cross-sections can be found in Takács *et al* (2003) (recommended values for the reactions used for PET isotope production) and Experimental Nuclear Reaction Database EXFOR (<http://www-nds.iaea.org/exfor/exfor.htm>). For real PET applications, one should achieve a total activity of $\sim 0.2\text{--}1\text{ GBq}$ within the isotope lifetime. Spencer *et al* (2001) performed experiments on isotope production using a glass

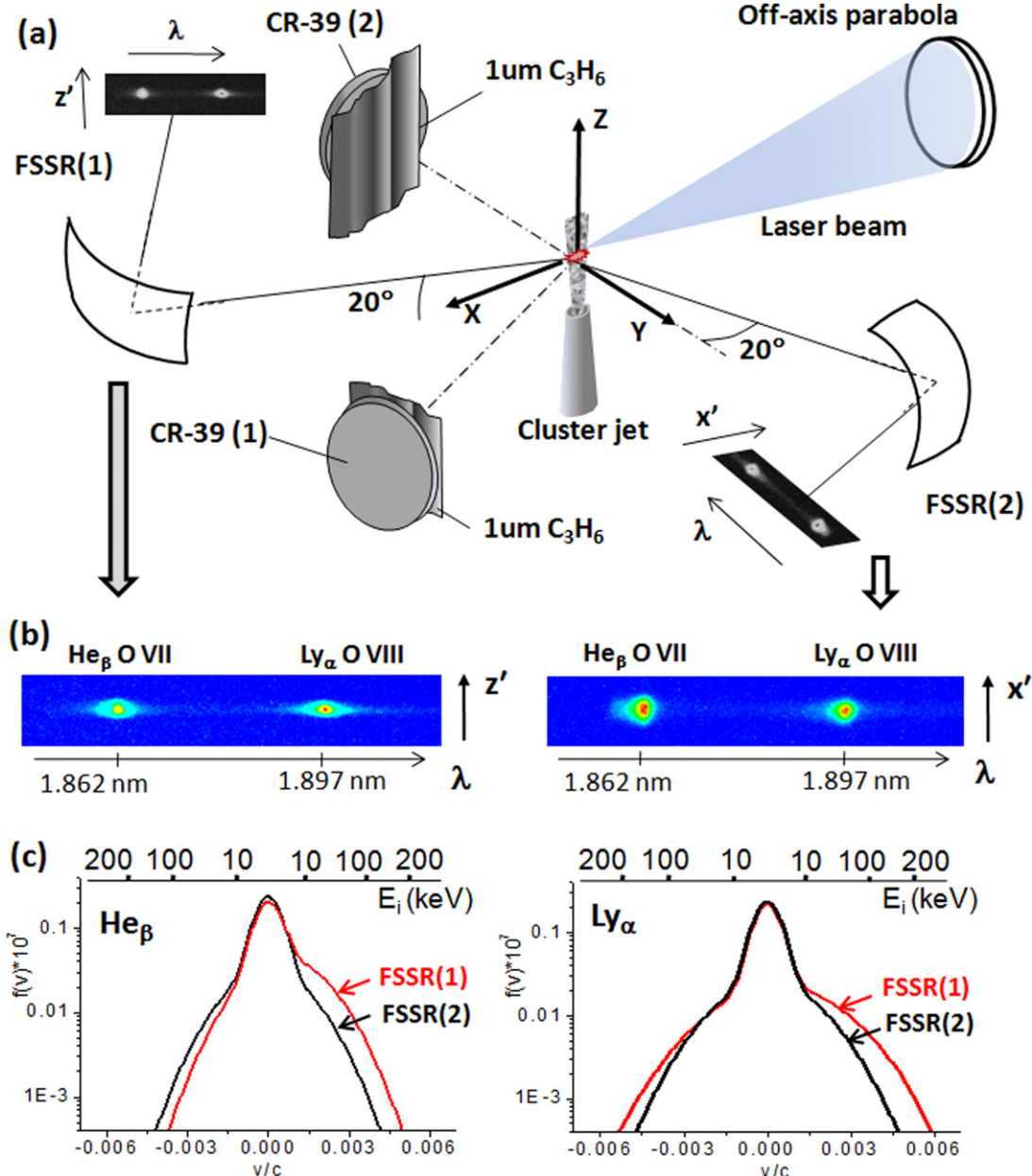


Figure 52. (a) Schematic view of the experimental setup of ion radiography (ionography) of micro- and nanoscale objects (Faenov *et al* 2009a, 2009b). The cluster jet target is irradiated with a femtosecond laser. The resulting plasma parameters are characterized with the bent crystal x-ray spectrometers FSSR(1) and FSSR(2). Two CR-39 ion track detectors record the contact images of the nanometre-thick samples using ions from the cluster target. (b) Raw data of the x-ray spectrometers indicated in the figure. (c) Oxygen ion velocity distribution functions obtained from the shape of He- β and Ly- α lines (Magunov *et al* 2003); the forward spectrograph FSSR(1) records faster ions than the side spectrograph FSSR(2). (Courtesy of Prof. Anatoly Faenov).

laser which delivered 1 ps, 100 J pulses. Based on the results, they arrived to the conclusion that a 1 ps, 100 J, 10 Hz laser is necessary to provide the required activity; another possibility includes a shorter pulse, smaller energy, high repetition rate laser. Fritzler *et al* (2003) proposed using a laser system delivering 30 fs, 1 J energy pulses focused to 10^{20} W cm^{-2} with a repetition rate of 1 kHz. Implementation of both laser kinds up to now represents significant challenges. For comparison, at present a few-metre-diameter cyclotron in a hospital can deliver a proton current of a few hundred μA with 10–30 MeV beam energy, which can make the desired radioactive fluorine atoms for PET (Milton 1995). Thus, further development of

high-intensity lasers is necessary to reduce construction and operation costs.

Another possible application of laser-driven proton beams is thin layer activation (TLA) (Racolta *et al* 1995, Ogura *et al* 2009). TLA allows measuring the wear or corrosion of machine parts or tools; for example, cutting tools made of various metals, boron nitride (BN) or even artificial polycrystalline diamond (DIA) taking advantage of a small admixture of Fe (Conlon 1985, Vasváry *et al* 1994). In TLA, the surface of the tool is activated; the activation depth is controlled by selecting the appropriate energy range of the proton beam. The surface activity after or even during

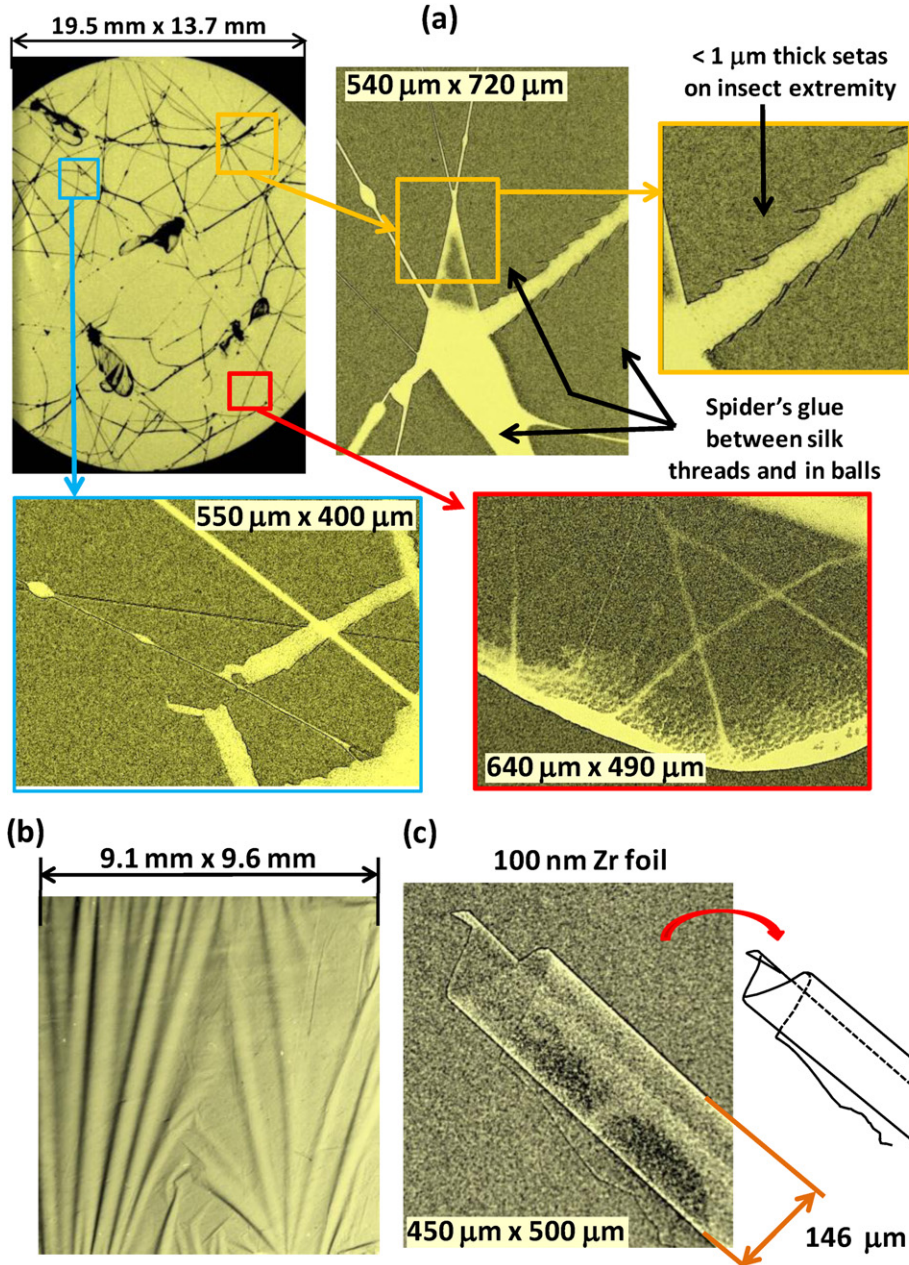


Figure 53. Examples of contact ion images produced by carbon and oxygen ions employing the setup shown in figure 52 (Faenov *et al* 2009a, 2009b). (a) Images of biological objects, namely a spider's web and insects fixed on it. Organic threads and hairs having a typical scale of $<1\text{ }\mu\text{m}$ are resolved; the spatial resolution is determined by the pit size on the detector (CR-39). The total number of laser shots is of the order of 1000. Contact ion images of (b) waving 1 μm thick polypropylene foil and (c) folding 100 nm thick Zr foil demonstrating the high sensitivity of the technique to thickness variations. (Courtesy of Prof. Anatoly Faenov).

use (*i.e. in situ*) provides information of how much surface material is lost; the sensitivity of the technique is quite high. Various materials can be activated, such as Fe, Ti and Cr, which opens wide possibilities for industrial diagnostics. Typical reaction thresholds are in the range of several to 10 MeV, which means that a compact laser system can be used. Ogura *et al* (2009) demonstrated activation of a BN sample employing a repetitive proton beam produced by a 1 J, 30 fs laser irradiating polyimide tape target, figure 54; the $^{11}\text{B}(\text{p},\text{n})^{11}\text{C}$ reaction was employed with a threshold of 2.76 MeV. The sample activity (11.1 ± 0.4 Bq after 60 shots) was estimated detecting radiation of annihilating positrons emitted by the ^{11}C isotope.

The authors also estimated activities which can potentially be achieved with 10 min irradiation employing a 10 Hz, 1.7 J, 34 fs laser focused up to the intensity of 10^{20} W cm^{-2} , assuming 1% conversion efficiency to proton beam. For the reactions $^{48}\text{Ti}(\text{p},\text{n})^{48}\text{V}$, $^{52}\text{Cr}(\text{p},\text{n})^{52}\text{Mn}$ and $^{56}\text{Fe}(\text{p},\text{n})^{56}\text{Co}$ with reaction thresholds of 4.79 MeV, 5.49 MeV and 5.60 MeV and half-decay times of 16 days, 5.6 days and 79 days, respectively, the predicted activities are 35 kBq, 28 kBq and 1.4 kBq, which are sufficiently high for typical TLA applications; due to long decay times, longer irradiation can be used, if necessary.

McKenna *et al* (2005) demonstrated the usefulness of a broad-energy-band proton beam for spallation-related physics,

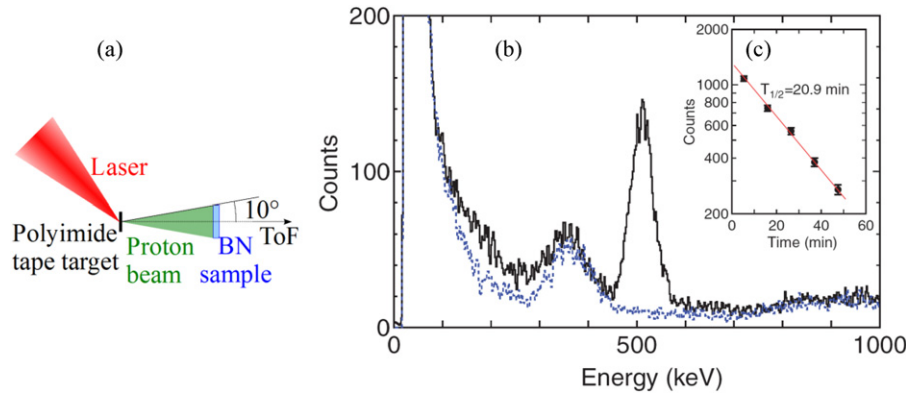


Figure 54. Example of TLA by a laser-driven proton source. (a) Schematic of the experimental setup; laser irradiates a tape target producing a repetitive proton beam which irradiates the BN sample; when the sample is removed, the time-of-flight spectrometer (TOF) is used to measure the proton beam spectrum. (b) Solid line, radiation spectrum measured using GSO ($\text{Gd}_2\text{SiO}_5(\text{Ce})$) scintillation counter; blue dotted line, the background. (c) Decay curve with the fitted half-life time of $T_{1/2} = 20.9 \pm 0.7 \text{ min}$, which agrees well with the decay time of ^{11}C ($T_{1/2} = 20.39 \pm 0.02 \text{ min}$). (b) and (c) are reprinted with permission from Ogura *et al* (2009).

because in high-energy proton (energy of 1 GeV) collisions with thick, high atomic number materials (typically lead), it is the high yield of lower energy (tens of MeV) secondary protons and neutrons produced in the intranuclear cascade and through evaporation which is responsible for the production of residual nuclides through secondary reactions. The laser-driven proton source can deliver a similar beam as that from the 1 GeV proton interaction with a high atomic number material. Thus, without a 1 GeV proton beam, one can study the secondary reactions and, e.g., judge the validity of a nuclear Monte Carlo simulation code. Such a study contributes to the nuclear data programme for high-energy proton beam driven systems, such as the HINDAS (High and Intermediate energy Nuclear Data for Accelerator-driven Systems) project (Koning *et al* 2002). In this case, a proton source is required which can deliver a tens of MeV (up to 50 MeV) proton beam with a broad energy spectrum. The required repetition rate is not very high because the half-lives of the residual nuclei listed in the paper by McKenna *et al* (2005) are more than one hour.

When sufficiently high-energy (hundreds of MeV or GeV) laser-driven proton beams are generated, they can be used for the production of other secondary particles. In particular, pions can be generated (Bychenkov *et al* 2001a) at the proton beam dump, with a proton energy threshold of ~ 140 MeV and the cross-section increasing for higher proton energies. The decay of pions produced by a $\sim 1\text{--}2$ GeV proton beam will result in a short burst of neutrinos, which can be used for studying the neutrino physics (Bulanov S V *et al* 2005b).

4.5. High-energy electron beam transport characterization

In the TNSA (section 2.2.1) and SCSF (section 2.2.2) regimes the proton beams are produced by the hot electrons propagating through the target. Thus, details of electron beam transport through various materials or interfaces can be determined from the proton beam properties. In particular, Fuchs *et al* (2003) demonstrated that the electron beams passed through light-atom, insulating targets (CH) or conductor/insulator interface (Au/CH) are disrupted, resulting in characteristic proton beam profiles with caustics. On the other hand, for electron beams

passing through heavier atoms, conducting targets (Au) are relatively uniform, which results in smooth proton beam footprints; further, in this case the laser focal spot features, recorded by the electrons, are transferred to the proton beam. Strong influence of the electron beam filamentation on the proton beam emittance is discussed in Kemp *et al* (2007). Yuan *et al* (2010) used the dependence of maximum proton energy on target thickness (up to 1.4 mm) to estimate the effect of self-generated magnetic field on the electron transport. McKenna *et al* (2011) demonstrated that the technique is sensitive to the lattice structure of materials: the proton beam remains smooth in the case of diamond targets, but becomes increasingly distorted as the ordering of the carbon allotropes decreases from diamond to pyrolytic carbon and finally to vitreous carbon, indicating that the electron beam propagation through the diamond target is smooth, while it is heavily filamented after the propagation through vitreous carbon. The results are explained by the increased metallic-like conductivity of the diamond targets rapidly heated to the transient WDM state by the highly collisional return current of cold electrons; the conductivity of the warm dense diamond is larger due to the longer mean-free path of cold electrons diffracting coherently on the ordered lattice rather than scattering randomly.

Thus, the laser-driven proton beam properties can reveal electron propagation dynamics important for fusion studies, WDM research and in general for any applications of high-power lasers which involve large currents of energetic electrons.

4.6. Space-related applications

Apart from applications in extreme state of matter research relevant to astrophysics, section 4.3.3, high-power lasers can potentially contribute to space exploration programmes, namely to Earth-based study of cosmic radiation damage to live organisms (in particular, humans) and spacecraft components (in particular, solar cells). Although several radiation kinds can be modelled using lasers, here we primarily consider energetic protons and ions.

Protons and high-charge, high-energy ions represent a significant threat for living organisms, as the energetic portion of their spectra can hardly be stopped by shields of reasonable thickness. Cancer caused by exposure to this radiation is one of the major concerns for manned missions to Mars and outer planets. However, a large uncertainty in estimating cancer risks does not allow conscious mission planning and development of countermeasures, therefore Earth-based radiobiological experiments must be performed (for more information on this topic, see Durante and Cucinotta (2008)). In contrast to conventional accelerators, laser-driven sources can better simulate space conditions via simultaneous irradiation with broad ion spectra as well as other radiation kinds (electrons, gamma rays), which is an advantage in animal tests, where multiple consecutive irradiations are inconvenient and can potentially change the results. Radiobiological experiments with laser-based proton sources have already been started (Yogo *et al* 2009, 2011, Kraft *et al* 2010), but for perfect modelling of interplanetary missions the ion energy should be increased up to ~ 1 GeV/nucleon, which up to now represents a significant challenge, sections 2.11 and 3. An additional benefit from such radiobiological experiments can be understanding the risk of secondary cancer in ion beam cancer therapy, section 4.7.

Another important problem is radiation-induced solar cell damage. In this case, low-energy (sub-MeV) protons cause notable degradation of single-crystal Si or GaAs cells (Anspaugh 1996) as well as multi-junction cells (Sumita *et al* 2003) at fluences of $\sim 10^{10}$ – 10^{12} cm $^{-2}$. At the moment, mono-energetic proton beams from conventional accelerators are used to investigate the damage resistance of cells using the displacement damage dose method, which allows calculating the dependence of solar cell damage on the particle energy and fluence using mono-energetic data only (Summers *et al* 1995). A broadband sub-MeV proton beam with accumulated fluence necessary for radiation damage research can be readily obtained with a relatively small, repetitive laser. In addition, the laser plasma existing during proton acceleration also produces x-rays and electrons in the MeV region, leading to simultaneous bombardment of solar cells by these beams, which is typical for space conditions. For obtaining quantitative data on the cell radiation damage, a precise characterization of the laser-driven radiation and particle beams is the key issue.

4.7. Research activities towards laser-driven proton and ion medical accelerators

In this sub-section, we mainly describe the development of medical laser-driven accelerators, although much of the discussion is relevant to other- or general-purpose laser-driven accelerators.

From the engineering point of view, the conventional, RF-wave based accelerators, including linear, cyclotron- and synchrotron-type ones, have been thoroughly optimized. Two revolutionary principles contributed to a dramatic increase in acceleration energy, namely the principle of strong focus and that of phase stability for a synchrotron accelerator, resulting

in an acceleration of 50 GeV proton beams (Sawada 2010) which is 100–1000 times higher energy than that of a cyclotron. The typical acceleration gradient is 1 MeV m $^{-1}$ (Humphries 1990), and typical diameters are a few tens of metres for an ion energy of 100 MeV/nucleon. The space and cost are rather big for practical applications, especially for medical ones (Goitein *et al* 2002). Based on the present situation, one research direction is the implementation of a compact laser-driven proton/ion accelerator.

Although tremendous fundamental research and development on laser-driven proton and heavy ion sources have been performed, still a lot of long-term effort is required for the implementation of laser-driven medical accelerators proposed by several groups, in particular, for cancer treatment (Bulanov S V and Khoroshkov 2002a, Bulanov S V *et al* 2002b, 2004b, Fourkal *et al* 2002, 2003a, 2003b, Malka V *et al* 2004, Murakami M *et al* 2008, Bolton *et al* 2010). Lintz and Alonso (2007) pointed out the difficulties of the present laser-driven sources compared with the well-developed conventional accelerators. The subjects to be developed are as follows. Firstly, we can point out the development of a compact, low-cost, energy efficient, stable, ultra-high-intensity and ultra-short pulse laser with a repetition rate of $\gg 10$ Hz. For this purpose, solid-state laser technology is one of the promising candidates. Secondly, the design and construction of the laser transport line is an issue which includes not only a flexible laser beam pointing but also, e.g., the technique of a deformable mirror to keep the quality of the laser wavefront. The significant feature of the laser-driven ion source is that the laser itself and the laser beam line do not become radioactive; this dramatically reduces the shielded volume and amount of radioactive materials to be utilized later. Thirdly, the acceleration mechanism should be chosen and the conditions optimized in order to obtain the ion beam spectrum and divergence which match well the desired application requirements, otherwise the rejected unwanted parts of the spectrum and/or angular distribution can cause significant activation when it is stopped by shields; we also mention that production of other high-energy particles, in particular, electrons and hard x-rays, should be minimized (interestingly, thinner targets, which are advantageous from the point of view of ion acceleration, also produce a smaller amount of secondary particles and radiation). Ideally, a monochromatic or spectrally tailored low-divergence ion/proton beam produced in the laser-driven plasma itself is desired, section 2.11. Fourthly, we point out the development of a high repetition rated target supply system matched to the repetition rate of the driving laser and suitable for the chosen acceleration mechanism. For example, a tape target system (Nayuki *et al* 2003) can be used, figure 55. A mass-limited target (MLT) can be injected into the irradiation area as a pellet, similarly to, e.g., water droplet targets (Hemberg *et al* 2000). Another candidate is a gas or a cluster target (Willingale *et al* 2006, Fukuda *et al* 2009). A robotic technique may also contribute to the repetitive operation (Notley *et al* 2009). The fifth issue includes the development of a proton or ion beam guiding system. Note that this system should compensate for the possible excessive beam divergence and spectral bandwidth. If the beam divergence angle and/or its spectral bandwidth are

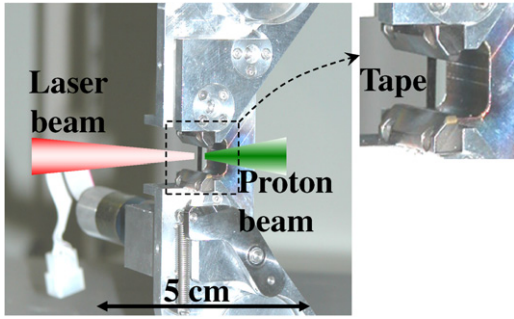


Figure 55. Photo of the tape target system for a repetitive laser-driven proton source; tapes of various materials with thickness down to a few μm can be used.

too large, the complexity and size of the beam guiding system can exceed the ones of a conventional accelerator, and the inherent advantage of compactness of laser-driven accelerator can be lost. That is why a high-quality beam originating from the plasma is of crucial importance (Bulanov S V and Khoroshkov 2002a). For beam guiding, one can employ not only conventional (magnetic-based) beam lines, but also innovative compact plasma-based techniques (Toncian *et al* 2006, 2011, Willi *et al* 2007, Kar *et al* 2008b), section 4.8. The sixth subject includes the development of various online real-time monitors of ion beam, laser and plasma parameters for the feedback control of the whole system. Finally, we note that the energies required for cancer therapy ($>200\text{ MeV}$ for protons, $\sim 400\text{ MeV/nucleon}$ for carbon ions, section 2.11) have not yet been demonstrated, although the developed theoretical models predict several possible ways, section 2.

For medical applications, we also point out an ultra-high average current, relatively low particle energy proton machine for neutron generation via nuclear reaction. The required current is a few tens to a few hundreds of mA and the proton energy is a few to several tens of MeV, depending on the nuclear reaction employed (e.g. Yonai *et al* 2004, Forton *et al* 2009). Such a high-current machine can deliver the epi-thermal or thermal neutrons whose intensity is $10^9\text{ neutrons cm}^{-2}\text{ s}^{-1}$ for boron neutron capture therapy of cancer (BNCT) (Barth *et al* 2005). For this purpose, the properties of laser-driven sources such as divergence, wide spectral bandwidth and relatively low particle energy do not cause a serious problem. However, if a current of 0.1 A is required, $10^{18}\text{ protons s}^{-1}$ with an energy of 3 MeV should be produced. If we assume 1 kHz repetition rate, a proton number of $10^{15}/\text{shot}$ is necessary. In this case, the proton beam power is $\sim 500\text{ kW}$ and that of required average laser power is $>5\text{ MW}$, which is rather ambitious at this moment. On the other hand, one can use a laser-driven neutron source generated without a proton beam, via nuclear fusion reaction such as D-T (deuterium–tritium) or D-D (deuterium–deuterium). Ditmire *et al* (1999) demonstrated a neutron yield of 10^5 per one Joule of laser energy via the $\text{D} + \text{D} \rightarrow \text{He}^3 + \text{n}$ reaction, in which a 2.45 MeV neutron is released. They used a table-top laser with 120 mJ, 35 fs pulses irradiating a cooled deuterium cluster target. On the other hand, Daido *et al* (1987) demonstrated a D-D neutron yield of 10^8 without laser-driven compression using a CD_2 solid target produced by a 7 kJ energy glass laser. The yield per unit laser energy is similar. Anyway

obtaining a neutron yield of the order of 10^9 s^{-1} by a table-top laser is rather ambitious at this moment.

A possible contribution to medical accelerator technology is the development of an injector into the RF-wave based post-accelerators (Krushelnick *et al* 2000a, Antici *et al* 2008b). The idea of an ion cancer therapy machine employing laser-driven ion injectors was suggested by Noda *et al* (2006). The machine consists of a laser-driven ion source, phase rotation device (see section 4.8.1) for monochromatization of the laser-driven beam, beam cooling by an electron cooling ring and finally a compact high gradient 200 MeV/nucleon synchrotron, which can be potentially implemented (Fang *et al* 2005). On the other hand, Okamura *et al* (2006) have demonstrated a high-current (60 mA), relatively low-energy (up to 1 MeV) carbon beam using the direct plasma injection scheme employing a nanosecond YAG/ CO_2 laser-driven plasma coupled with a specially designed radio frequency quadrupole (RFQ). The ions are transported through the neutralizing plasma to the post-accelerator. Thus, the space-charge effect, which is the major loss mechanism in high-charge low-energy beam transport lines, is minimized.

4.8. Demonstration of beam monochromatization and transport systems

For many applications, a proton or ion beam should be quasi-monochromatized with a desired bandwidth. We have described quasi-monoenergetic proton and ion beam acceleration techniques employing specially configured targets irradiated with high-quality laser pulses in sections 2.3, 2.6 and 3.6. Here we describe two monochromatization techniques applicable when proton or ion beam with a wider spectral bandwidth than the necessary value is generated, namely the phase rotation technique (Noda *et al* 2006, Nakamura S *et al* 2007, Wakita *et al* 2009, Ikegami *et al* 2009) and the plasma-based technique (Toncian *et al* 2006, 2011, Willi *et al* 2007, Kar *et al* 2008b).

4.8.1. Monochromatization using the phase rotation technique. Figure 56 shows the working principle of the phase rotation technique for monochromatization of a laser-driven proton beam. At the source, the proton pulse duration is of the order of a ps, which is much shorter than the flight time of the protons from the source to the RF cavity. The beam duration is expanded due to the velocity spread. If the phase of the RF field is properly tuned, the faster protons arriving earlier to the RF cavity are decelerated while the slower protons arriving later are accelerated, giving a significantly narrower proton energy spectral band, as shown in the inset of figure 56. The proof-of-principle experiment was performed by Nakamura S *et al* (2007). Note that the synchronization between the laser pulse and phase of the RF field is very important; in this experiment, an accuracy of the synchronization between the laser pulse and the RF field of $<30\text{ ps}$ (1 degree of RF phase) has been achieved, which is sufficient for the technical demonstration. An example of controllable monochromatization of the laser-driven proton beam can be found in Wakita *et al* (2009), where the protons

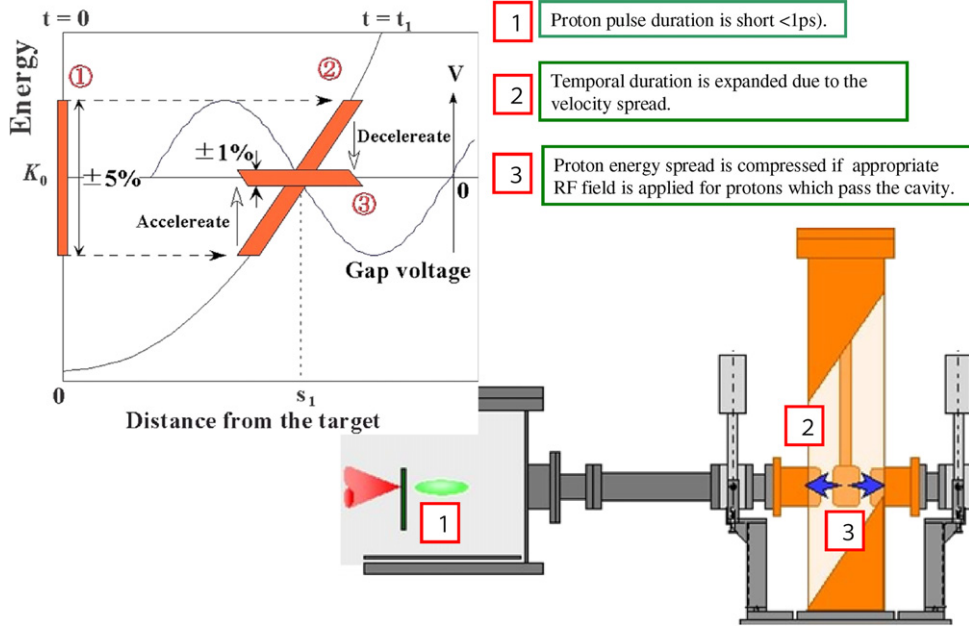


Figure 56. Schematic diagram and working principle of the phase rotation cavity for monochromatization of a laser-driven proton beam (Nakamura S *et al* 2007). The total distance between the target and the detector is 1.7 m.

from 10% energy bandwidth have been concentrated to 1.6% bandwidth around 1.4 MeV. Transverse beam dynamic effects, such as radial focusing and defocusing, have also been demonstrated in experiments (Ikegami *et al* 2009, Wakita *et al* 2009). The phase rotation technique can be applied to a high repetition rated operation. Further, it is potentially applicable to much higher particle energies, e.g. a several metre long RF cavity can be used for quasi-monochromatization of a proton beam with central energy \sim 200 MeV and originally a few tens of MeV energy spread to a much narrower bandwidth of a few MeV.

4.8.2. Focusing and monochromatization using a laser-driven microlens. Toncian *et al* (2006) demonstrated an elegant idea of laser-driven proton beam focusing with a laser-driven plasma microlens, figure 57. The CPA₁ pulse ($I = 5 \times 10^{19} \text{ W cm}^{-2}$) is used to accelerate an originally diverging proton beam. The CPA₂ pulse ($I = 3 \times 10^{18} \text{ W cm}^{-2}$), which is focused onto the hollow cylinder wall, injects hot electrons into the cylinder. These electrons spread evenly along the inner surface of the cylinder (the physics of the lateral electron transport along the target surface was studied by McKenna *et al* (2007a)). In the early stage (frame (b)), the electrons, confined over a Debye length, generate a charge-separation electric field, which then drives plasma expansion towards the cylinder's centre; the field is largest along the ion front position, analogous to the field which accelerates ions from the target rear side in the plasma expansion models, section 2.1 (frame (c)). This field is radial, and it focuses the proton beam as it passes through the cylinder. The focusing field is time-dependent; employing the TOF difference, a particular energy component of the proton beam can be focused most, such that a properly positioned aperture can be used to partly monochromatize the focused beam. A detailed experimental

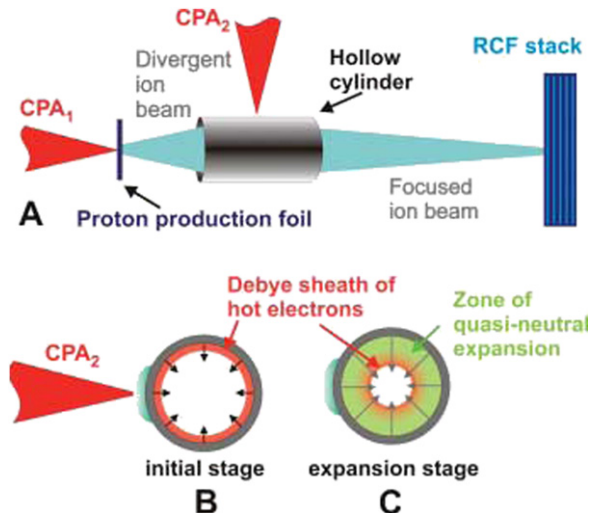


Figure 57. (a) Schematic view of the plasma microlens for ion beam focusing. The CPA₁ laser pulse generates an originally diverging proton beam, which propagates through a hollow cylinder irradiated by the CPA₂ laser pulse from a side. (b) and (c) show cross-sections of the cylinder with the radial electric field indicated by arrows at initial and plasma expansion stages. Reprinted with permission from Toncian *et al* (2006).

and computational study of the plasma microlens properties can be found in Toncian *et al* (2011).

The plasma microlens can be incorporated into the target ('lens target'), in which case it is charged with the main laser pulse itself (Kar *et al* 2008b); thus, only one laser pulse is sufficient. Further, by choosing an appropriate target material and geometry, it is possible to tune the lens discharge time in such a way that its chromatic aberration, i.e. dependence of focusing power on the proton/ion energy, is substantially reduced.

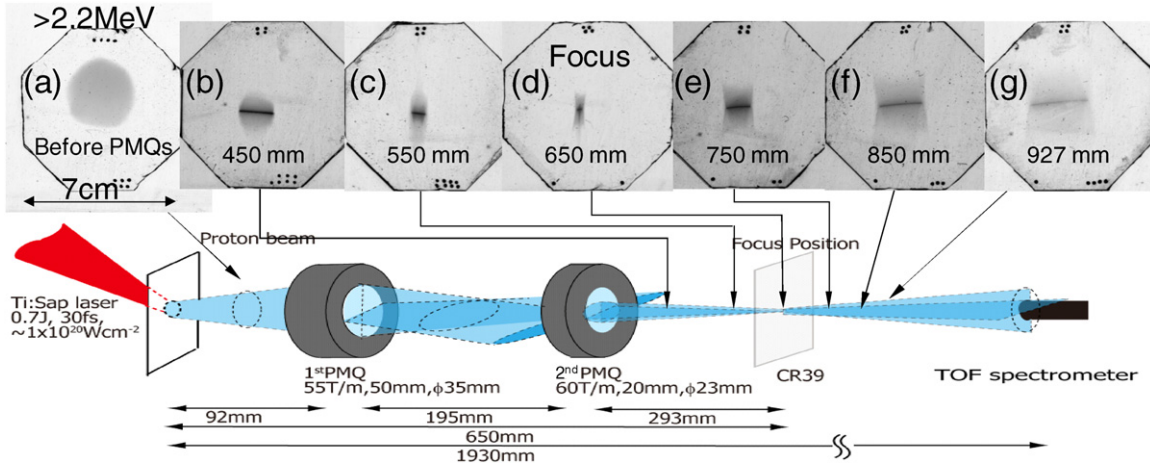


Figure 58. Repetitive (1 Hz) laser-driven proton beam focusing and monochromatization employing two PMQs (Nishiuchi *et al* 2009). The reproducible quasi-monoenergetic proton spectra after the PMQs with an energy of 2.4 ± 0.1 MeV evidence the high stability of the acceleration and transport system. The first PMQ has an acceptance half-angle of $\sim 10^\circ$, which is similar to the whole proton beam divergence; however, the beam is partly clipped by the second PMQ, giving an overall transmission of $\sim 30\%$. The octagonal frames show the proton beam profiles recorded with the CR-39 nuclear track detectors, the darker regions correspond to the higher proton density. (a) The original beam profile before the PMQs (Al $40 \mu\text{m}$ filter, 1.9–2.8 MeV protons). (b)–(g) Proton beam profiles (2.2–3.1 MeV) at indicated distances from the target. At the best focus (d), the visible beam size is $\sim 3 \text{ mm} \times 8 \text{ mm}$; however, these dimensions are overestimated due to CR-39 saturation at the image centre.

4.8.3. Ion beam control with permanent magnets and solenoids. Several groups have demonstrated controlled propagation of a laser-driven proton beam employing permanent magnets (Schollmeier *et al* 2008, Ter-Avetisyan *et al* 2008b, Nishiuchi *et al* 2009, 2010). For example, Nishiuchi *et al* (2009) have conducted a proton focusing experiment using a laser-driven proton source operated at 1 Hz repetition rate, figure 58. The laser-produced diverging proton beam is focused with a pair of permanent magnet quadrupoles (PMQ). From the spectral information obtained with the absolutely calibrated TOF spectrometer and the angular distribution obtained with the CR-39, the number of protons generated at the target within the energy interval of 2.4 ± 0.1 MeV is 1.3×10^7 /shot. The calculated transmittance of this proton beam through the PMQ pair is 30%. Most of the proton beam loss is attributed to the mismatch between the collected proton beam shape and that of the second PMQ. On the other hand, Roth *et al* (2009) and Harres *et al* (2010) demonstrated the collimation of a 2.5 MeV laser-driven proton beam with a solenoid magnet (7 cm long, 4 cm diameter, 8 T). The most significant advantage of solenoid magnet compared with a pair of quadrupole magnets is the collection efficiency of almost 100%. However, Harres *et al* (2010) pointed out that the electrons co-moving with protons are focused inside the solenoid and this causes the space charge effect. Anyway, such magnetic collimation and focusing devices which will bring us fruitful applications should be developed further for laser-driven sources.

4.9. Section 4 summary

In this section, we have summarized the application aspects of the laser-driven proton and ion sources, including typical beam properties and their characterization techniques, as well as techniques which allow control of the beam spectrum and

divergence. There are many applications of laser-driven proton and ion sources, which have already been demonstrated, or are yet to be demonstrated. Some of these applications benefit from the original and unique properties of laser-driven beams such as divergence, wide spectral bandwidth, short pulse duration and small source size, while other applications require proton/ion beam modifications or further source development. At present, the most attractive applications of the laser-driven source are those which inherently need high intensity, short pulse and good beam laminarity (small emittance); in particular, we mention here the demonstrated proton imaging/radiography/deflectometry (Borghesi *et al* 2001, Mackinnon *et al* 2004). On the other hand, potential applications which require high average power still suffer from the present limitations of high-power laser technology. As described in the previous sections, higher energy proton and ion beams should be developed step by step. Such properties as spectral bandwidth, number of particles per shot, repetition rate, stability, emittance and angular distributions should be optimized for each particular application.

The achievements in the experiments described in this section and design studies coupled with proof-of-principle experiments open up the possibility of laser accelerators, including industrial as well as future cancer therapy machines (Bulanov S V and Khoroshkov 2002a, Bulanov S V *et al* 2002b, 2004b, Fourkal *et al* 2002, 2003a, 2003b, Malka V *et al* 2004, Murakami M *et al* 2008, Bolton *et al* 2010). Unfortunately the complicated magnetic devices for shaping and guiding the beam may reduce the advantages of laser-driven sources. New regimes of proton and ion acceleration (sections 2.3 and 2.6) as well as special target designs (sections 3.6 and 4.8) may open ways to manipulate the beam divergence and spectrum directly during the acceleration process itself, thus eliminating the need for external devices or significantly simplifying them.

We can identify the following application aspects as goals and directions for future research.

- (1) Achieving parameters necessary for cancer therapy, namely 250 MeV proton or \sim 400 MeV/nucleon light ion energies, 1% energy bandwidth or a highly controllable tailored spectrum and $\sim(1\text{--}5) \times 10^{10}$ particles/second; these should be achieved with a relatively compact laser, which may be cost-effective compared with conventional accelerators.
- (2) Achieving parameters necessary for ion-driven fast ignition (e.g. \sim 10 kJ proton or carbon ion beam in a suitable particle energy range) using a driver with 100 kJ laser pulse energy or less.
- (3) Significant improvement of average ion/proton beam power, which is required for many potential applications.
- (4) Increasing stability of high repetition rated laser-driven ion/proton accelerators.
- (5) Development of a high repetition rated target supply and alignment system even for originally single-shot targets such as mass-limited targets and flat-top cones.
- (6) Application of very successful proton probing techniques for many phenomena in laser-produced and other kinds of plasmas and matter, including warm dense matter (WDM).

5. Summary and future prospects

In this review we first gave a historical overview of early laser-driven ion acceleration research originating mainly from the laser fusion programme. We also briefly described the present status of relativistic optics, which studies related phenomena taking place in a relativistic laser-produced plasma. In section 2 we reviewed the theoretical aspects and simulations of laser-driven ion acceleration. We listed several acceleration mechanisms and discussed their properties, optimum conditions, scalings and future prospects. In section 3 we reviewed the experimental aspects, including the description of typical high-power laser facilities used for ion acceleration with an emphasis on the contrast requirements, diagnostic instruments for characterising ion/proton sources and several kinds of targets used in the experiments. We summarized the experimental results on laser-driven proton and ion acceleration achieved with larger, single-shot as well as smaller, repetitive laser systems. We provided figures and table with selected experimental data, from which one can see typical trends and dependences of the achievable maximum proton energy on the laser pulse energy, irradiance, as well as target parameters. In section 4 we reviewed the application aspects, including typical properties of presently available laser-driven ion beams as well as demonstrated and prospective applications. We emphasized the difference between those applications employing the ultra-short duration of laser-driven ion beams and those where an integrated particle flux is required. For the former, there are no alternative ion sources at present, only lasers can generate sufficiently short and intense ion bunches.

Let us now turn to future prospects. We believe that as research progresses, we will see an improvement in the achievable ion beam parameters, such as an increase in the ion

energy and conversion efficiency, decrease in the divergence, controllability of the spectrum including the possibility of quasi-monoenergetic beam generation and spectrum tailoring, etc. This progress will be based on both high-power laser development and better understanding and control of the acceleration process itself, despite the inherent complexity of laser–plasma interaction. We also expect that the gap, which still exists between the theoretical predictions and simulations on the one hand and experimental results on the other, will decrease. At the moment one of the most successful applications is the proton probing technique, which utilizes the unique properties of the laser-driven ion beam, namely ultra-short duration at the source, large particle number and high degree of laminarity (low transverse emittance). Another application which relies on the same or similar properties is ion (proton) pumping (e.g. fast heating of fusion plasma or material samples, WDM physics, etc), which also has great potential. These two applications employ ion beam properties which cannot be provided by other accelerator types. We believe probing and pumping with laser-driven ion beams will have a large impact on many areas of science and technology, including high-field science, all kinds of plasma sciences (not only laser-produced plasmas), fusion, etc. On the other hand, there are many other applications in which the ion beam duration is not essential and therefore conventional (RF-wave-based) accelerators are employed. Among these applications, there are several attractive industrial and medical ones. For such applications, the laser-driven accelerators can potentially be advantageous if they provide similar or better ion beam characteristics with smaller total installation size and operation cost. Therefore, it is necessary to develop and optimize compact, low-cost, stable and repetitive driver lasers, target fabrication and target driving techniques in conjunction with theoretical studies and realistic simulations. A real-time feedback-loop system which includes monitoring and control of laser, plasma and ion beam parameters will be one of the key components of novel laser-driven ion sources for industrial and medical applications.

Laser-driven ion acceleration is a quickly developing research field attractive both from the point of view of fundamental science and applications. At present a large number of research groups are working on this problem. A lot of results in experiments, applications, theory and simulations have been obtained, which contribute to the understanding of the relevant phenomena. As laser ion accelerators mature, we will see an increasing number of their applications. Some of them, like ultrafast proton probe and ultra-fast uniform matter heating, have already been successfully demonstrated, others, like the compact medical accelerator for cancer treatment and the accelerator for ion-driven fast ignition, are already anticipated, while some are probably not yet proposed. Thus, we are looking forward to seeing the transition from mostly basic research and proof-of-principle experiments to systematic study, optimization employing advanced acceleration regimes and elaborated target designs, and applications with high scientific, industrial and social impacts.

Acknowledgments

The authors thank Drs Paul Bolton, Marco Borghesi, Sergey Bulanov, Stepan Bulanov, Il Woo Choi, Timur Esirkepov, Anatoly Faenov, Julian Fuchs, Yoshiaki Kato, Jongmin Lee, David Neely, Koshichi Nemoto, Akira Noda, Yuji Oishi, Matteo Passoni, Marcus Roth, Theodor Schlegel, Toshiki Tajima, Motonobu Tampo, Mitsuru Uesaka and Alexei Zhidkov for valuable scientific discussions. They acknowledge support of the Photo Medical Valley Project and the Advanced Compact Accelerator Development Project supported by the Ministry of Education, Culture, Sports, Science and Technology (MEXT) of Japan. The authors also thank all the members of these projects for discussions. HD specially thanks Ms Ayako Iwata for her assistance in the preparation of this review.

References

- Ahlstrom H G 1981 Laser fusion experiments, facilities, and diagnostics at Lawrence Livermore National Laboratory *Appl. Opt.* **20** 1902–25
- Albright B J, Yin L, Bowers J, Hegelich B M, Flippo K A, Kwan T J and Fernandez J C 2007 Relativistic Buneman instability in the laser breakout afterburner *Phys. Plasmas* **14** 094502
- Amemiya Y and Miyahara J 1988 Imaging plate illuminates many fields *Nature* **336** 89–90
- Amitani H, Esirkepov T, Bulanov S, Nishihara K, Kuznetsov A and Kamenets F 2002 Accelerated dense ion filament formed by ultra intense laser in plasma slab *AIP Conf. Proc.* **611** 340–5
- Andreev A, Lévy A, Ceccotti T, Thaury C, Platonov K, Loch R A and Martin P 2008 Fast-ion energy-flux enhancement from ultrathin foils irradiated by intense and high-contrast short laser pulses *Phys. Rev. Lett.* **101** 155002
- Andreev A A, Steinke S, Sokollik T, Schnurer M, Ter-Avetisyan S, Platonov K Y and Nickles P V 2009 Optimal ion acceleration from ultrathin foils irradiated by a profiled laser pulse of relativistic intensity *Phys. Plasmas* **16** 013103
- Andriyash I A, Bychenkov V Y and Kovalev V F 2010 Laser acceleration of light ions from a thin homogeneous foil of complex atomic composition *Fiz. Plazmy* **36** 81–93
- Andriyash I A, Bychenkov V Y and Kovalev V F 2010 *Plasma Phys. Rep.* **36** 77–89
- Anspaugh B E 1996 *GaAs Solar Cell Radiation Handbook* (Pasadena, CA: Jet Propulsion Laboratory) pp 96–9
- Antici P et al 2007 Energetic protons generated by ultrahigh contrast laser pulses interacting with ultrathin targets *Phys. Plasmas* **14** 030701
- Antici P et al 2008a Hot and cold electron dynamics following high-intensity laser matter interaction *Phys. Rev. Lett.* **101** 105004
- Antici P, Fazi M, Lombardi A, Migliorati M, Palumbo L, Audebert P and Fuchs J 2008b Numerical study of a linear accelerator using laser-generated proton beams as a source *J. Appl. Phys.* **104** 124901
- Antici P, Fuchs J, d'Humières E, Robiche J, Brambrink E, Atzeni S, Schiavi A, Sentoku Y, Audebert P and Pepin H 2009 Laser acceleration of high-energy protons in variable density plasmas *New J. Phys.* **11** 023038
- Apollonov V V, Corkum P B, Taylor R S, Alcock A J and Baldis H A 1980 20-J nanosecond-pulse CO₂ laser system based on an injection-mode-locked oscillator *Opt. Lett.* **5** 333–5
- Bach D R et al 1983 Intensity-dependent absorption in 10.6-m laser-illuminated spheres *Phys. Rev. Lett.* **50** 2082–5
- Backus S, Kapteyn H C, Murnane M M, Gold D M, Nathel H and White W 1993 Prepulse suppression for high-energy ultrashort pulses using self-induced plasma shuttering from a fluid target *Opt. Lett.* **18** 134–6
- Baez A V 1952 A study in diffraction microscopy with special reference to x-rays *J. Opt. Soc. Am.* **42** 756
- Bahk S W, Rousseau P, Planchon T A, Chvykov V, Kalintchenko G, Maksimchuk A, Mourou G A and Yanovsky V 2004 Generation and characterization of the highest laser intensities (10^{22} W/cm²) *Opt. Lett.* **29** 2837–9
- Bahk S W, Rousseau P, Planchon T, Chvykov V, Kalintchenko G, Maksimchuk A, Mourou G and Yanovsky V 2005 Characterization of focal field formed by a large numerical aperture paraboloidal mirror and generation of ultra-high intensity (10^{22} W/cm²) *Appl. Phys. B* **80** 823–32
- Barth R F, Coderre J A, Craca M, Vicente H and Blue T E 2005 Boron neutron capture therapy of cancer: current status and future prospects *Clin. Cancer Res.* **11** 3987–4002
- Barnes D C, Kurki-Suonio T and Tajima T 1987 Laser self-trapping for the plasma fiber accelerator *IEEE Trans. Plasma Sci.* **15** 154–60
- Basov N G, Krokhin O N and Popov Y M 1961 Generation, amplification, and detection of infrared and optical radiation by quantum-mechanical systems *Phys.—Usp.* **3** 702–28
- Baumhacker H, Pretzler G, Witte K J, Hegelich M, Kaluza M, Karsch S, Kudryashov A, Samarkin V and Roukossouev A 2002 Correction of strong phase and amplitude modulations by two deformable mirrors in a multistaged Ti : sapphire laser *Opt. Lett.* **27** 1570–2
- Beg F N, Bell A R, Dangor A E, Danson C N, Fews A P, Glinsky M E, Hammel B A, Lee P, Norreys P A and Tatarakis M 1997 A study of picosecond laser-solid interactions up to 10^{19} W cm⁻² *Phys. Plasmas* **4** 447–57
- Bellei C et al 2010 Micron-scale fast electron filaments and recirculation determined from rear-side optical emission in high-intensity laser-solid interactions *New J. Phys.* **12** 073016
- Benjamin R F, McCall G H and Ehler A W 1979 Measurement of return current in a laser-produced plasma *Phys. Rev. Lett.* **42** 890–3
- Bolton P R, Hori T, Kiriyama H, Mori M, Sakaki H, Sutherland K, Suzuki M, Wu J and Yogo A 2010 Toward integrated laser-driven ion accelerator systems at the photo-medical research center in Japan *Nucl. Instrum. Methods Phys. Res. A* **620** 71–5
- Boody F P, Hopel R, Hora H and Kelly J C 1996 Laser-driven ion source for reduced-cost implantation of metal ions for strong reduction of dry friction and increased durability *Laser Part. Beams* **14** 443–8
- Borghesi M, Giulietti A, Giulietti D, Gizzi L, Macchi A and Willi O 1996 Characterization of laser plasmas for interaction studies: progress in time-resolved density mapping *Phys. Rev. E* **54** 6769–73
- Borghesi M, Mackinnon A J, Gaillard R, Willi O and Riley D 1999 Absorption of subpicosecond UV laser pulses during interaction with solid targets *Phys. Rev. E* **60** 7374–81
- Borghesi M, Schiavi A, Campbell D H, Haines M G, Willi O, MacKinnon A J, Gizzi L A, Galimberti M, Clarke R J and Ruhl H 2001 Proton imaging: a diagnostic for inertial confinement fusion/fast ignitor studies *Plasma Phys. Control. Fusion* **43** A267–A276
- Borghesi M et al 2002a Macroscopic evidence of soliton formation in multiterawatt laser-plasma interaction *Phys. Rev. Lett.* **88** 135002
- Borghesi M et al 2002b Electric field detection in laser-plasma interaction experiments via the proton imaging technique *Phys. Plasmas* **9** 2214–20
- Borghesi M et al 2003 Measurement of highly transient electrical charging following high-intensity laser-solid interaction *Appl. Phys. Lett.* **82** 1529–31
- Borghesi M, Mackinnon A J, Campbell D H, Hicks D G, Kar S, Patel P K, Price D, Romagnani L, Schiavi A and Willi O 2004

- Multi-MeV proton source investigations in ultraintense laser–foil interactions *Phys. Rev. Lett.* **92** 055003
- Borghesi M *et al* 2005 Plasma ion evolution in the wake of a high-intensity ultrashort laser pulse *Phys. Rev. Lett.* **94** 195003
- Borghesi M, Fuchs J, Bulanov S V, Mackinnon A J, Patel P K and Roth M 2006 Fast ion generation by high-intensity laser irradiation of solid targets and applications *Fusion Sci. Technol.* **49** 412–39
- Borghesi M *et al* 2009 Laser-driven proton acceleration and applications: recent results *Eur. Phys. J. Special Top.* **175** 105–10
- Bortfeld T 1997 An analytical approximation of the Bragg curve for therapeutic proton beams *Med. Phys.* **24** 2024–33
- Bourdier A 1983 Oblique incidence of a strong electromagnetic wave on a cold inhomogeneous electron plasma. Relativistic effects *Phys. Fluids* **26** 1804–7
- Brahme A, Lewensohn R, Ringborg U, Amaldi U, Gerardi F and Rossi S 2001 Design of a centre for biologically optimised light ion therapy in Stockholm *Nucl. Instrum. Methods Phys. Res. B* **184** 569–88
- Brambrink E, Roth M, Blazevic A and Schlegel T 2006a Modeling of the electrostatic sheath shape on the rear target surface in short-pulse laser-driven proton acceleration *Laser Part. Beams* **24** 163–8
- Brambrink E, Schreiber J, Schlegel T, Audebert P, Cobble J, Fuchs J, Hegelich M and Roth M 2006b Transverse characteristics of short-pulse laser-produced ion beams: a study of the acceleration dynamics *Phys. Rev. Lett.* **96** 154801
- Brantov A V, Tikhonchuk V T, Klimo O, Romanov D V, Ter-Avetisyan S, Schnurer M, Sokollik T and Nickles P V 2006 Quasi-mono-energetic ion acceleration from a homogeneous composite target by an intense laser pulse *Phys. Plasmas* **13** 122705
- Bratman V L and Samsonov S V 1995 Radiation and radiative damping of a charged plane, oscillating with a relativistic velocity *Phys. Lett. A* **206** 377–82
- Brunel F 1987 Not-so-resonant, resonant absorption *Phys. Rev. Lett.* **59** 52–5
- Buffechoux S *et al* 2010 Hot electrons transverse refluxing in ultraintense laser–solid interactions *Phys. Rev. Lett.* **105** 015005
- Bulanov S S *et al* 2008a Accelerating protons to therapeutic energies with ultraintense, ultraclean, and ultrashort laser pulses *Med. Phys.* **35** 1770–6
- Bulanov S S *et al* 2008b Accelerating monoenergetic protons from ultrathin foils by flat-top laser pulses in the directed-Coulomb-explosion regime *Phys. Rev. E* **78** 026412
- Bulanov S S *et al* 2010 Generation of GeV protons from 1 PW laser interaction with near critical density targets *Phys. Plasmas* **17** 043105
- Bulanov S V 1975 An exactly solvable problem in electrodynamics *Izv. Vyssh. Uchebn. Zaved. Radiofiz.* **18** 1511–9
- Bulanov S V 1975 *Radiophys. Quantum Electron.* **18** 1116–23
- Bulanov S V, Inovenkov I N, Kirsanov V I, Naumova N M and Sakharov A S 1992 Nonlinear depletion of ultrashort and relativistically strong laser pulses in an underdense plasma *Phys. Fluids B* **4** 1935–42
- Bulanov S V, Naumova N M and Pegoraro F 1994 Interaction of an ultrashort, relativistically strong laser pulse with an overdense plasma *Phys. Plasmas* **1** 745–57
- Bulanov S V and Khoroshkov V S 2002a Feasibility of using laser ion accelerators in proton therapy *Plasma Phys. Rep.* **28** 453–6
- Bulanov S V, Esirkepov T Z, Kamenets F F, Kato Y, Kuznetsov A V, Nishihara K, Pegoraro F, Tajima T and Khoroshkov V S 2002b Generation of high-quality charged particle beams during the acceleration of ions by high-power laser radiation *Plasma Phys. Rep.* **28** 975–91
- Bulanov S V, Esirkepov T Zh, Koga J and Tajima T 2004a Interaction of electromagnetic waves with plasma in the radiation-dominated regime *Plasma Phys. Rep.* **30** 196–213
- Bulanov S V, Daido H, Esirkepov T Zh, Khoroshkov V S, Koga J, Nishihara K, Pegoraro F, Tajima T and Yamagawa M 2004b Feasibility of using laser ion accelerators in proton therapy *AIP Conf. Proc.* **740** 414–29
- Bulanov S V, Dylov D, Esirkepov T Z, Kamenets F and Sokolov D 2005a Ion acceleration in a dipole vortex in a laser plasma corona *Plasma Phys. Rep.* **31** 369–81
- Bulanov S V, Esirkepov T, Migliozzi P, Pegoraro F, Tajima T and Terranova F 2005b Neutrino oscillation studies with laser-driven beam dump facilities *Nucl. Instrum. Methods Phys. Res. A* **540** 25–41
- Bulanov S V and Esirkepov T Zh 2007 Comment on collimated multi-MeV ion beams from high-intensity laser interactions with underdense plasma *Phys. Rev. Lett.* **98** 049503
- Bulanov S V, Esirkepov T Z, Pegoraro F and Borghesi M 2009 On the ion acceleration by high power electromagnetic waves in the radiation pressure dominated regime *C. R. Physique* **10** 216–26
- Bulanov S V, Echkina E Yu, Esirkepov T Zh, Inovenkov I N, Kando M, Pegoraro F and Korn G 2010a Unlimited ion acceleration by radiation pressure *Phys. Rev. Lett.* **104** 1350034
- Bulanov S V, Echkina E Y, Esirkepov T Z, Inovenkov I N, Kando M, Pegoraro F and Korn G 2010b Unlimited energy gain in the laser-driven radiation pressure dominant acceleration of ions *Phys. Plasmas* **17** 063102
- Bunkin F V, Korobkin V V, Kurinyi Y A, Polonskii L Y and Pyatnitskii L N 1983 Laser spark with a continuous channel in air *Sov. J. Quantum Electron.* **13** 254–5
- Bychenkov V Yu, Sentoku Y, Bulanov S V, Mima K, Mourou G and Tolokonnikov S V 2001a Pion production under the action of intense ultrashort laser pulse on a solid target *JETP Lett.* **74** 586–9
- Bychenkov V Yu, Rozmus W, Maksimchuk A, Umstadter D and Capjack C 2001b Fast ignitor concept with light ions *Plasma Phys. Rep.* **27** 1017–20
- Bychenkov V Yu and Kovalev V F 2005a On the maximum energy of ions in a disintegrating ultrathin foil irradiated by a high-power ultrashort laser pulse *Quantum Electron.* **35** 1143–5
- Bychenkov V Yu and Kovalev V F 2005b Coulomb explosion in a cluster plasma *Fiz. Plazmy* **31** 203–8
- Bychenkov V Yu and Kovalev V F 2005b *Plasma Phys. Rep.* **31** 178–83
- Carlson R, Carpenter J, Casperson D, Gibson R, Godwin R, Haglund R, Hanlon J, Jolly E and Stratton T 1981 Helios: a 15 TW carbon dioxide laser-fusion facility *IEEE J. Quantum Electron.* **17** 1662–78
- Carman R L, Forslund D W and Kindel J M 1981 Visible harmonic emission as a way of measuring profile steepening *Phys. Rev. Lett.* **46** 29–32
- Carrié M, Lefebvre E, Flacco A and Malka V 2009 Influence of subpicosecond laser pulse duration on proton acceleration *Phys. Plasmas* **16** 053105
- Carroll D C, Brummitt P, Neely D, Lindau F, Lundh O, Wahlström C G and McKenna P 2010a A modified Thomson parabola spectrometer for high resolution multi-MeV ion measurements—application to laser-driven ion acceleration *Nucl. Instrum. Methods Phys. Res. A* **620** 23–7
- Carroll D C *et al* 2010b Carbon ion acceleration from thin foil targets irradiated by ultrahigh-contrast, ultraintense laser pulses *New J. Phys.* **12** 045020
- Cecchetti C A *et al* 2009 Magnetic field measurements in laser-produced plasmas via proton deflectometry *Phys. Plasmas* **16** 043102
- Ceccotti T, Levy A, Popescu H, Reau F, D’Oliveira P, Monot P, Geindre J P, Lefebvre E and Martin P 2007 Proton acceleration with high-intensity ultrahigh-contrast laser pulses *Phys. Rev. Lett.* **99** 185002
- Chambaret J P *et al* 2010 Extreme light infrastructure: laser architecture and major challenges *Proc. SPIE* **7721** 77211D

- Chen C D *et al* 2008 A bremsstrahlung spectrometer using k -edge and differential filters with image plate dosimeters *Rev. Sci. Instrum.* **79** 10E305
- Chen H, Link A J, Maren R v, Patel P K, Shepherd R, Wilks S C and Beiersdorfer P 2008a High performance compact magnetic spectrometers for energetic ion and electron measurement in ultraintense short pulse laser solid interactions *Rev. Sci. Instrum.* **79** 10E533
- Chen H *et al* 2008b Absolute calibration of image plates for electrons at energy between 100 keV and 4 MeV *Rev. Sci. Instrum.* **79** 033301
- Chen M, Pukhov A, Sheng Z M and Yan X Q 2008 Laser mode effects on the ion acceleration during circularly polarized laser pulse interaction with foil targets *Phys. Plasmas* **15** 113103
- Chen M, Pukhov A, Yu T P and Sheng Z M 2009 Enhanced collimated GeV monoenergetic ion acceleration from a shaped foil target irradiated by a circularly polarized laser pulse *Phys. Rev. Lett.* **103** 024801
- Cherepenin V A and Kulagin V V 2004 Dynamics and radiation of thin foil in the field of super-intense laser pulse *Phys. Lett. A* **321** 103–10
- Choi I W *et al* 2009a Ion spectrometer composed of time-of-flight and Thomson parabola spectrometers for simultaneous characterization of laser-driven ions *Rev. Sci. Instrum.* **80** 053302
- Choi I W, Kim C M, Sung J H, Kim I J, Yu T J, Lee S K, Jin Y-Y, Pae K H, Hafz N and Lee J 2009b Absolute calibration of a time-of-flight spectrometer and imaging plate for the characterization of laser-accelerated protons *Meas. Sci. Technol.* **20** 115112
- Choi I W *et al* 2011 Simultaneous generation of ions and high-order harmonics from thin conjugated polymer foil irradiated with ultrahigh contrast laser *Appl. Phys. Lett.* **99** 181501
- Chvykov V, Rousseau P, Reed S, Kalinchenko G and Yanovsky V 2006 Generation of 10^{11} contrast 50 TW laser pulses *Opt. Lett.* **31** 1456–8
- Clady R *et al* 2006 Architecture of a blue high contrast multiterawatt ultrashort laser *Appl. Phys. B* **82** 347–58
- Clark E L, Krushelnick K, Zepf M, Beg F N, Tatarakis M, Machacek A, Santala M I K, Watts I, Norreys P A and Dangor A E 2000 Energetic heavy-ion and proton generation from ultraintense laser–plasma interactions with solids *Phys. Rev. Lett.* **85** 1654–7
- Clarke R J *et al* 2006a Detection of short lived radioisotopes as a fast diagnostic for intense laser–solid interactions *Appl. Phys. Lett.* **89** 141117
- Clarke R J *et al* 2006b Radiological characterisation of photon radiation from ultra-high-intensity laser–plasma and nuclear interactions *J. Radiol. Prot.* **26** 277–86
- Clarke R J *et al* 2008 Nuclear activation as a high dynamic range diagnostic of laser–plasma interactions *Nucl. Instrum. Methods Phys. Res. A* **583** 117–120
- Collier J, Hernandez-Gomez C, Allott R, Danson C and Hall A 2001 A single-shot third-order autocorrelator for pulse contrast and pulse shape measurements *Laser Part. Beams* **19** 231–5
- Conlon T W 1985 Nuclear physics for materials technology accelerator based methods *Contemp. Phys.* **26** 521–58
- Corkum P B and Krausz F 2007 Attosecond science *Nature Phys.* **3** 381–7
- Cowan T E *et al* 1999 High energy electrons, nuclear phenomena and heating in petawatt laser–solid experiments *Laser Part. Beams* **17** 773–83
- Cowan T E *et al* 2004 Ultralow emittance, multi-MeV proton beams from a laser virtual-cathode plasma accelerator *Phys. Rev. Lett.* **92** 204801
- Cowan T E *et al* 2005 Ultra-low emittance, high current proton beams produced with a laser-virtual cathode sheath accelerator *Nucl. Instrum. Methods Phys. Res. A* **544** 277–84
- Crow J E, Auer P L and Allen J E 1975 The expansion of a plasma into a vacuum *J. Plasma Phys.* **14** 65–76
- Da Silva L B *et al* 1995 Electron density measurements of high density plasmas using soft x-ray laser interferometry *Phys. Rev. Lett.* **74** 3991–4
- Daido H, Miki F, Mima K, Fujita M, Sawai K, Fujita H, Kitagawa Y, Nakai S and Yamanaka C 1986 Generation of a strong magnetic field by an intense CO₂ laser pulse *Phys. Rev. Lett.* **56** 846–9
- Daido H, Yamanaka M, Mima K, Nishihara K, Nakai S, Kitagawa Y, Miura E, Yamanaka C and Hasegawa A 1987 Neutron production from a shell confined carbon–deuterium plasma by 1.06 μm laser irradiations *Appl. Phys. Lett.* **51** 2195–6
- Daido H 2002 Review of soft x-ray laser researches and developments *Rep. Prog. Phys.* **65** 1513–76
- Daido H *et al* 2007 Intense femto-second laser-driven x-ray source coupled with multiple directional quantum beams for applications *Proc. 10th Int. Conf. on X-Ray Lasers (Max Born Institute, Berlin)* (Berlin: Springer) pp 595–605
- Danson C N *et al* 2004 Vulcan Petawatt—an ultra-high-intensity interaction facility *Nucl. Fusion* S239–46
- Davies J R 2009 Laser absorption by overdense plasmas in the relativistic regime *Plasma Phys. Control. Fusion* **51** 014006
- Denavit J 1979 Collisionless plasma expansion into a vacuum *Phys. Fluids* **22** 1384–92
- Denavit J 1992 Absorption of high-intensity subpicosecond lasers on solid density targets *Phys. Rev. Lett.* **69** 3052–5
- Didenko N V, Konyashchenko A V, Lutsenko A P and Tenyakov S Y 2008 Contrast degradation in a chirped-pulse amplifier due to generation of prepulses by postpulses *Opt. Express* **16** 3178–90
- Ditmire T, Donnelly T, Rubenchik A M, Falcone R W and Perry M D 1996 Interaction of intense laser pulses with atomic clusters *Phys. Rev. A* **53** 3379–402
- Ditmire T, Zweiback J, Yanovsky V P, Cowan T E, Hays G and Wharton K B 1999 Nuclear fusion from explosions of femtosecond laser-heated deuterium clusters *Nature* **398** 489–92
- Divall E J and Ross I N 2004 High dynamic range contrast measurements by use of an optical parametric amplifier correlator *Opt. Lett.* **29** 2273–5
- Dorozhkina D S and Semenov V E 1998 Exact solution of Vlasov equations for quasineutral expansion of plasma bunch into vacuum *Phys. Rev. Lett.* **81** 2691–4
- Dorrer C, Bromage J and Zuegel J D 2008 High-dynamic-range single-shot cross-correlator based on an optical pulse replicator *Opt. Express* **16** 13534–44
- Doumy G, Quéré F, Gobert O, Perdris M, Martin P, Audebert P, Gauthier J C, Geindre J P and Wittmann T 2004 Complete characterization of a plasma mirror for the production of high-contrast ultraintense laser pulses *Phys. Rev. E* **69** 026402
- Druon F, Chériaux G, Faure J, Nees J, Nantel M, Maksimchuk A, Mourou G, Chanteloup J C and Vdovin G 1998 Wave-front correction of femtosecond terawatt lasers by deformable mirrors *Opt. Lett.* **23** 1043–5
- Dubietis A, Jonusauskas G and Piskarskas A 1992 Powerful femtosecond pulse generation by chirped and stretched pulse parametric amplification in BBO crystal *Opt. Commun.* **88** 437–40
- Dunne M 2006 A high-power laser fusion facility for Europe *Nature Phys.* **2** 2–5
- Durante M and Cucinotta F A 2008 Heavy ion carcinogenesis and human space exploration *Nature Rev. Cancer* **8** 465–72
- Dyer G M, Bernstein A C, Cho B I, Osterholz J, Grigsby W, Dalton A, Shepherd R, Ping Y and Chen H 2008 Equation-of-state measurement of dense plasmas heated with fast protons *Phys. Rev. Lett.* **101** 015002
- D'yachenko V F and Imshennik V S 1979 Anomalous interaction of intense light beams with dense plasmas *Sov. J. Plasma Phys.* **5** 413–7

- Esarey E, Schroeder C B and Leemans W P 2009 Physics of laser-driven plasma-based electron accelerators *Rev. Mod. Phys.* **81** 1229–85
- Esirkepov T Zh *et al* 1999 Ion acceleration by superintense laser pulses in plasmas *JETP Lett.* **70** 82–9
- Esirkepov T Zh, Bingham R, Bulanov S V, Honda T, Nishihara K and Pegoraro F 2000 Coulomb explosion of a cluster irradiated by a high intensity laser pulse *Laser Part. Beams* **18** 503–6
- Esirkepov T Zh *et al* 2002 Proposed double-layer target for the generation of high-quality laser-accelerated ion beams *Phys. Rev. Lett.* **89** 175003
- Esirkepov T Zh, Borghesi M, Bulanov S V, Mourou G and Tajima T 2004 Highly efficient relativistic-ion generation in the laser-piston regime *Phys. Rev. Lett.* **92** 175003
- Esirkepov T Zh, Yamagiwa M and Tajima T 2006 Laser ion-acceleration scaling laws seen in multiparametric particle-in-cell simulations *Phys. Rev. Lett.* **96** 105001
- Estabrook K and Krueer W L 1978 Properties of resonantly heated electron distributions *Phys. Rev. Lett.* **40** 42–5
- Faenov A Ya, Pikuz S A, Erko A I, Bryunetkin B A, Dyakin V M, Ivanenkov G V, Mingaleev A R, Pikuz T A, Romanova V M and Shelkovenko T A 1994 High-performance x-ray spectroscopic devices for plasma microsources investigations *Phys. Scr.* **50** 333–8
- Faenov A Ya *et al* 2009a Ionography of nanostructures with the use of a plasma of cluster targets *JETP Lett.* **89** 485–91
- Faenov A Ya *et al* 2009b Submicron ionography of nanostructures using a femtosecond-laser-driven-cluster-based source *Appl. Phys. Lett.* **95** 101107
- Fang Z, Endo K, Egawa K, Endo K, Yamanaka S, Hirashima T, Fusato T and Cho Y 2005 Present status of RF system for medical proton synchrotron *Proc. Particle Accelerator Conf. (Knoxville, TN, 16–20 May 2005)* (Piscataway, NJ: IEEE) pp 3185–7
- Feurer T, Theobald W, Sauerbrey R, Uschmann I, Altenbernd D, Teubner U, Gibbon P, Forster E, Malka G and Miquel J L 1997 Onset of diffuse reflectivity and fast electron flux inhibition in 528-nm-laser solid interactions at ultrahigh intensity *Phys. Rev. E* **56** 4608–14
- Fews A P, Norreys P A, Beg F N, Bel A R, Dangor A E, Danson C N, Lee P and Rose S J 1994 Plasma ion emission from high-intensity picosecond laser-pulse interactions with solid targets *Phys. Rev. Lett.* **73** 1801–4
- Fiedorowicz H, Bartnik A, Daido H, Choi I W, Suzuki M and Yamagami S 2000 Strong extreme ultraviolet emission from a double-stream xenon/helium gas puff target irradiated with a Nd : YAG laser *Opt. Commun.* **184** 161–7
- Fill E E 2005 Ultrashort-pulse laser plasmas: fraction of hot electrons escaping from the target and electron spectra in planar and spherical geometry *Phys. Plasmas* **12** 052704
- Flacco A, Sylla F, Veltcheva M, Carrié M, Nuter R, Lefebvre E, Batani D and Malka V 2010a Dependence on pulse duration and foil thickness in high-contrast-laser proton acceleration *Phys. Rev. E* **81** 036405
- Flacco A *et al* 2010b Comparative study of laser ion acceleration with different contrast enhancement techniques *Nucl. Instrum. Methods Phys. Res. A* **620** 18–22
- Flippo K, Hegelich B M, Albright B J, Yin L, Gautier D C, Letzring S, Schollmeier M, Schreiber J, Schulze R and Fernandez J C 2007 Laser-driven ion accelerators: spectral control, monoenergetic ions and new acceleration mechanisms *Laser Part. Beams* **25** 3–8
- Flippo K *et al* 2008 Increased efficiency of short-pulse laser-generated proton beams from novel flat-top cone targets *Phys. Plasmas* **15** 056709
- Forslund D W, Kindel J M and Lee K 1977 Theory of hot-electron spectra at high laser intensity *Phys. Rev. Lett.* **39** 284–8
- Forslund D W and Brackbill J U 1982 Magnetic-field-induced surface transport on laser-irradiated foils *Phys. Rev. Lett.* **48** 1614–7
- Forton E, Stichelbaut F, Cambriani A, Kleeven W, Ahlback J and Jongen Y 2009 Overview of the IBA accelerator-based BNCT system *Appl. Radiat. Isot.* **67** 5262–5
- Fourkal E, Shahine B, Ding M, Li J S, Tajima T and Ma C M 2002 Particle in cell simulation of laser-accelerated proton beams for radiation therapy *Med. Phys.* **29** 2788–98
- Fourkal E, Li J S, Ding M, Tajima T and Ma C M 2003a Particle selection for laser-accelerated proton therapy feasibility study *Med. Phys.* **30** 1660–70
- Fourkal E, Li J S, Xiong W, Nahum A and Ma C M 2003b Intensity modulated radiation therapy using laser-accelerated protons: a Monte Carlo dosimetric study *Phys. Med. Biol.* **48** 3977–4000
- Fourmaux S, Payeur S, Buffeouchou S, Lassonde P, St-Pierre C, Martin F and Kieffer J C 2011 Pedestal cleaning for high laser pulse contrast ratio with a 100 TW class laser system *Opt. Express* **19** 8486–97
- Frenje J A *et al* 2002 Absolute measurements of neutron yields from DD and DT implosions at the OMEGA laser facility using CR-39 track detectors *Rev. Sci. Instrum.* **73** 2597–605
- Fritzler S, Malka V, Grillon G, Rousseau J P, Burgy F, Lefebvre E, d’Humières E, McKenna P and Ledingham K W D 2003 Proton beams generated with high-intensity lasers: applications to medical isotope production *Appl. Phys. Lett.* **83** 3039–41
- Fuchs J *et al* 2003 Spatial uniformity of laser-accelerated ultrahigh-current MeV electron propagation in metals and insulators *Phys. Rev. Lett.* **91** 255002
- Fuchs J *et al* 2005 Comparison of laser ion acceleration from the front and rear surfaces of thin foils *Phys. Rev. Lett.* **94** 045004
- Fuchs J *et al* 2006 Laser-driven proton scaling laws and new paths towards energy increase *Nature Phys.* **2** 48–54
- Fuchs J *et al* 2007a Comparative spectra and efficiencies of ions laser-accelerated forward from the front and rear surfaces of thin solid foils *Phys. Plasmas* **14** 053105
- Fuchs J *et al* 2007b Laser-foil acceleration of high-energy protons in small-scale plasma gradients *Phys. Rev. Lett.* **99** 015002
- Fukuda Y *et al* 2009 Energy increase in multi-MeV ion acceleration in the interaction of a short pulse laser with a cluster-gas target *Phys. Rev. Lett.* **103** 165002
- Fukumi A *et al* 2005 Laser polarization dependence of proton emission from a thin foil target irradiated by a 70-fs, intense laser pulse *Phys. Plasmas* **12** 100701
- Gaillard S, Fuchs J, Galloudec N R-L and Cowan T E 2007 Study of saturation of CR39 nuclear track detectors at high ion fluence and of associated artifact patterns *Rev. Sci. Instrum.* **78** 013304
- Gaillard S A, Flippo K A, Lowenstein M E, Mucino J E, Rassuchine J M, Gautier D C, Workman J and Cowan T E 2010 Proton acceleration from ultrahigh-intensity short-pulse laser-matter interactions with Cu micro-cone targets at an intrinsic $\sim 10^{-8}$ contrast *J. Phys.: Conf. Ser.* **244** 022034
- Gaillard S A *et al* 2011 Increased laser-accelerated proton energies via direct laser-light-pressure acceleration of electrons in microcone targets *Phys. Plasmas* **18** 056710
- Gibbon P and Bell A R 1992 Collisionless absorption in sharp-edged plasmas *Phys. Rev. Lett.* **68** 1535–8
- Ginsburg V L 1961 *Propagation of Electromagnetic Waves in Plasmas* (New York: Gordon and Breach)
- Gitomer S J, Jones R D, Begay F, Ehler A W, Kephart J F and Kristal R 1986 Fast ions and hot-electrons in the laser-plasma interaction *Phys. Fluids* **29** 2679–88
- Gizzi L A, Giulietti D, Giulietti A, Afshar-Rad T, Biancalana V, Chessa P, Danson C, Schifano E, Viana S M and Willi O 1994 Characterization of laser plasmas for interaction studies *Phys. Rev. E* **49** 5628
- Glenzer S H *et al* 1999 Thomson scattering from laser plasmas *Phys. Plasmas* **6** 2117–28

- Glover T E, Donnelly T D, Lipman E A, Sullivan A and Falcone R W 1994 Subpicosecond Thomson scattering measurements of optically ionized helium plasmas *Phys. Rev. Lett.* **73** 78–81
- Goitein M, Lomax A J and Pedroni E S 2002 Treating cancer with protons *Phys. Today* **55** 45–50
- Gold D M, Nathel H, Bolton P R, White W E and Van Woerkom L D 1991 Prepulse suppression using a self-induced ultrashort pulse plasma mirror *Proc. SPIE* **1413** 41–52
- Gold D M 1994 Direct measurement of prepulse suppression by use of a plasma shutter *Opt. Lett.* **19** 2006–8
- Green J S *et al* 2009 Multi-channel system for imaging laser accelerated proton beams *CLF Annual Report 2008/2009* p 311
- Green J S *et al* 2010 Enhanced proton flux in the MeV range by defocused laser irradiation *New J. Phys.* **12** 085012
- Grismayer T and Mora P 2006 Influence of a finite initial ion density gradient on plasma expansion into a vacuum *Phys. Plasmas* **13** 032103
- Gurevich A V, Pariiskaya L V and Pitaevskii L P 1965 Self-similar motion of rarefied plasma *Zh. Eksp. Teor. Fiz.* **49** 647 (in Russian)
- Gurevich A V, Pariiskaya L V and Pitaevskii L P 1966 Self-similar motion of rarefied plasma *Sov. Phys.—JETP* **22** 449–54 (Engl. transl.)
- Gurevich A V, Pariiskaya L V and Pitaevskii L P 1972 Ion acceleration on expansion of a rarefied plasma *Zh. Eksp. Teor. Fiz.* **63** 516–31 (in Russian)
- Gurevich A V, Pariiskaya L V and Pitaevskii L P 1972 Ion acceleration on expansion of a rarefied plasma *Sov. Phys.—JETP* **36** 274 (Engl. transl.)
- Gurevich A V and Meshcherkin A P 1981 Ion acceleration in an expanding plasma *Zh. Eksp. Teor. Fiz.* **80** 1810–26 (in Russian)
- Gurevich A V and Meshcherkin A P 1981 Ion acceleration in an expanding plasma *Sov. Phys.—JETP* **53** 937–45 (Engl. transl.)
- Hafz N A M *et al* 2008 Stable generation of GeV-class electron beams from self-guided laser plasma channels *Nature Photon.* **2** 571–7
- Haines M G, Wei M S, Beg F N and Stephens R B 2009 Hot-electron temperature and laser-light absorption in fast ignition *Phys. Rev. Lett.* **102** 045008
- Hamster H, Sullivan A, Gordon S, White W and Falcone R W 1993 Subpicosecond electromagnetic pulses from intense laser-plasma interaction *Phys. Rev. Lett.* **71** 2725–8
- Harres K *et al* 2008 Development and calibration of a Thomson parabola with microchannel plate for the detection of laser-accelerated MeV ions *Rev. Sci. Instrum.* **79** 093306
- Harres K *et al* 2010 Beam collimation and transport of quasineutral laser-accelerated protons by a solenoid field *Phys. Plasmas* **17** 023107
- Hatchett S P *et al* 2000 Electron, photon, and ion beams from the relativistic interaction of petawatt laser pulses with solid targets *Phys. Plasmas* **7** 2076–82
- Hauer A and Mason R J 1983 Return-current heating and implosion of cylindrical CO₂-laser-driven target *Phys. Rev. Lett.* **51** 459–62
- Hegelich M *et al* 2002 MeV ion jets from short-pulse-laser interaction with thin foils *Phys. Rev. Lett.* **89** 085002
- Hegelich B M *et al* 2005 Spectral properties of laser-accelerated mid-Z MeV/u ion beams *Phys. Plasmas* **12** 056314
- Hegelich B M, Albright B J, Cobble J, Flippo K, Letzring S, Paffett M, Ruhl H, Schreiber J, Schulze R K and Fernandez J C 2006 Laser acceleration of quasi-monoenergetic MeV ion beams *Nature* **439** 441–4
- Hegelich B, Yin L, Albright B, Bowers K, Gautier C, Henig A, Hoerlein R, Dromey B, Jung D and Kiefer D 2010 Laser-driven ion-, electron- and photon-beams from relativistically overdense plasmas *Bull. Am. Phys. Soc.* **55** PO7.00005
- Henig A *et al* 2009a Laser-driven shock acceleration of ion beams from spherical mass-limited targets *Phys. Rev. Lett.* **102** 095002
- Henig A *et al* 2009b Radiation pressure acceleration of ion beams driven by circularly polarized laser pulses *Phys. Rev. Lett.* **103** 245003
- Henig A *et al* 2009c Enhanced laser-driven ion acceleration in the relativistic transparency regime *Phys. Rev. Lett.* **103** 045002
- Hemberg O, Hansson B A M, Barglund M and Hertz 2000 Stability of droplet-target laser-plasma soft x-ray sources *J. Appl. Phys.* **88** 5421
- Hey D S, Key M H, Mackinnon A J, MacPhee A G, Patel P K, Freeman R R, Van Woerkom L D and Castaneda C M 2008 Use of GafChromic film to diagnose laser generated proton beams *Rev. Sci. Instrum.* **79** 053501
- Homoelle D, Gaeta A L, Yanovsky V and Mourou G 2002 Pulse contrast enhancement of high-energy pulses by use of a gas-filled hollow waveguide *Opt. Lett.* **27** 1646–8
- Hong K H, Hou B, Nees J A, Power E and Mourou G A 2005 Generation and measurement of $>10^8$ intensity contrast ratio in a relativistic kHz chirped-pulse amplified laser *Appl. Phys. B* **81** 447–57
- Honrubia J J, Fernandez J C, Temporal M, Hegelich B M and Meyer-ter-Vehn J 2009 Fast ignition of inertial fusion targets by laser-driven carbon beams *Phys. Plasmas* **16** 102701
- d'Humières E, Lefebvre E, Gremillet L and Malka V 2005 Proton acceleration mechanisms in high-intensity laser interaction with thin foils *Phys. Plasmas* **12** 062704
- d'Humières E, Feugeas J L, Nicolai P, Gaillard S, Cowan T, Sentoku Y and Tikhonchuk V 2010 Investigation of high intensity laser proton acceleration with underdense targets *J. Phys.: Conf. Ser.* **244** 042023
- Humphries S Jr 1990 *Charged Particle Beams* (New York: Wiley)
- Hörlein R, Dromey B, Adams D, Nomura Y, Kar S, Markey K, Foster P, Neely D, Krausz F and Tsakiris G D 2008 High contrast plasma mirror: spatial filtering and second harmonic generation at 10^{19} W cm⁻² *New J. Phys.* **10** 083002
- Ikegami M *et al* 2009 Radial focusing and energy compression of a laser-produced proton beam by a synchronous rf field *Phys. Rev. ST Accel. Beams* **12** 063501
- Ilic R and Durrani S 2003 Solid state track detectors *Handbook of Radioactivity Analysis* ed M F L Annunziata (New York: Academic) pp 179–238
- Jullien A *et al* 2005 10 to 10 temporal contrast for femtosecond ultraintense lasers by cross-polarized wave generation *Opt. Lett.* **30** 920–2
- Jung D *et al* 2011 Development of a high resolution and high dispersion Thomson parabola *Rev. Sci. Instrum.* **82** 013306
- Kalashnikov M P, Risse E, Schonnagel H and Sandner W 2005 Double chirped-pulse-amplification laser: a way to clean pulses temporally *Opt. Lett.* **30** 923–5
- Kaluza M, Schreiber J, Santala M I K, Tsakiris G D, Eidmann K, Meyer-ter-Vehn J and Witte K J 2004 Influence of the laser prepulse on proton acceleration in thin-foil experiments *Phys. Rev. Lett.* **93** 045003
- Kapteyn H C, Murnane M M, Szoke A and Falcone R W 1991 Prepulse energy suppression for high-energy ultrashort pulses using self-induced plasma shuttering *Opt. Lett.* **16** 490–2
- Kar S *et al* 2007 Dynamics of charge-displacement channeling in intense laser-plasma interactions *New J. Phys.* **9** 402
- Kar S *et al* 2008a Plasma jets driven by ultraintense-laser interaction with thin foils *Phys. Rev. Lett.* **100** 225004
- Kar S *et al* 2008b Dynamic control of laser-produced proton beams *Phys. Rev. Lett.* **100** 105004
- Kemp A J, Fuchs J, Sentoku Y, Sotnikov V, Bakeman M, Antici P and Cowan T E 2007 Emittance growth mechanisms for laser-accelerated proton beams *Phys. Rev. E* **75** 056401
- Keldysh L V 1964 Ionization in the field of a strong electromagnetic wave (multiphonon absorption processes and ionization probability for atoms and solids in strong electromagnetic field) *Zh. Eksp. Teor. Fiz.* **47** 1945–57 (in Russian)

- Keldysh L V 1965 Ionization in the field of a strong electromagnetic wave (multiphonon absorption processes and ionization probability for atoms and solids in strong electromagnetic field) *Sov. Phys.—JETP* **20** 1307–14 (Engl. transl.)
- Key M H *et al* 1998 Hot electron production and heating by hot electrons in fast ignitor research *Phys. Plasmas* **5** 1966–72
- Khoroshkov V S and Minakova E I 1998 Proton beams in radiotherapy *Eur. J. Phys.* **19** 523–36
- Kiefer D *et al* 2009 First observation of quasi-monoenergetic electron bunches driven out of ultra-thin diamond-like carbon (DLC) foils *Eur. Phys. J. D* **55** 427–32
- Kiriyama H *et al* 2007 High-energy, high-contrast, multiterawatt laser pulses by optical parametric chirped pulse amplification *Opt. Lett.* **32** 2315–7
- Kiriyama H *et al* 2009 Generation of high-contrast and high-intensity laser pulses using an OPCPA preamplifier in a double CPA, Ti : sapphire laser system *Opt. Commun.* **282** 625–8
- Kiriyama H *et al* 2010 High temporal and spatial quality petawatt-class Ti : sapphire chirped-pulse amplification laser system *Opt. Lett.* **35** 1497–9
- Kishimoto Y, Mima K, Watanabe T and Nishikawa K 1983 Analysis of fast-ion velocity distributions in laser plasmas with a truncated Maxwellian velocity distribution of hot-electrons *Phys. Fluids* **26** 2308–15
- Klimo O, Psikal J, Limpouch J and Tikhonchuk V T 2008 Monoenergetic ion beams from ultrathin foils irradiated by ultrahigh-contrast circularly polarized laser pulses *Phys. Rev. ST Accel. Beams* **11** 031301
- Kodama R *et al* 2001 Fast heating of ultrahigh-density plasma as a step towards laser fusion ignition *Nature* **412** 798–802
- Koning A *et al* 2002 HINDAS: a European nuclear data program for accelerator-driven systems *J. Nucl. Sci. Technol.* **2** (Suppl.) 1161–6
- Kovalev V F and Bychenkov V Y 2003 Analytic solutions to the Vlasov equations for expanding plasmas *Phys. Rev. Lett.* **90** 185004
- Kovalev V F and Bychenkov V Y 2005 Kinetic description of the Coulomb explosion of a spherically symmetric cluster *JETP* **101** 212–23
- Kovalev V F, Bychenkov V Y and Mima K 2007a Quasimonoenergetic ion bunches from exploding microstructured targets *Phys. Plasmas* **14** 103110
- Kovalev V F, Popov K I, Bychenkov V Y and Rozmus W 2007b Laser triggered Coulomb explosion of nanoscale symmetric targets *Phys. Plasmas* **14** 053103
- Kraft S D *et al* 2010 Dose-dependent biological damage of tumour cells by laser-accelerated proton beams *New J. Phys.* **12** 085003
- Kruer W L and Estabrook K 1985 J × B heating by very intense laser light *Phys. Fluids* **28** 430–2
- Krushelnick K *et al* 1999 Multi-MeV ion production from high-intensity laser interactions with underdense plasmas *Phys. Rev. Lett.* **83** 737–40
- Krushelnick K *et al* 2000a Ultrahigh-intensity laser-produced plasmas as a compact heavy ion injection source *IEEE Trans. Plasma Sci.* **28** 1184–9
- Krushelnick K *et al* 2000b Energetic proton production from relativistic laser interaction with high density plasmas *Phys. Plasmas* **7** 2055–61
- Kuznetsov A V, Esirkepov T Z, Kamenets F F and Bulanov S V 2001 Efficiency of ion acceleration by a relativistically strong laser pulse in an underdense plasma *Plasma Phys. Rep.* **27** 211–20
- Landau L D and Lifshitz E M 2003 *The Classical Theory of Fields* 4th edn (Oxford: Butterworth-Heinemann)
- Ledingham K W D, McKenna P and Singhal R P 2003 Applications for nuclear phenomena generated by ultra-intense lasers *Science* **300** 1107–11
- Ledingham K W D *et al* 2004 High power laser production of short-lived isotopes for positron emission tomography *J. Phys. D: Appl. Phys.* **37** 2341–5
- Leemans W P *et al* 2006 Observation of terahertz emission from a laser-plasma accelerated electron bunch crossing a plasma–vacuum boundary *Phys. Rev. Lett.* **91** 074802
- Lefebvre E *et al* 2010 Proton acceleration by moderately relativistic laser pulses interacting with solid density targets *New J. Phys.* **12** 045017
- Lévy A, Ceccotti T, D’Oliveira P, Fabrice R, Perdrix M, Quere F, Monot P, Bougeard M, Lagadec H and Martin P 2007 Double plasma mirror for ultrahigh temporal contrast ultraintense laser pulses *Opt. Lett.* **32** 310–2
- Li C K *et al* 2008 Monoenergetic-proton-radiography measurements of implosion dynamics in direct-drive inertial-confinement fusion *Phys. Rev. Lett.* **100** 225001
- Li Z *et al* 2006 Measurements of energy and angular distribution of hot electrons and protons emitted from a p- and s-polarized intense femtosecond laser pulse driven thin foil target *Phys. Plasmas* **13** 043104
- Lindau F, Lundh O, Persson A, McKenna P, Osvay K, Batani D and Wahlström C G 2005 Laser-accelerated protons with energy-dependent beam direction *Phys. Rev. Lett.* **95** 175002
- Limpouch J, Psikal J, Andreev A A, Platonov K Y and Kawata S 2008 Enhanced laser ion acceleration from mass-limited targets *Laser Part. Beams* **26** 225–34
- Lindl J 1995 Development of the indirect-drive approach to inertial confinement fusion and the target physics basis for ignition and gain *Phys. Plasmas* **2** 3933–4024
- Link A, Freeman R R, Schumacher D W and Woerkom L D V 2011 Effects of target charging and ion emission on the energy spectrum of emitted electrons *Phys. Plasmas* **18** 053107
- Lintz U and Alonso J 2007 What will it take for laser driven proton accelerators to be applied to tumor therapy? *Phys. Rev. ST Accel. Beams* **10** 094801
- Liseikina T V and Macchi A 2007 Features of ion acceleration by circularly polarized laser pulses *Appl. Phys. Lett.* **91** 171502
- Liseykina T V, Borghesi M, Macchi A and Tuveri S 2008 Radiation pressure acceleration by ultraintense laser pulses *Plasma Phys. Control. Fusion* **50** 124033
- London R A and Rosen M D 1986 Hydrodynamics of exploding foil x-ray lasers *Phys. Fluids* **29** 3813–22
- Lontano M and Passoni M 2006 Electrostatic field distribution at the sharp interface between high density matter and vacuum *Phys. Plasmas* **13** 042102
- Lorusso A *et al* 2005 Modification of materials by high energy plasma ions *Nucl. Instrum. Methods Phys. Res. B* **240** 229–33
- Luan S, Hutchinson M H R, Smith R A and Zhou F 1993 High dynamic range third-order correlation measurement of picosecond laser pulse shapes *Meas. Sci. Technol.* **4** 1426–9
- Lundh O, Lindau F, Persson A, Wahlström C G, McKenna P and Batani D 2007 Influence of shock waves on laser-driven proton acceleration *Phys. Rev. E* **76** 026404
- Lundh O, Glinec Y, Homann C, Lindau F, Persson A, Wahlström C G, Carroll D C and McKenna P 2008 Active steering of laser-accelerated ion beams *Appl. Phys. Lett.* **92** 011504
- Macchi A, Cattani F, Liseykina T V and Cornolti F 2005 Laser acceleration of ion bunches at the front surface of overdense plasmas *Phys. Rev. Lett.* **94** 165003
- Macchi A, Veghini S and Pegoraro F 2009a ‘Light sail’ acceleration reexamined *Phys. Rev. Lett.* **103** 085003
- Macchi A, Liseikina T V, Tuveri S and Veghini S 2009b Theory and simulation of ion acceleration with circularly polarized laser pulses *C. R. Physique* **10** 207–15
- Macchi A, Veghini S, Liseykina T V and Pegoraro F 2010 Radiation pressure acceleration of ultrathin foils *New J. Phys.* **12** 045013
- Mackinnon A J, Borghesi M, Hatchett S, Key M H, Patel P K, Campbell H, Schiavi A, Snively R, Wilks S C and Willi O

- 2001 Effect of plasma scale length on multi-MeV proton production by intense laser pulses *Phys. Rev. Lett.* **86** 1769–72
- Mackinnon A J, Sentoku Y, Patel P K, Price D W, Hatchett S, Key M H, Andersen C, Snavely R and Freeman R R 2002 Enhancement of proton acceleration by hot-electron recirculation in thin foils irradiated by ultraintense laser pulses *Phys. Rev. Lett.* **88** 215006
- Mackinnon A J, Patel P K, Price D W, Hicks D, Borghesi M and Romagnani L 2003a First observation of Moiré fringes in a proton beam generated by a 100 fs laser pulse *Rev. Sci. Instrum.* **74** 1917–20
- Mackinnon A J, Patel P K, Price D W, Hicks D, Romagnani L and Borghesi M 2003b Proton Moiré fringes for diagnosing electromagnetic fields in opaque materials and plasmas *Appl. Phys. Lett.* **82** 3188–90
- Mackinnon A J *et al* 2004 Proton radiography as an electromagnetic field and density perturbation diagnostic (invited) *Rev. Sci. Instrum.* **75** 3531–6
- Mackinnon A J *et al* 2006 Proton radiography of a laser-driven implosion *Phys. Rev. Lett.* **97** 045001
- MacPhee A G *et al* 2008 Diagnostics for fast ignition science (invited) *Rev. Sci. Instrum.* **79** 10F302
- Magunov A *et al* 2003 X-ray spectra of fast ions generated from clusters by ultrashort laser pulses *Laser Part. Beams* **21** 73–9
- Maiman T H 1960 Stimulated optical radiation in ruby *Nature* **187** 493–4
- Mako F and Tajima T 1984 Collective ion-acceleration by a reflexing electron-beam—model and scaling *Phys. Fluids* **27** 1815–20
- Maksimchuk A, Gu S, Flippo K, Umstadter D and Bychenkov V Y 2000 Forward ion acceleration in thin films driven by a high-intensity laser *Phys. Rev. Lett.* **84** 4108–11
- Maksimchuk A *et al* 2004 High-energy ion generation by short laser pulses *Plasma Phys. Rep.* **30** 473–95
- Malka G and Miquel J L 1996 Experimental confirmation of ponderomotive-force electrons produced by an ultrarelativistic laser pulse on a solid target *Phys. Rev. Lett.* **77** 75–8
- Malka V *et al* 2002 Electron acceleration by a wake field forced by an intense ultrashort laser pulse *Science* **298** 1596–600
- Malka V *et al* 2004 Practicability of proton therapy using compact laser systems *Med. Phys.* **31** 1587–92
- Mančić A, Fuchs J, Antici P, Gaillard S A and Audebert P 2008 Absolute calibration of photostimulable image plate detectors used as (0.5–20 MeV) high-energy proton detectors *Rev. Sci. Instrum.* **79** 073301
- Mančić A *et al* 2010 Picosecond short-range disordering in isochorically heated aluminum at solid density *Phys. Rev. Lett.* **104** 035002
- Mancossi M, Santos J J, Batani D, Faure J, Debayle A, Tikhonchuk V T and Malka V 2006 Study of ultraintense laser-produced fast-electron propagation and filamentation in insulator and metal foil targets by optical emission diagnostics *Phys. Rev. Lett.* **96** 125002
- Markey K *et al* 2010 Spectral enhancement in the double pulse regime of laser proton acceleration *Phys. Rev. Lett.* **105** 195008
- Marsh S P (ed) 1980 *LASL Shock Hugoniot Data* (Berkeley, CA: University of California Press)
- Matsukado K *et al* 2003 Energetic protons from a few-micron metallic foil evaporated by an intense laser pulse *Phys. Rev. Lett.* **91** 215001
- Matsuoka T *et al* 2010 Energetic electron and ion generation from interactions of intense laser pulses with laser machined conical targets *Nucl. Fusion* **50** 055006
- McKenna P *et al* 2003 Effect of target heating on ion-induced reactions in high-intensity laser-plasma interactions *Appl. Phys. Lett.* **83** 2763–5
- McKenna P *et al* 2004 Characterization of proton and heavier ion acceleration in ultrahigh-intensity laser interactions with heated target foils *Phys. Rev. E* **70** 036405
- McKenna P *et al* 2005 Broad energy spectrum of laser-accelerated protons for spallation-related physics *Phys. Rev. Lett.* **94** 084801
- McKenna P, Lindau F, Lundh O, Neely D, Persson A and Wahlström C-G 2006 High-intensity laser-driven proton acceleration: influence of pulse contrast *Phil. Trans. R. Soc. A* **364** 711–23
- McKenna P *et al* 2007a Lateral electron transport in high-intensity laser-irradiated foils diagnosed by ion emission *Phys. Rev. Lett.* **98** 145001
- McKenna P *et al* 2007b Low- and medium-mass ion acceleration driven by petawatt laser plasma interactions *Plasma Phys. Control. Fusion* **49** B223–31
- McKenna P *et al* 2008 Effects of front surface plasma expansion on proton acceleration in ultraintense laser irradiation of foil targets *Laser Part. Beams* **26** 591–6
- McKenna P *et al* 2011 Effect of lattice structure on energetic electron transport in solids irradiated by ultraintense laser pulses *Phys. Rev. Lett.* **106** 185004
- McLaughlin W L, Chen, Y-D, Soares C G, Miller A, Van Dyk G and Lewis D F 1991 Sensitometry of the response of a new radiochromic film dosimeter to gamma radiation and electron beams *Nucl. Instrum. Methods Phys. Res. A* **302** 165–76
- McLeod J H 1954 The Axicon: a new type of optical element *J. Opt. Soc. Am.* **44** 592–7
- Milton B F 1995 Commercial compact cyclotrons in the 90s *Proc. 14th Int. Conf. ‘Cyclotrons and their Applications’ (Cape Town, South Africa)* pp 99–106
- Mironov S Y *et al* 2012 Second-harmonic generation of super powerful femtosecond pulses under strong influence of cubic nonlinearity *IEEE J. Sel. Top. Quantum Electron.* **18** 7–13
- Modena A *et al* 2002 Electron acceleration from the breaking of relativistic plasma-waves *Nature* **377** 606–8
- Mora P 2003 Plasma expansion into a vacuum *Phys. Rev. Lett.* **90** 185002
- Mora P 2005 Thin-foil expansion into a vacuum *Phys. Rev. E* **72** 056401
- Mori M *et al* 2006 New detection device for Thomson parabola spectrometer for diagnosis of the laser-plasma ion beam *Plasma Fusion Res.* **1** 042–4
- Morita T, Esirkepov T Zh, Bulanov S V, Koga J and Yamagawa M 2008 Tunable high-energy ion source via oblique laser pulse incident on a double-layer target *Phys. Rev. Lett.* **100** 145001
- Moulton P F 1986 Spectroscopic and laser characteristics of Ti : Al₂O₃ *J. Opt. Soc. Am. B* **3** 125–33
- Mourou G A, Barty C P J and Perry M D 1998 Ultrahigh-intensity lasers: physics of the extreme on a tabletop *Phys. Today* **51** 22–8
- Mourou G, Chang Z, Maksimchuk A, Nees J, Bulanov S V, Bychenkov V Y, Esirkepov T Z, Naumova N M, Pegoraro F and Ruhl H 2002 On the design of experiments for the study of relativistic nonlinear optics in the limit of single-cycle pulse duration and single-wavelength spot size *Plasma Phys. Rep.* **28** 12–27
- Mourou G, Tajima T and Bulanov S V 2006 Optics in the relativistic regime *Rev. Mod. Phys.* **76** 309–71
- Mróz W, Norek P, Prokopiuk A, Parys P, Pfeifer M, Laska L, Stockli M P, Fry D and Kasuya K 2000 Method of processing ion energy distributions using a Thomson parabola ion spectrograph with a microchannel plate image converter camera *Rev. Sci. Instrum.* **71** 1417–20
- Murakami Y, Kitagawa Y, Sentoku Y, Mori M, Kodama R, Tanaka K A, Mima K and Yamanaka T 2001 Observation of proton rear emission and possible gigagauss scale magnetic fields from ultra-intense laser illuminated plastic target *Phys. Plasmas* **8** 4138–43
- Murakami M and Basko M M 2006 Self-similar expansion of finite-size non-quasi-neutral plasmas into vacuum: relation to the problem of ion acceleration *Phys. Plasmas* **13** 012105

- Murakami M *et al* 2008 Radiotherapy using a laser proton accelerator *AIP Conf. Proc.* **1024** 275–300
- Nagatomo H, Johzaki T, Mima K and Sakagami H 2010 Multi-scale simulations for laser plasma physics *High Performance Computing on Vector Systems 2009* ed M Resch *et al* (Berlin: Springer) pp 243–50
- Nakamura S *et al* 2006 Real-time optimization of proton production by intense short-pulse laser with time-of-flight measurement *Japan. J. Appl. Phys.* **45** L913–L916
- Nakamura S *et al* 2007 High-quality laser-produced proton beam realized by the application of a synchronous RF electric field *Japan. J. Appl. Phys.* **46** L717–L720
- Nakamura T and Mima K 2008a Magnetic-dipole vortex generation by propagation of ultraintense and ultrashort laser pulses in moderate-density plasmas *Phys. Rev. Lett.* **100** 205006
- Nakamura T, Mima K, Ter-Avetisyan S, Schnurer M, Sokollik T, Nickles P V and Sandner W 2008b Lateral movement of a laser-accelerated proton source on the target's rear surface *Phys. Rev. E* **77** 036407
- Nakamura T, Bulanov S V, Esirkepov T Zh and Kando M 2010 High-energy ions from near-critical density plasmas via magnetic vortex acceleration *Phys. Rev. Lett.* **105** 135002
- Nakatsutsumi M, Kon A, Buffeau S, Audebert P, Fuchs J and Kodama R 2010 Fast focusing of short-pulse lasers by innovative plasma optics toward extreme intensity *Opt. Lett.* **35** 2314–6
- Naumova N, Schlegel T, Tikhonchuk V T, Labaune C, Sokolov I V and Mourou G 2009 Hole boring in a DT pellet and fast-ion ignition with ultraintense laser pulses *Phys. Rev. Lett.* **102** 025002
- Nayuki T, Oishi Y, Fujii T, Nemoto K, Kayoiji T, Okano Y, Hironaka Y, Nakamura K G, Kondo K and Ueda K 2003 Thin tape target driver for laser ion accelerator *Rev. Sci. Instrum.* **74** 3293–6
- Nayuki T, Oishi Y, Fujii T, Takano K, Wang X, Andreev A A, Nemoto K and Ueda K-i 2006 Influence of target properties and laser fluence on energetic protons accelerated by a laser-produced plasma *J. Appl. Phys.* **100** 043111
- Neely D, Foster P, Robinson A, Lindau F, Lundh O, Persson A, Wahlström C G and McKenna P 2006 Enhanced proton beams from ultrathin targets driven by high contrast laser pulses *Appl. Phys. Lett.* **89** 021502
- Nemoto K, Maksimchuk A, Banerjee S, Flippo K, Mourou G, Umstadter D and Bychenkov V Y 2001 Laser-triggered ion acceleration and table top isotope production *Appl. Phys. Lett.* **78** 595–7
- Nilson P M *et al* 2006 Magnetic reconnection and plasma dynamics in two-beam laser–solid interactions *Phys. Rev. Lett.* **97** 255001
- Niroomand-Rad A, Blackwell R, Coursey B, Gall K, Galvin J, McLaughlin W, Meigooni A, Nath R, Rodgers J and Soare C 1998 Radiochromic film dosimetry: recommendations of AAPM Radiation Therapy Committee Task Group 55 *Med. Phys.* **25** 2093–115
- Nishihara K, Amitani H, Murakami M, Bulanov S V and Esirkepov T Z 2001 High energy ions generated by laser driven Coulomb explosion of cluster *Nucl. Instrum. Methods Phys. Res. A* **464** 98–102
- Nishiuchi M *et al* 2006 The laser proton acceleration in the strong charge separation regime *Phys. Lett. A* **357** 339–44
- Nishiuchi M *et al* 2007 Repetitive highly collimated intense proton beam with sub-MeV energy range driven by a compact few terawatt femto-second laser *Appl. Phys. B* **87** 615–21
- Nishiuchi M *et al* 2008 Efficient production of a collimated MeV proton beam from a polyimide target driven by an intense femtosecond laser pulse *Phys. Plasmas* **15** 053104
- Nishiuchi M, Daito I, Ikegami M, Daido H, Mori M, Orimo S, Ogura K, Sagisaka A, Yogo A and Pirozhkov A 2009 Focusing and spectral enhancement of a repetition-rated, laser-driven, divergent multi-MeV proton beam using permanent quadrupole magnets *Appl. Phys. Lett.* **94** 061107
- Nishiuchi M *et al* 2010 Measured and simulated transport of 1.9 MeV laser-accelerated proton bunches through an integrated test beam line at 1 Hz *Phys. Rev. ST Accel. Beams* **13** 071304
- Noda A *et al* 2006 Phase rotation scheme of laser-produced ions for reduction of the energy spread *Int. J. Laser Phys.* **16** 647–53
- Norreys P A, Fews A P, Beg F N, Bell A R, Dangor A E, Lee P, Nelson M B, Schmidt H, Tatarakis M and Cable M D 1998 Neutron production from picosecond laser irradiation of deuterated targets at intensities of 10^{19} cm^{-2} *Plasma Phys. Control. Fusion* **40** 175–82
- Norreys P A *et al* 1999 Observation of a highly directional γ -ray beam from ultrashort, ultraintense laser pulse interactions with solids *Phys. Plasmas* **6** 2150–6
- Notley M M *et al* 2009 Central laser facility high power laser capabilities applied to x-ray laser science *X-Ray Laser 2008: Proc. 11th Int. Conf. on X-Ray Lasers (Belfast, 17–22 Aug. 2008)* (*Springer Proceedings in Physics* vol 130) (Berlin: Springer) pp 59–63
- Nuckolls J, Wood L, Thiessen A and Zimmerman G 1972 Laser compression of matter to super-high densities: thermonuclear (CTR) applications *Nature* **239** 139–42
- Nürnberg F *et al* 2009 Radiochromic film imaging spectroscopy of laser-accelerated proton beams *Rev. Sci. Instrum.* **80** 033301
- Offermann D T *et al* 2010 Carbon ion beam focusing using laser irradiated, heated diamond hemispherical shells *J. Phys.: Conf. Ser.* **244** 022053
- Offermann D T, Flippo K A, Cobble J, Schmitt M J, Gaillard S A, Bartal T, Rose D V, Welch D R, Geissel M and Schollmeier M 2011 Characterization and focusing of light ion beams generated by ultra-intensely irradiated thin foils at the kilojoule scale *Phys. Plasmas* **18** 056713
- Ogura K *et al* 2009 Proton-induced nuclear reactions using compact high-contrast high-intensity laser *Appl. Phys. Express* **2** 066001
- Okamura M, Kashiwagi H, Sakakibara K, Takano J, Hattori T, Hayashizaki N, Jameson R A and Yamamoto K 2006 High current carbon beam production with direct plasma injection scheme *Rev. Sci. Instrum.* **77** 03B303
- Oishi Y *et al* 2005 Dependence on laser intensity and pulse duration in proton acceleration by irradiation of ultrashort laser pulses on a Cu foil target *Phys. Plasmas* **12** 073102
- Okihara S I, Fujimoto M, Takahashi H, Matsukado K, Ohsuka S, Aoshima S I, Okazaki S, Ito T and Tsuchiya Y 2006 Generation of over 5 MeV carbon ions from a fibrous polytetrafluoroethylene film irradiated with a 2.4 TW, 50 fs tabletop laser *Appl. Phys. Lett.* **89** 121502
- Ollinger J M and Fessler J A 1997 Positron emission tomography *IEEE Signal Process. Mag.* **14** 43–55
- Olsen J, Kuswa G and Jones E 1973 Ion-expansion energy spectra correlated to laser plasma parameters *J. Appl. Phys.* **44** 2275–83
- Pae K H, Choi I W, Hahn S J, Cary J R and Lee J 2009 Proposed hole-target for improving maximum proton energy driven by a short intense laser pulse *Phys. Plasmas* **16** 073106
- Palaniyappan S *et al* 2010 Pulse shape measurements using single shot-frequency resolved optical gating for high energy (80 J) short pulse (600 fs) laser *Rev. Sci. Instrum.* **81** 10E103
- Palmer C A J *et al* 2011 Monoenergetic proton beams accelerated by a radiation pressure driven shock *Phys. Rev. Lett.* **106** 014801
- Passoni M and Lontano M 2004 One dimensional model for the electrostatic ion acceleration in the ultraintense laser–solid interaction *Laser Part. Beams* **22** 163–9
- Passoni M, Tikhonchuk V T, Lontano M and Bychenkov V Y 2004 Charge separation effects in solid targets and ion acceleration with a two-temperature electron distribution *Phys. Rev. E* **69** 026411
- Passoni M and Lontano 2008 Theory of light-ion acceleration driven by a strong charge separation *Phys. Rev. Lett.* **101** 115001
- Passoni M, Bertagna L and Zani A 2010a Target normal sheath acceleration: theory, comparison with experiments and future perspectives *New J. Phys.* **12** 045012

- Passoni M, Bertagna L and Zani A 2010b Energetic ions from next generation ultraintense ultrashort lasers: scaling laws for target normal sheath acceleration *Nucl. Instrum. Methods Phys. Res. A* **620** 46–50
- Patel P K, Mackinnon A J, Key M H, Cowan T E, Foord M E, Allen M, Price D F, Ruhl H, Springer P T and Stephens R 2003 Isochoric heating of solid-density matter with an ultrafast proton beam *Phys. Rev. Lett.* **91** 125004
- Pegoraro F, Esirkepov T Zh and Bulanov S V 2005 Special relativity in action in laser produced plasmas *Phys. Lett. A* **347** 133–42
- Pegoraro F and Bulanov S V 2007 Photon bubbles and ion acceleration in a plasma dominated by the radiation pressure of an electromagnetic pulse *Phys. Rev. Lett.* **99** 065002
- Pegoraro F and Bulanov S V 2009 Nonlinear relativistic dynamics of a plasma foil driven by radiation pressure *AIP Conf. Proc.* **1153** 263–73
- Pelka A *et al* 2010 Ultrafast melting of carbon induced by intense proton beams *Phys. Rev. Lett.* **105** 265701
- Perego C, Zani A, Batani D and Passoni M 2011 Extensive comparison among target normal sheath acceleration theoretical models *Nucl. Instrum. Methods Phys. Res. A* **653** 89–93
- Perry M D and Mourou G 1994 Terawatt to petawatt subpicosecond lasers *Science* **264** 917–24
- Perry M D *et al* 1999 Petawatt laser pulses *Opt. Lett.* **24** 160–2
- Pfotenhauer S M *et al* 2008 Spectral shaping of laser generated proton beams *New J. Phys.* **10** 033034
- Pfotenhauer S M, Jäckel O, Polz J, Steinke S, Schlenvoigt H-P, Heymann J, Robinson A P L and Kaluza 2010 A cascaded laser acceleration scheme for the generation of spectrally controlled proton beams *New J. Phys.* **12** 103009
- Ping Y *et al* 2008 Absorption of short laser pulses on solid targets in the ultrarelativistic regime *Phys. Rev. Lett.* **100** 085004
- Pirozhkov A S, Bulanov S V, Esirkepov T Zh, Mori M, Sagisaka A and Daido H 2006a Generation of high-energy attosecond pulses by the relativistic-irradiance short laser pulse interacting with a thin foil *Phys. Lett. A* **349** 256–63
- Pirozhkov A S, Bulanov S V, Esirkepov T Zh, Mori M, Sagisaka A and Daido H 2006b Attosecond pulse generation in the relativistic regime of the laser–foil interaction: the sliding mirror model *Phys. Plasmas* **13** 013107
- Pirozhkov A S *et al* 2009a Diagnostic of laser contrast using target reflectivity *Appl. Phys. Lett.* **94** 241102
- Pirozhkov A S *et al* 2009b Laser-driven proton acceleration and plasma diagnostics with J-KAREN laser *Proc. SPIE* **7354** 735414
- Pirozhkov A S, Daido H, Nishiuchi M and Ogura K 2010 Laser-driven proton acceleration research and development *Advances in Solid State Lasers Development and Applications* ed M Grishin (Vukovar: InTech) (<http://sciyo.com/articles/show/title/laser-driven-proton-acceleration-research-and-development>)
- Popov V S 2004 Tunnel and multiphoton ionization of atoms and ions in a strong laser field (Keldysh theory) *Phys.—Usp.* **47** 855–85
- Popov K I, Rozmus W, Bychenkov V Y, Naseri N, Capjack C E and Brantov A V 2010 Ion response to relativistic electron bunches in the blowout regime of laser-plasma accelerators *Phys. Rev. Lett.* **105** 195002
- Prasad R *et al* 2010 Calibration of Thomson parabola—MCP assembly for multi-MeV ion spectroscopy *Nucl. Instrum. Methods Phys. Res. A* **623** 712–5
- Price D F, More R M, Walling R S, Guethlein G, Shepherd R L, Stewart R E and White W E 1995 Absorption of ultrashort laser pulses by solid targets heated rapidly to temperatures 1–1000 eV *Phys. Rev. Lett.* **75** 252
- Priedhorsky W, Lier D, Day R and Gerke D 1981 Hard-x-ray measurements of 10.6 μm laser-irradiated targets *Phys. Rev. Lett.* **47** 1661–4
- Pukhov A 2001 Three-dimensional simulations of ion acceleration from a foil irradiated by a short-pulse laser *Phys. Rev. Lett.* **86** 3562–5
- Qiao B, Zepf M, Borghesi M and Geissler M 2009 Stable GeV ion-beam acceleration from thin foils by circularly polarized laser pulses *Phys. Rev. Lett.* **102** 145002
- Quinn K *et al* 2009 Laser-driven ultrafast field propagation on solid surfaces *Phys. Rev. Lett.* **102** 194801
- Racolta P M, Popa-Simil L, Pascoiu G, Ivanov G E A and Alexandreanu B 1995 *Application of Particle and Laser Beams in Materials Technology (NATO Science Series E: Applied Sciences)* ed P Misaelides (London: Kluwer) p 415
- Ragozin E N *et al* 2006 Extreme ultraviolet diagnostics of preformed plasma in laser-driven proton acceleration experiments *Rev. Sci. Instrum.* **77** 123302
- Ravasio A *et al* 2010 Proton radiography of a shock-compressed target *Phys. Rev. E* **82** 016407
- Robinson A P L, Zepf M, Kar S, Evans R G and Bellei C 2008 Radiation pressure acceleration of thin foils with circularly polarized laser pulses *New J. Phys.* **10** 013021
- Robinson A P L, Gibbon P, Pfotenhauer S M, Jäckel O and Polz J 2009a Scaling of the proton density reduction scheme for the laser acceleration of proton beams with a narrow energy spread *Plasma Phys. Control. Fusion* **51** 024001
- Robinson A P L *et al* 2009b Spectral modification of laser-accelerated proton beams by self-generated magnetic fields *New J. Phys.* **11** 083018
- Robinson A P L, Gibbon P, Zepf M, Kar S, Evans R G and Bellei C 2009c Relativistically correct hole-boring and ion acceleration by circularly polarized laser pulses *Plasma Phys. Control. Fusion* **51** 024004
- Robson L *et al* 2007 Scaling of proton acceleration driven by petawatt-laser-plasma interactions *Nature Phys.* **3** 58–62
- Romagnani L *et al* 2005 Dynamics of electric fields driving the laser acceleration of multi-MeV protons *Phys. Rev. Lett.* **95** 195001
- Romagnani L *et al* 2008 Observation of collisionless shocks in laser-plasma experiments *Phys. Rev. Lett.* **101** 025004
- Rosinski M *et al* 2005 Application of laser ion source for ion implantation technology *Vacuum* **78** 435–8
- Ross I N, Matousek P, Towrie M, Langley A J and Collier J L 1997 The prospects for ultrashort pulse duration and ultrahigh intensity using optical parametric chirped pulse amplifiers *Opt. Commun.* **144** 125–33
- Roth M *et al* 2001 Fast ignition by intense laser-accelerated proton beams *Phys. Rev. Lett.* **86** 436–9
- Roth M *et al* 2002 Energetic ions generated by laser pulses: a detailed study on target properties *Phys. Rev. ST Accel. Beams* **5** 061301
- Roth M *et al* 2005 Laser accelerated ions in ICF research prospects and experiments *Plasma Phys. Control. Fusion* **47** B841–50
- Roth M *et al* 2006 Laser accelerated heavy particles—tailoring of ion beams on a nano-scale *Opt. Commun.* **264** 519–24
- Roth M *et al* 2009 Proton acceleration experiments and warm dense matter research using high power lasers *Plasma Phys. Control. Fusion* **51** 124039
- Ruhl H, Cowan T and Fuchs J 2004 The generation of micro-fiducials in laser-accelerated proton flows, their imaging property of surface structures and application for the characterization of the flow *Phys. Plasmas* **11** L17–L20
- Rykovanov S G, Schreiber J, Meyer-ter-Vehn J, Bellei C, Henig A, Wu H C and Geissler M 2008 Ion acceleration with ultra-thin foils using elliptically polarized laser pulses *New J. Phys.* **10** 113005
- Rygg J R *et al* 2008 Proton radiography of inertial fusion implosions *Science* **319** 1223–5
- Safronov K V, Vikhlyaev D A, Vladimirov A G, Gavrilov D S, Gorokhov S A, Kakshin A G, Loboda E A, Lykov V A,

- Mokicheva E S and Potapov A V 2008 Experimental study of the acceleration of protons emitted from thin foils irradiated by ultrahigh-contrast laser pulses *JETP Lett.* **88** 716–9
- Safronov K *et al* 2010 Proton acceleration from targets irradiated by ultraintense high-contrast laser pulses in the SOKOL-P facility *Plasma Phys. Rep.* **36** 443–5
- Sagisaka A *et al* 2006 Development of a two-color interferometer for observing wide range electron density profiles with a femtosecond time resolution *Appl. Phys. B* **84** 415–9
- Sagisaka A *et al* 2008 Simultaneous generation of a proton beam and terahertz radiation in high-intensity laser and thin-foil interaction *Appl. Phys. B* **90** 373–7
- Sagisaka A, Nagatomo H, Daido H, Pirozhkov A S, Ogura K, Orimo S, Mori M, Nishiuchi M, Yogo A and Kado M 2009 Experimental and computational characterization of hydrodynamic expansion of a preformed plasma from thin-foil target for laser-driven proton acceleration *J. Plasma Phys.* **75** 609–17
- Santala M I K *et al* 2001 Production of radioactive nuclides by energetic protons generated from intense laser-plasma interactions *Appl. Phys. Lett.* **78** 19–21
- Santos J J *et al* 2002 Fast electron transport in ultraintense laser pulse interaction with solid targets by rear-side self-radiation diagnostics *Phys. Rev. Lett.* **89** 025001
- Santos J J, Debayle A, Nicolai P, Tikhonchuk V, Mancossi M, Batani D, Guennie-Tafo A, Faure J, Malka V and Honrubia J J 2007 Fast-electron transport and induced heating in aluminum foils *Phys. Plasmas* **14** 103107
- Sarukura N, Ishida Y and Nakano H 1991 Generation of 50-fsec pulse from a pulse-compressed, cw, passively mode-locked Ti-sapphire laser *Opt. Lett.* **16** 153–5
- Sawada S 2010 J-PARK facility *Nucl. Phys. A* **834** 701c–706c
- Schawlow A L and Townes C H 1958 Infrared and optical masers *Phys. Rev.* **112** 1940–9
- Schlegel T, Naumova N, Tikhonchuk V T, Labaune C, Sokolov I V and Mourou G 2009 Relativistic laser piston model: ponderomotive ion acceleration in dense plasmas using ultraintense laser pulses *Phys. Plasmas* **16** 083103
- Schollmeier M *et al* 2008 Controlled transport and focusing of laser-accelerated protons with miniature magnetic devices *Phys. Rev. Lett.* **101** 055004
- Schreiber J *et al* 2004 Source-size measurements and charge distributions of ions accelerated from thin foils irradiated by high-intensity laser pulses *Appl. Phys. B* **79** 1041–5
- Schreiber J *et al* 2006a Analytical model for ion acceleration by high-intensity laser pulses *Phys. Rev. Lett.* **97** 045005
- Schreiber J, Ter-Avetisyan S, Risso E, Kalachnikov M P, Nickles P V, Sandner W, Schramm U, Habs D, Witte J and Schnurer 2006b Pointing of laser-accelerated proton beams *Phys. Plasmas* **13** 033111
- Schwoerer H, Gibbon P, Dusterer S, Behrens R, Ziener C, Reich C and Sauerbrey R 2001 MeV X rays and photoneutrons from femtosecond laser-produced plasmas *Phys. Rev. Lett.* **86** 2317–20
- Schwoerer H, Pfotenhauer S, Jackel O, Amthor K-U, Liesfeld B, Ziegler W, Sauerbrey R, Ledingham K W D and Esirkepov T 2006 Laser-plasma acceleration of quasi-monoenergetic protons from microstructured targets *Nature* **439** 445–8
- Séguin F H *et al* 2003 Spectrometry of charged particles from inertial-confinement-fusion plasmas *Rev. Sci. Instrum.* **74** 975–95
- Sentoku Y *et al* 2000 High density collimated beams of relativistic ions produced by petawatt laser pulses in plasmas *Phys. Rev. E* **62** 7271
- Sentoku Y, Bychenkov V Y, Flippo K, Maksimchuk A, Mima K, Mourou G, Sheng Z M and Umstadter D 2002 High-energy ion generation in interaction of short laser pulse with high-density plasma *Appl. Phys. B* **74** 207–15
- Sentoku Y, Cowan T E, Kemp A and Ruhl H 2003 High energy proton acceleration in interaction of short laser pulse with dense plasma target *Phys. Plasmas* **10** 2009–15
- Shah R C, Johnson R P, Shimada T and Hegelich B M 2009 Large temporal window contrast measurement using optical parametric amplification and low-sensitivity detectors *Eur. Phys. J. D* **55** 305–9
- Silk E C H and Barnes R S 1959 Examination of fission fragment tracks with an electron microscope *Phil. Mag.* **4** 970–2
- Silva L O, Mati M, Davies R, Fonseca R A, Ren C, Tsung F S and Mori W B 2004 Proton shock acceleration in laser-plasma interaction *Phys. Rev. Lett.* **92** 015002
- Snavely R A *et al* 2000 Intense high-energy proton beams from petawatt-laser irradiation of solids *Phys. Rev. Lett.* **85** 2945–8
- Sokollik T *et al* 2008 Transient electric fields in laser plasmas observed by proton streak deflectometry *Appl. Phys. Lett.* **92** 091503
- Spence D E, Kean P N, Sibbett W 1991 60-fsec pulse generation from a self-mode-locked Ti: sapphire laser *Opt. Lett.* **16** 42–4
- Spencer I *et al* 2001 Laser generation of proton beams for the production of short-lived positron emitting radioisotopes *Nucl. Instrum. Methods Phys. Res. B* **183** 449–58
- Spencer I *et al* 2003 Experimental study of proton emission from 60-fs, 200-mJ high-repetition-rate tabletop-laser pulses interacting with solid targets *Phys. Rev. E* **67** 046402
- Stamper J A 1991 Review on spontaneous magnetic-fields in laser-produced plasmas—phenomena and measurements *Laser Part. Beams* **9** 841–62
- Steinke S *et al* 2010 Efficient ion acceleration by collective laser-driven electron dynamics with ultra-thin foil targets *Laser Part. Beams* **28** 215–21
- Strangio C *et al* 2007 Production of multi-MeV per nucleon ions in the controlled amount of matter mode (CAM) by using causally isolated targets *Laser Part. Beams* **25** 85–91
- Streeter M J V *et al* 2011 Relativistic plasma surfaces as an efficient harmonic generator *New J. Phys.* **13** 023041
- Strehl K 1895 Aplanatische und fehlerhafte Abbildung im Fernrohr *Z. Instrumenten.* **15** 362–70
- Strickland D and Mourou G 1985 Compression of amplified chirped optical pulses *Opt. Commun.* **55** 447–9
- Sumita T, Imaizumi M, Matsuda S, Ohshima T, Ohi A and Itoh H 2003 Proton radiation analysis of multi-junction space solar cells *Nucl. Instrum. Methods Phys. Res. B* **206** 448–51
- Summers G P, Burke E A and Xapsos M A 1995 Displacement damage analogs to ionizing radiation effects *Radiat. Meas.* **24** 1–8
- Sun G-Z, Ott E, Lee Y C and Guzdar P 1987 Self-focusing of short intense pulses in plasmas *Phys. Fluids* **30** 526–32
- Symes D R, Wegner U, Ahlsweide H C, Streeter M J V, Gallegos P L, Divall E J, Smith R A, Rajeev P P and Neely D 2010 Ultrafast gated imaging of laser produced plasmas using the optical Kerr effect *Appl. Phys. Lett.* **96** 011109
- Tabak M, Hammer J, Glinsky M E, Kruer W L, Wilks S C, Woodworth J, Campbell E M, Perry M D and Mason R 1994 Ignition and high gain with ultrapowerful lasers *Phys. Plasmas* **1** 1626–34
- Tajima T and Dawson J M 1979 Laser electron accelerator *Phys. Rev. Lett.* **43** 267–70
- Takács S, Tárkányi F, Hermann A and Paviotti de Corcuera R 2003 Validation and upgrading of the recommended cross section data of charged particle reactions used for production of PET radioisotopes *Nucl. Instrum. Methods Phys. Res. B* **211** 169–89
- Tan T H, McCall G H and Williams A H 1984 Determination of laser intensity and hot-electron temperature from fastest ion velocity measurement on laser-produced plasma *Phys. Fluids* **27** 296–301
- Tanaka K A *et al* 2000 Studies of ultra-intense laser plasma interactions for fast ignition *Phys. Plasmas* **7** 2014–22

- Tanaka K A, Yabuuchi T, Sato T, Kodama R, Kitagawa Y, Takahashi T, Ikeda T, Honda Y and Okuda S 2005 Calibration of imaging plate for high energy electron spectrometer *Rev. Sci. Instrum.* **76** 013507
- Tanimoto T *et al* 2009 Measurements of fast electron scaling generated by petawatt laser systems *Phys. Plasmas* **16** 062703
- Tapié J-L and Mourou G 1992 Shaping of clean, femtosecond pulses at 1.053 m for chirped pulse amplification *Opt. Lett.* **17** 136–8
- Temporal M, Honrubia J J and Atzeni S 2002 Numerical study of fast ignition of ablatively imploded deuterium–tritium fusion capsules by ultra-intense proton beams *Phys. Plasmas* **9** 3098–107
- Temporal M 2006 Fast ignition of a compressed inertial confinement fusion hemispherical capsule by two proton beams *Phys. Plasmas* **13** 122704
- Ter-Avetisyan S, Schnurer M and Nickles P V 2005 Time resolved corpuscular diagnostics of plasmas produced with high-intensity femtosecond laser pulses *J. Phys. D: Appl. Phys.* **38** 863–7
- Ter-Avetisyan S, Schnurer M, Nickles P V, Kalashnikov, Risse E, Sokollik T, Sandner W, Andreev A and Tikhonchuk V 2006 Quasimonoenergetic deuteron bursts produced by ultraintense laser pulse *Phys. Rev. Lett.* **94** 145006
- Ter-Avetisyan S, Schnurer M, Nickles P V, Sokollik T, Risse E, Kalashnikov M, Sandner W and Priebe G 2008a The Thomson deflectometer: a novel use of the Thomson spectrometer as a transient field and plasma diagnostic *Rev. Sci. Instrum.* **79** 03303
- Ter-Avetisyan S, Schnurer M, Polster R, Nickles P V and Sandner W 2008b First demonstration of collimation and monochromatisation of a laser accelerated proton burst *Laser Part. Beams* **26** 637–42
- Ter-Avetisyan S, Schnurer M, Sokollik T, Nickles P V, Sandner W, Reiss H R, Stein J, Habs D, Nakamura T and Mima K 2008c Proton acceleration in the electrostatic sheaths of hot electrons governed by strongly relativistic laser-absorption processes *Phys. Rev. E* **77** 016403
- Ter-Avetisyan, Schnurer M, Nickles P V, Sandner W, Nakamura T and Mima K 2009 Correlation of spectral, spatial, and angular characteristics of an ultrashort laser driven proton source *Phys. Plasmas* **16** 043108
- Terranova F, Bulanov S, Esirkepov T, Migliozzi P, Pegoraro F and Tajima T 2005 Laser-driven proton sources: technological challenges and applications to neutrino physics *Nucl. Phys. B* **143** 572
- Teubner U, Eidmann K, Wagner U, Andiel U, Pisani F, Tsakiris G D, Witte K, Meyer-ter-Vehn J, Schlegel T and Förster E 2004 Harmonic emission from the rear side of thin overdense foils irradiated with intense ultrashort laser pulses *Phys. Rev. Lett.* **92** 185001
- Teubner U and Gibbon P 2009 High-order harmonics from laser-irradiated plasma surfaces *Rev. Mod. Phys.* **81** 445–79
- Thomson J J 1911 Rays of positive electricity *Phil. Mag.* **21** 225–49
- Tikhonchuk V T, Andreev A A, Bochkarev S G and Bychenkov V Y 2005 Ion acceleration in short-laser-pulse interaction with solid foils *Plasma Phys. Control. Fusion* **47** B869–77
- Tomassini P, Galimberti M, Giulietti A, Giulietti D, Gizzi L A and Labate L 2003 Spectroscopy of laser-plasma accelerated electrons: a novel concept based on Thomson scattering *Phys. Plasmas* **10** 917–20
- Toncian T *et al* 2006 Ultrafast laser-driven microlens to focus and energy-select mega-electron volt protons *Science* **312** 410–3
- Toncian T *et al* 2011 Properties of a plasma-based laser-triggered micro-lens *AIP Adv.* **1** 022142
- Torrisi L, Mezzasalma A M, Gammino S, Badziak J, Parys P, Wolowski J, Laska L and Franco G 2003 Implantation of ions produced by the use of high power iodine laser *Appl. Surf. Sci.* **252** 8533–8
- Vasváry L, Ditrói F, Takács S, Szabó Z, Szűcs J, Kundrák J and Mahunka I 1994 Wear measurement of the cutting edge of superhard turning tools using TLA technique *Nucl. Instrum. Methods Phys. Res. B* **85** 255–9
- Vatnitsky S M 1997 Radiochromic film dosimetry for clinical proton beams *Appl. Radiat. Isot.* **48** 643–51
- Veksler V I 1956 Coherent principle of acceleration of charged particles *Proc. CERN Symp. of High Energy Accelerators and Pion Physics (Geneva, Switzerland)* vol 1, p 80
- Veksler V I 1957 *Atomnaya Energiya* **2** 427
- Villeneuve D M, Enright G D and Richardson M C 1983 Features of lateral energy transport in CO₂-laser-irradiated microdisk targets *Phys. Rev. A* **27** 2656–62
- Vshivkov V A, Naumova N M, Pegoraro F and Bulanov S V 1998 Nonlinear electrodynamics of the interaction of ultra-intense laser pulses with a thin foil *Phys. Plasmas* **5** 2727–41
- Wakita A *et al* 2009 Characteristics of a laser-produced proton beam improved by a synchronous RF field *Nucl. Instrum. Methods Phys. Res. A* **599** 15–19
- Wei M S *et al* 2004 Ion acceleration by collisionless shocks in high-intensity-laser-underdense-plasma interaction *Phys. Rev. Lett.* **93** 155003
- Wilks S C, Krueer W L, Tabak M and Langdon A B 1992 Absorption of ultra-intense laser-pulses *Phys. Rev. Lett.* **69** 1383–6
- Wilks S C and Krueer W L 1997 Absorption of ultrashort, ultra-intense laser light by solids and overdense plasmas *IEEE J. Quantum Electron.* **33** 1954–68
- Wilks S C, Langdon A B, Cowan T E, Roth M, Singh M, Hatchett S, Key M H, Pennington D, MacKinnon A and Snavely R A 2001 Energetic proton generation in ultra-intense laser-solid interactions *Phys. Plasmas* **8** 542–9
- Willi O *et al* 2007 Laser triggered micro-lens for focusing and energy selection of MeV protons *Laser Part. Beams* **25** 71–7
- Willingale L *et al* 2006 Collimated multi-MeV ion beams from high-intensity laser interactions with underdense plasma *Phys. Rev. Lett.* **96** 245002
- Willingale L *et al* 2007 Willingale *et al* reply: Comment on ‘Collimated multi-MeV ion beams from high-intensity laser interactions with underdense plasma’ *Phys. Rev. Lett.* **98** 049504
- Willingale L *et al* 2008 Longitudinal ion acceleration from high-intensity laser interactions with underdense plasma *IEEE Trans. Plasma Sci.* **36** 1825–32
- Wu H C, Sheng Z M and Zhang J 2008 Single-cycle powerful (MW-GW) terahertz pulse generation from a wavelength-scale plasma oscillator *Phys. Rev. E* **77** 046405
- Yamanaka C, Nakai S, Matoba M, Fujita H, Kawamura Y, Daido H, Inoue M, Fukumaru F and Terai T 1981a The LEKKO VIII CO₂gas laser system *IEEE J. Quantum Electron.* **17** 1678–88
- Yamanaka C, Kato Y, Izawa Y, Yoshida K, Yamanaka T, Sasaki T, Nakatsuka M, Mochizuki T, Kuroda J and Nakai S 1981b Nd-doped phosphate glass laser systems for laser-fusion research *IEEE J. Quantum Electron.* **17** 1639–49
- Yan X Q, Lin C, Sheng Z M, Guo Z Y, Liu B C, Lu Y R, Fang J X and Chen J E 2008 Generating high-current monoenergetic proton beams by a circularly polarized laser pulse in the phase-stable acceleration regime *Phys. Rev. Lett.* **100** 135003
- Yan X Q, Wu H C, Sheng Z M, Chen J E and Meyer-ter-Vehn J 2009 Self-organizing GeV, nanocoulomb, collimated proton beam from laser foil interaction at $7 \times 10^{21} \text{ W cm}^{-2}$ *Phys. Rev. Lett.* **103** 135001
- Yates M A, van Hulsteyn D B, Rutkowski H, Kyrala G and Brackbill J U 1982 Experimental evidence for self-generated magnetic fields and remote energy deposition in laser-irradiated targets *Phys. Rev. Lett.* **49** 1702–4

- Yin L, Albright B J, Hegelich B M and Fernandez J C 2006 GeV laser ion acceleration from ultrathin targets: the laser break-out afterburner *Laser Part. Beams* **24** 291–8
- Yin L, Albright B J, Hegelich B M, Bowers K J, Flippo K A, Kwan T J T and Fernandez J C 2007 Monoenergetic and GeV ion acceleration from the laser breakout afterburner using ultrathin targets *Phys. Plasmas* **14** 056706
- Yogo A *et al* 2007 Laser prepulse dependency of proton-energy distributions in ultraintense laser–foil interactions with an online time-of-flight technique *Phys. Plasmas* **14** 043104
- Yogo A *et al* 2008 Laser ion acceleration via control of the near-critical density target *Phys. Rev. E* **77** 016401
- Yogo A *et al* 2009 Application of laser-accelerated protons to the demonstration of DNA double-strand breaks in human cancer cells *Appl. Phys. Lett.* **94** 181502
- Yogo A *et al* 2011 Measurement of relative biological effectiveness of protons in human cancer cells using a laser-driven quasimonoenergetic proton beamline *Appl. Phys. Lett.* **98** 053701
- Yonai S, Itoga T, Baba M, Nakamura T, Yokobori H and Tahara Y 2004 Benchmark experiment for cyclotron-based neutron source for BNCT *Appl. Radiat. Isot.* **61** 997–1001
- Yoon G-Y *et al* 1998 Enhancement of x-ray lasing due to wavefront correction of line-focusing optics with a large-aperture deformable mirror *Appl. Phys. Lett.* **72** 2785–7
- Yuan X H *et al* 2010 Effect of self-generated magnetic fields on fast-electron beam divergence in solid targets *New J. Phys.* **12** 063018
- Zeil K, Kraft S D, Bock S, Bussmann M, Cowan T E, Kluge T, Metzkes J, Richter T, Sauerbrey R and Schramm U 2010 The scaling of proton energies in ultrashort pulse laser plasma acceleration *New J. Phys.* **12** 045015
- Zepf M *et al* 2001 Fast particle generation and energy transport in laser–solid interactions *Phys. Plasmas* **8** 2323–30
- Zhang X, Shen B, Li X, Jin Z and Wang F 2007a Multistaged acceleration of ions by circularly polarized laser pulse: monoenergetic ion beam generation *Phys. Plasmas* **14** 073101
- Zhang X, Shen B, Li X, Jin Z, Wang F and Wen M 2007b Efficient GeV ion generation by ultraintense circularly polarized laser pulse *Phys. Plasmas* **14** 123108
- Zhang X, Shen B, Ji L, Wang F, Wen M, Wang W, Xu J and Yu Y 2010 Ultrahigh energy proton generation in sequential radiation pressure and bubble regime *Phys. Plasmas* **17** 123102
- Zhang D, Qian L, Yuan P, Zhu H, Wen S and Xu C 2008 Fiber-array-based detection scheme for single-shot pulse contrast characterization *Opt. Lett.* **33** 1969–71
- Zhidkov A G, Sasaki A, Tajima T, Auguste T, D’Olivera P, Hulin S, Monot P, Faenov A Y, Pikuz T A and Skobelev I Y 1999 Direct spectroscopic observation of multiple-charged-ion acceleration by an intense femtosecond-pulse laser *Phys. Rev. E* **60** 3273–8
- Zhidkov A and Sasaki A 2000 Effect of field ionization on interaction of an intense subpicosecond laser pulse with foils *Phys. Plasmas* **7** 1341–4
- Zhidkov A, Uesaka M, Sasaki A and Daido H 2002 Ion acceleration in a solitary wave by an intense picosecond laser pulse *Phys. Rev. Lett.* **89** 215002
- Ziener Ch, Foster P S, Divall E J, Hooker C J, Hutchinson M H R, Langley A J and Neely D 2003 Specular reflectivity of plasma mirrors as a function of intensity pulse duration, and angle of incidence *J. Appl. Phys.* **93** 768–70
- Zvorykin V D, Ionin A A, Levchenko A O, Seleznev L V, Sinitsyn D V and Ustinovskii N N 2010 Multiterawatt Ti : sapphire/KrF laser GARPUN-MTW as a test bench facility for verification of combined amplification of nanosecond and subpicosecond pulses *J. Phys.: Conf. Ser.* **244** 032014